

**Computational analysis of electronic properties and
mechanism of formation of endohedral fullerenes and
graphene with Fe atoms**

DISSERTATION

zur Erlangung des akademischen Grades

Doctor rerum naturalium

**(Dr. rer. nat.)
vorgelegt**

**der Fakultät Mathematik und Naturwissenschaften
der Technischen Universität Dresden**

von

M.Sc. Qingming Deng

geboren am 30th, June, 1984 in Heilongjiang

Eingereicht am 15,12,2015

Die Dissertation wurde in der Zeit von Februar/2015 bis Dezember/2015 im Leibniz-
Institut für Festkörper- und Werkstoffforschung Dresden angefertigt.

Abstract

In this thesis, a series of computational studies based on density functional theory (DFT) and density functional tight-binding (DFTB) is presented to deeply understand experimental results on the synthesis of endohedral fullerenes and graphene/iron hybrids at atomic level. In the first part, a simple and efficient model is proposed to evaluate the strain experienced by clusters encapsulated in endohedral metallofullerenes (EMFs). Calculations for the sole cluster, either in the neutral or the charged state, cannot be used for this goal. However, when the effect of the carbon cage is mimicked by small organic π -systems (such as pentalene and sumanene), the cluster has sufficient freedom to adopt the optimal configuration, and therefore the energetic characteristics of the EMF-induced distortion of the cluster can be evaluated. Both nitride and sulfide clusters were found to be rather flexible. Hence, they can be encapsulated in carbon cages of different size and shape. For carbide M_2C_2 cluster the situation is more complex. The optimized cluster can adopt either butterfly or linear shapes, and these configurations have substantially different metal-metal distance. Whereas for Sc_2C_2 both structures are isoenergetic, linear form of the Y_2C_2 cluster is substantially less stable than the butterfly-shaped configuration. These results show that phenomenon of the “nanoscale fullerene compression” once proposed by Zhang *et al.* (*J. AM. CHEM. SOC.* (2012),134(20)) should be “nanoscale fullerene stretching”. Finally, the results also reveal that both Ti_2S and Ti_2C_2 cluster are strained in corresponding EMF molecules, but the origin of the strain is opposite: $C_{78}-D_{3h}(5)$ cage imposes too long $Ti \cdots Ti$ distance for the sulfide cluster and too short distance for the carbide cluster.

In the second part of the thesis, possible fullerene geometries and electronic structures have been explored theoretically for the species detected in mass spectra of the Sc-EMF extract synthesized using CH_4 as a reactive gas. Two most promising candidates, namely $Sc_4C@C_{80}-I_h(7)$ and $Sc_4C_3@C_{80}-I_h(7)$, have been identified and further studied at the DFT level. For $Sc_4C@C_{80}$, the tetrahedral Sc_4 cluster with the central μ_4-C atom was found to be 10 kJ/mol more stable than the square cluster. For $Sc_4C_3@C_{80}$, the calculation showed that the most stable is the Sc_4C_3 cluster in which the triangular C_3 moiety is η^3 - and η^2 -coordinated to Sc atoms. Whereas $Sc_4C@C_{80}$ has rather small HOMO-LUMO

gap and low ionization potential, the HOMO-LUMO gap of $\text{Sc}_4\text{C}_3@\text{C}_{80}$ is substantially higher and exceeds that of $\text{Sc}_4\text{C}_2@\text{C}_{80}$.

In the third part, computational studies of structures and reactivity are described for a new type of EMFs with a heptagon that has been produced in the arc-discharge synthesis. DFT computations predict that $\text{LaSc}_2\text{N}@C_s(\text{hept})-\text{C}_{80}$ is more stable than $\text{LaSc}_2\text{N}@D_{5h}-\text{C}_{80}$, so the former should be synthesized in much higher yield than observed. This disagreement may be ascribed to the kinetic factors rather than thermodynamic stability. Because of prospective applications of this EMFs by introducing functional groups, the influence of the heptagon on the chemical properties have been further evaluated. Thermodynamically and kinetically preferred reaction sites are studied computationally for Prato and Bingel-Hirsch cycloaddition reactions. In both types of reactions the heptagon is not affected, and chemical reactivity is determined by the adjacent pentalene units. Thermodynamically controlled Prato addition is predicted to proceed regioselectively across the pentagon/pentagon edges, whereas the most reactive sites in kinetically-controlled Bingel-Hirsch reaction are the carbon atoms next to the pentagon/pentagon edge.

Fourth, although various EMFs have been successfully synthesized and characterized, the formation mechanism is still not known in details, and hence control of the synthesis products is rather poor. Therefore, EMF self-assembly process in Sc/carbon vapor in the presence and absence of cooling gas (helium) and reactive gas (NH_3 and CH_4) is systematically investigated using quantum chemical molecular dynamics (QM/MD) simulations based on the DFTB potentials. The cooling gas effect is that the presence of He atoms accelerates formation of pentagons and hexagons and reduces the size of formed carbon cages in comparison to the analogous He-free simulations. As a result, the Sc/C/He system yields a large number of successful trajectories (i.e. leading to the Sc-EMFs) with more realistic cage-size distribution than the Sc/C system. Encapsulation of Sc atoms within the carbon cage was found to proceed via two parallel mechanisms. The main mechanism involves nucleation of the several hexagons and pentagons with Sc atoms already at the early stages of the carbon vapor condensation. In such proto-cages, both Sc-C σ -bonds and coordination bonds between Sc atoms and the π -system of the carbon network are present. Sc atoms are thus rather labile and can move along the carbon network, but the overall bonding is sufficiently strong to prevent dissociation even at high temperatures. Further growth of the carbon cage results in encapsulation of one or two Sc atoms within the forming fullerene. Another encapsulation mechanism is

observed in rare cases. In this process, the closed cage is formed with Sc being a part of the carbon network, i.e. being bonded by three or four Sc–C σ -bonds. However, such intermediates are found to be unstable, and transform into the endohedral fullerenes within few picoseconds of annealing. In perfect agreement with experimental studies, extension of the simulation to Fe and Ti showed that Fe-EMFs are not formed at all, whereas Ti is prone to form Ti-EMFs with small cage sizes, including Ti@C₂₈-*T_d* and Ti@C₃₀-C_{2v}(3).

The role of “reactive gas” in the EMF synthesis is revealed in dedicated simulations of the fullerene formation in the presence of several molecules of CH₄ or NH₃. When concentration of reactive gas is high, carbon vapor tends to form graphene flakes or other carbon species terminated by hydrogen atoms, whereas the yield of empty fullerenes is very low. Conversely, with additional metal atoms (Sc) and the same number of NH₃ molecules, the yield of fullerenes constantly increase from 5 to 65% which is ascribed to the catalytic activity of metal atoms in the nucleation of carbon cages already at early stage. Moreover, due to the presence of hydrogen atoms from the reactive gas, the carbon cage formation requires much longer time, which provides sufficient reaction time to encapsulate 3 or 4 Sc atoms within one cage. It explains preferential formation of clusterfullerenes in experiments with reactive gas. At the same time, monometallofullerenes and dimetallofullerenes are the main products in absence of reactive gas. We also provide possible growth mechanisms of carbide and cyano-clusterfullerenes in details to elucidate how the intracuster goes into the cage. A possible growth mechanism of nitride clusterfullerenes has been proposed based on DFT results.

In the last part, a free-standing crystalline single-atom thick layer of Fe has been studied theoretically. By investigating the energy difference, ΔE , between a suspended Fe monolayer and a nanoparticle using the equivalent number of Fe atoms, one can estimate that the largest stable membrane should be ca. 12 atoms wide or $3 \times 3 \text{ nm}^2$ which is in excellent agreement with the experimental observation. Otherwise, the possibility of C, O, N atoms embedded into the Fe membrane can be fully excluded by DFTB and DFT simulations, which agrees with electron energy loss spectroscopy (EELS) measurement. A significantly enhanced magnetic moment for single atom thick Fe membranes ($3.08 \mu_B$) is predicted by DFT as compared to the bulk BCC Fe ($2.1 \mu_B$), which originates from the 2D nature of the Fe membrane since the d_z^2 orbital is out-of-plane while the d_{xy} orbital is in-plane.

Keywords: endohedral metallofullerenes, internal strain, electronic structure, cycloaddition reactions, density functional theory, molecular dynamics, iron membrane, graphene edge

Contents

Abstract	I
Contents	V
List of Figures	VII
List of Tables	XIII
Chapter 1. Introduction	1
1.1 Introduction of endohedral metallofullerenes	1
1.2 Stability of endohedral metallofullerenes	4
1.2.1 Charge transfer phenomenon	4
1.2.2 Cage form factor and strain in the endohedral cluster	5
1.3 Hypothetical models of fullerene formation	8
Chapter 2. Methodology	13
2.1 Density Functional Theory (DFT)	13
2.2 Molecular Dynamics Simulations	15
2.4 DFTB	19
2.4.1 Zeroth order non-self-consistent charge approach, NCC-DFTB	19
2.4.2 Second order self-consistent charge extension, SCC-DFTB	21
Chapter 3. Clusters encapsulated in Endohedral Metallofullerenes: How strained they are?	27
3.1 Introduction	27
3.2 Model and Computational Methods	28
3.3 Results and Discussion	30
3.3.1 Nitride clusterfullerenes	30
3.3.2 Sulfide clusterfullerenes	32
3.3.3 Carbide clusterfullerenes	35
3.3.4 $Ti_2C_2@C_{78}$ and $Ti_2S@C_{78}$	42
3.4 Conclusions	44
Chapter 4. Carbide clusterfullerenes with odd number of carbon atoms: molecular and electronic structures of $Sc_4C@C_{80}$, $Sc_4C@C_{82}$, and $Sc_4C_3@C_{80}$	45
4.1 Introduction	45
4.2. Computational studies of $Sc_4C_{1-3}@C_{80}$	46
4.2.1 General remarks on Sc_4 -type clusterfullerenes	46
4.2.2 Molecular and electronic structure of $Sc_4C@C_{80}$	47
4.2.3 Molecular and electronic structure of $Sc_4C_3@C_{80}$	50
4.2.5 Vibrational spectra of $Sc_4C_x@C_{80}$	56
4.2.6 $Sc_4C_3@C_{78}$ and $Sc_4C@C_{82}$	60
4.3. Conclusions	61
Chapter 5. Structures of heptagon-containing $LaSc_2N@C_5(\text{hept})-C_{80}$ and its Prato and Bingel-Hirsch cycloaddition	63
5.1 Introduction	63

5.2. Computational Methods	63
5.3 Results and Discussion	64
5.4 Conclusions	79
Chapter 6. QM/MD simulations of dynamic metallofullerene self-Assembly with cooling gas and reactive gas	81
6.1 Introduction.....	81
6.2 Models and Computational Methods	82
6.3 Results and Discussion	84
6.3.1 Influence of He on the empty fullerene formation	84
6.3.2 Sc endohedral fullerene formation	89
6.3.3 Effect of reactive gas during Sc based EMFs formation	99
6.3.4 Iron and Titanium metallofullerenes	110
6.4 Conclusions.....	115
Chapter 7. Free-standing single-atom thick iron membranes suspended in graphene pores	117
7.1 Introduction.....	117
7.2 Computational Methods.....	118
7.3 Results and Discussion	118
7.4 Conclusions.....	128
Reference	131
Acknowledgement.....	131
List of publications	157

List of Figures

- Figure 1.1** Optimized structures by DFT of $\text{Sc}_3\text{N}@C_{2n}$ isomers with $2n=68-76$ (C-gray, N-blue, Sc-pink, pairs of adjacent pentagons are highlighted in black). Rproduced from Ref. 73 7
- Figure 1.2** Pentagon road to empty fullerene formation 9
- Figure 1.3** The Stone-Wales rearrangement 10
- Figure 2.1** Molecular dynamics simulation flow chart 17
- Figure 3.1** (a) Structural formulae of pentalene C_8H_6 ; (b) coordination of pentalene by Sc atom (the same coordination is used for Y atoms); (c) structural formulae of modified sumanene C_{21}H_9 ; (d) coordination of sumanene fragment by Ti. 29
- Figure 3.2** (a) DFT-optimized molecular structures of $\text{Sc}_3\text{N}(\text{C}_8\text{H}_6)_3$; Sc is magenta, nitrogen is blue, carbon atoms are grey, hydrogen atoms are not shown for clarity. (b-d) Energy profiles computed for: (b) variation of Sc–N bond lengths in $\text{Sc}_3\text{N}(\text{C}_8\text{H}_6)_3$; (c) variation of Sc–N–Sc angle in $\text{Sc}_3\text{N}(\text{C}_8\text{H}_6)_3$; (d) variation of Y–N bond lengths in $\text{Y}_3\text{N}(\text{C}_8\text{H}_6)_3$. In the range of computed values (110–130°), Y–N–Y angle energy profile is identical to that for Sc analogue. 31
- Figure 3.3** DFT optimized structures of $\text{Sc}_2\text{S}(\text{C}_8\text{H}_6)_2$ (a) and Sc-sulfide clusterfullerenes: (b) $\text{Sc}_2\text{S}@C_{70}-C_2(7892)$; (c) $\text{Sc}_2\text{S}@C_{72}-C_3(10528)$; (d) $\text{Sc}_2\text{S}@C_{74}-C_2(13333)$; (e) $\text{Sc}_2\text{S}@C_{82}-C_{3v}(8)$; (f) $\text{Sc}_2\text{S}@C_{82}-C_3(6)$ 32
- Figure 3.4** Energy profiles computed for (a) variation of Sc–S bond lengths in $\text{Sc}_2\text{S}(\text{C}_8\text{H}_6)_2$; (b) variation of Sc–S–Sc angle in $\text{Sc}_2\text{S}(\text{C}_8\text{H}_6)_2$; (c) variation of Y–S bond lengths in $\text{Y}_2\text{S}(\text{C}_8\text{H}_6)_2$; (b) variation of Y–S–Y angle in $\text{Y}_2\text{S}(\text{C}_8\text{H}_6)_2$ 34
- Figure 3.5** Butterfly (a) and linear (b) configurations of the Sc_2C_2 cluster in $\text{Sc}_2\text{C}_2(\text{C}_8\text{H}_6)_2$. (c-g) DFT optimized structures of Sc-carbide clusterfullerenes: (c) $\text{Sc}_2\text{C}_2@C_{70}-C_2(7892)$; (d) $\text{Sc}_2\text{C}_2@C_{72}-C_3(10528)$; (e) $\text{Sc}_2\text{C}_2@C_{80}-C_{2v}(5)$; (f) $\text{Sc}_2\text{C}_2@C_{82}-C_{3v}(8)$; (g) $\text{Sc}_2\text{C}_2@C_{84}-D_{2d}(23)$. (h-l) DFT optimized structures of Y-carbide clusterfullerenes: (h) $\text{Y}_2\text{C}_2@C_{82}-C_{3v}(8)$; (i) $\text{Y}_2\text{C}_2@C_{84}-C_1(51383)$; (j) $\text{Y}_2\text{C}_2@C_{88}-D_2(35)$; (k) $\text{Y}_2\text{C}_2@C_{92}-D_3(85)$; (l) $\text{Y}_2\text{C}_2@C_{100}-D_5(450)$. Sc atoms are magenta, Y atoms are green, carbon atoms are grey or red (in adjacent pentagon pairs), hydrogen atoms in (a-b) are omitted for clarity. 36
- Figure 3.6** Energy profiles computed for (a) variation of Sc–Sc distance in $\text{Sc}_2\text{C}_2(\text{C}_8\text{H}_6)_2$; (b) variation of Y–Y distance in $\text{Y}_2\text{C}_2(\text{C}_8\text{H}_6)_2$. The energy minima corresponding to butterfly and linear configurations of M_2C_2 clusters are pointed by arrows. 37
- Figure 3.7** Evolution of the $\text{Y}_2\text{C}_2(\text{C}_8\text{H}_6)_2$ molecular structure with the increase of the Y···Y distance from 4.5 to 6.0 Å. The energies are: (a) 1.0 $\text{kJ}\cdot\text{mol}^{-1}$; (b) 4.2 $\text{kJ}\cdot\text{mol}^{-1}$; (c) 15.2 $\text{kJ}\cdot\text{mol}^{-1}$; (d) 20.0 $\text{kJ}\cdot\text{mol}^{-1}$; (e) 18.6 $\text{kJ}\cdot\text{mol}^{-1}$; (f) 16.6 $\text{kJ}\cdot\text{mol}^{-1}$. Y atoms are green, carbon atoms are grey, hydrogen atoms are omitted for clarity. 40
- Figure 3.8** The energy profiles computed for $[\text{M}_2\text{C}_2]^{4+}$ ions with variation of the M–M distance. 41
- Figure 3.9** DFT-optimized molecular structures of $\text{Ti}_2\text{C}_2@C_{78}$ (a), $\text{Ti}_2\text{S}@C_{78}$ (b), $\text{Ti}_2\text{C}_2(\text{C}_{21}\text{H}_9)_2$ (c), and $\text{Ti}_2\text{S}(\text{C}_{21}\text{H}_9)_2$. Ti atoms are cyan, sulfur is yellow, carbon atoms are grey, hydrogen atoms in (c) and (d) are omitted for clarity. 42
- Figure 3.10** Energy profiles computed for (a) variation of Ti–S bond lengths in $\text{Ti}_2\text{S}(\text{C}_{21}\text{H}_9)_2$; (b) variation of Ti–S–Ti angle in $\text{Ti}_2\text{S}(\text{C}_{21}\text{H}_9)_2$; (c) variation of Ti–Ti distance in $\text{Ti}_2\text{C}_2(\text{C}_{21}\text{H}_9)_2$ 43
- Figure 4.1** Positive ion mode MALDI-TOF mass-spectrum of the extract of Sc-EMFs obtained by arc-discharge in the Sc- CH_4 system: (a) measured without matrix; (b) measured with sulfur as a matrix. The inset in (a) shows isotopic pattern and mass numbers of the group of peaks corresponding to

Sc ₄ C ₈₁ ⁺ . These values are in good agreement with theoretical mass numbers for the three main peaks of Sc ₄ C ₈₁ (1151.82, 1152.83, and 1153.83). Reproduced from Ref. 174	46
Figure 4.2 DFT-optimized molecular structures of Sc ₄ C@C ₈₀ isomers with tetrahedral (a) and square (b) cluster. Part (c) shows enlarged structure of the tetrahedral (left) and planar (right) Sc ₄ C clusters and transition state between them (middle).	48
Figure 4.3 Frontier molecular orbitals in the Sc ₄ C@C ₈₀ isomers with tetrahedral (a) and square (b) cluster.	49
Figure 4.4 DFT-optimized molecular structures of Sc ₄ C ₃ @C ₈₀ (a) and Sc ₄ C ₂ @C ₈₀ (b). Enlarged structures of the Sc ₄ C ₃ (c) and Sc ₄ C ₂ (d) are shown with the atom numbering used in the QTAIM analysis.	51
Figure 4.5 Frontier molecular orbitals in the Sc ₄ C ₃ @C ₈₀ (a) and Sc ₄ C ₂ @C ₈₀ (b).	52
Figure 4.6 DFT-computed IR spectra of Sc ₄ C _x @C ₈₀ (x = 1–3). Blue arrows mark cluster modes with considerable IR intensity in the 400–1600 cm ⁻¹	59
Figure 5.1 Two views of the structure of LaSc ₂ N@C _s (hept)-C ₈₀ as determined by a single crystal X-ray diffraction study of the cocrystal, LaSc ₂ N@C _s (hept)-C ₈₀ •2Ni(OEP)•2toluene, drawn with 30% thermal contours. The position of the heptagon and the two adjacent pentalene units are highlighted in red in the left figure while only the heptagon, which is non-planar, is coloured red in the right drawing. The dashed lines show the contacts between the metal ion and the nearest cage carbon atoms. The second orientation of the cage, the toluene molecules, and the hydrogen atoms were omitted for clarity. Reproduced from Ref. 45	64
Figure 5.2 Molecular structures of LaSc ₂ N@C ₈₀ isomers and related structures: (a) LaSc ₂ N@C _s (hept)-C ₈₀ ; (b) LaSc ₂ N@I _h -C ₈₀ . The cage fragment near the heptagon is highlighted in red, the C-C bond which is “rotated” in the 7/5-6/6 realignment is highlighted in light green; (c) LaSc ₂ N@C ₇₈ with the C ₂ (22010) cage which can be obtained from the LaSc ₂ N@C _s (hept)-C ₈₀ via removal of one C ₂ fragment; position of the removed fragment is shown as “ghost” atoms; the second pentagon pair in C ₂ (22010)-C ₇₈ formed after removal of the C ₂ fragment is highlighted in black; (d) LaSc ₂ N@C _{3v} (8)-C ₈₂ ; removal of the yellow-highlighted C ₂ fragment from this structure and formation of missing C-C bonds (thin yellow lines) yields the LaSc ₂ N@C _s (hept)-C ₈₀ . In all structures, Sc atoms are magenta, La is orange, and N is blue.	67
Figure 5.3 HOMO and LUMO of LaSc ₂ N@C _s (hept)-C ₈₀ (isovalue 0.035 a.u.) computed at the PBE/TZVP level.	68
Figure 5.4 Schlegel diagram of LaSc ₂ N@C _s (hept)-C ₈₀ with quasi-spiral numbering system of carbon atoms used in this work. Heptagon and pairs of adjacent pentagons are highlighted in green and red, respectively, whereas position of Sc and La atoms are marked with magenta and orange circles.	69
Figure 5.5 The most stable LaSc ₂ N@C ₈₀ (CH ₂) ₂ NH, bis LaSc ₂ N@C ₈₀ [(CH ₂) ₂ NH] ₂ , and Sc ₃ N@C ₆₈ (CH ₂) ₂ NH cycloadducts. Heptagon ring is highlighted in green, pentalene units are highlighted in red. N, Sc and La atoms are blue, magenta and orange, respectively.	71
Figure 5.6 Schlegel diagram of Sc ₃ N@C ₆₈	73
Figure 5.7 The most kinetically favoured LaSc ₂ N@C ₈₀ CH ₂ adducts: 11–16 , 1–12 , 3–8 . Also shown is the LUMO of LaSc ₂ N@C _s (hept)-C ₈₀	78
Figure 6.1 (a,b) Evolution of the number of (a) C-sp and (b) C-sp ² atoms during MD simulations of the fullerene formation with different number of He atoms. (c,d) Evolution of the number of carbon atoms in C ₂ and C ₃ fragments and chains of different length (C ₄ –C ₁₀ , C ₁₁ –C ₂₀ , and C ₂₁ –C ₄₀) in MD simulations without He (c) and in the presence of 200 He atoms (d). Each curve is averaged over 10 independent trajectories.	83

- Figure 6.2** (a-c) Evolution of the number of (a) pentagons, (b) hexagons, and (c) heptagons formed during MD simulations of the fullerene formation with different number of He atoms; (d) number of pentagons, hexagons, and heptagons formed in simulation with 200 He atoms. Each curve is averaged over 10 independent trajectories. 85
- Figure 6.3** (a-c) Examples of the carbon clusters obtained in He-free conditions: (a) “flake”, (b) half-cage; (c) fullerene cage with carbon chain “antenna”. (d-e) Typical structures with endohedral carbons obtained at high He pressure: 300 He (d) and 500 He (e). Endohedral carbon atoms are colored in red. Note that the structure obtained with 500 He is more compact (has less empty space) than the structure obtained with 300 He atoms. 87
- Figure 6.4** Comparison of the number of produced fullerenes in 10 trajectories with different number of He atoms (0, 100, and 200) and with/without 6 Sc atoms. For trajectories with Sc atoms, the yield of Sc-EMF is shown separately (rightmost columns) as well as together with empty cages (columns in the middle). 89
- Figure 6.5** (a) Bonding of Sc to small carbon clusters at different moments of the trajectory in He-free conditions: two Sc–C₂ fragments, bonding to carbon chain, carbon ring, simultaneous bonding to C₂ and two C₄ fragments, and bonding to an early nucleation center. (b-e) development of the flake from nucleation center, (e-h) curling of the flake up into the fullerene cage. (i) the “final” cage after additional 140 ps annealing. Note that Sc atom in (f) is bonded to the forming cage and simultaneously to C₂ and longer chains. Also shown above (h) and (i) is the “networked” Sc atom on a place of a carbon atom in the fullerene cage: this fragment was formed near 260 ps and survived till the end of simulation at 400 ps. 91
- Figure 6.6** Left: the fraction of time when metal atom has at least one carbon atom at the distance shorter than 3 Å. Each histogram is based on 60 values obtained after analysis of 10 trajectories in 80×80×80 Å³ box with 200 C atoms, 6 metal atoms (Sc, Ti, or Fe), and indicated number of He atoms (0, 100, 200, or 300). Right: the same for metal-He distance shorter than 3 Å. In effect, the left column describes the net lifetime of metal-carbon bonds, whereas the right column visualizes the frequency of metal-He collisions. Note that when metal atom is encapsulated in the fullerene, it always has carbon atoms at short distances and at the same time it is shielded from He atoms. Hence, fast formation of Ti-EMFs results in the sharp Ti–C distribution at 85–100% and the short time of exposure to He, which can be compared to that of Fe not forming EMFs. 92
- Figure 6.7** Examples of Sc-EMFs formed in MD simulation: (a) in the He-free 200 C/6 Sc system inside the 80×80×80 Å³ box; (b) in the 200 C/6 Sc/100 He system inside the 80×80×80 Å³ box; (c) in the 100 C/6 Sc/100 He system inside the 80×80×80 Å³ box; (d) in the 100 C/6 Sc/50 He system in the 50×50×50 Å³ box. Carbon atom and CC bonds are shown as cyan (pentagons and hexagon), light green (heptagon and other non-classical rings), or pink (carbene atoms). Endohedral carbons in Sc₂C₂@C₉₈ are shown in blue. 94
- Figure 6.8** Representative examples of the Sc encapsulation during the Sc-EMF formation: (a) 200 C/6 Sc/100 He system, the procedure resulted in dimetallofullerenes Sc₂@C₈₂ (an empty fullerene was also formed in this trajectory); three Sc atoms are coordinated to the growing cage just before its closure (310 ps), but only two of them are eventually encapsulated within the fullerene; (b) 100 C/6 Sc/50 He system; two Sc atoms were coordinated to the carbon cluster, but only of them is eventually encapsulated; note that the cage after its closure is rather small and is fused to two large carbon rings, which are absorbed by the cage in the course of further annealing to make Sc@C₇₂ (see also Fig. 6.7d and Fig. 6.9); (c) another trajectory from the 100 C/6 Sc/50 He system; the structure formed at 66 ps is highly defected Sc@C₆₆, which then grew to Sc@C₉₆ (see Fig. 6.7d) by capture of other carbon fragments. 95
- Figure 6.9** An overview of the Sc-EMF formation mechanism based on the trajectory, which resulted in Sc@C₇₂. Detailed mechanism of the cage formation in this trajectory is shown in Fig. 6.8b. Each color filled correspond to the carbon cluster, its height scales as the number of carbon atoms: after 100 ps, only two clusters are left, Sc@C₇₂ and C₂₈. 96
- Figure 6.10** (a) Yields of empty fullerenes (EFs) as function of different number of NH₃ in absence of Sc atoms. (b) Yields of EFs and Sc based EMFs as function of different number of Sc with 8NH₃. (c)

Yields of EFs and Sc based EMFs as function of different number of NH ₃ with 6Sc. (d) Average time of successful fullerene formation based on the systems of (a) and (c). EFs and EMFs are colored in light cyan and pink respectively.	99
Figure 6.11 (a) and (b) are a typical empty fullerene and a Sc based EMFs. (c) and (d) are graphene flake and half cage as PAHs productions respectively. (e) An open Sc based EMFs after 400 ps. Carbon, nitrogen, hydrogen, scandium atoms are coloured in cyan, blue, white and pink, respectively. Heptagon and pentagon pairs are highlighted in light green and red.	101
Figure 6.12 Evolution of the average number of (a) C-sp and (b) C-sp ² atoms during 20 times MD simulations of the fullerene formation with 50 C ₂ (light cyan), 50 C ₂ /8 NH ₃ (blue) and 50 C ₂ /8 NH ₃ /6 Sc atoms (pink).	102
Figure 6.13 Evolution of the average number of (a) pentagons (b) hexagons and (c) heptagons during 20 times MD simulations of the fullerene formation with 50 C ₂ (light cyan), 50 C ₂ /8 NH ₃ (blue) and 50 C ₂ /8 NH ₃ /6 Sc atoms (pink). (d) Average number of pentagons (red), hexagons (purple), and heptagons (light green) formed in simulation with 50 C ₂ /8 NH ₃ /6 Sc atoms.	102
Figure 6.14 (a) is an open cage fullerene coordinating with 4 Sc atoms and CN unit inside. (b) is cyano-clusterfullerene after annealing another 400 ps from (a). (c) is tri-metallofullerene clusterfullerene after annealing another 400 ps from (a) without H. Carbon, nitrogen, hydrogen, scandium atoms are coloured in cyan, blue, white and pink, respectively.	103
Figure 6.15. Key snapshots of half empty carbon cage (a) and the cage saturated with H atoms (b) coordinating with single Sc atom.	104
Figure 6.16 The number of intracage Sc atoms in the endohedral fullerenes formed after 400 ps in the system containing 100 C, 15 Sc/40 He/6 CH ₄ (green bars) or without CH ₄ (red bars). 20 trajectories were studied for each system. Due to very long formation time with CH ₄ gas, Sc atoms encapsulated by half-cages were also counted.	105
Figure 6.17 Key typical snapshot of EMF formation at early stage (5ps) with 50 C ₂ (cyan), 40 He (not shown), 4 NH ₃ gas and 10 N (blue for N and white for H) and 10 Sc (pink).	107
Figure 6.18 Key snapshots of cyano-clusterfullerene formation. CN at 200 ps unit is highlighted in red-green ball-stick.	107
Figure 6.19 Reaction path from Sc ₃ CN@C ₈₀ to Sc ₃ N@C ₈₀ +C by GGA/DFT. Carbon, Sc and N are coloured in grey, pink and blue, respectively.	109
Figure 6.20 Stable Ti-C _n clusters and EMFs formed in MD simulations: (a) Ti-C ₁₀ ring; (b) Ti@C ₁₆ proto-cage; (c-g) structures with common Ti@C ₂₈ -T _d motif with additional (c) carbon atom, (d) carbon chain, (e) two chains, (f) fused rings, and (g) fused “flake”; (h) defect-free Ti@C ₃₀ -C _{2v} (3); (i) Ti@C ₃₀ -C _{2v} (3) with an additional C ₃ chain; (j) Ti@C ₆₆ ; (k) small-cage di-Ti EMF with an additional carbon chain C ₉ ; (l) large-cage di-Ti EMF. In (c-i) fragments of regular Ti@C ₂₈ or Ti@C ₃₀ cages are shown in light green, all other carbon are shown in cyan color, Ti atoms are dark red.	111
Figure 6.21 Mechanism of the Ti@C ₃₀ -C _{2v} (3) formation in MD simulations. (a) formation of the Ti-C ₉ cluster and its growth to Ti-C ₂₇ ; (b) condensation of long chains into the fullerene cage surrounding Ti atom; (c, c') molecular structure and Schlegel diagram of Ti@C ₂₇ resembling Ti@C ₂₈ -T _d (1) with one atom missing (position of the missing atom is shown as a “ghost” atom in (c) and is indicated with pale lines in (c')); (d) attachment of the C ₃ chain to Ti@C ₂₇ and its migration along the fullerene surface to the orifice with subsequent ingestion; (e) Ti@C ₃₀ isomer with four-membered ring, its SW transformation into the structure with two four-membered ring, and formation of Ti@C ₃₀ -C _{2v} (3) after the next SW transformation; (f) formation of Ti@C ₃₀ -C _{2v} (3) from the isomer with one four-membered ring in a direct SW transformation; (g) Schlegel diagrams describing stages (e) and (f), relative energies are for PBE/TZ2P-optimized structures. The Ti-C distances shorter than 2.8 Å are denoted as bonds for the structures formed before 90 ps; at later stages these bonds are omitted for the sake of clarity. In (e) and (f), square rings are highlighted in	

purple, and the bonds to undergo a SW transformation are highlighted in yellow (or green in Schlegel diagrams); in (e) and (f) this coloring is preserved in $Ti@C_{30}-C_{2v}(3)$ to highlight its genetic relationships to the structures with square rings..... 113

Figure 7.1 Graphene perforations and different Fe clusters. (A) graphene perforations (highlighted). (B) BCC Fe nanocrystal with atomic structure and image simulation as inset. (C) Hexagonal close packed Fe nanocrystal which has a step on it. The atomic structure and an image simulation is provided in the inset. (D) A several atom cluster embedded in graphene. (E) Many individual Fe atoms residing on the edges of graphene. (F,G) Two typical mono-atomic Fe layers suspended in a perforation in graphene. The scale bars is 1nm. Reproduced from Ref. 127 119

Figure 7.2 Left figure represents a virtual Fe carbide configuration. DFT calculations indicate such a configuration is unstable. Gold atoms (Fe), Brown atoms (C). Right figure is dynamical calculation of a C atom in a 2D Fe membrane under electron beam irradiation. The C atom cannot stay in the lattice as it is easily ejected by the electron beam..... 121

Figure 7.3 The interface between a mono-atomic Fe layer and graphene and local strain mapping (A) LVACTEM image of the Z1 configuration as illustrated in (D). The insets shows the highlighted edge structure with carbon (black) atoms and Fe (orange) atoms highlighted. (B,C) LVACTEM images of the Z2 and A1 configurations (E and F respectively). The insets shows the highlighted edge structure with carbon (black) atoms and Fe (orange) atoms highlighted. The scale bars in (A-C) are 1nm. (D-I) first principle calculation results showing top and cross-section views of different single Fe atoms binding to different graphene edge configurations. The insets for (D-F) show the corresponding image simulations from the stick and ball structure provided in the main panel. (J, K) The (110) Fe with armchair edge visible in a LVACTEM image and first principle calculated configuration, respectively. The scale bar in (J) is 0.5 nm. 122

Figure 7.4 Formation and collapse of a suspended single-atom Fe layer under electron irradiation (A) A Fe cluster at the edge of a graphene pore (highlighted). (B) After three seconds, the Fe atoms move in to the perforation and form a single atom Fe membrane sealing the entire graphene pore. (C-J) Continued electron irradiation leads to the collapse of the 2D Fe membrane. The Fe (110) - armchair graphene interfaces are the most stable and are highlighted in (E,F). All scale bars denote 1nm. Reproduced from Ref. 127..... 125

Figure 7.5 The energy difference between a 2D Fe membrane and a 3D Fe nanoparticle. The crossover where a nanoparticle becomes more favorable than a 2D membrane occurs around a membrane width comprised 12 atoms. 126

Figure 7.6 (A) Partial density of states (pDOS) for bulk BCC Fe and (B) pDOS for a monoatomic layer of Fe with a square lattice having a lattice spacing 2.65 \AA . The colors of the lines are illustrated below each figure, i.e. d alpha stands for the spin up orbital for d electrons while d beta stands for the spin down orbital for d electrons..... 127

Figure 7.7 The two most probable configurations for Fe atom placement at the interface of a membrane based on DFT calculations..... 128

List of Tables

Table 3-1 Distortion energies and cluster geometry parameters (M–X bond lengths and M–X–M angles) in selected nitride and sulfide clusterfullerenes ^a	33
Table 3-2 Distortion energies and cluster geometry parameters (M–M distances and M–X–M angles) in selected carbide clusterfullerenes ^a	38
Table 4-1 Frontier MO energies, IP, and EA values (eV) of Sc ₄ C _x @C ₈₀ (x = 1–3)	53
Table 4-2 QTAIM atomic charges, <i>q</i> , in Sc ₄ C _{1–3} @C ₈₀ and selected other EMFs.....	54
Table 4-3 Intracluster delocalization indices in Sc ₄ C _{1–3} @C ₈₀ and selected other EMFs	54
Table 5-1 Relative energies (kJ/mol) of three C ₈₀ ⁶⁻ and M ₃ N@C ₈₀ cage isomers.....	65
Table 5-2 Selected LaSc ₂ N@C ₈₀ (CH ₂) ₂ NH isomers, their relative energies and HOMO-LUMO gaps, and corresponding geometry parameters in pristine LaSc ₂ N@C ₈₀	70
Table 5-3. POAV pyramidalization angles in DFT-optimized LaSc ₂ N@C _s (hept)-C ₈₀	72
Table 5-4 CC bond lengths (<i>d</i> (CC), in Å) in DFT-optimized LaSc ₂ N@C _s (hept)-C ₈₀	72
Table 5-5 Relative energies of Sc ₃ N@C ₆₈ (CH ₂) ₂ NH adducts (kJ/mol).....	74
Table 5-6 Relative energies of intermediates [LaSc ₂ N@C ₈₀ CH ₂ Br] ⁻	76
Table 5-7 The lowest energy [LaSc ₂ N@C ₈₀ CH ₂ Br] ⁻ intermediates (ΔE_1), transition states of Br ⁻ removal (ΔE_{TS}), and relative energies of corresponding LaSc ₂ N@C ₈₀ CH ₂ cycloadducts (ΔE_{CA}) ^a	77
Table 7-1 The calculated energy for different lattice distance 2D Fe membrane	121
Table 7-2 The calculated binding energy for different configurations of Fe atom and graphene edges .	124

Chapter 1. Introduction

1.1 Introduction of endohedral metallofullerenes

In 1985, Kroto *et al.* made the surprising discovery that C_{60}^+ was unusually stable among the gas-phase carbon cluster produced by laser vaporization of graphite.¹ They proposed that this stability resulted from its truncated icosahedron structure and dubbed the ion buckminsterfullerene after the famous architect Richard Buckminster Fuller. Many gas-phase experiments and theoretical investigations that followed supported this claim, and the soccer-ball structure of C_{60} was finally confirmed in 1990, when Krätschmer and Huffman discovered a method for making macroscopic quantities of C_{60} and other larger fullerenes via resistive evaporation of graphite in the arc-discharge process². Krätschmer and Huffman's finding opened up new avenues for fullerene research. Since then, fullerenes as new allotrope of carbon has always been regarded as promising material in applications for nanoelectronics, superconductors, optical switching and field-effect transistor et al. Due to the intrinsic nature of fullerene molecules, the empty space inside the carbon cages could be utilized to host atom, atoms, clusters and even molecules. Soon after the discovery of C_{60} , the encapsulation of lanthanum metal ion into fullerene cages was achieved. In the process of laser vaporization of the mixture of $LaCl_3$ and graphite, LaC_{60} was detected as the first endohedral metallofullerene which indicated a wide prospect of all lanthanide metals.³ In the following years, plenty of metals has been trapped into the fullerene cages which included not only lanthanide metals but Group I-III metals as well which further classified as mono-,⁴ di-⁵ and tri-⁶ metallofullerenes according to the number of metal ions. Clusterfullerenes are a new class of fullerene family which includes metal nitride clusters,⁷ metal carbide clusters,⁸ metal cyano clusters⁹, oxide clusters¹⁰, metal sulfide clusters¹¹, molecule¹² and inert gas¹³. First synthesis of metal-nitride clusterfullerene, $Sc_3N@C_{80}$, was achieved unexpectedly when N_2 leaked into fullerene generator chamber (which has to be avoid at that time)⁷. A small portion of nitrogen gas as nitrogen source was introduced into the Krätschmer-Huffman generator² with graphite rods containing metal oxides producing a yield 3–5% of NCFs. Generally yield of EMFs reached only 2% or less in the fullerene soot and was exceeded by 10-fold higher amounts of empty

fullerenes. While by substitution from nitrogen gas to NH_3 as the reactive gas^{14,15}, relative yield of the NCFs has been dramatically enhanced, and for the first time NCFs were obtained as the main fullerene products in the soot with less than 5% empty cages^{16,17}. The improvement of the NH_3 method is that the empty fullerenes are significantly depressed, so the task of separating the NCFs from the empty fullerenes (EF) is less complicated when compared to the synthesis with N_2 gas. Since then, great efforts have been made for enhancing the yield and producing new structures. Dunsch *et al.* proposed a new strategy to modify arc discharge process with the idea of the reactive-gas atmosphere which powerfully extended the family endohedral fullerenes.^{15,18} Metal carbide clusterfullerenes were found as the minor structures during the production of metallofullerenes. The low yield of metal carbide clusterfullerenes hindered the deep studies on their properties. Furthermore, carbide metallofullerenes are synthesized with graphite and the metal sources as the same sources as the metallofullerenes fullerenes synthesis¹⁹. As the result, it is impossible to distinguish them from conventional dimetallofullerenes from only mass spectrum in view of their structural features. Thus, many carbide metallofullerenes were first assigned erroneously to di-EMFs or tri-EMFs. Although now the C_2 unit coordinated with 2-4 metal atoms, e.g. Sc, Y, Ti, Lu, Er, Gd, in carbon cages have already been well characterized by X-ray crystallography and NMR techniques as well as DFT calculations, how the intracluster forms and where the C_2 fragment comes from (from cage or outer carbon source) is still lack of direct evidence. Zhang *et al.* isolated and characterized an intermediate carbide metallofullerenes with asymmetric cage $\text{C}_{84}\text{-C}_1(51383)$, and the cage undergoes C_2 units ejection yielding conventional C_{82} and C_{80} cages with different symmetries by “top-down” mechanisms.²⁰ Wang and *et al.* characterized a new type of EMFs whose intracluster is consistent with both of C_2 and CN units coordinated three Sc in $\text{C}_{80}\text{-I}_h(7)$ cage²¹. If internal cluster changes even when cage closure, derivation of $\text{Sc}_3\text{C}_2\text{CN}@C_{80}\text{-I}_h(7)$ may be $\text{Sc}_3\text{C}_2@C_{81}\text{N-C}_{3v}(8)$, $\text{Sc}_3\text{CN}@C_{82}\text{-C}_{3v}(8)$ under C_2 ejection and Stone–Wales transformation on the cage. Wang’s group discovered the first cyano-metallofullerene $\text{Sc}_3\text{NC}@C_{80}\text{-I}_h(7)$ by introducing mixed He and N_2 gas and verified its structure by a single-crystal X-ray diffraction measurement⁹. The intracluster of $\text{Sc}_3\text{NC}@C_{80}$ is planar with central nitrogen atom and a carbon surrounded by three Sc atoms. After that, the same group reported another type of cyano-metallofullerene $\text{Sc}_3\text{NC}@C_{78}\text{-C}_2(22010)$, whose properties were revealed by UV–vis, vibrational spectroscopy and DFT computations²². The family of oxide clusterfullerenes including $\text{Sc}_4\text{O}_2@C_{80}$ ²³ (the most

abundant), $\text{Sc}_4\text{O}_3@C_{80}$ ²⁴ and $\text{Sc}_2\text{O}@C_{82}$ ²⁵ has been produced by Stevenson *et al.* in 2008 and characterized by single-crystal X-ray diffraction studies. Sc atoms form a distorted tetrahedron, and μ^3 -oxygen atoms are placed above its faces. While in Sc_2O , the angle of Sc–O–Sc is 157° with Sc–O distances of 1.93 and 1.87 Å. ^{13}C and ^{45}Sc NMR spectroscopic study of $\text{Sc}_4\text{O}_2@C_{80}$ indicated that the cluster is fast rotating only showing two ^{13}C signals as the same as other EMFs with the $C_{80}\text{-I}_h(7)$ carbon cage. Sulfide clusterfullerenes were first discovered in 2010 and were presented to have different structures than the most abundant oxide clusterfullerenes.^{26,27} UV–vis–NIR absorption spectra of $\text{M}_2\text{S}@C_{82}$ (M = Sc, Y, Dy, Lu) resembled closely those of $\text{M}_2\text{C}_2@C_{82}\text{-C}_{3v}(8)$ which indicated that the cage of $\text{M}_2\text{S}@C_{82}$ should be $C_{82}\text{-C}_{3v}(8)$ which was also supported by DFT calculations and IR spectroscopy of $\text{Sc}_2\text{S}@C_{82}$.

Classical fullerenes contain only pentagons and hexagons, and fullerenes with polygons other than hexagon and pentagon have been extensively studied theoretically.^{28–32} The structural consequences from Euler's theorem applied to fullerenes with pentagons, hexagons, and heptagons were discussed in detail by Fowler *et al.*³⁰ For such a polyhedron, the difference between the number of pentagonal and heptagonal faces is twelve. Therefore, addition of a heptagon increases the number of pentagons by one, while decreasing the number of hexagons by two. Fowler *et al.* also showed that, in contrast to strongly destabilizing pentagon/pentagon edges, the pentagon/heptagon edges are energetically favorable and their number should be maximized.³⁰ As a result, the most stable isomers of heptagon-containing fullerenes are often non-IPR ones, in which the heptagon is fused to an adjacent pentagon pair. The heptagon-containing fullerenes are usually less stable than IPR cages, and their formation in a standard arc-discharge synthesis has never been observed. However, if the fullerene π -system is modified and some cage atoms are sp^3 -hybridized, the stability factors such as the IPR are no longer applicable. Exohedral derivatization can stabilize the “defects” (e.g., pentagon adjacencies),³³ which makes heptagon-containing fullerenes possible. Among the seven reported fullerene structures with heptagonal faces, six were obtained by “etching” the fullerene surface with fluorine or chlorine under relatively harsh conditions,^{34–38} and one was synthesized via introduction of CCl_4 to the carbon arc.³⁹ In all of these structures except for one (which has no adjacent pentagons³⁶), the pentagon adjacencies accompanying the heptagon ring are stabilized by exohedral addition of halogen atoms, consequently transforming the halogenated carbon atoms from sp^2 to sp^3 . Metal ions encapsulated inside the fullerene cage can also stabilize pentagon adjacencies.^{33,40–44} In

fact, the number of structurally characterized non-IPR endohedral metallofullerenes (EMFs) is comparable to that of IPR-obeying ones. Thus, the IPR is only a suggestion, not a rule, for endohedral fullerenes.^{43,44} Zhang and his coworkers demonstrated that endohedral metallofullerenes with heptagonal rings are successfully produced for the first time in the arc-discharge synthesis and characterize the first EMF with a heptagon, namely $\text{LaSc}_2\text{N}@C_s(\text{hept})\text{-C}_{80}$, by single-crystal X-ray diffraction.⁴⁵ Computational study reveals that an EMF with heptagonal rings can be as stable as conventional EMFs, and the reason for the missing of heptagon-containing EMFs in previous research is their low yields, not their thermodynamic stability.

1.2 Stability of endohedral metallofullerenes

1.2.1 Charge transfer phenomenon

The electron transfer from encapsulated species to the fullerene cage dramatically affects molecular structures of EMFs. Therefore, carbon cage isomers in structurally characterized EMFs are usually different from those of empty fullerenes because charging can affect relative stabilities of fullerene isomers.^{46,47} The milestone in the computational studies of EMFs was the finding that the $I_h(7)$ isomer of C_{80} , being the least stable structure for neutral C_{80} and C_{80}^{2+} , has the lowest energy structure for multiply charged C_{80}^{4-} and C_{80}^{6-} states.^{47,48} The preference of the $\text{C}_{80}\text{-}I_h(7)$ cage in highly charged state was a clear explanation why the most stable isomer is $\text{La}_2@\text{C}_{80}\text{-}I_h(7)$, as opposed to the D_2 -symmetric hollow C_{80} .⁴⁹ In another work, variation of the relative energies of negatively charged isomers of C_{82} was analyzed to explain isomerism of $\text{M}@\text{C}_{82}$.^{50,51} The most stable neutral C_{82} cage is $\text{C}_{2v}(3)$, whereas $\text{C}_{2v}(9)$ cage was proved to be the lowest energy isomer of C_{82}^{2-} and C_{82}^{3-} . Therefore, the lowest energy isomers of $\text{M}@\text{C}_{82}$ ($\text{M}=\text{Ca}$, Sc , Y , La , etc.) have the $\text{C}_{2v}(9)$ cage isomer.^{50,51} The electron transfer also explains the violation of the isolated-pentagon rule (IPR) first proposed by Kroto for empty fullerenes in 1987.⁵² This rule is strictly followed by empty fullerenes, but often violated by EMFs. Fowler and Zerbetto found that the negatively charged non-IPR $\text{C}_{2v}(1809)$ isomer of C_{60} with two pairs of adjacent pentagons is quite stable.⁴⁷ In the C_{60}^{4-} state, its relative energy equals that of the IPR C_{60} , whereas in the hexa-anionic state, the non-IPR isomer is already more stable. Pentalene (a unit of two fused pentagons) is an 8π anti-aromatic system in the neutral state, but its dianion with 10π electrons is aromatic.⁵³ Therefore, electron transfer from metal atoms to the carbon cage can stabilize non-IPR isomers. The

first computational proof was reported by Kobayashi *et al.* in 1997 in the studies of Ca@C₇₂ isomers,⁵⁴ whereas the first experimental evidence of the violation of IPR in EMFs was provided in 2000, with the isolation of Sc₂@C₆₆-C_{2v}(4348)⁴¹ and Sc₃N@C₆₈-D₃(6140).⁴⁰ Since that time, a lot of non-IPR EMFs have been reported by both experimental synthesis^{20,55-65} and theoretical predications.⁶⁶⁻⁷² Hence, the IPR is no longer valid for EMFs.

Violation of the IPR makes prediction of the most stable EMF isomers more complex than for empty fullerenes. Hence, much larger number of empty cage isomers need to be considered, and cluster inside also can have many different bonding sites for each cage isomer. Correlation between stability of EMF and appropriately charged empty fullerene isomers can substantially facilitate a search of the most stable isomers of EMFs because computations of empty fullerenes are less demanding and more reliable than those of metal-containing EMFs. Typically, thousands of isomers of empty fullerenes in their charged form are screened at the semi empirical level (e.g., AM1), whereas DFT calculations of EMFs are then performed for a limited number of the most stable isomers (10–20 isomers is usually sufficient).⁷³ This procedure has become a routine now and allows one to locate the most stable isomers within 1–2 weeks.

1.2.2 Cage form factor and strain in the endohedral cluster

The charge transfer is a key factor of determining stability of the EMFs as mentioned in the previous section (1.2.1). The role of charge transfer to the carbon cage in stabilizing a particular cage isomer is well established now^{73 74 75 49}, so we can routinely predict the most preferable isomers through charged empty fullerene isomers.^{55,56,73,76} However, this factor is not the only one determining the stabilities of EMFs. The size and the shape of the fullerene cage also need to fit the shape and size of the encapsulated cluster. High distortions of the cluster may increase its energy and even destabilize the whole clusterfullerene molecule. A typical example of the cage form factor is the case of M₃N@C₇₈. The lowest energy isomer of C₇₈⁶⁻ is D_{3h}(5), so many types of clusters are encapsulated within this cage isomer, e.g. M₂@C₇₈ (M=La, Ce),⁷⁷ Ti₂C₂@C₇₈,⁷⁸ Ti₂S@C₇₈,⁷⁹ and Sc₃N@C₇₈.⁸⁰ However, the non-IPR C₂(22010) isomer cage becomes much more stable for clusters of much larger size such as containing Y or lanthanides due to providing larger space than D_{3h}(5) cage. As a result, M₃N and even mixed-metal MSc₂N (M=Y or lanthanides) clusters prefer to be in non-IPR C₂(22010).

The absence of $\text{Sc}_3\text{N}@C_{72}$ and $\text{Sc}_3\text{N}@C_{74}$ is also caused by the absence of the suitably shaped stable isomers of C_{72} and C_{74} cages to accommodate triangular Sc_3N cluster.⁸¹ For the common cases of dimetallofullerenes $\text{M}_2@C_{72}$ ($\text{M}=\text{Ce}, \text{La}$) the most preferable C_{72}^{6-} isomer is $D_2(10611)$ owing to an elongated shape with two pentagon pairs located on the opposite poles of the molecule. This shape perfectly fits di-EMFs whose metal atoms coordinate adjacent pentagon pairs with a relatively large $\text{M}\cdots\text{M}$ distance, but is not well-matched with the triangular shape of the M_3N cluster (see figure 1.1). The Sc atoms cannot fully coordinate two pentagon pairs of $C_{72}\text{-}D_2(10611)$, so $\text{M}_3\text{N}@C_{72}\text{-}D_2(10611)$ is very unstable.⁷³ An analogous reason for the low energy C_{74}^{6-} isomers also explains why $\text{M}_3\text{N}@C_{74}$ NCFs have never been observed.⁷³ Similarly, for $\text{Sc}_3\text{N}@C_{70}\text{-}C_{2v}(7854)$, the cluster is highly distorted by coordinating three pentagon pairs without equilateral triangle shape remaining. Therefore, the yields are much lower than for other Sc-based NCFs.⁵⁵ The most stable isomer of C_{76}^{6-} cage should be the $C_{76}\text{-}C_s(17490)$, but neither Sc_3N nor Dy_3N cluster fits the cage well. However, the asymmetric shape of the mixed metal cluster DySc_2N fits the cage better, and hence, $\text{DySc}_2\text{N}@C_{76}$ is the only C_{76} -based NCF obtained in isolable amounts.⁶⁰ The size of the fullerene cage can also dramatically affect the bond lengths or even the shape of the internal clusters. For instance, a systematic experimental and computational NMR study of a series of $\text{Y}_2\text{C}_2@C_{2n}$ ($2n=82, 84, 92, 100$) by Dorn *et al.* showed that the internal yttrium carbide cluster prefers to adopt a stretched linear shape when the cage is sufficiently large (e.g., in C_{100}), whereas it bends to a compressed butterfly shape in relatively small cages (e.g., in C_{82}).⁸²

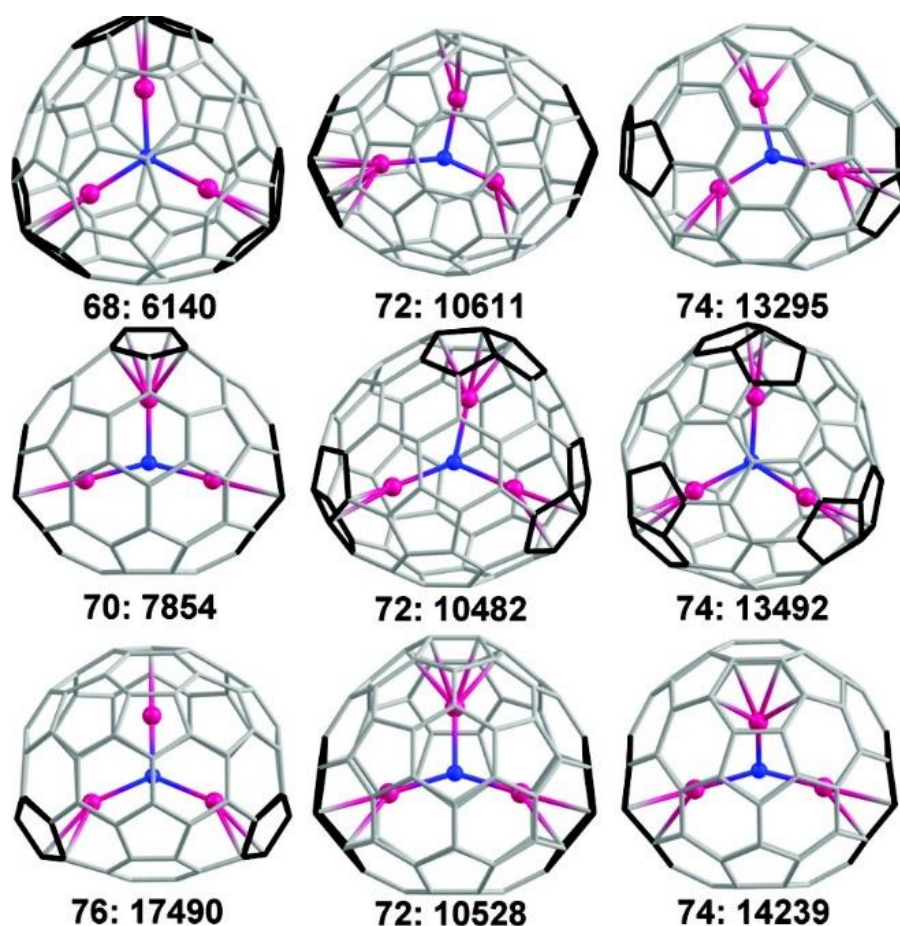


Figure 1.1 Optimized structures by DFT of $\text{Sc}_3\text{N}@C_{2n}$ isomers with $2n=68-76$ (C-gray, N-blue, Sc-pink, pairs of adjacent pentagons are highlighted in black). Reproduced from Ref. 73

From the examples discussed above, we can finally conclude that the cage form factor is much more important for stability of clusterfullerene than that of conventional EMFs. Although for the former the shape and size of the cluster play a limiting role in the cage size distribution, for mono- and dimetallofullerenes these factors are not so crucial and a much broader range of structures can be obtained.⁸³⁻⁸⁷ In spite of the obvious vital role played by the cage form factor in stability of clusterfullerenes, numerical estimation of the strain energy and optimal geometrical characteristics of encapsulated clusters are not known because in all real systems they are always templated by the carbon cage. That is, it is hard to predict which cluster geometry is strained and which is not, and how large the strain is if it is considered to be present. A computational study of the isolated cluster (e.g., Sc_3N) taken outside of the carbon cage is not relevant because of the different electronic structures of the free cluster and the same cluster inside the carbon cage. At the same time, the study of the isolated charged cluster with the formal charge taken as a real one (e.g., Sc_3N^{6+}) also does not give a reliable answer. The real charges of the

endohedral atoms in EMFs are much smaller than the formal ones because of the significant degree of covalence in metal–cage interactions,⁸⁸ so computations for highly charged naked clusters will severely overestimate Coulomb repulsion of metal atoms. This problem has been solved in this work by using a simple scheme in which metal atoms are coordinated with small organic π -systems mimicking the real electronic situation in EMFs. The endohedral cluster owns sufficient freedom to adjust its geometrical parameters in the most optimal way. Then by comparing the energetic difference between optimal and strained clusters, we can understand how large the strain of the intracluster is in the cage (see details in chapter 3).

1.3 Hypothetical models of fullerene formation

Since their discovery in 1985, scientists have been intrigued by the efficiency with which C_{60} and other fullerenes form from a condensing carbon vapor and have sought to explain this process. Thus far, it has only been ascertained that fullerenes form from small fragments of carbon based on experiments.⁸⁹ Doubtless, scientists will continue to search for answers to the fullerene formation. Until now, many mechanisms⁹⁰ have been proposed by both experiments and theoretical predictions.

Party Line mechanism

Party line mechanism first proposed by Smalley and co-workers⁹¹ assumed that small carbon particles come together to form linear chains, which then react with other chains to make monocyclic rings. Further addition of small linear chains increases the size of the rings until they form polycyclic networks in 25-35 atom range. The party line mechanism assumes that, in that size domain, polycyclic networks resembling open graphitic sheets become thermodynamically most favorable. Smalley and co-workers postulated that these graphitic sheets are more reactive than rings or linear chains because they have more dangling bonds, and that to minimize the number of dangling bonds, the polycyclic network incorporates some pentagons, causing curvature. Occasionally, one of these cuplike pieces of graphite gathers enough pentagons in the right places to force it to close into a hollow cage, thereby forming a fullerene. However, this mechanism failed to explain why C_{60} can be produced in macroscopic quantities, with yields of 20% and more.

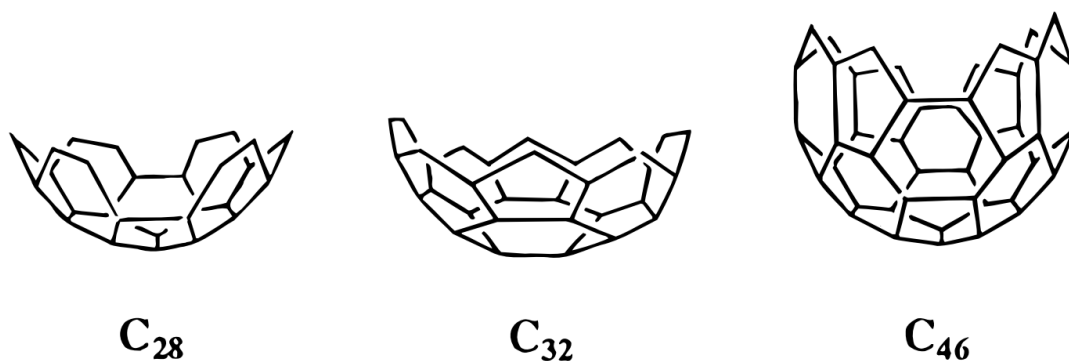


Figure 1.2 Pentagon road to empty fullerene formation

Pentagon Road

With the discovery of a bulk method for production of fullerenes, Smalley and co-workers improved their original party line scheme, proposing an appealing mechanism which they dubbed the pentagon road.^{92,93} This view of carbon nucleation assumes that the lowest-energy form of any small graphitic fragment has the following properties: (1) it is made up only of hexagons and pentagons, (2) it includes as many pentagons as possible, and (3) none of the pentagons are adjacent. In addition, according to the pentagon road, for carbon clusters that have more than 20-30 atoms but are too small to make a closed fullerene with isolated pentagons, such open graphitic cups are lower in energy than any other structure. Furthermore, in the slow-cooling environment of bulk fullerene production, annealing allows the carbon clusters to find the energy minimum among structures. Thus, thermochemical stability dictates the formation of these graphitic cups as shown as in figure 1.2, and kinetic reactivity determines the continuous growth toward fullerenes. The main mechanism for this growth, according to the original pentagon road scheme, is addition of C_2 and other small carbon particles to the reactive edges of the developing graphitic network. The closed fullerenes, once formed, have no open edges and, therefore, generally do not grow any further. Thus, any nucleation path that leads to C_{60} , as many would according to the annealing described above, is ultimately a dead end in cluster growth. There is no experimental evidence to support the presence, in the later stages of fullerene formation, of the abundant supply of small carbon particles necessary for this scheme. Curl has proposed a modification to the pentagon road, in which the growing graphitic cups react with intermediate-sized rings, according to the equation $C_{n,graphitic} + C_{x,ring} \rightarrow C_{n+2,graphitic} + C_{x-2,ring}$, thus forming a larger graphitic cup and a smaller ring. Such reactions would obviate the need for a constant supply of C_2 and C_3 . In addition, neither reactant would need to rearrange significantly,

and therefore these reactions should occur with relatively low energy barriers. However, the pentagon road can't explain the production of C_{70} which is present in significant amounts.

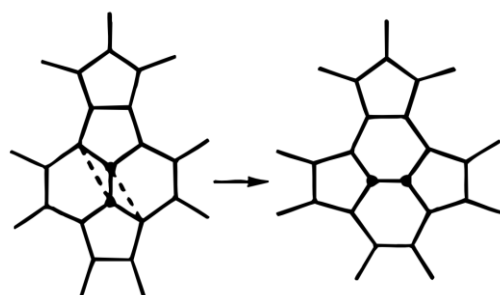


Figure 1.3 The Stone-Wales rearrangement

The Fullerene Road

Another mechanism has been proposed by James Heath⁹⁴, Smalley's doctoral student, which incorporates these clusters as intermediates. His "Fullerene Road" scheme describes the growth of fullerenes in four stages: (1) growth of carbon chains up to a length of C_{10} from initial reactants in carbon vapour. (2) growth from chains to monocyclic rings of C_{10} - C_{20} . (3) production and growth of three-dimensional reactive carbon networks C_{21} - C_{40} . (4) growth of fullerene cages by addition of small carbon species via a closed shell mechanism producing C_{60} , C_{70} and higher fullerenes as stable products. Besides, Heath also invokes the Stone-Wales rearrangement,⁹⁵ shown in fig. 1.3, as a method for producing the fullerene isomer with the fewest adjacent pentagons. The advantage of Heath's mechanism is that it is based on the most abundant, and thermodynamically most stable species in the 50-60 atom size range.⁹⁶⁻⁹⁹ However the fullerene road does not account for the fact that metal ions can be encapsulated since the early fullerene cages are too small to hold a metal ion.

Shrinking Hot Giant Road

Morokuma, Irlé, and coworkers have performed extensive quantum chemical molecular dynamics (QM/MD) simulations¹⁰⁰⁻¹⁰⁷ based on density-functional based tight-binding (DFTB)¹⁰⁸⁻¹¹¹ simulations to reveal formation mechanism of fullerenes, nanotubes and graphene. In the studies of the fullerene formation, the simulations usually were performed shooting carbon dimers (C_2 units) on a single preformed nucleus cluster at high carbon density, typically leading to a formation of giant fullerenes. Post annealing simulations revealed the possibility of shrinking such giant cages to smaller ones. Based on these simulations, a "Shrinking Hot Giant (SHG)" road of fullerene formation was proposed. According to this SHG mechanism, giant fullerenes C_n with $n > 80$ self-

assembled in a “size-up” process through irreversible autocatalytic reactions of polyyne chains and macrocycles. Such cages have a lot of defects and unsaturated carbon chains. Subsequently a “size-down” process of shrinking down in size dominated by ‘fall-off’ of exohedral carbon chains and ‘pop-out’ of C_2 units were proposed. However, regular defect-free cages were not produced so far in such simulations since with the healing of the defects the cages become more and more kinetically stable and rearrangement of the cage structure or a loss of C_2 becomes rare event and requires thus long simulation times. Besides, the scheme has limitations in that the simultaneous growth of multiple nuclei and their coalescence is automatically excluded in the C_2 shooting simulations.

Other fullerene formation mechanisms

Until now, there is still no generally accepted mechanism in the fullerene community. Moreover, it's extremely difficult to design an experiment that could directly provide evidence for any kind of mechanism. Hence, many other fullerene formation mechanisms have also been proposed by diverse research groups. For instance, Goeres and Sedlmayr suggested that C_{60} can be formed by six naphthalenic C_{10} units fused.¹¹² Wakabashi and Achiba proposed the mechanism of a "ring stacking" model¹¹³ in which a sequential stacking of monocyclic rings combined to open graphitic cup. C_{10} and C_{18} can fuse to C_{28} (see figure 1.2) as intermediate which has an open structure containing the five and six membered ring network of C_{60} . Further stacking of appropriately sized rings forms the closed fullerene C_{60} . Mechanism of endohedral fullerene formation is even less understood than that of empty fullerenes. In addition to the carbon cage formation, the role of the metal in the fullerene growth and the mechanism of the metal encapsulations needs to be clarified. Besides, one has to understand why certain conditions preferably lead to mono- and dimetallofullerenes, while different clusterfullerenes can be formed in other conditions.^{43,114,115} e.g., considering pure metal-carbon system, formation of mono-, di-, tri-metallofullerenes and carbide clusterfullerenes should be understood. Molecular dynamics simulations of EMF formation at 3000 K were performed by Maruyama and Yamaguchi using Brenner classical potentials augmented with potential functions derived from DFT calculations of small metal-containing clusters.^{116,117} For Sc, their work showed relatively weak influence of metal on the fullerene formation. Sc preferred to be located on the edge of the growing cage and could slip into the cage just before its closure. On the other hand, La was shown to have a stronger influence on the fullerene growth by serving as a nucleation center. With no doubt, finding formation mechanisms

will still remain active area of fullerene science, because of the difficulty inherent in designing an experiment that will provide conclusive evidence for any kind of mechanism.

Chapter 2. Methodology

2.1 Density Functional Theory (DFT)

Density functional theory (DFT) is a well-established method for efficiently solving the Schrödinger equation of complex many-body systems from first principles. The term first principles (also known as *ab initio*, the Latin term meaning “from the beginning”) implies that this method is only based on the laws of quantum mechanics without requiring any empiric or semi-empiric parameters involved in the calculation. This approach therefore can be expected to yield highly accurate predictions regarding different combination of atomic properties. In this thesis, the vast majority of calculations is performed with DFT to predict structural, electronic, magnetic, and mechanical properties of carbon based materials (fullerenes and graphene), such as determination of molecular or material structures, transition state structures, activation energies, reaction pathways, molecular orbitals or band structures, the assignment of various kinds of spectra etc.

The DFT method is based on the concept of energy as a function of the electron density distribution, and it is fundamentally different from the Hartree-Fock approach that is used traditionally in electronic structure calculations and aims at solving the Schrödinger equation from the many-electron wave functions. The development of the DFT method started with the demonstration by P. Hohenberg and W. Kohn¹¹⁸ that for a given system of interacting particles under the influence of an external potential $V_{ext}(\mathbf{r})$, the potential is a unique function of the electron density distribution $n(\mathbf{r})$; consequently, since $V_{ext}(\mathbf{r})$ contributes to the Hamiltonian, all the properties of the system can be expressed as functions of $n(\mathbf{r})$. One year later, W. Kohn and L. J. Sham¹¹⁹ proposed a feasible method to apply this concept to the determination of electronic structure by adding a non-interacting auxiliary system for easier calculation to predict the properties of the true interacting system. According to this method, the ground state energy E of the system can be written as a functional of the electron density distribution $n(\mathbf{r})$,

$$E[n(\mathbf{r})] = \frac{1}{2} \sum_i^N \int d^3r |\nabla \Psi_i(\mathbf{r})|^2 + \int d^3r V_{ext}(\mathbf{r}) n(\mathbf{r}) + \frac{1}{2} \int d^3r d^3r' \frac{n(\mathbf{r})n(\mathbf{r}')}{|\mathbf{r}-\mathbf{r}'|} + E_{XC}[n(\mathbf{r})] \quad (2.1)$$

Atomic units are used in this equation ($\hbar = m_e = e = 1$). The first term represents the kinetic energy of a non-interacting particle system; the second term is the interaction of electrons with the external potential $V_{ext}(\mathbf{r})$ due to the atomic nuclei and other external fields; the third term, which also can be defined as $E_H[n(\mathbf{r})]$, arises from the electron-electron classical Coulombic forces; the last term, $E_{XC}[n(\mathbf{r})]$, described as the exchange-correlation function, accounts for all the non-classical effects not described by the previous terms. The family of functions $\Psi_i(\mathbf{r})$ are called Kohn-Sham orbitals for $i = 1, \dots, N$ electrons, which correspond to the eigenfunctions of the auxiliary system of non-interacting electrons under an average effective potential, as described by the eigenvalue problem:

$$\left\{ -\frac{1}{2}\nabla^2 + V_{ext}(\mathbf{r}) + V_H[n(\mathbf{r})] + V_{XC}[n(\mathbf{r})] \right\} \Psi_i(\mathbf{r}) = \varepsilon_i \Psi_i(\mathbf{r}) \quad (2.2)$$

where $V_m[n(\mathbf{r})]$, for $m = \{H, XC\}$, are potentials of the corresponding functions $E_m[n(\mathbf{r})]$, defined as $V_m[n(\mathbf{r})] = \frac{\delta E_m[n(\mathbf{r})]}{\delta n(\mathbf{r})}$.

The electronic density $n(\mathbf{r})$ is then expressed in terms of Kohn-Sham eigenstates $\Psi_i(\mathbf{r})$ according to

$$n(\mathbf{r}) = \sum_i^N |\Psi_i(\mathbf{r})|^2 \quad (2.3)$$

Spin polarization is not taken into account in above equations, but the methodology can be easily extended to account for this, by assigning electron density distributions for electrons with spins up $n_\uparrow(\mathbf{r})$ and down $n_\downarrow(\mathbf{r})$ instead of a single electron density distribution $n(\mathbf{r})$.

In principle the KS equations allow us to determine the ground-state energy and density exactly. However, the exact exchange-correlation term E_{XC} is not known yet, so approximations need to be made depending on different practical applications. Usually E_{XC} is decomposed into $E_{XC} = E_X + E_C$. E_X can be expressed exactly at least in terms of the single particle wavefunctions $|\psi\rangle$, but exact expression for E_C is unknown.

The simplest approximation of E_{XC} that has been used successfully in condensed-matter problems is the so called Local Density Approximation (LDA); the corresponding expression for the exchange-correlation functional is

$$E_{XC}[n(\mathbf{r})] \approx E_{XC}^{LDA}[n(\mathbf{r})] = \int d^3r n(\mathbf{r}) \varepsilon_{XC}^{HEG}(n) \quad (2.3)$$

where $\varepsilon_{XC}^{HEG}(n) = \varepsilon_X^{HEG}(n) + \varepsilon_C^{HEG}(n)$ is the exchange-correlation energy density for a homogeneous electron gas. For a uniform electron gas, the exchange energy, $\varepsilon_X^{HEG}(n)$,

has an analytical form, while for the correlation energy $\varepsilon_c^{HEG}(n)$, different parameterizations have been proposed, such as the one by Perdew and Zunger¹²⁰.

LDA systematically underestimates E_C but systematically overestimates E_X , resulting in a fortuitous error cancellation, and LDA has been proven surprisingly successful for many types of calculations, like band structures, structural properties or phonon modes. The systematic character of this error cancellation is a consequence of the fact that the LDA XC-hole satisfies the sum rule which means the XC interaction displaces exactly one electron from the environment of \mathbf{r} . LDA also gives a good approximation of the spherical average of the XC-hole since the LDA XC-hole exhibits *a priori* circular symmetry. LDA works well for slowly varying electron densities' system. However, its most serious shortcomings is its underestimation of bandgaps of up to 100%. It also tends to overestimate interatomic bond strengths resulting in slightly too small bond lengths and too high cohesion energies.

A further development attempting to correct deficiencies of the LDA, is the so called Generalized Gradient Approximation (GGA), which employs not only the electron density but also its gradient in the estimation of exchange-correlation effects, in order to account for the non-homogeneity of electron density in real material systems:

$$E_{XC}[n(\mathbf{r})] \approx E_{XC}^{GGA}[n(\mathbf{r})] = \int d^3r n(\mathbf{r}) \varepsilon_{XC}(n, |\nabla n|) \quad (2.4)$$

Different expressions and parameterizations have been proposed for $\varepsilon_{XC}(n, |\nabla n|)$ within the GGA, such as the one by Perdew, Burke and Ernzerhof¹²¹, which is widely known as PBE and employed in all DFT calculations in this thesis.

2.2 Molecular Dynamics Simulations

Molecular dynamics (MD) simulations is a powerful tool for capturing different ranges of time and length scales to understand the underlying formation mechanisms occurring at the atomic scale. The central part of MD simulations is to find the solution of the atomic and molecular many body problem by using Newton's equations of motion. The forces F_i acting on the particle i of mass m_i will move it to new positions by solving

$$F_i = m_i \frac{\partial^2 r_i}{\partial t^2} \quad (2.5)$$

where F_i can be determined from the negative partial derivative of the potential function $V(r_1, r_2 \dots r_N)$

According to how the potential function or force for each step is treated, MD simulation is branched out into three methodologies. The first one is classical MD, where

forces are derived from predefined potential models by analytical gradient applications. It is used for monitoring very large systems consisting 100-100,000 atoms at ns to ms time, but the downside is that it cannot describe the electronic properties and usually its accuracy is too low. The second approach is *ab initio* MD, where forces on nuclei are obtained from the electronic structure calculations based on *first-principles* DFT. It overcomes the disadvantages of classical MD, but it is too expensive and only can deal with super small system (less than 100 atoms) within 1 ns. The third way to calculate energy potential is the density function based tight binding method which is approximation of the Kohn-Sham total energy in DFT. Without integrals DFTB is roughly 1000 times faster than DFT and can handle a large system containing more than 1000 atoms at nanosecond scale. It has been used to predict the structure and properties of carbon based materials^{104,122,123}, molecules¹²⁴, solid state^{125,126}, ions¹²⁷, or even biological systems¹²⁸ which fit both DFT and experimental results very well. In my QM/MD simulations this method has been employed as potential (see details in chapter 2.4) for obtaining the evolution of coordinates and velocities of the particles.

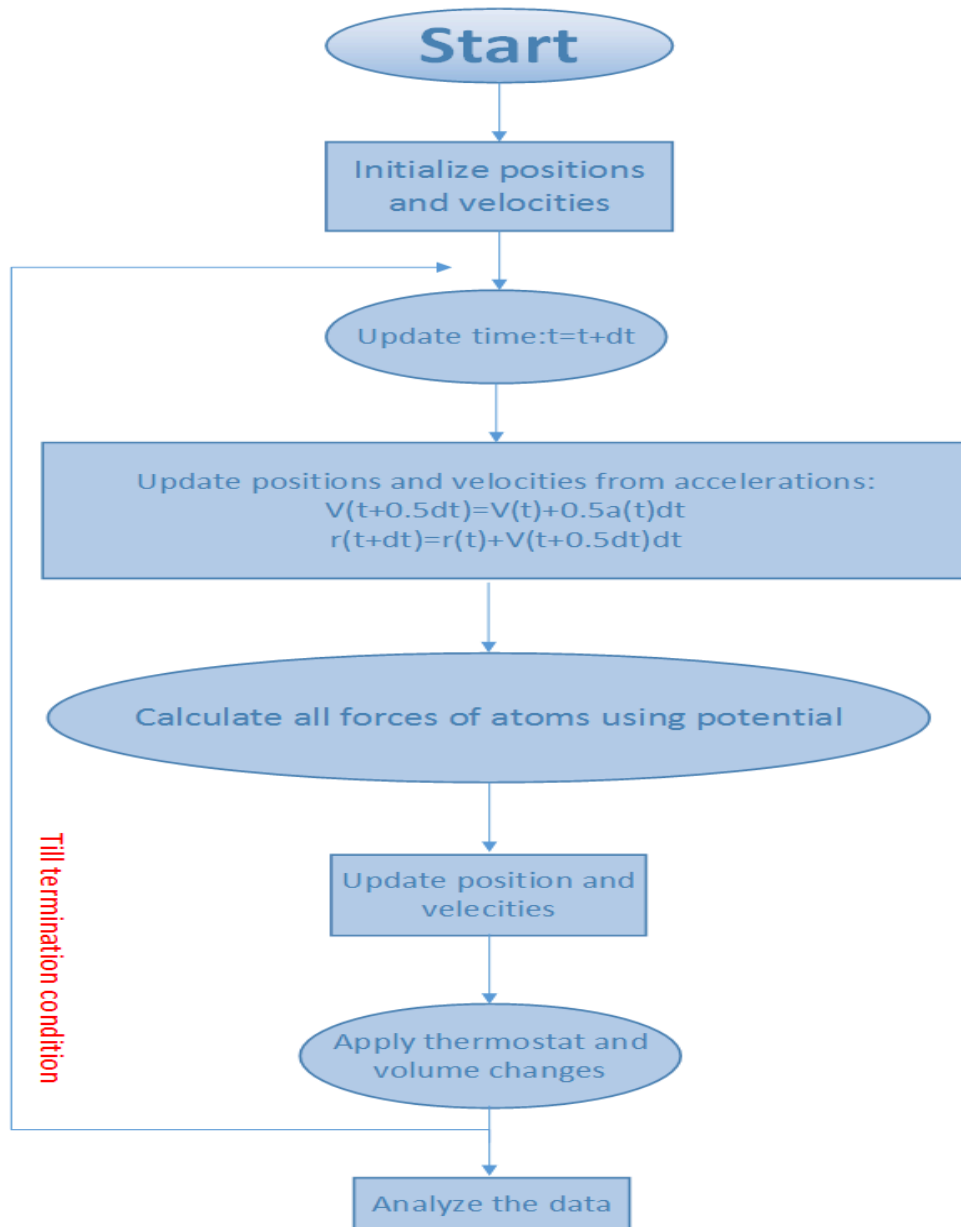


Figure 2.1 Molecular dynamics simulation flow chart

For MD simulations, we first need the initial positions and velocities of all the atoms in the system as shown in figure 2.1. The initial velocities of particles can be assigned manually or generated from the Maxwell velocity distribution according to target temperature.

$$f_v(v_x, v_y, v_z) = \left(\frac{m}{2\pi kT}\right)^{\frac{3}{2}} \exp\left[-\frac{m(v_x^2 + v_y^2 + v_z^2)}{2kT}\right] \quad (2.6)$$

where f_v is probability density of velocity, k is Boltzmann constant, T is target temperature and v_x, v_y, v_z are the velocity components. The initial velocities are available but after several steps kinetic energy is changed as the minimized structure

changes to the equilibrium structure, and the temperature also changes during dynamics. In order to maintain the correct temperature, the velocities have to be adjusted appropriately to the right target following the correct statistical ensembles. This means the probability of occurrence of a certain configuration obeys the laws of statistical mechanics. For constant-temperature, constant-volume dynamics (NVT) several algorithms for temperature control exist, e.g. velocity scaling, Berendsen, Anderson, and Nosé-Hoover temperature coupling. The one which is often used is Nosé-Hoover thermostat.¹²⁹⁻¹³¹

The central idea of Nosé-Hoover thermostat¹²⁹⁻¹³¹ is that an additional degree of freedom is added to the real physical system which is given a mass Q . The equations of motion for the extended system are then solved. If the potential chosen for that degree of freedom is correct, the constant-energy dynamics (or the micro canonical dynamics, NVE) of the extended system produces the canonical ensemble (NVT) of the real physical system. The new Hamiltonian H of the extended system is given by:

$$H = \sum_i \frac{p_i^2}{2m_i s^2} + \Phi(q) + \frac{Q}{2} \zeta^2 + gkT \ln s \quad (2.7)$$

where g is the number of independent momentum degrees of freedom of the system, and Q is an imaginary mass. $\Phi(q)$ is interaction potential. The relationships of real-atom coordinates q , momenta p , the fictitious coordinates s and associated momentum ζ are followed by:

$$\begin{aligned} \frac{dq_i}{dt} &= \frac{p_i}{m_i} \\ \frac{dp_i}{dt} &= -\frac{\phi}{dp_i} - \zeta p_i \\ \frac{d\zeta}{dt} &= \frac{\sum_i \frac{p_i^2}{m_i} - gkT}{Q} \end{aligned} \quad (2.8)$$

A well-known problem with the Nosé-Hoover thermostat is that in some situations, they are non-ergodic. The most famous example is for a collection of harmonic oscillators. This problem can be circumvented by using Nosé-Hoover chains, i.e. coupling the variable p_η itself to a Nosé-Hoover-type thermostat using a new set of variables $\tilde{\eta}$ and \tilde{p}_η which are in turn coupled to thermostat *ad infinitum*¹³². In the thesis, Nosé-Hoover chains method is applied with a coupling constant of 500 cm^{-1}

2.4 DFTB

Total energy of a system of N_e electrons in the field of M nuclei at positions R may be written within DFT as a functional of the charge density $n(\mathbf{r})$:

$$E = \sum_i^{occup} \langle \psi_i | -\frac{1}{2}\nabla^2 + V_{ext} + \frac{1}{2} \int d\mathbf{r}' \frac{n(\mathbf{r}')}{|\mathbf{r}-\mathbf{r}'|} | \psi_i \rangle + E_{xc}[n(\mathbf{r})] + \frac{1}{2} \sum_{\alpha,\beta} \frac{Z_\alpha Z_\beta}{|\mathbf{R}_\alpha + \mathbf{R}_\beta|} \quad (2.9)$$

where the first sum is over occupied Kohn-Sham eigenstates ψ_i , the second term is the exchange–correlation energy function and the last term represents the ion-ion core repulsive energy, E_{ii} . Substitute the charge density into this equation by a superposition of a reference or input density $n'_0 = n_0(\mathbf{r}')$ and a small fluctuation $\delta n' = \delta n(\mathbf{r}')$. Then it can be re-written as matrix elements by following Foulkes and Haydock's method¹³³

$$E = \sum_i^{occup} \langle \psi_i | -\frac{1}{2}\nabla^2 + V_{ext} + \int d\mathbf{r}' \frac{n'_0}{|\mathbf{r}-\mathbf{r}'|} + V_{xc}[n_0] | \psi_i \rangle - \frac{1}{2} \iint d\mathbf{r} d\mathbf{r}' \frac{n'_0(n_0 + \delta n)}{|\mathbf{r}-\mathbf{r}'|} - \int d\mathbf{r} V_{xc}(n_0 + \delta n)n_0 + E_{xc}[n_0 + \delta n] + E_{ii} + \frac{1}{2} \iint d\mathbf{r} d\mathbf{r}' \frac{n'_0(n_0 + \delta n)}{|\mathbf{r}-\mathbf{r}'|} \quad (2.10)$$

The second term of this equation corrects the double counting of the new Hartree, the third term for the new xc contribution in the leading matrix element, and the last term comes from dividing the full Hartree energy into a part related to n_0 and δn . E_{xc} can be expanded as second order in the density fluctuations at the reference density and the terms linear in δn cancel each other at any arbitrary input density n_0 :

$$E = \sum_i^{occup} \langle \psi_i | H_0 | \psi_i \rangle - \frac{1}{2} \iint d\mathbf{r} d\mathbf{r}' \frac{n'_0 n_0}{|\mathbf{r}-\mathbf{r}'|} + E_{xc}[n_0] - \int d\mathbf{r} V_{xc}(n_0)n_0 + E_{ii} + \frac{1}{2} \iint d\mathbf{r} d\mathbf{r}' \left(\frac{1}{|\mathbf{r}-\mathbf{r}'|} + \frac{\delta^2 E_{xc}}{\delta n \delta n'} |_{n_0} \right) \delta n \delta n'. \quad (2.11)$$

2.4.1 Zeroth order non-self-consistent charge approach, NCC-DFTB

The traditional non-self-consistence-charge TB approach is to neglect the last term in the final expression in Eq. (2.11), with H_0 as the Hamiltonian operator resulting from an input density n_0 . As usual, a frozen-core approximation is applied to reduce the computational efforts by only considering the valence orbitals. The Kohn-Sham equations are solved non-self-consistently and the second-order correction is neglected.

The contributions in Eq. (2.11) which depend on the input density n_0 only and the core-core repulsion are taken to be the sum of one- and two-body potentials^{133,134}. The latter, denoted by E_{rep} , are strictly pairwise, repulsive and short ranged. The total energy then reads

$$E_0^{TB} = \sum_i^{occup} \langle \psi_i | H_0 | \psi_i \rangle + E_{rep} \quad (2.12)$$

which is similar to the general TB energy equation in the general Hartree-Fock-Roothaan approximation.

In order to solve the KS equations, the single-particle wavefunctions ψ_i within an LCAO ansatz are expanded into a suitable set of localized atomic orbitals φ_v ,

$$\psi_i(r) = \sum_v c_{vi} \varphi_v(\mathbf{r} - \mathbf{R}_\alpha) \quad (2.13)$$

If we employ confined atomic orbitals in a Slater-type representation¹³⁴, these are determined by solving a modified Schrödinger equation for a free neutral pseudoatom with self-consistence field (SCF)-LDA calculations¹³⁵. The effective one-electron potential of the many-atom structure¹³⁴ is approximated to a sum of spherical KS potentials of neutral pseudoatoms due to their confined electron density. By applying the variational principle to the zeroth-order energy functional (2.12), we obtain the non-SCF KS equations, which, finally, within the pseudoatomic basis, transform to a set of algebraic equations:

$$\sum_v^{N_e} c_{vi} (H_{uv}^0 - \epsilon_i S_{uv}) = 0, \forall \mu, i; \quad H_{uv}^0 = \langle \varphi_\mu | H_0 | \varphi_\nu \rangle, S_{uv} = \langle \varphi_\mu | \varphi_\nu \rangle \quad \forall \mu \in \alpha \quad (2.14)$$

Consistent with the construction of the effective one-electron potential we neglect several contributions to the Hamiltonian matrix elements H_{uv} yielding

$$H_{uv}^0 = \begin{cases} \epsilon_\mu^{neutral \ free \ atom} & \text{if } \mu = \nu; \\ \langle \varphi_\mu^\alpha | T + V_0^\alpha + V_0^\beta | \varphi_\mu^\beta \rangle & \text{if } \alpha \neq \beta; \\ 0 & \text{otherwise.} \end{cases} \quad (2.15)$$

Since indices α and β indicate the atoms on which the wavefunctions and potentials are centred, only two-centre Hamiltonian matrix elements are treated and explicitly evaluated in combination with the two-centre overlap matrix elements. As follows from Eq. (2.15), the eigenvalues of the free atom serve as diagonal elements of the Hamiltonian, thus guaranteeing the correct limit for isolated atoms.

By solving the general eigenvalue problem, Eq. (2.14), the first term in Eq. (2.12) becomes a simple summation over all occupied KS orbitals with energy ϵ_i (occupation number n_i), while E_{rep} can easily be determined as a function of distance by taking the

difference of the SCF-LDA cohesive and the corresponding TB band-structure energy for a suitable reference system,

$$E_{rep}(\mathbf{R}) = \{E_{LDA}^{SCF}(\mathbf{R}) - \sum_i^{occup} n_i \epsilon_i(\mathbf{R})\}_{\text{reference structure}} \quad (2.16)$$

Interatomic forces for molecular dynamics simulation applications can easily be derived from an explicit calculation of the gradients of the total energy at the considered atom sites,

$$M_\alpha \ddot{\mathbf{R}}_\alpha = -\frac{\partial E_0^{TB}}{\partial \mathbf{R}_\alpha} = -\sum_i n_i \sum_\mu \sum_\nu c_{\mu i} c_{\nu i} \left[\frac{\partial H_{\mu\nu}^0}{\partial \mathbf{R}_\alpha} - \epsilon_i \frac{\partial S_{\mu\nu}}{\partial \mathbf{R}_\alpha} - \sum_{\beta \neq \alpha} \frac{\partial E_{rep}(|\mathbf{R}_\alpha - \mathbf{R}_\beta|)}{\mathbf{R}_\alpha} \right] \quad (2.17)$$

This is the non-SCC-DFTB approach, which has been successfully applied to various problems in different systems and materials, covering carbon¹³⁴, silicon¹³⁶, and germanium structures¹³⁷, boron and carbon nitride^{138,139}, silicon carbide¹⁴⁰ and oxides and GaAs surfaces¹⁴¹. In my thesis, the approach has been used to study Sc or Ti based metallofullerene formations.

2.4.2 Second order self-consistent charge extension, SCC-DFTB

NCC-DFTB is a good approximation when the electron density of the many atom structure may be represented as a sum of atomic-like densities. However in some cases standard DFTB fail to correctly describe charge transfer between different atomic constituents, especially in heteronuclear molecules such as biomolecules, and in polar semiconductors. Thus, extension of the approach is necessary to improve accuracy of total energies, forces in the presence of long-range Coulomb interactions. Starting from Eq. (2.11), and now explicitly consider the second-order term in the density fluctuations in order to include associated effects in a simple and efficient TB concept, $\delta n(\mathbf{r})$ is decomposed into atom-centered contributions, which decay fast with increasing distance from the corresponding center. The second-order term then reads

$$E_{2nd} = \frac{1}{2} \sum_{\alpha, \beta}^M \iint d\mathbf{r} d\mathbf{r}' \Gamma[\mathbf{r}, \mathbf{r}', n_0 \delta n_\alpha(\mathbf{r}) \delta n_\beta(\mathbf{r}')] \quad (2.18)$$

where we have used the functional Γ to denote the Hartree and xc coefficients. Second, δn_α may be expanded in a series of radial and angular functions:

$$\delta_\alpha(\mathbf{r}) = \sum_{l,m} K_{ml} F_{ml}^\alpha(|\mathbf{r} - \mathbf{R}_\alpha|) Y_{lm} \left(\frac{\mathbf{r} - \mathbf{R}_\alpha}{|\mathbf{r} - \mathbf{R}_\alpha|} \right) \approx \Delta q_\alpha F_{00}^\alpha(|\mathbf{r} - \mathbf{R}_\alpha|) Y_{00} \quad (2.19)$$

where F_{ml}^α denotes the normalized radial dependence of the density fluctuation on atom α for the corresponding angular momentum. Truncating the multipole expansion (2.12) after the monopole term accounts for the most important contributions of this kind while avoiding a substantial increase in the numerical complexity of the scheme. Also, it should

be noted that higher-order interactions decay much more rapidly with increasing interatomic distance. Finally, the expression (2.19) preserves the total charge in the system, i.e.,

$$\sum_{\alpha} \Delta q_{\alpha} = \int \delta n(r) \quad (2.20)$$

Substitution of Eq. (2.19) into (2.18):

$$E_{2nd} = \frac{1}{2} \sum_{\alpha, \beta}^M \Delta q_{\alpha} \Delta q_{\beta} \gamma_{\alpha\beta} \quad (2.21)$$

where

$$\gamma_{\alpha\beta} = \iint d\mathbf{r} d\mathbf{r}' \Gamma[\mathbf{r}, \mathbf{r}', n_0] \frac{F_{00}^{\alpha} |\mathbf{r} - \mathbf{R}_{\alpha}| F_{00}^{\beta} |\mathbf{r} - \mathbf{R}_{\beta}|}{4\pi} \quad (2.22)$$

is introduced as shorthand notation. In the limit of large interatomic distances, the xc contribution vanishes within LDA and E_{2nd} may be viewed as a pure Coulomb interaction between two point charges Δq_{α} and Δq_{β} . In the opposite case, where the charges are located at one and the same atom, a rigorous evaluation of $\gamma_{\alpha\alpha}$ would require the knowledge of the actual charge distribution. This could be calculated by expanding the charge density into an appropriate basis set of localized orbitals. In order to avoid the numerical effort associated with the basis set expansion of δn and to consider at least approximately the self-interaction contributions, a simple approximation of $\gamma_{\alpha\alpha}$, which is widely used in semiempirical quantum chemistry methods relying on Pariser observation that $\gamma_{\alpha\alpha}$ can be approximated by the difference of atomic ionization potential and the electron affinity¹⁴². This is related to the chemical hardness η_{α} , or the Hubbard parameter U_{α} ,

$$\gamma_{\alpha\alpha} \approx I_{\alpha} - A_{\alpha} \approx 2\eta_{\alpha} \approx U_{\alpha} \quad (2.23)$$

The expression for $\gamma_{\alpha\beta}$ then only depends on the distance between atoms α and β and on the parameters U_{α} and U_{β} . The latter constants can be calculated for any atom type within LDA-DFT as the second derivative of the total energy of a single atom with respect to the occupation number of the highest occupied atomic orbital. These values are therefore neither adjustable nor empirical parameters. Indeed, the necessary corrections for a TB total energy in the presence of charge fluctuations turns out to be a typical Hubbard-type correlation in combination with long-range interatomic Coulomb interactions. There are common functional forms of $\gamma_{\alpha\beta}$, examples are presented in the work of Ohno¹⁴³, Klopman¹⁴⁴ and Mataga-Nishimoto¹⁴⁵. It has been observed that these may cause severe numerical problems when applied to periodic systems since Coulomb like behaviour is only accomplished for at large atomic distance. By using expressions

like in ref. ^{143,144} for periodic systems yield ill-conditioned energies with respect to Hubbard parameters, i.e., small changes in the Hubbard parameters may result in considerable variations of total energy and should therefore not be used. In order to obtain a well-defined expression useful for all scale systems and consistent with previous approximations, an analytical approach is made to obtain the function $\gamma_{\alpha\beta}$. In accordance with the Slater-type orbitals used as a basis set to solve the Kohn-Sham equations ¹³⁴, an exponential decay of the normalized spherical charge densities

$$n_{\alpha}(r) = \frac{\tau_{\alpha}^3}{8\pi} e^{-\tau_{\alpha}|r-R_{\alpha}|} \quad (2.24)$$

is assumed. Neglecting for the moment the second-order contributions of E_{xc} in Eq. (2.18), we obtain:

$$\gamma_{\alpha\beta} = \iint d\mathbf{r}d\mathbf{r}' \frac{1}{|\mathbf{r}-\mathbf{r}'|} \frac{\tau_{\alpha}^3}{8\pi} e^{-\tau_{\alpha}|\mathbf{r}-\mathbf{R}_{\alpha}|} \frac{\tau_{\beta}^3}{8\pi} e^{-\tau_{\beta}|\mathbf{r}-\mathbf{R}_{\beta}|} \quad (2.25)$$

Integrating over \mathbf{r}' gives

$$\gamma_{\alpha\beta} = \int d\mathbf{r} \left[\frac{1}{|\mathbf{r}-\mathbf{R}_{\alpha}|} - \left(\frac{\tau_{\alpha}}{2} + \frac{1}{|\mathbf{r}-\mathbf{R}_{\alpha}|} \right) e^{-\tau_{\alpha}|\mathbf{r}-\mathbf{R}_{\alpha}|} \right] \frac{\tau_{\beta}^3}{8\pi} e^{-\tau_{\beta}|\mathbf{r}-\mathbf{R}_{\beta}|} \quad (2.26)$$

By setting $R = R_{\alpha} - R_{\beta}$ and some coordinate transformations, one obtains

$$\gamma_{\alpha\beta} = \frac{1}{R} - S(\tau_{\alpha}, \tau_{\beta}, R) \quad (2.27)$$

S is an exponentially decay short-range function with

$$S(\tau_{\alpha}, \tau_{\beta}, R)|_{R \rightarrow 0} = \frac{5}{16} \tau_{\alpha} + \frac{1}{R} \quad (2.28)$$

Here it is assumed that at $R = 0$ the second order contribution can be expressed approximately via the so-called chemical hardness for a spin-polarized atom or Hubbard parameter U_{α} , to obtain

$$\frac{1}{2} \Delta q_{\alpha}^2 \gamma_{\alpha\alpha} = \frac{1}{2} \Delta q_{\alpha}^2 U_{\alpha} \quad (2.29)$$

therefore from Eq. (2.28) for the exponents:

$$\tau_{\alpha} = \frac{16}{5} U_{\alpha} \quad (2.30)$$

The results are interpreted by noting that elements with a high chemical hardness tend to have localized wavefunctions. The chemical hardness for a non-spin-polarized atom is the derivative of the highest molecular orbital with respect to its occupation number. This chemical hardness is calculated with a fully self-consistent *ab-initio* method and therefore include the influence of the second-order contribution of E_{xc} in $\gamma_{\alpha\beta}$ for small distances

where it is important. In the limit of large interatomic distances, $\gamma_{\alpha\beta} \rightarrow 1/R$ and thus represents the Coulomb interaction between two point charges Δq_α and Δq_β . This accounts for the fact that at large interatomic distances, the exchange-correlation contributions vanish within the local density approximation. In periodic systems, this long range part is evaluated using the standard Ewald technique, whereas the short-range part S decays exponentially and can therefore be summed over a small number of unit cells. Hence, Eq. (2.27) is a well-defined expression for extended and periodic systems. Finally, the DFT total energy in (2.11) is conveniently transformed to a transparent TB form,

$$E_2^{TB} = \sum_i^{occup} \langle \psi_i | H_0 | \psi_i \rangle + \frac{1}{2} \sum_{\alpha\beta}^M \gamma_{\alpha\beta} \Delta q_\alpha \Delta q_\beta + E_{rep} \quad (2.31)$$

where $\gamma_{\alpha\beta} = \gamma(U_\alpha, U_\beta, |\mathbf{R}_\alpha - \mathbf{R}_\beta|)$. As discussed earlier, the contribution due to H_0 depends only on n_0 and is therefore exactly the same as in previous non-SCC studies.

However, since the atomic charges depend on the one-particle wavefunction ψ_i , a self-consistent procedure is required to find the minimum of expression (2.31). To solve the KS equations, the single-particle wavefunctions ψ_i are expanded into a suitable set of localized atomic orbitals φ_v , denoting the expansion coefficients by c_{vi} . According to the previous scheme¹³⁴, confined Slater-type atomic orbitals are employed. These are determined by solving the Schrödinger equation for a free atom within SCF-LDA calculations. By applying the variational principle to the energy function (2.31), we obtain the KS equations, which, within the pseudoatomic basis, transform to a set of algebraic equations. In order to estimate the charge fluctuations $\Delta q_\alpha = q_\alpha - q_\alpha^0$, a Mulliken charge analysis is employed.

$$q_\alpha = \frac{1}{2} \sum_i^{occup} n_i \sum_{\mu \in \alpha} \sum_v^M (c_{\mu i}^* c_{vi} S_{\mu v} + c_{vi}^* c_{\mu i} S_{v \mu}) \quad (2.32)$$

We obtain

$$\sum_v^{N_e} c_{vi} (H_{\mu v} - \epsilon_i S_{\mu v}) = 0, \forall \mu, i, \quad (2.33)$$

$$\begin{aligned} H_{\mu v} &= \langle \varphi_\mu | H_0 | \varphi_v \rangle + \frac{1}{2} S_{\mu v} \sum_\xi^M (\gamma_{\alpha\xi} + \gamma_{\beta\xi}) \Delta q_\xi = H_{\mu v}^0 + H_{\mu v}^1, \\ S_{\mu v} &= \langle \varphi_\mu | \varphi_v \rangle, \forall \mu \in \alpha, \forall \mu \in \beta \end{aligned} \quad (2.34)$$

Since the overlap matrix elements $S_{\mu v}$ generally extend over a few nearest-neighbour distances, they introduce multiparticle interactions. The second-order correction due to

charge fluctuations is now represented by the non-diagonal Mulliken charge dependent contribution $H_{\mu\nu}^1$ to the matrix elements $H_{\mu\nu}$.

A simple analytic expression for the interatomic forces for use in MD simulations is easily derived by taking the derivative of the final TB energy Eq. (2.31) (for SCC-DFTB method) with respect to the nuclear coordinates yielding,

$$F_{\alpha} = -\sum_i^{occup} n_i \sum_{\mu\nu} c_{\mu\nu} c_{\nu i} \left[\frac{\partial H_{\mu\nu}^0}{\partial \mathbf{R}_{\alpha}} - \left(\epsilon_i - \frac{H_{\mu\nu}^1}{S_{\mu\nu}} \right) \frac{\partial S_{\mu\nu}}{\partial \mathbf{R}_{\alpha}} \right] - \Delta q_{\alpha} \sum_{\xi}^M \frac{\partial \gamma_{\alpha\xi}}{\partial \mathbf{R}_{\alpha}} \Delta q_{\xi} - \frac{\partial E_{rep}}{\partial \mathbf{R}_{\alpha}} \quad (2.35)$$

Chapter 3. Clusters encapsulated in Endohedral Metallofullerenes: How strained they are?

3.1 Introduction

The charge transfer from the encased species to the outer frameworks is considered to be the main factor determining stability of the clusterfullerenes as mentioned in chapter 1.2. Another important factor which also strongly influences the stability of the clusterfullerenes was defined as the cage form factor.^{74,146} Namely, the size and the shape of the carbon cage should fit the size and the shape of the encapsulated cluster. When this condition is violated, the preferable cage isomer can be switched or a given fullerene may be not formed at all. A typical example is the case of $M_3N@C_{78}$ NCFs. Whereas $D_{3h}(5)$ is preferable for relatively small Sc_3N ,⁸⁰ the non-IPR $C_2(22010)$ isomer is much more stable for $M = Y, Dy$ *etc.* because of the much larger size of the cluster and more suitable shape of the C_2 -symmetric cage.⁷⁶ The absence of $Sc_3N@C_{72}$ and $Sc_3N@C_{74}$ in the $Sc_3N@C_{2n}$ family is also caused by the absence of the suitably shaped stable isomers of C_{72} and C_{74} cages to accommodate triangular Sc_3N cluster.⁷³ On the one hand, the size of fullerene cage can also dramatically influence the bond lengths or even the shape of the internal clusters. For example, a systematic experimental and computational NMR study of a series of $Y_2C_2@C_{2n}$ ($2n = 82, 84, 92, 100$) by Dorn *et al.* showed that the internal yttrium carbide cluster prefers to adopt a stretched linear shape when the cage is sufficiently large (e.g., in C_{100}), while it will bend to a compressed “butterfly shape” in relatively small cages (e.g., in C_{82}).¹⁴⁷

It is obvious that the factor of internal clusters plays a vital role in stability of clusterfullerenes, but exact energy and geometrical characteristics of encapsulated clusters are not known because in all real systems they are always templated by the carbon cage. It is therefore difficult to give a definitive answer about what an ideal structure of

the internal cluster in each case should be? A computational study of the “isolated” cluster (e.g., Sc_3N) taken outside of the carbon cage cannot answer the question because of the different electronic structures of the free cluster and the same cluster inside the carbon cage. The electron transfer from the cluster to the cage plays an important role in their mutual stabilization. However, the study of the isolated charged cluster (e.g., Sc_3N^{6+}) is also not able to give a reliable answer due to the huge Coulomb repulsion in such highly charged systems. The real charges of the endohedral cluster in EMFs are much smaller than formal ones because of the significant covalent contributions to the metal-cage interactions.¹⁴⁸

In this chapter a simple yet efficient model has been proposed to overcome these problems. Coordination of metal atoms to the small organic π -system acting as a two-electron acceptor mimics the real electronic situation of the clusterfullerenes and at the same time bestows the cluster a freedom to adjust its geometrical parameters in the most optimal way. We use this model to address fundamental questions about the structure and stability of three types of EMFs with M_3N , M_2S , and M_2C_2 clusters ($\text{M} = \text{Sc}, \text{Y}$), in particular: (i) what is an “ideal” structure of the cluster? (ii) how does the energy of each cluster change during compression, stretching and bending?

3.2 Model and Computational Methods

In nitride, sulfide, and carbide clusterfullerenes each metal atom formally donates two electrons to the carbon cage, and one electron to the non-metal bridge (N, S, and C_2 , respectively). Besides, although endohedral cluster interact with the whole cage, there is a certain degree of locality in the metal-cage interactions. i.e., metal atoms adjust the electron density of the “islands” of the fullerene cage, and each “island” strongly interacting with one metal atom comprises ca 8–12 carbon atoms.¹⁴⁸ Hence, to mimic the electronic situation we coordinate metal atoms to the small organic fragment capable of being a 2-electron acceptor. The fragment however should be small enough to avoid steric hindrances when the cluster geometry is varied. The pentalene unit (two fused pentagons, C_8H_6 , see Fig 3.1a-b) is an ideal model system fulfilling both conditions. The use of s-indacene to model metal-cage interactions was also considered and gave qualitatively similar results. In titanium clusterfullerenes $\text{Ti}_2\text{C}_2@C_{78}$ and $\text{Ti}_2\text{S}@C_{78}$, each titanium atom donates three electrons to the cage. To model Ti-cage interactions in Ti-EMFs we have used sumanene-like C_{21}H_9 , which resembles a Ti-coordinated part of the carbon cage. The difference from sumanene is that only one hydrogen atoms is left in each

pentagon (Fig. 3.1c). Ti is coordinated then to the central hexagon in a η^6 -manner (Fig. 3.1d).

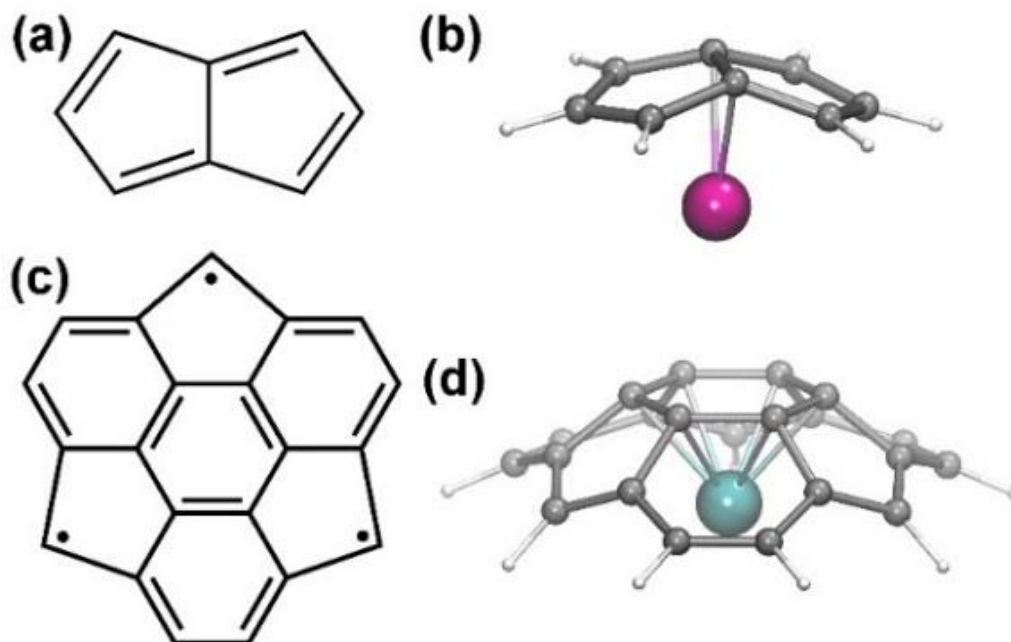


Figure 3.1 (a) Structural formulae of pentalene C_8H_6 ; (b) coordination of pentalene by Sc atom (the same coordination is used for Y atoms); (c) structural formulae of modified sumanene $C_{21}H_9$; (d) coordination of sumanene fragment by Ti.

First, we optimized molecular coordinates of the clusters $M_3N(C_8H_6)_3$, $M_2S(C_8H_6)_2$, $M_2C_2(C_8H_6)_2$ ($M=Sc, Y$), $Ti_2S(C_{21}H_9)_2$ and $Ti_2C_2(C_{21}H_9)_2$. Then, the metal-pentalene or metal-sumanene fragments were kept frozen, and only internal coordinates of the cluster (i.e. the angles and metal–N, metal–S, or metal– C_2 distances) were varied. When the fragments were moved too close to each other during bending or compression of the cluster so that inter-fragment interaction could not be ignored (the shortest interatomic distance are less than 3.0 \AA), the interaction energies were calculated separately.

Density functional theory computations were carried out within a generalized gradient approximation (GGA) with PBE¹²¹ for the exchange correlation term, as implemented in PRIRODA package.¹⁴⁹⁻¹⁵¹ Original TZ2P-quality full-electron basis set {8,7,5,2}/(23s,18p,13d,7f), {6,3,2}/(11s,6p,2d), {6,3,2}/(11s,6p,2d) and {3,1}/(5s,1p) were used for Sc, C, N, and H atoms, respectively. SBK-type effective core potentials for Y and Ti atoms are treated with {5,5,4}(9s,9p,8d) and {6,3,2}/(11s,6p,2d) valence parts. Molecular structures were visualized using VMD package.¹⁵²

3.3 Results and Discussion

3.3.1 Nitride clusterfullerenes

The Sc_3N cluster in the $\text{Sc}_3\text{N}(\text{C}_8\text{H}_6)_3$ molecule is a planar triangle with an optimized Sc–N bond length of 2.020 Å and a Sc–N–Sc bond angle of 120° (Fig. 3.2a). The Sc–N bond lengths in $\text{Sc}_3\text{N}@C_{68}$, $\text{Sc}_3\text{N}@C_{78}$, and $\text{Sc}_3\text{N}@C_{80}$ optimized at the same level of theory are 1.993, 2.010 and 2.033 Å, respectively, and a Sc–N–Sc bond angles are all 120°. Analogous variations of the Sc–N bond length in the $\text{Sc}_3\text{N}(\text{C}_8\text{H}_6)_3$ complex produced only small changes in the energy (1.8, 0.2, 0.5 $\text{kJ}\cdot\text{mol}^{-1}$, respectively). However, when the cluster in $\text{Sc}_3\text{N}(\text{C}_8\text{H}_6)_3$ was distorted in the same way as in $\text{Sc}_3\text{N}@C_{70}$ (the Sc–N–Sc bond angles are 150° and $2\times 105^\circ$, whereas the bond lengths are 1.988 and 2.059 Å), the energy increased dramatically to 50 $\text{kJ}\cdot\text{mol}^{-1}$. This large strain value may explain the low yield of $\text{Sc}_3\text{N}@C_{70}$ in comparison to $\text{Sc}_3\text{N}@C_{68}$ and $\text{Sc}_3\text{N}@C_{78}$.⁵⁵ To get a more detailed description of the structure-energy relations, we have computed the energy profiles along the Sc–N bond stretching/elongation in the 1.900–2.150 Å range and along the Sc–N–Sc angle bending in the 105–150° range (Fig. 3.2b-c). Corresponding distortion energies will be hereafter denoted as E_{dist} and E_{bend} . The E_{dist} energy of the $\text{Sc}_3\text{N}(\text{C}_8\text{H}_6)_3$ molecule remains within the 10 $\text{kJ}\cdot\text{mol}^{-1}$ in the 2.02 ± 0.06 Å range of the Sc–N bond lengths. Thus, the Sc_3N cluster in NCFs is rather flexible in terms of the Sc–N bond lengths. The Sc–N–Sc bending profile is also rather flat within the 110–135° range (the energy of the system remains below 10 $\text{kJ}\cdot\text{mol}^{-1}$). For larger distortion angles, the steep increase of E_{bend} is observed.

The free $\text{Y}_3\text{N}(\text{C}_8\text{H}_6)_3$ molecule has similar structure to the $\text{Sc}_3\text{N}(\text{C}_8\text{H}_6)_3$ with the exception of the Y–N bond length elongated to 2.190 Å. Compression of the Y–N average bond lengths in $\text{Y}_3\text{N}@C_{78-C_2}$ and $\text{Y}_3\text{N}@C_{80}$ to 2.099 Å and 2.060 Å, respectively, increases the energy by 21 and 42 $\text{kJ}\cdot\text{mol}^{-1}$. One Y–N–Y angle in $\text{Y}_3\text{N}@C_{78}$ is bended to 125.5°, and those in $\text{Y}_3\text{N}@C_{80}$ are slightly changed to 119.8°. Cluster distortion energy in hypothetical $\text{Y}_3\text{N}@C_{78-D_{3h}(5)}$ (i.e. with the same carbon cage as in $\text{Sc}_3\text{N}@C_{78}$) is as high as 72 $\text{kJ}\cdot\text{mol}^{-1}$. In $\text{Y}_3\text{N}@C_{82}$, the average Y–N length became 2.131 Å resulting in the distortion energy of 14 $\text{kJ}\cdot\text{mol}^{-1}$. With the further increase of the cage size, the average Y–N bond length increases to 2.162 Å in $\text{Y}_3\text{N}@C_{84}$, 2.173 Å in $\text{Y}_3\text{N}@C_{86}$, and 2.194 Å in the $\text{Y}_3\text{N}@C_{88}$, whereas the angles deviate from 120° by no more than by 10°. With these geometrical parameters, distortion energies of the $\text{Y}_3\text{N}(\text{C}_8\text{H}_6)_3$ molecule are 2, 5, and 1 $\text{kJ}\cdot\text{mol}^{-1}$, respectively.

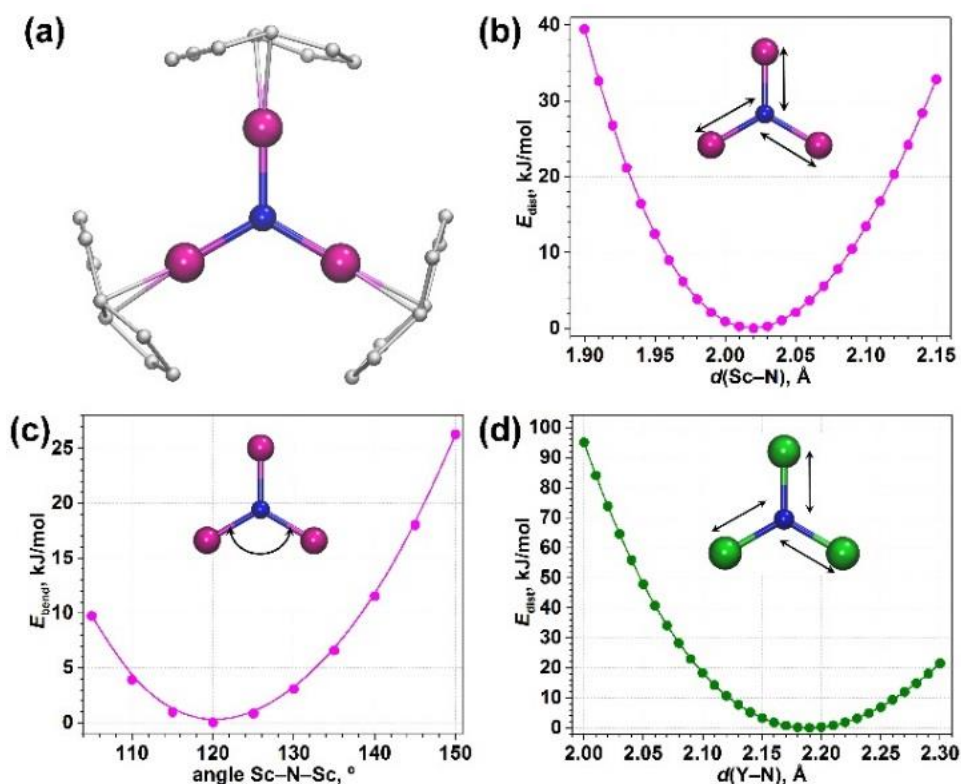


Figure 3.2 (a) DFT-optimized molecular structures of $\text{Sc}_3\text{N}(\text{C}_8\text{H}_6)_3$; Sc is magenta, nitrogen is blue, carbon atoms are grey, hydrogen atoms are not shown for clarity. (b-d) Energy profiles computed for: (b) variation of Sc–N bond lengths in $\text{Sc}_3\text{N}(\text{C}_8\text{H}_6)_3$; (c) variation of Sc–N–Sc angle in $\text{Sc}_3\text{N}(\text{C}_8\text{H}_6)_3$; (d) variation of Y–N bond lengths in $\text{Y}_3\text{N}(\text{C}_8\text{H}_6)_3$. In the range of computed values (110–130°), Y–N–Y angle energy profile is identical to that for Sc analogue.

Our results show that the Y_3N cluster is significantly strained in $\text{Y}_3\text{N}@\text{C}_{80}$ and the strain is much lower in the large cages $\text{C}_{82}\text{--}\text{C}_{88}$. Extraordinary high stability of the $[\text{C}_{80}\text{-}I_h]^{6-}$ cage results in the higher yield of $\text{Y}_3\text{N}@\text{C}_{80}\text{-}I_h$ in the synthesis in comparison to $\text{Y}_3\text{N}@\text{C}_{2n}$ ($2n = 82\text{--}88$), but further increase of the metal (Gd and beyond) leads to drastic decrease of the relative yield of $\text{M}_3\text{N}@\text{C}_{80}$. Besides, the yield of $\text{Y}_3\text{N}@\text{C}_{80}$ is much lower than that of $\text{Sc}_3\text{N}@\text{C}_{80}$ (the cluster is not strained in the latter), and high strain of the nitride cluster is presumably one of the reasons.

The energy profile along the Y–N bond length variation (Fig. 3.2d) shows that the optimal bond length of $\text{Y}_3\text{N}(\text{C}_8\text{H}_6)_3$ is about 2.19 ± 0.07 Å, which is 0.17 Å longer than the Sc–N bond length. Variation of the Y–N–Y angles from 110 to 130° (the range of experimentally known clusterfullerenes) has a small effect on the energy. These data clearly show that the cages larger than C_{82} are preferable for the Y_3N cluster and that the E_{dist} is the main component in the cluster distortion energies of the $\text{Y}_3\text{N}@\text{C}_{2n}$ molecules.

3.3.2 Sulfide clusterfullerenes

Since its discovery in 2010,¹⁵³ the family of sulfide clusterfullerenes $\text{Sc}_2\text{S}@C_{2n}$ expanded to 4 members with the cage sizes from C_{70} to C_{82} .^{56,154,155} Analysis of the geometrical parameters of the Sc_2S cluster in these molecules reveals that the Sc_2S unit is very flexible and can adopt substantially different Sc–S–Sc bond angles in different cages (Fig. 3.3). In the X-ray characterized isomers of $\text{Sc}_2\text{S}@C_{82}$, the Sc_2S clusters is bent with the Sc–S–Sc angles of 114° and 97° in $C_s(6)$ and $C_{3v}(8)$ cages, respectively.¹⁵⁵ DFT studies of $\text{Sc}_2\text{S}@C_{70}\text{-}C_2(7892)$ ⁵⁶ and $\text{Sc}_2\text{S}@C_{72}\text{-}C_s(10528)$ ¹⁵⁴ also predict bent cluster with the angles of 98° and 124° , respectively, whereas computational study of the $\text{Sc}_2\text{S}@C_{74}\text{-}C_2(13333)$ shows that in this cage the Sc_2S cluster can be linear (note that this structure is not isolated so far). The question thus appears what the optimal shape of the sulfide cluster is and how sensitive is the stability of the sulfide clusterfullerene to the deformation of the cluster?

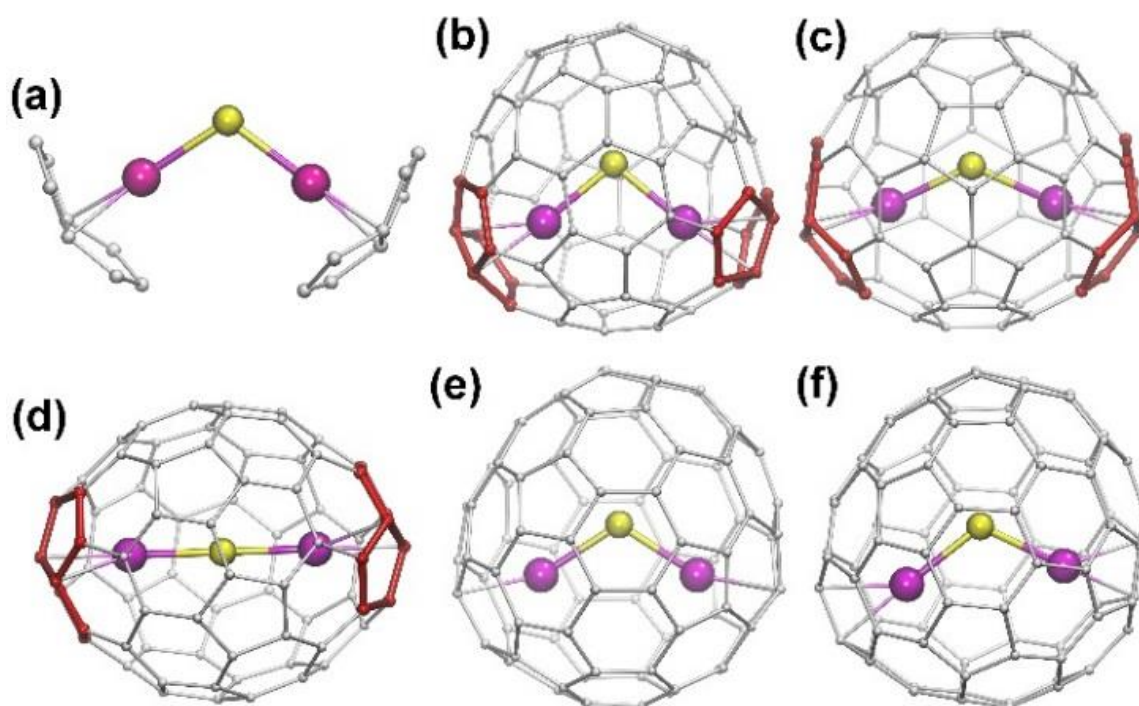


Figure 3.3 DFT optimized structures of $\text{Sc}_2\text{S}(\text{C}_8\text{H}_6)_2$ (a) and Sc-sulfide clusterfullerenes: (b) $\text{Sc}_2\text{S}@C_{70}\text{-}C_2(7892)$; (c) $\text{Sc}_2\text{S}@C_{72}\text{-}C_s(10528)$; (d) $\text{Sc}_2\text{S}@C_{74}\text{-}C_2(13333)$; (e) $\text{Sc}_2\text{S}@C_{82}\text{-}C_{3v}(8)$; (f) $\text{Sc}_2\text{S}@C_{82}\text{-}C_s(6)$.

The unconstrained optimization of the $\text{Sc}_2\text{S}(\text{C}_8\text{H}_6)_2$ molecule resulted in the bent Sc_2S cluster with the bond length of 2.411 \AA and the Sc–S–Sc angle of 110° (Fig. 3.3a). The distortion energies computed for the cluster in the experimentally available cages is $16 \text{ kJ}\cdot\text{mol}^{-1}$ for $\text{Sc}_2\text{S}@C_{70}$, and less than 10 kJ/mol for all other cages (Table 3-1).

Table 3-1 Distortion energies and cluster geometry parameters (M–X bond lengths and M–X–M angles) in selected nitride and sulfide clusterfullerenes^a

EMF molecule	E	E_{dist}	E_{bend}	d(M–X)	$\alpha(\text{M–X–M})$
Sc ₃ N(C ₈ H ₆) ₃	0.0	0.0	0.0	2.020	120.0
Sc ₃ N@C ₆₈ -D ₃ (6140)	1.8	1.7	0.0	1.993	120.0
Sc ₃ N@C ₇₀ -C _{2v} (7854)	49.6	0.1	47.1	1.988, 2.059	2×105.0, 150.0
Sc ₃ N@C ₇₈ -D _{3h} (5)	0.2	0.2	0.0	2.010	120.0
Sc ₃ N@C ₈₀ -I _h (7)	0.5	0.4	0.0	3.033	120.0
Y ₃ N(C ₈ H ₆) ₃	0.0	0.0	0.0	2.190	120.0
Y ₃ N@C ₇₈ -D _{3h} (5)	72.3	30.5	30.3	2.076	113.2
Y ₃ N@C ₇₈ -C ₂ (22010)	21.1	18.8	1.0	2.100	117.2–125.5
Y ₃ N@C ₈₀ -I _h (7)	41.5	50.7	0.5	2.060	119.9
Y ₃ N@C ₈₂ -C _s (39663)	13.8	7.5	4.8	2.131	113.5–131.0
Y ₃ N@C ₈₄ -C _s (51365)	5.4	2.3	2.5	2.156	113.5–125.9
Y ₃ N@C ₈₆ -D ₃ (19)	2.2	0.6	1.5	2.173	119.9
Y ₃ N@C ₈₈ -D ₂ (35)	1.2	0.1	1.2	2.195	117.6–124.9
Sc ₂ S(C ₈ H ₆) ₂	0.0	0.0	0.0	2.411	110.3
Sc ₂ S@C ₇₀ -C ₂ (7892)	16.0	2.4	10.4	2.363	97.6
Sc ₂ S@C ₇₂ -C _s (10528)	5.2	3.4	2.2	2.354	127.5
Sc ₂ S@C ₇₄ -C ₂ (13333)	9.0	3.4	6.1	2.354	175.8
Sc ₂ S@C ₈₂ -C _{3v} (8)	2.0	2.1	0.2	2.366	113.6
Sc ₂ S@C ₈₂ -C _s (6)	1.8	1.6	0.3	2.373	114.6
Y ₂ S(C ₈ H ₆) ₂	0.0	0.0	0.0	2.578	140.4
Y ₂ S@C ₇₀ -C ₂ (7892)	53.4	11.3	30.9	2.474	86.4
Y ₂ S@C ₇₂ -C _s (10528)	28.4	15.9	7.7	2.456	104.7
Y ₂ S@C ₈₂ -C _{3v} (8)	25.8	8.7	14.0	2.486	97.2

^a All energies are in kJ·mol⁻¹, distances are in Å, angles are in (°), X is either N or S, M is either Sc or Y. All parameters are for DFT-optimized structures. Distortion energies listed in the table are computed for model molecules (such as Sc₃N(C₈H₆)₃) whose geometrical parameters were adjusted to be identical to the cluster geometry in corresponding EMFs.

Similar to the Sc₃N, the Sc₂S cluster is rather flexible in terms of the metal-sulfur bond length. E_{dist} remains below 10 kJ/mol when the Sc–S distance is varied in the 2.32–2.50 Å range (i.e. ± 0.09 Å from the optimal value), and only at distances shorter than 2.32 Å the 10 kJ·mol⁻¹ threshold is overcome (Fig. 3.4a). Variation of the Sc–S–Sc angle from 95° to 180° also does not lead to the strong destabilization of the structure. The optimal

angle is about 110° , but it can vary in rather large limits with modest energy increase (Fig. 3.4b). The linear structure corresponds to the energy maximum with $E_{\text{bend}} = 6 \text{ kJ}\cdot\text{mol}^{-1}$, and similarly small energy changes are found when the Sc–S–Sc angle is decreased from 110° to 95° (at the angles below 95° the pentalene fragments start to interact strongly, which makes the values non-reliable). Thus, our calculations show that the Sc_2S cluster can adopt the shape dictated by the carbon cage without pronounced increase of the energy, which agrees with the variety of the geometry parameters of the Sc_2S cluster found in clusterfullerenes.

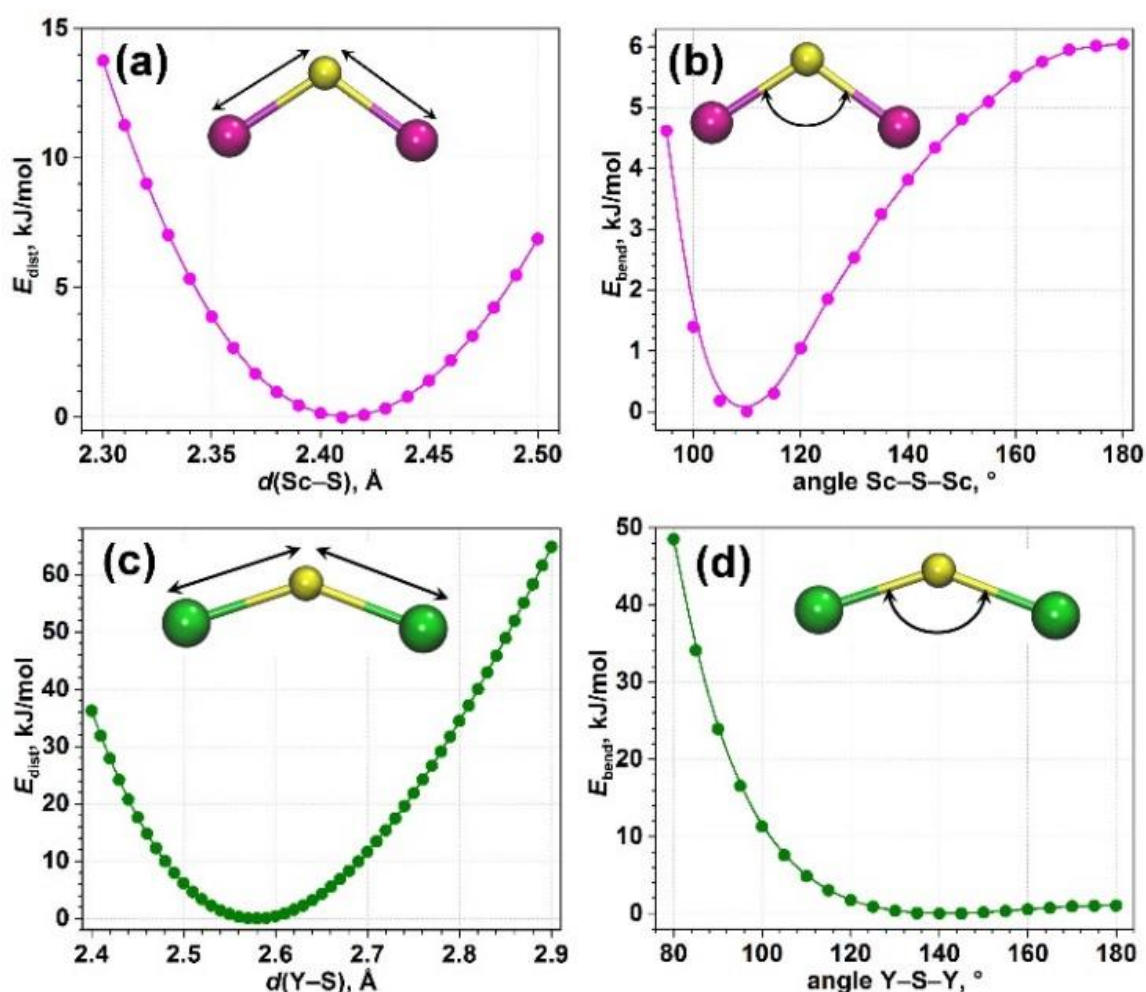


Figure 3.4 Energy profiles computed for (a) variation of Sc–S bond lengths in $\text{Sc}_2\text{S}(\text{C}_8\text{H}_6)_2$; (b) variation of Sc–S–Sc angle in $\text{Sc}_2\text{S}(\text{C}_8\text{H}_6)_2$; (c) variation of Y–S bond lengths in $\text{Y}_2\text{S}(\text{C}_8\text{H}_6)_2$; (d) variation of Y–S–Y angle in $\text{Y}_2\text{S}(\text{C}_8\text{H}_6)_2$.

For larger metal atoms (e.g., Y) only the $\text{M}_2\text{S}@\text{C}_{82}$ structures were observed so far,²⁶ but dedicated studies of such sulfides have not been performed yet. Optimization of the $\text{Y}_2\text{S}(\text{C}_8\text{H}_6)_2$ molecule yields the bond length of 2.58 \AA (0.17 \AA longer than in Sc_2S) and the Y–S–Y angle of 140° . In all $\text{Y}_2\text{S}@\text{C}_{2n}$ clusterfullerenes studies in this work (Table

3.1) the cluster is significantly strained with distortion energies from 26 $\text{kJ}\cdot\text{mol}^{-1}$ in $\text{Y}_2\text{S}@C_{82}\text{-}C_{3v}(8)$ to 53 $\text{kJ}\cdot\text{mol}^{-1}$ in $\text{Y}_2\text{S}@C_{70}\text{-}C_2(7892)$. The Y–S–Y angle in EMFs (86–105°) are all much smaller than in $\text{Y}_2\text{S}(\text{C}_8\text{H}_6)_2$, and the Y–S bonds (2.46–2.49 Å) are all noticeably shorter than the optimal value.

The energy profile computed along the Y–S bond length shows that distortion energy remains below 10 $\text{kJ}\cdot\text{mol}^{-1}$ when the bond length deviate from the optimal value of 2.58 Å within the ± 0.10 Å interval (Fig. 3.4c). However, the Y–S distances in $\text{Y}_2\text{S}@C_{2n}$ molecules are shorter, resulting in E_{dist} contributions to distortion energies of 8–16 $\text{kJ}\cdot\text{mol}^{-1}$. The E_{bend} profile shows that the Y_2S cluster is very flexible in the range of 125–180° (the energy is below 1 kJ/mol , see Fig. 3.4d). At smaller angles the energy rise is relatively steep reaching 8 $\text{kJ}\cdot\text{mol}^{-1}$ at 105° (as in $\text{Y}_2\text{S}@C_{72}$), 14 $\text{kJ}\cdot\text{mol}^{-1}$ at 97° ($\text{Y}_2\text{S}@C_{82}$), and 31 $\text{kJ}\cdot\text{mol}^{-1}$ at 86° ($\text{Y}_2\text{S}@C_{70}$). Thus, we can conclude that the Y_2S cluster is noticeably strained in C_{70} , C_{72} , and C_{82} cages. In $\text{Y}_2\text{S}@C_{72}$ and $\text{Y}_2\text{S}@C_{82}$, both compression of the cluster (E_{dist}) and its bending have comparable contributions to the distortion energy, whereas in $\text{Y}_2\text{S}@C_{70}$ E_{bend} is twice that of E_{dist} . $\text{Y}_2\text{S}@C_{2n}$ with larger cages have not been considered in this work, but based on the E_{dist} and E_{bend} profiles we can conclude that distortion energies in such sulfide clusterfullerenes will be small, and hence these molecules can be viable synthetic targets similar to already known carbide clusterfullerenes.

3.3.3 Carbide clusterfullerenes

The structural analysis of carbide clusters M_2C_2 ($\text{M} = \text{Sc}, \text{Y}$) is more complex than for M_3N and M_2S because C_2 unit can rotate and adopt different orientations with respect to metal atoms depending on the carbon cage (Fig. 3.5).^{147,156} For instance, Krause *et al.*¹⁵⁷ reported that C_2 unit of $\text{Sc}_2\text{C}_2@C_{84}$ is perpendicular to two Sc atoms, which are located on the S_4 axis of $C_{84}\text{-}D_{2d}$ cage. In the X-ray structure of $\text{Sc}_2\text{C}_2@C_{82}$ the cluster has butterfly shape with the average angle between two Sc–C–C planes of 130°.¹⁵⁶ In a recent study, Dorn *et al.*¹⁴⁷ reported that Y_2C_2 cluster is gradually changing its geometry from a stretched linear chain in $\text{Y}_2\text{C}_2@C_{100}$ to a compressed butterfly shape in $\text{Y}_2\text{C}_2@C_{82}$. The authors interpreted these changes as manifestation of the “nanoscale fullerene compression.”

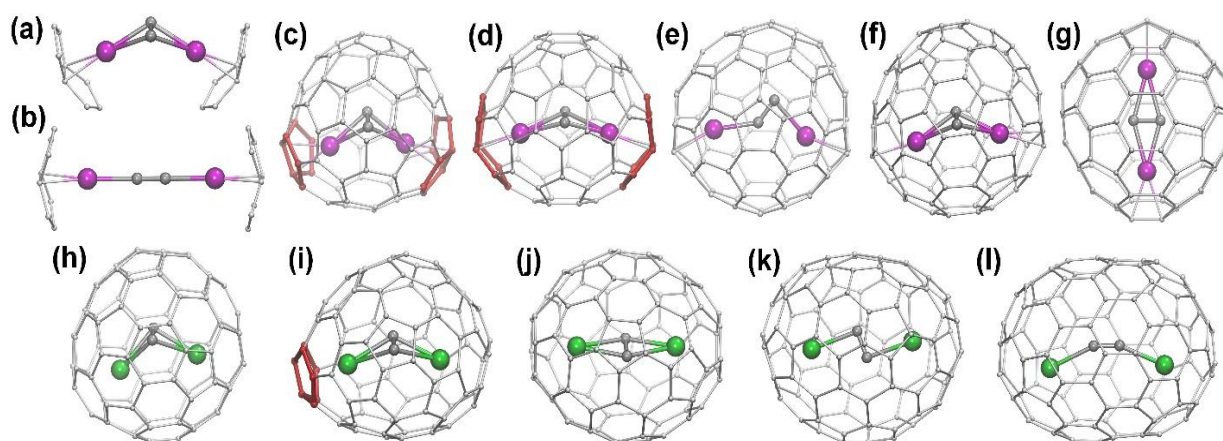


Figure 3.5 Butterfly (a) and linear (b) configurations of the Sc_2C_2 cluster in $\text{Sc}_2\text{C}_2(\text{C}_8\text{H}_6)_2$. (c-g) DFT optimized structures of Sc-carbide clusterfullerenes: (c) $\text{Sc}_2\text{C}_2@C_{70}\text{-C}_2(7892)$; (d) $\text{Sc}_2\text{C}_2@C_{72}\text{-C}_5(10528)$; (e) $\text{Sc}_2\text{C}_2@C_{80}\text{-C}_{2v}(5)$; (f) $\text{Sc}_2\text{C}_2@C_{82}\text{-C}_{3v}(8)$; (g) $\text{Sc}_2\text{C}_2@C_{84}\text{-D}_{2d}(23)$. (h-l) DFT optimized structures of Y-carbide clusterfullerenes: (h) $\text{Y}_2\text{C}_2@C_{82}\text{-C}_{3v}(8)$; (i) $\text{Y}_2\text{C}_2@C_{84}\text{-C}_1(51383)$; (j) $\text{Y}_2\text{C}_2@C_{88}\text{-D}_2(35)$; (k) $\text{Y}_2\text{C}_2@C_{92}\text{-D}_3(85)$; (l) $\text{Y}_2\text{C}_2@C_{100}\text{-D}_5(450)$. Sc atoms are magenta, Y atoms are green, carbon atoms are grey or red (in adjacent pentagon pairs), hydrogen atoms in (a-b) are omitted for clarity.

Sc-carbide clusters. The lowest energy structure of $\text{Sc}_2\text{C}_2(\text{C}_8\text{H}_6)_2$ has butterfly shape as shown in Figure 3.5a. The Sc–Sc distance is 4.044 Å, whereas the C_2 carbide unit is perpendicular to a line between the two metal atoms. The angle between two Sc–C–C planes (which is equal to the Sc–C–C–Sc dihedral angle) is 129°. This cluster shape closely resembles that found in $\text{Sc}_2\text{C}_2@C_{82}\text{-C}_{3v}(8)$. However, we have found that $\text{Sc}_2\text{C}_2(\text{C}_8\text{H}_6)_2$ with linear Sc–C–C–Sc cluster and Sc–Sc distance of 5.656 Å (Fig. 3.5b) is also an energy minimum and is only 1 $\text{kJ}\cdot\text{mol}^{-1}$ higher in energy than the butterfly-shaped configuration. We therefore decided to analyze how the energy of the system is changing in dependence on the Sc...Sc separation. Figure 3.6a shows the energy profile obtained by fixing Sc atoms at different distances and allowing C_2 unit to relax. The energy remains below 10 $\text{kJ}\cdot\text{mol}^{-1}$ in a broad range of Sc...Sc distances proving that Sc_2C_2 cluster is also rather flexible. Shortening the distance between metal atoms leads to the decrease of the Sc–C–C–Sc dihedral angle from 129° in the energy minimum at 4.044 Å to 109° at 3.600 Å. Decrease of the dihedral angle is accompanied by a gradual shortening of the Sc–C bond lengths (from 2.33 Å to 2.30 Å). These structural changes lead to moderate energy increase: at the shortest studied distance of 3.6 Å the energy is

increased to 7.6 $\text{kJ}\cdot\text{mol}^{-1}$.

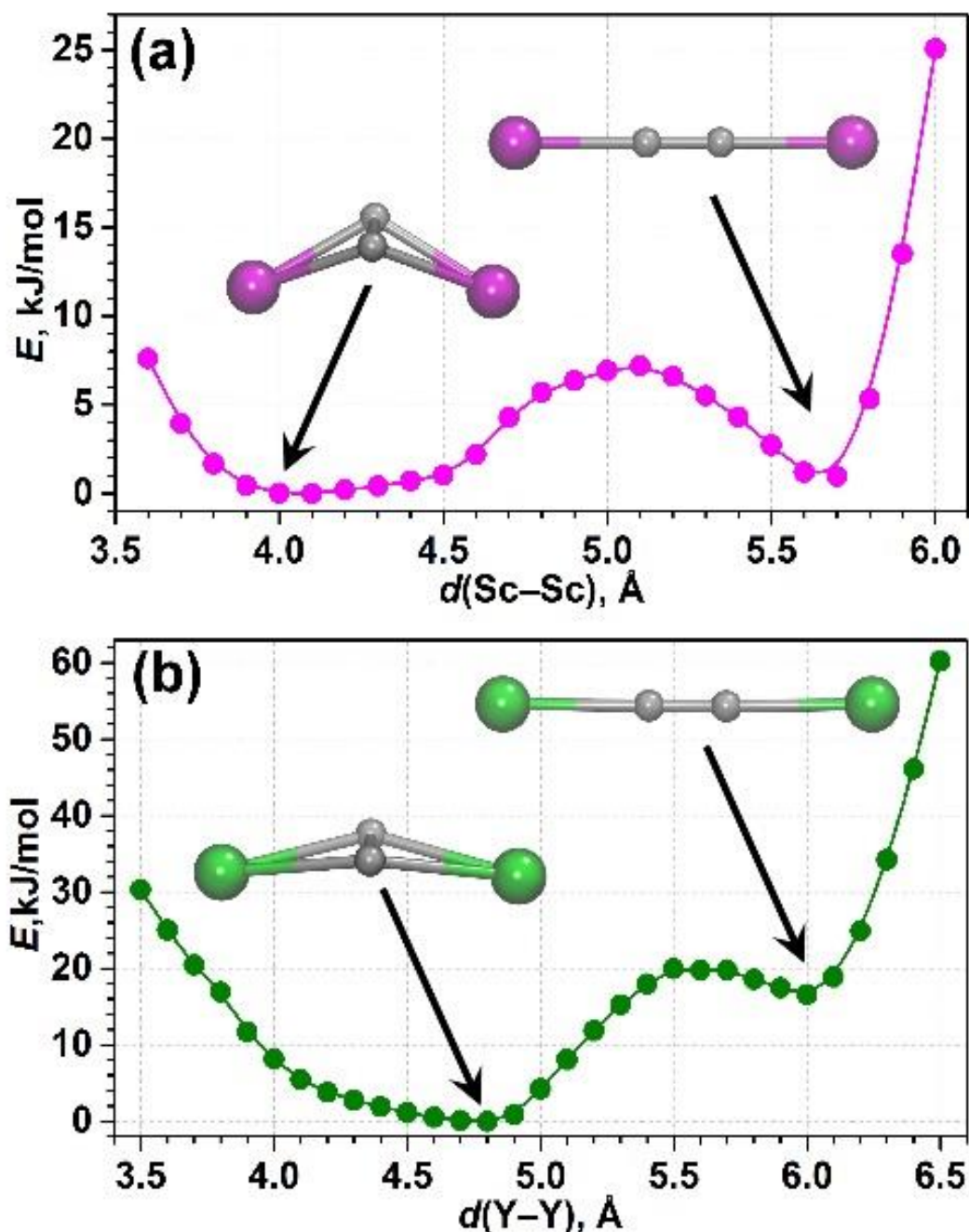


Figure 3.6 Energy profiles computed for (a) variation of Sc–Sc distance in $\text{Sc}_2\text{C}_2(\text{C}_8\text{H}_6)_2$; (b) variation of Y–Y distance in $\text{Y}_2\text{C}_2(\text{C}_8\text{H}_6)_2$. The energy minima corresponding to butterfly and linear configurations of M_2C_2 clusters are pointed by arrows.

The increase of the $\text{Sc}\cdots\text{Sc}$ distance beyond 4.04 Å first results in the flattening of the Sc_2C_2 cluster (decrease of the Sc–C–C–Sc dihedral angle), which adopts a planar shape at 4.5 Å. The Sc–C distances remain near 2.33 Å in the whole 4.0–4.5 range Å, and C_2 unit remains perpendicular to the Sc–Sc line. Further separation of Sc atoms leaves the cluster planar, but C_2 unit starts to rotate in the cluster plane till it reaches linear Sc–C–

C–Sc configuration at 5.656 Å. Transformation from perpendicular shape to the linear one requires an energy barrier of 7.2 kJ·mol⁻¹ which is reached at the Sc···Sc distance of 5.1 Å. Note that the center of the C₂ unit does not remain on the Sc–Sc line during rotation of the group. Besides, as the C₂ groups starts to rotate, two Sc–C distances for each Sc atoms become non-equivalent. The shortest one remains almost constant (2.18–2.19 Å) when the Sc···Sc distance is varied in the range of 4.8–5.6 Å; that is, till the cluster adopts a linear shape. Further increase of the Sc···Sc distance results in the increase of the Sc–C bond length and rapid increase of the energy. During the whole scan of Sc···Sc distances, the C₂ unit remains very rigid: the shortest and longest C≡C bond lengths found are 1.252 and 1.272 Å.

Table 3-2 Distortion energies and cluster geometry parameters (M–M distances and M–X–M angles) in selected carbide clusterfullerenes ^a

EMF molecule	<i>E</i>	M–M	C≡C	M–C–C–M
Sc ₂ C ₂ (C ₈ H ₆) ₂ -butterfly	0.0	4.044	1.271	129.0
Sc ₂ C ₂ (C ₈ H ₆) ₂ -linear	1.0	5.656	1.256	179.5
Sc ₂ C ₂ @C ₇₀ -C ₂ (7892)	20.5	3.587	1.263	108.5
Sc ₂ C ₂ @C ₇₂ -C _s (10528)	8.9	4.230	1.265	149.0
Sc ₂ C ₂ @C ₈₀ -C _{2v} (5)	14.8	4.390	1.258	179.8
Sc ₂ C ₂ @C ₈₂ -C _{3v} (8)	1.9	3.966	1.271	129.1
Sc ₂ C ₂ @C ₈₄ -D _{2d} (23)	1.6	4.451	1.274	180.0
Y ₂ C ₂ (C ₈ H ₆) ₂ -butterfly	0.0	4.809	1.270	167.5
Y ₂ C ₂ (C ₈ H ₆) ₂ -linear	16.3	5.991	1.254	173.7
Y ₂ C ₂ @C ₈₂ -C _{3v} (8)	25.0	3.793	1.267	109.7
Y ₂ C ₂ @C ₈₄ -C ₁ (51383)	9.4	4.257	1.266	131.5
Y ₂ C ₂ @C ₈₈ -D ₂ (35)	9.5	4.642	1.267	177.8
Y ₂ C ₂ @C ₉₂ -D ₃ (85)	5.5	4.880	1.266	176.0
Y ₂ C ₂ @C ₁₀₀ -D ₅ (450)	27.4	5.516	1.252	169.0

^a All energies are in kJ·mol⁻¹, distances are in Å, angles are in (°). All parameters are for DFT-optimized structures. Distortion energies listed in the table are computed for model molecules (such as Sc₂C₂(C₈H₆)₂) whose geometrical parameters were adjusted to be identical to the cluster geometry in corresponding EMFs.

Table 3-2 lists cluster distortion energies computed for five Sc-based carbide clusterfullerenes: Sc₂C₂@C₇₀-C₂(7892), Sc₂C₂@C₇₂-C_s(10528),¹⁵⁸ Sc₂C₂@C₈₀-C_{2v}(5),¹⁵⁹ Sc₂C₂@C₈₂-C_{3v}(8),¹⁶⁰ and Sc₂C₂@C₈₄-D_{2d}(23).¹⁶¹ Sc₂C₂@C₇₀ is not characterized yet but was studied here as an analogous structure to Sc₂S@C₇₀. The Sc···Sc distance in these

molecules varies from 3.587 Å in $\text{Sc}_2\text{C}_2@C_{70}$ to 4.451 Å in $\text{Sc}_2\text{C}_2@C_{84}$. These values correspond to the range of the butterfly-shaped Sc_2C_2 found in calculations for $\text{Sc}_2\text{C}_2(\text{C}_8\text{H}_6)_2$, and four of five carbide clusterfullerene molecules indeed have such a shape of the cluster. The outlier is $\text{Sc}_2\text{C}_2@C_{80}$: the shape of its cluster resembles that of the $\text{Sc}_2\text{C}_2(\text{C}_8\text{H}_6)_2$ molecule with the $\text{Sc}\cdots\text{Sc}$ distance fixed at 4.8–4.9 Å, i.e. the cluster is planar, the C_2 unit is rotated in the cluster plane, and its center is shifted from the $\text{Sc}\text{--}\text{Sc}$ line. Variation of the Sc_2C_2 cluster geometry in different carbon cages was analyzed in ref. ¹⁶². In $\text{Sc}_2\text{C}_2@C_{90}$ with elongated $C_{90}\text{-}D_{5h}$ cage, the authors showed that the cluster can have almost a linear configuration.

The carbide cluster of $\text{Sc}_2\text{C}_2@C_{70}$ has the shortest $\text{Sc}\text{--}\text{Sc}$ distance (3.587 Å) and the highest distortion energy of 21 $\text{kJ}\cdot\text{mol}^{-1}$. The least strained clusters with distortion energies less than 2 $\text{kJ}\cdot\text{mol}^{-1}$ are found in $\text{Sc}_2\text{C}_2@C_{82}$ and $\text{Sc}_2\text{C}_2@C_{84}$. Distortion energies in $\text{Sc}_2\text{C}_2@C_{72}$ and $\text{Sc}_2\text{C}_2@C_{80}$ have intermediate values of 9 and 15 $\text{kJ}\cdot\text{mol}^{-1}$. Note that the cluster distortion energies in $\text{Sc}_2\text{C}_2@C_{70}$, $\text{Sc}_2\text{C}_2@C_{72}$ and $\text{Sc}_2\text{C}_2@C_{80}$ are higher than might be expected from the $\text{Sc}_2\text{C}_2(\text{C}_8\text{H}_6)_2$ calculations with the same $\text{Sc}\cdots\text{Sc}$ distances, whereas the shape of the cluster in $\text{Sc}_2\text{C}_2@C_{80}$ (see above) and to some extent in $\text{Sc}_2\text{C}_2@C_{72}$ deviate from that in $\text{Sc}_2\text{C}_2(\text{C}_8\text{H}_6)_2$. This result shows that the way how Sc atoms are coordinated to the cage fragments may also play some role in determining the shape of the cluster and its stability. However, deviations of distortion energies are still very high and show that Sc_2C_2 is rather flexible and can adopt different configurations following the shape of the host carbon cage.

Y-carbide clusters. Similar to $\text{Sc}_2\text{C}_2(\text{C}_8\text{H}_6)_2$, calculations of $\text{Y}_2\text{C}_2(\text{C}_8\text{H}_6)_2$ revealed the presence of two energy minimas, with butterfly- and linear-shaped Y_2C_2 cluster. However, in contrast to the Sc case, these minimas are not isoenergetic. The structure with the butterfly-shaped Y_2C_2 cluster ($\text{Y}\cdots\text{Y}$ distance 4.809 Å) is 16 $\text{kJ}\cdot\text{mol}^{-1}$ lower in energy than configuration with linear cluster ($\text{Y}\cdots\text{Y}$ distance 5.991 Å). The profile computed in the $\text{Y}\cdots\text{Y}$ range from 4.0 Å to 6.5 Å shows very flat region at 4.0–5.1 Å, where energy remain below 10 $\text{kJ}\cdot\text{mol}^{-1}$ (Fig. 3.6b). At longer $\text{Y}\cdots\text{Y}$ distances the energy increases to 20 $\text{kJ}\cdot\text{mol}^{-1}$ (at 5.5 Å), then slowly decreases to 17 $\text{kJ}\cdot\text{mol}^{-1}$ near 5.9–6.0 Å, and then grows fast to 62 $\text{kJ}\cdot\text{mol}^{-1}$ at 6.5 Å. Figure 3.7 shows evolution of the Y_2C_2 structure with the increase of the $\text{Y}\cdots\text{Y}$ distance.

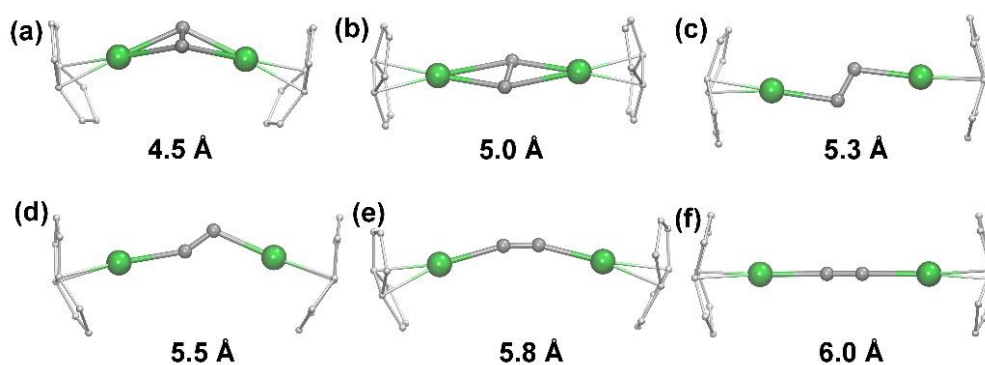


Figure 3.7 Evolution of the $Y_2C_2(C_8H_6)_2$ molecular structure with the increase of the Y...Y distance from 4.5 to 6.0 Å. The energies are: (a) 1.0 $\text{kJ}\cdot\text{mol}^{-1}$; (b) 4.2 $\text{kJ}\cdot\text{mol}^{-1}$; (c) 15.2 $\text{kJ}\cdot\text{mol}^{-1}$; (d) 20.0 $\text{kJ}\cdot\text{mol}^{-1}$; (e) 18.6 $\text{kJ}\cdot\text{mol}^{-1}$; (f) 16.6 $\text{kJ}\cdot\text{mol}^{-1}$. Y atoms are green, carbon atoms are grey, hydrogen atoms are omitted for clarity.

Distortion energies computed for the Y_2C_2 cluster in experimentally available carbide clusterfullerenes $Y_2C_2@C_{82}-C_{3v}(8)$,¹⁶³ $Y_2C_2@C_{84}-C_1(51383)$,^{20,164} $Y_2C_2@C_{88}-D_2(35)$,⁸⁴ $Y_2C_2@C_{92}-D_3(85)$,^{86,147,165} and $Y_2C_2@C_{100}-D_5(450)$ ¹⁴⁷ (see Table 3.2) agree with the trend found in the Y...Y energy profile of $Y_2C_2(C_8H_6)_2$. The largest distortion energy, 27 $\text{kJ}\cdot\text{mol}^{-1}$, is found in $Y_2C_2@C_{100}$ with the largest carbon cage and longest Y...Y distance (5.516 Å). This distance corresponds to the energy maximum of $Y_2C_2(C_8H_6)_2$ (Fig. 3.6b). Similarly large distortion energy, 25 $\text{kJ}\cdot\text{mol}^{-1}$, is also found in $Y_2C_2@C_{82}$. Here Y...Y distance, 3.793 Å, is too short because of the small size of the cage. The least strained cluster is in $Y_2C_2@C_{92}$ (6 $\text{kJ}\cdot\text{mol}^{-1}$), whereas in $Y_2C_2@C_{84}$ and $Y_2C_2@C_{88}$ the energies are higher but still do not exceed 10 $\text{kJ}\cdot\text{mol}^{-1}$. The Y...Y distance for the latter three structure fall in the range from 4.257 to 4.880 Å, and the cluster adopts butterfly shape with different Y–C–C–Y dihedral angles.

For the sake of comparison, we have also performed calculations for $[M_2C_2]^{4+}$ clusters. In agreement with earlier results,¹⁴⁷ both for Sc and Y we found only one energy minimum corresponding to the linear configuration of the cluster. M...M distance in these configurations are 5.794 Å for Y and 5.528 Å for Sc. At shorter metal-metal distances, the energy of $[M_2C_2]^{4+}$ clusters is increasing dramatically reaching 150 kJ/mol for $[Y_2C_2]^{4+}$ at 4.8 Å and 280 kJ/mol for $[Sc_2C_2]^{4+}$ at 4.0 Å as shown as in figure 3.8. These should be compared to the results of computations for $M_2C_2(C_8H_6)_2$ species, which show two energy minima (see Figure 3.6). The minimum with linear M_2C_2 configuration is found at similar distances to the $[M_2C_2]^{4+}$ species, however the second minimum with butterfly configuration of the cluster is much lower (over 100 kJ/mol) in energy and

corresponds to shorter M-M distances. Thus, we believe that because of uncompensated Coulomb repulsion, $[M_2C_2]^{4+}$ model gives wrong description of the cluster energetics at short $M\cdots M$ distance. Coordinating the metal atoms to pentalene fragments reduces unphysical repulsion and gives more correct description of the cluster in EMFs.

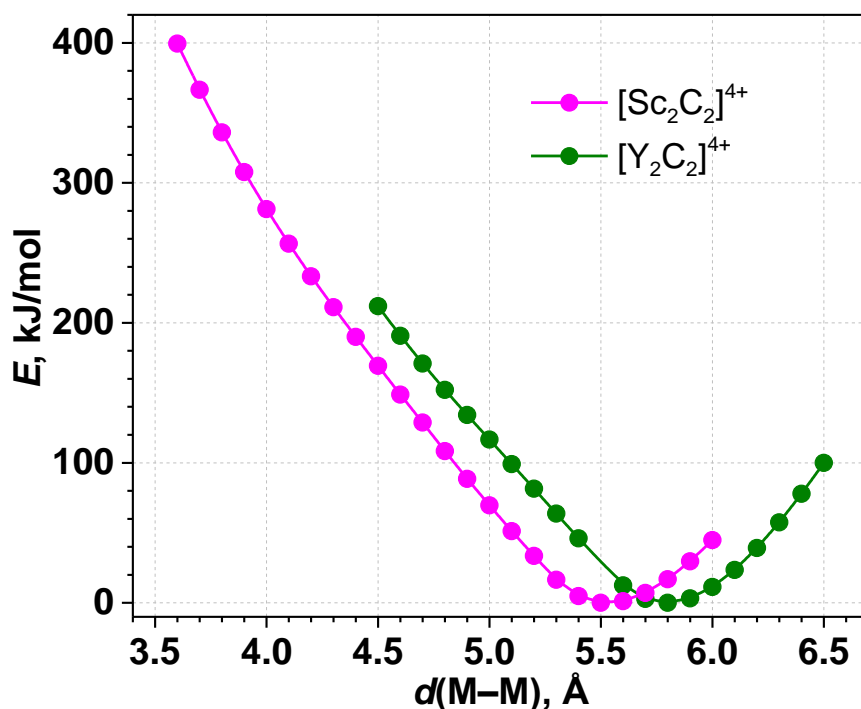


Figure 3.8 The energy profiles computed for $[M_2C_2]^{4+}$ ions with variation of the M-M distance.

Our results show that the background of the “nanoscale fullerene compression”, which implies that the least strained structure of Y_2C_2 is linear and that the butterfly shape is forced by cage-induced compression, should be reconsidered. In fact, butterfly shape of the M_2C_2 cluster is more energetically favorable and it is realized when metal-metal distance is of ca 4-5 Å. At shorter distances the energy is increasing and “nanoscale compression” is really an appropriate term. However, at longer distances the energy is also increasing and the linear form is higher in energy, especially for Y_2C_2 . Thus, “nanoscale stretching” would be an appropriate term for the longer metal-metal distances. In fact, the shape and the size of the carbon cage determine position of metal atoms and the $M\cdots M$ distance (M-cage distances are more or less constant), whereas C_2 unit then finds its best configuration for a given position of metal atoms.

3.3.4 $\text{Ti}_2\text{C}_2@C_{78}$ and $\text{Ti}_2\text{S}@C_{78}$

Titanium plays a special role in EMFs since so far it is the only genuine transition metal which can be encapsulated inside the carbon cage. Two all-titanium EMFs characterized with high degree of certainty are carbide $\text{Ti}_2\text{C}_2@C_{78}$ ¹⁶⁶⁻¹⁶⁸ and sulfide $\text{Ti}_2\text{S}@C_{78}$,¹⁶⁹ both with $D_{3h}(5)$ carbon cage (mixed Ti-Sc¹⁷⁰ and Ti-Y¹⁷¹ nitride clusterfullerenes are not considered here). Both EMFs have similar structure in that Ti atoms are η^6 -coordinated to the poles of C_{78} (which has elongated shape) and the Ti_2C_2 and Ti_2S clusters are almost linear (Fig. 3.9a,b). Since Ti formally transfers three electrons to the carbon cage, pentalene is not able to mimic the metal-cage interactions and is replaced here by sumanene $C_{21}H_9$ (Fig. 3.9c,d).

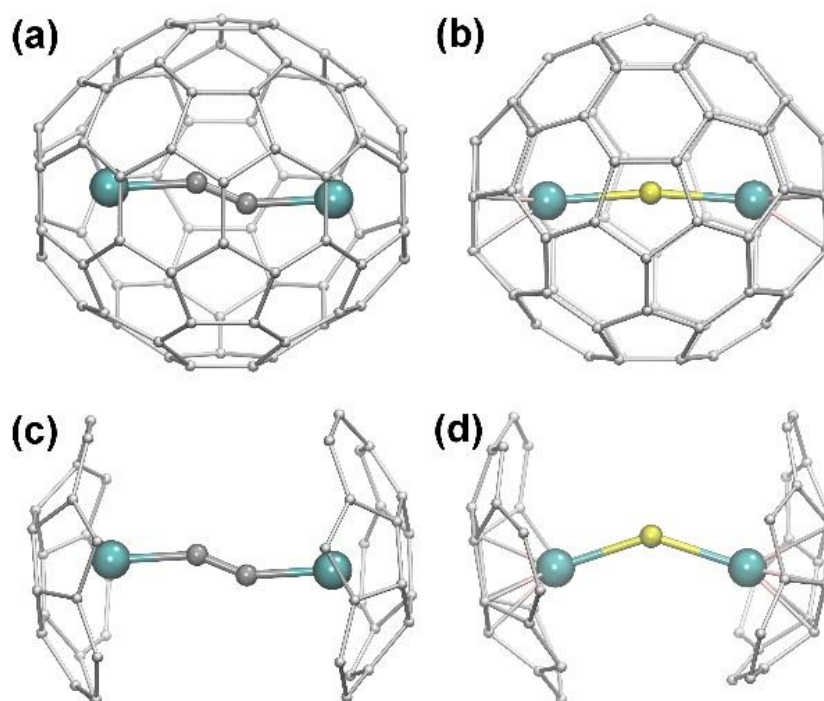


Figure 3.9 DFT-optimized molecular structures of $\text{Ti}_2\text{C}_2@C_{78}$ (a), $\text{Ti}_2\text{S}@C_{78}$ (b), $\text{Ti}_2\text{C}_2(\text{C}_{21}\text{H}_9)_2$ (c), and $\text{Ti}_2\text{S}(\text{C}_{21}\text{H}_9)_2$. Ti atoms are cyan, sulfur is yellow, carbon atoms are grey, hydrogen atoms in (c) and (d) are omitted for clarity.

DFT optimization of $\text{Ti}_2\text{S}(\text{C}_{21}\text{H}_9)_2$ results in the structure with bent Ti_2S cluster (Ti–S–Ti bond angle is 143°), the Ti–S bond length of 2.328 \AA , and the Ti \cdots Ti distance of 4.417 \AA . For comparison, in $\text{Ti}_2\text{S}@C_{78}$ these structural have the values of 172° (Ti–S–Ti angle), 2.375 \AA (Ti–S bond length), and 4.737 \AA (Ti \cdots Ti distance). Distortion energy of the Ti_2S cluster in $\text{Ti}_2\text{S}@C_{78}$ is estimated to be $10 \text{ kJ}\cdot\text{mol}^{-1}$. Computations of the energy profile along the cluster bending and Ti–S bond stretching show that the Ti–S–Ti angle can vary in relatively large range with modest energy increase (Fig. 3.10a,b). The linear cluster is the energy maximum, but it is only $7 \text{ kJ}\cdot\text{mol}^{-1}$ less stable

than the lowest energy configuration. Variation of the Ti–S bond length shows that the energy remains below 10 kJ·mol⁻¹ in the range of 2.24–2.43 Å. These results prove that the Ti₂S cluster is rather flexible in similar fashion to Sc₂S and Y₂S clusters discussed above and can change its shape in rather broad range of geometrical parameters.

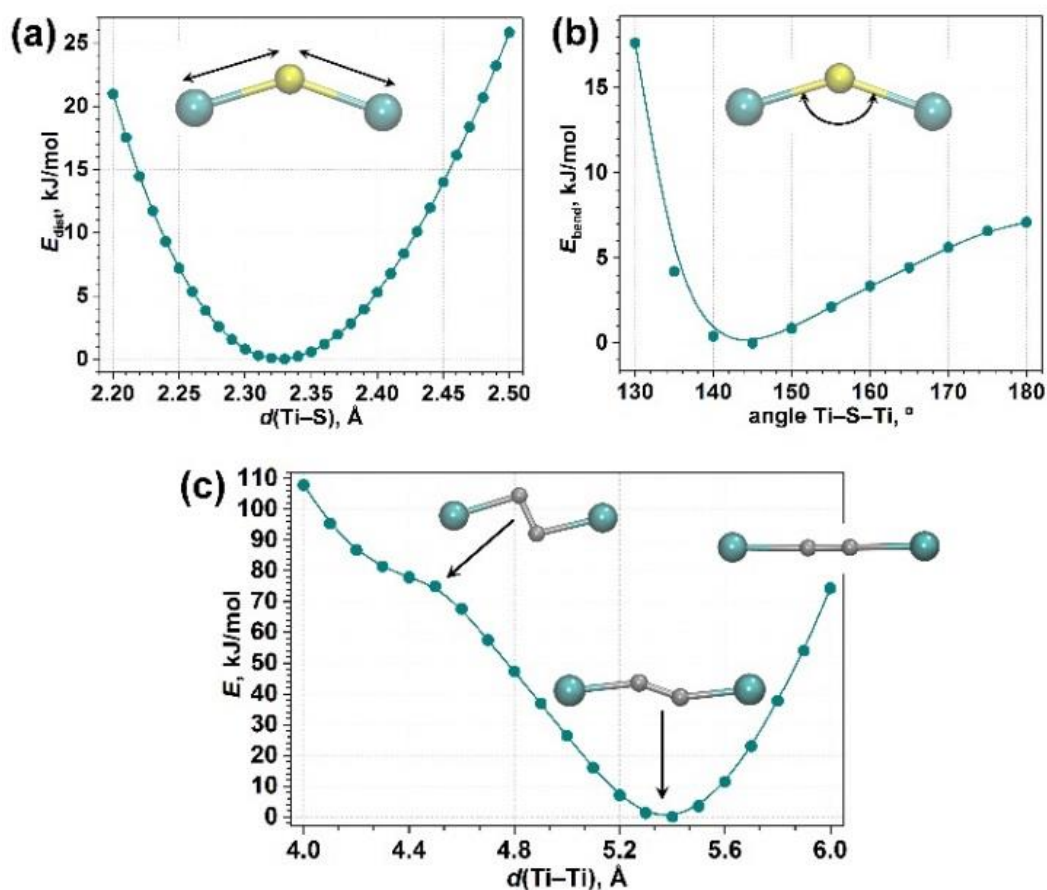


Figure 3.10 Energy profiles computed for (a) variation of Ti–S bond lengths in $\text{Ti}_2\text{S}(\text{C}_{21}\text{H}_9)_2$; (b) variation of Ti–S–Ti angle in $\text{Ti}_2\text{S}(\text{C}_{21}\text{H}_9)_2$; (c) variation of Ti–Ti distance in $\text{Ti}_2\text{C}_2(\text{C}_{21}\text{H}_9)_2$.

Unconstrained optimization of $\text{Ti}_2\text{C}_2(\text{C}_{21}\text{H}_9)_2$ shows that Ti_2C_2 cluster prefers almost linear configuration (Ti–C–C angle is 174.5°, see Fig. 3.9c) with Ti···Ti distance of 5.377 Å (*ca* 1 Å longer than in Ti_2S) and Ti–C bond length of 2.073 Å. In $\text{Ti}_2\text{C}_2@C_{78}$ Ti atoms are closer to each other (5.094 Å), Ti–C bonds are shorter (1.976 Å), and the cluster is more deviated from the linear shape (Ti–C–C angle is 154.2°). These structural changes increase the energy of the cluster by 26 kJ·mol⁻¹. Significant distortion energy shows that Ti_2C_2 cluster is more rigid than sulfide or Sc_2C_2 cluster, and the same conclusion can be drawn from the analysis of the Ti···Ti energy profile (Fig. 3.10c). In contrast to the flat Sc_2C_2 profile (Fig. 3.6a), distortion energy of the Ti_2C_2 cluster remains below 10 kJ·mol⁻¹ only in the 5.2–5.6 Å range and increases sharply outside these limits either with stretching or compressing the cluster. We could not find an energy minimum

corresponding to the butterfly configuration down to the distances of 4.0 Å. The bend on the curve near 4.4 Å can be well seen, but the energy continues to increase at shorter Ti···Ti distance and exceeds 100 kJ·mol⁻¹ at 4.0 Å. Thus, Ti₂C₂@C₇₈ is a real example of the nanoscale fullerene compression.

Our analysis shows that although Ti₂S@C₇₈ and Ti₂C₂@C₇₈ are isostructural, they exhibit different kinds of the cluster strain. For Ti₂S, the C₇₈ cage appears to be too large, whereas for Ti₂C₂ it is too small, which in both cases results in non-negligible distortion energy. Note that the effect is sufficient to induce measurable differences of the geometrical parameters of the carbon cage. In Ti₂C₂@C₇₈ the distance between centroids of two Ti-coordinating hexagons, 8.219 Å, is 0.176 Å longer than in Ti₂S@C₇₈, 8.045 Å. Likewise, Ti-hexagon distance in Ti₂C₂@C₇₈, 1.571 Å, is shorter than in Ti₂S@C₇₈, 1.659 Å. In other words, in Ti₂C₂@C₇₈ the cage is elongated and Ti–C₆ distance is shortened to allow more space for the Ti₂C₂ cluster.

3.4 Conclusions

In this work a simple approach is presented and evaluated allowing analysis of the strain experienced by clusters encapsulated in endohedral metallofullerenes. We argue that calculations for the sole cluster, either in the neutral or the charged state, cannot be used for this goal. However, when the effect of the carbon cage is mimicked by small organic π -systems (such as pentalene and sumanene), the cluster has sufficient freedom to adopt the optimal configuration, and therefore the energetic characteristics of the EMF-induced distortion of the cluster can be evaluated. Both nitride and sulfide clusters were found to be rather flexible, i.e. their distortion energy is small in broad range of geometrical parameters. Hence, they can be encapsulated in carbon cages of different size and shape. For carbide M₂C₂ cluster the situation is more complex. The optimized cluster can adopt either butterfly or linear shapes, and these configurations have substantially different metal-metal distance. Whereas for Sc₂C₂ both structures are isoenergetic, linear form of the Y₂C₂ cluster is substantially less stable than the butterfly-shaped configuration. These results show that phenomenon of the nanoscale fullerene compression should be analyzed more carefully. Finally, we show that both Ti₂S and Ti₂C₂ cluster are strained in corresponding EMF molecules, but the origin of the strain is opposite: C₇₈-D_{3h}(5) cage imposes too long Ti···Ti distance for the sulfide cluster and too short distance for the carbide cluster.

Chapter 4. Carbide clusterfullerenes

with odd number of carbon atoms:

molecular and electronic structures of

$\text{Sc}_4\text{C}@C_{80}$, $\text{Sc}_4\text{C}@C_{82}$, and $\text{Sc}_4\text{C}_3@C_{80}$

4.1 Introduction

Very recently, two new species with molecular composition Sc_4C_{81} and Sc_4C_{83} were discovered during the arc-discharge synthesis of $\text{Sc}_3\text{CH}@C_{80}$ using methane as a reactive atmosphere gas¹⁷² following the method described by Krause and *et al.*¹⁷³ Mass-spectra of the soluble part of the raw synthesis products are shown in figure 4.1. The positive ion mode (laser desorption ionization) LDI-TOF mass-spectrum of the extract is dominated by the Sc_4C_{81} , Sc_4C_{82} , and Sc_4C_{83} species (Fig. 4.1). Whereas the Sc_4C_{82} can be undoubtedly assigned to the well-known carbide clusterfullerene $\text{Sc}_4\text{C}_2@C_{80}$ ¹⁷⁴, the species with 81 and 83 carbon atoms are detected for the first time. Since fullerene cages have only even number of carbons, Sc_4C_{81} and Sc_4C_{83} inevitably should have an odd number of carbon atoms in their endohedral clusters and hence represent a new type(s) of carbon containing EMFs. Unfortunately, further isolation of Sc_4C_{81} and Sc_4C_{83} was not unsuccessful. Stability of Sc_4C_{83} in the HPLC was not sufficient (i.e. corresponding peaks could not be detected in the mass spectrum after the fullerene extract was run through the chromatographic column). The $\text{Sc}_4\text{C}_{81}^+$ signal survived after HPLC treatment, but after chromatographic separation of the extract this signals was detected in several chromatographic fraction. Such behavior again points to the ease of ionization and precludes reliable control of the isolation procedure. Thus, low stability and enhanced ionization precluded isolation and detailed characterization of Sc_4C_{81} and Sc_4C_{83} , which motivated us to perform computational analysis of possible molecular structures and

properties of these species with the aim to clarify the possibility of their future isolation. Therefore, a set of computational analysis is presented to understand the possible molecular and electronic structures of two new members of carbon-containing EMFs, $\text{Sc}_4\text{C}@C_{80}$ and $\text{Sc}_4\text{C}_3@C_{80}$, which were discovered during the arc-discharge synthesis in the presence of methane.

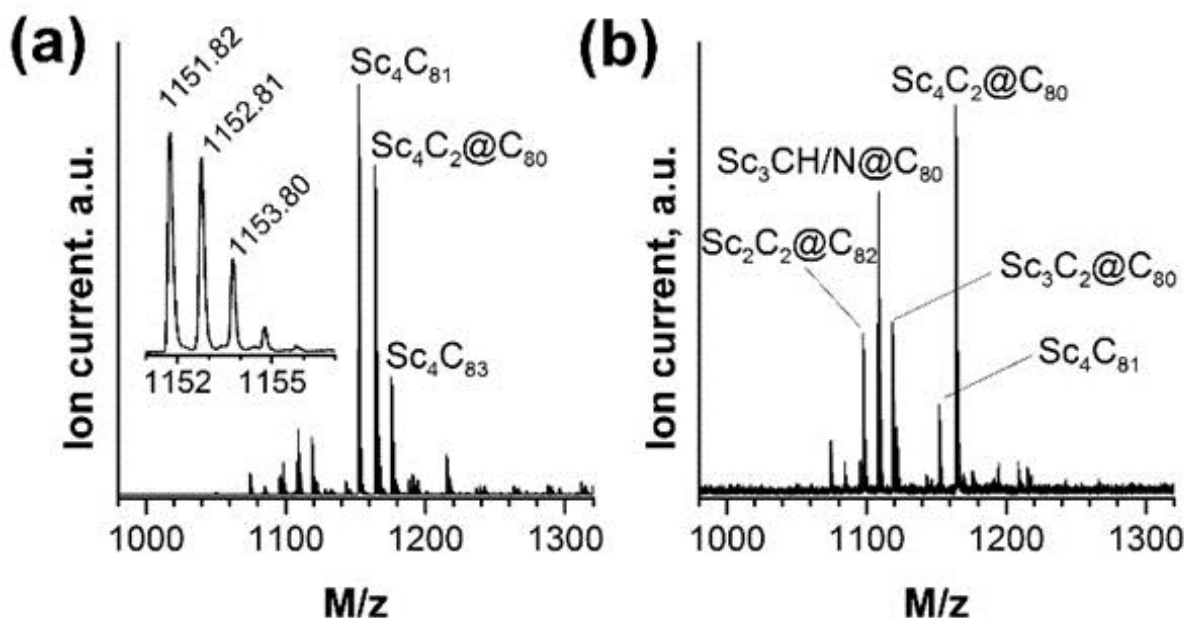


Figure 4.1 Positive ion mode MALDI-TOF mass-spectrum of the extract of Sc-EMFs obtained by arc-discharge in the Sc-CH₄ system: (a) measured without matrix; (b) measured with sulfur as a matrix. The inset in (a) shows isotopic pattern and mass numbers of the group of peaks corresponding to $\text{Sc}_4\text{C}_{81}^+$. These values are in good agreement with theoretical mass numbers for the three main peaks of Sc_4C_{81} (1151.82, 1152.83, and 1153.83). Reproduced from Ref. 174

4.2. Computational studies of $\text{Sc}_4\text{C}_{1-3}@C_{80}$

4.2.1 General remarks on Sc_4 -type clusterfullerenes

Several clusterfullerenes with four Sc atoms are already known, and all of them are proved to have $C_{80}-I_h$ carbon cage. Endohedral Sc atoms preferably form a tetrahedron, whereas non-metals have different positions depending on their nature. In the carbide clusterfullerene $\text{Sc}_4\text{C}_2@C_{80}$, one carbon atom is in the center of the tetrahedron, whereas another one is located above one of the Sc_3 faces^{174,175}. The DFT-predicted structure of $\text{Sc}_4\text{C}_2\text{H}@C_{80}$ is very similar, the hydrogen atom is bonded to the non-central carbon atom so that CCH fragment is almost linear¹⁷⁶. Tetrahedral Sc_4 clusters were also described

for oxide clusterfullerenes, Sc₄O₂@C₈₀¹⁰ and Sc₄O₃@C₈₀¹⁷⁷. In both oxide structures the μ₃-O atoms are located above the Sc₃ faces of the Sc₄ tetrahedron.

Large number of Sc atoms in Sc₄-type endohedral clusters implies a large electron transfer to the carbon cage. So far, the highest formal number of electrons transferred to the carbon cage in EMFs is 6, and the most preferable six-fold charged carbon cage is C₈₀-I_h(7)^{48,81,178-180}. It is therefore not surprising that all EMFs with four Sc atoms described so far have C₈₀-I_h(7) cage; furthermore, encapsulation of Sc₄-cluster in fullerenes cages of other sizes is not reported. Based on this line of arguments, we may tentatively propose that the Sc₄C₈₁ and Sc₄C₈₃ species correspond to clusterfullerenes with two types of clusters, Sc₄C@C₈₀-I_h and Sc₄C₃@C₈₀-I_h. Yet, we cannot completely exclude a situation that both new species have the same type of cluster and therefore are either a pair Sc₄C₃@C₇₈ / Sc₄C₃@C₈₀, or Sc₄C@C₈₀ / Sc₄C@C₈₂. We will analyze this possibility further below, after we clarify the principal details of the molecular and electronic structures of Sc₄C@C₈₀ and Sc₄C₃@C₈₀. All calculations described below were performed at the using PBE¹²¹ density functional and Priroda code^{149,181,182}. For structural optimization C atoms were treated with original TZ2P-quality full-electron basis set {6,3,2}/(11s,6p,2d), and SBK-type effective core potentials were used for Sc with {5,5,4}/{9s,9p,8d} valence parts. For frontier MO, IP, and EA values, the carbon atoms of cages and internal clusters were treated with basis set {4,3,2}/{12s,8p,4d} and {8,7,5,3,1}/{14s,10p,7d,5f,3g} respectively. Sc atoms were set with full-electron basis set {10,9,7,5,3,1}/{27s,22p,16d,10f,8g,4h}. For QTAIM analysis, the wave functions are obtained from single point energy computations with full-electron TZVP-quality basis set for the carbon cage and def2-TZVPP basis set for the intraclusters by Orca 2.8 package.¹⁸³ QTAIM calculations were performed using AIMAll suite¹⁸⁴.

4.2.2 Molecular and electronic structure of Sc₄C@C₈₀

DFT optimization of Sc₄C@C₈₀ with different arrangement of Sc atoms around the central carbon resulted in two plausible shapes of the cluster. In three most stable nearly isoenergetic conformers (ΔE = 0–3 kJ/mol), Sc atoms form a distorted tetrahedron around the central carbon atom with the average Sc–C bond length of 2.11–2.12 Å and the average Sc–Sc distance of 3.45 Å. The conformers are somewhat different in the distribution of Sc–C–Sc angles and orientation of the cluster with respect to the carbon cage atoms. For instance, the Sc–C–Sc angles in the lowest energy C₁-symmetric conformer span the range of 103–119° (compare to 109° in an ideal tetrahedron), whereas

in the second lowest energy C_2 -symmetric structure ($\Delta E = 1.5$ kJ/mol) the Sc_4 tetrahedron is more distorted with the Sc–C–Sc angles in the range of 95 – 124° . Note similar structure of the endohedral cluster was found in a computational study of $\text{Al}_4\text{C}@C_{80}$ ¹⁸⁵.

Another plausible shape of the Sc_4C cluster is a square with carbon atom in the middle. This isomer is somewhat less stable ($\Delta E = 12.6$ kJ/mol) than the structures with tetrahedral cluster. Sc–C bonds in the cluster are 2.139 Å long, and the Sc–C–Sc angles are 88.5° and 91.5° (the isomer has rigorous C_{2h} symmetry, and the cluster shape deviates slightly from the regular square). The Sc–Sc distances in the square cluster are 2.991 and 3.064 Å. Transition state search followed by intrinsic reaction coordinate (IRC) calculations showed that the planar and tetrahedral cluster shapes can transform to each other with the transition state of 38.3 kJ/mol (Fig. 4.2c). This relatively small barrier ensures that the Sc_4C cluster should exhibit fluxional behaviour at room temperature.

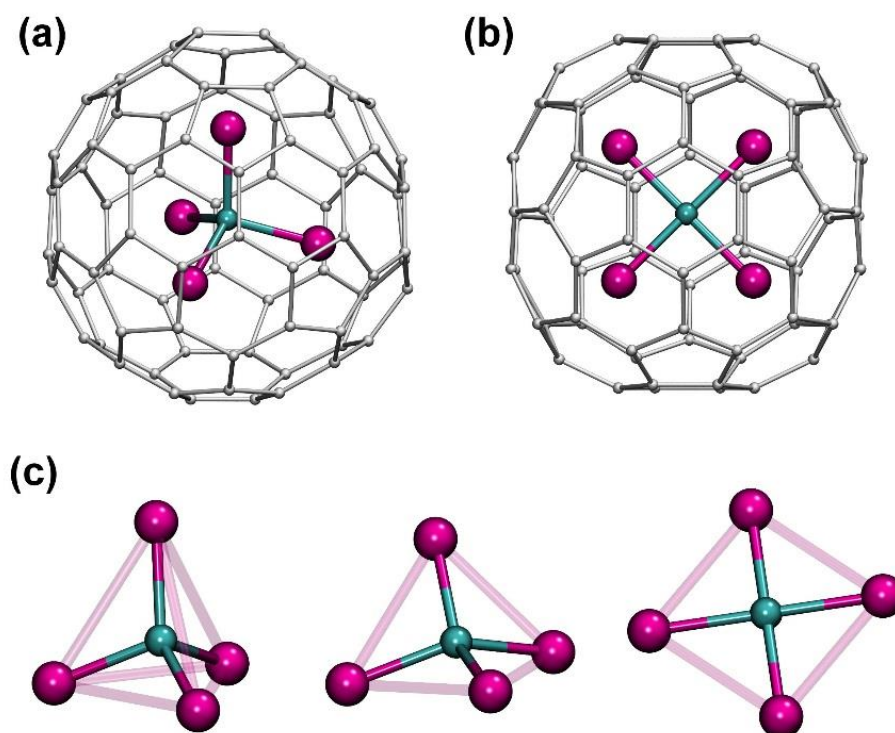


Figure 4.2 DFT-optimized molecular structures of $\text{Sc}_4\text{C}@C_{80}$ isomers with tetrahedral (a) and square (b) cluster. Part (c) shows enlarged structure of the tetrahedral (left) and planar (right) Sc_4C clusters and transition state between them (middle).

The formal cage charge (-6) and the largest reasonable negative charge of the central carbon (-4) require that the net charge of Sc atoms should not exceed $+10$. This implies that the oxidation state of some Sc atoms is less than $+3$. Although Sc usually adopts a

+3 state in EMFs, a divalent state of Sc can be realized in certain cases such as $\text{Sc}_2@C_{82}$ ¹⁸⁶ or $\text{Sc}_4\text{O}_2@C_{80}$ ¹⁰. The latter is especially similar to $\text{Sc}_4\text{C}@C_{80}$ in that the net charge of Sc ion is also +10. Computational and experimental studies showed that two Sc atoms in $\text{Sc}_4\text{O}_2@C_{80}$ are in the +3 state, whereas two others are in the +2 state and exhibit pronounced Sc–Sc bonding interactions¹⁸⁷⁻¹⁸⁹, which is manifested in the Sc–Sc bonding nature of the highest occupied molecular orbital (HOMO). Frontier MO analysis of $\text{Sc}_4\text{C}@C_{80}$ shows that the HOMO of the isomer with both tetrahedral and planar clusters is predominantly localized on Sc atoms and is evenly distributed between all of them (Fig. 4.3), so the formal charge state of Sc in $\text{Sc}_4\text{C}@C_{80}$ is +2.5. Contribution of each Sc atom to the HOMO resembles 3*d* atomic orbitals. These atomic orbitals partially overlap, which may be at first sight interpreted as the presence of delocalized Sc–Sc bonding. However, analysis of the bond orders (see below) shows that the degree of Sc–Sc bonding is rather low. The LUMO as well as LUMO+1 of $\text{Sc}_4\text{C}@C_{80}$ is also predominantly a metal-based orbital irrespective of the cluster shape, whereas HOMO–1 is the cage-based MO. The central carbon atoms has no noticeable contribution to the frontier MOs of $\text{Sc}_4\text{C}@C_{80}$.

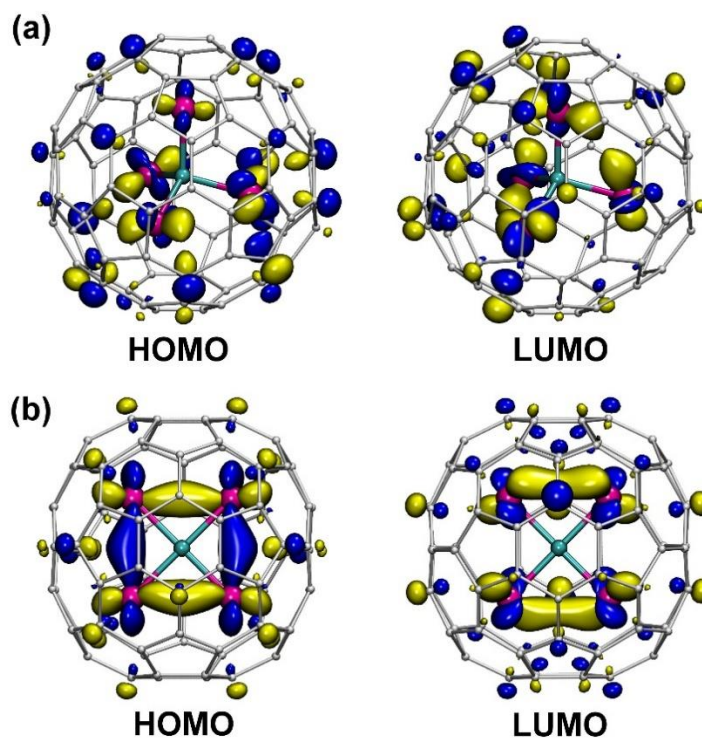


Figure 4.3 Frontier molecular orbitals in the $\text{Sc}_4\text{C}@C_{80}$ isomers with tetrahedral (a) and square (b) cluster.

The energy of frontier MOs as well as the HOMO-LUMO gap depend on the cluster geometry. In the lowest energy isomer with tetrahedral cluster the gap is quite small, only 0.48 eV, whereas in the second most stable isomer, also with the tetrahedral cluster, the gap is already increased to 0.71 eV. Finally, in the isomer with the planar cluster the HOMO-LUMO gap is 1.05 eV. These values show that HOMO and LUMO energies of $\text{Sc}_4\text{C}@C_{80}$ are very sensitive to the cluster geometry. In the view of the high fluxionality of the molecular structure, the electronic properties of $\text{Sc}_4\text{C}@C_{80}$ are expected to be a result of the averaging over different cluster configurations with high statistical weight of the low-energy conformers with tetrahedral cluster. The small HOMO-LUMO gap values of such configuration indicate that $\text{Sc}_4\text{C}@C_{80}$ should have low kinetic stability.

4.2.3 Molecular and electronic structure of $\text{Sc}_4\text{C}_3@C_{80}$

DFT optimization of $\text{Sc}_4\text{C}_3@C_{80}$ gave much larger variety of possible Sc_4C_3 geometries in comparison to the Sc_4C cluster. In the most stable structures, three carbon atoms form triangle in the center of the cluster, to which two Sc atoms are coordinated on both sides in the η^3 -manner forming the trigonal bipyramid, whereas two other Sc atoms are located in the plane of the carbon cluster and are η^2 -coordinated to the two sides of the C_3 triangle (Fig. 4.4). Several isomers with this cluster motif and somewhat different geometry parameters and cluster orientation span the energy range of 0–25 kJ/mol. In the lowest energy one, the C_3 triangle is isosceles, with two equal longer sides of 1.627 Å, and one shorter C–C distance of 1.400 Å. For comparison, C–C distances in $\text{Sc}_2\text{C}_2@C_{82}$ (a C_2^{2-} unit) and $\text{Sc}_4\text{C}_2@C_{80}$ (formally a C_2^{6-} unit) are 1.272 Å and 1.459 Å, respectively. The η^2 -Sc atoms are coordinated to the longer sides of the triangle with Sc–C distance of 2.102 and 2.088 Å. The bipyramid is slightly distorted, with Sc–C distances of 2.194, 2.196, and 2.256 Å.

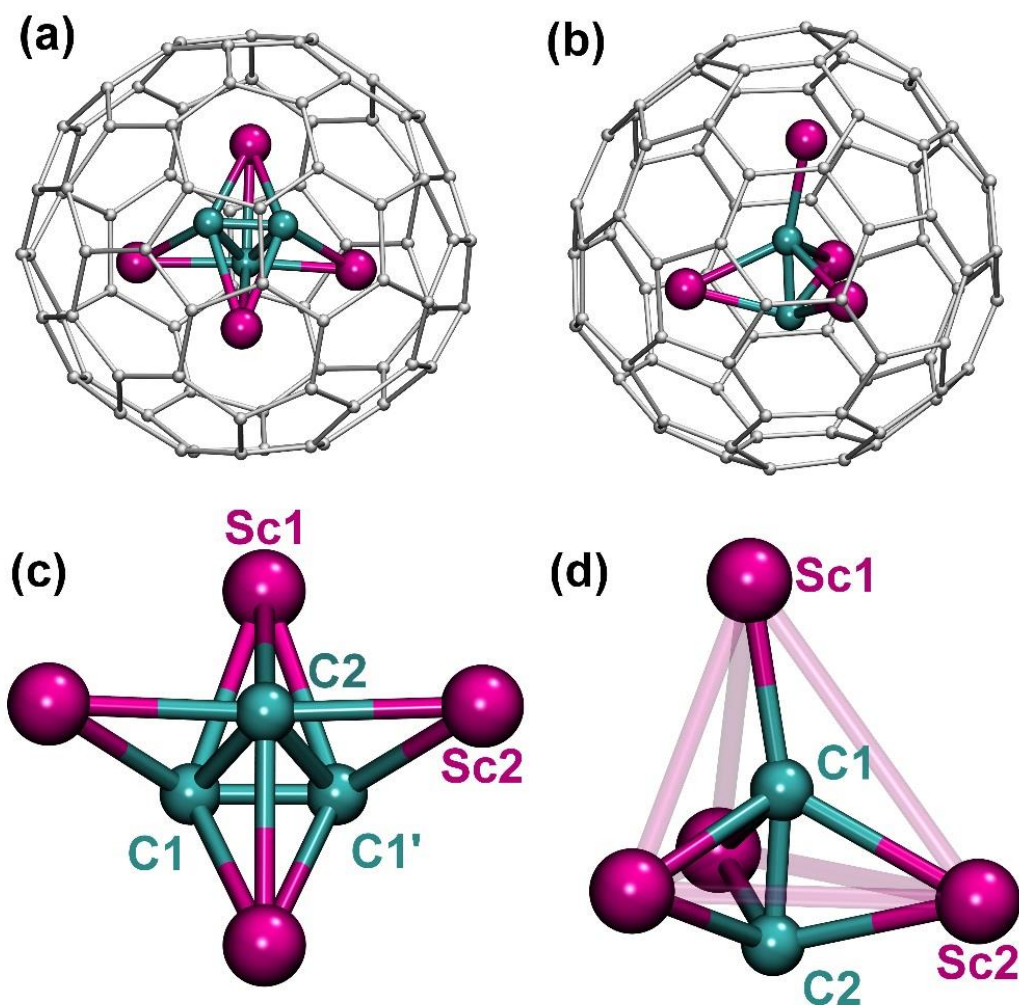


Figure 4.4 DFT-optimized molecular structures of $\text{Sc}_4\text{C}_3@C_{80}$ (a) and $\text{Sc}_4\text{C}_2@C_{80}$ (b). Enlarged structures of the Sc_4C_3 (c) and Sc_4C_2 (d) are shown with the atom numbering used in the QTAIM analysis.

Other shapes of the Sc_4C_3 cluster in $\text{Sc}_4\text{C}_3@C_{80}$ are substantially higher in energy. For instance, the second most stable type of the cluster has Sc_4 tetrahedron, one $\mu_4\text{-C}$ atom in the center and two $\mu_3\text{-C}$ atoms above two Sc_3 faces. The isomers with this shape of the endohedral cluster are 80–100 kJ/mol less stable.

The six-fold negative charge of the fullerene cage and an assumption of the +3 oxidation state of all Sc atoms in $\text{Sc}_4\text{C}_3@C_{80}$ requires the -6 charge state of the C_3 moiety. This is not an unrealistic assumption, taking into account a versatility of charge state of endohedral carbon clusters in carbide clusterfullerenes. For instance, the C_2 unit in $\text{Sc}_4\text{C}_2@C_{80}$ also adopts a formal charge -6 . Analysis of the frontier MOs shows that $\text{Sc}_4\text{C}_3@C_{80}$ exhibits a certain degree of similarity to $\text{Sc}_4\text{C}_2@C_{80}$. In both clusterfullerenes, the cluster-localized HOMO has complex character and can be best described as

intracluster Sc–C bonding/C–C antibonding MO. Similar shape is also found for the HOMO–1. The LUMO of $\text{Sc}_4\text{C}_3@C_{80}$ is predominantly a cage orbital with small contributions of Sc atoms. In the $\text{Sc}_4\text{C}_2@C_{80}$, the contributions of Sc atoms and the carbon cage to the LUMO are roughly equivalent.

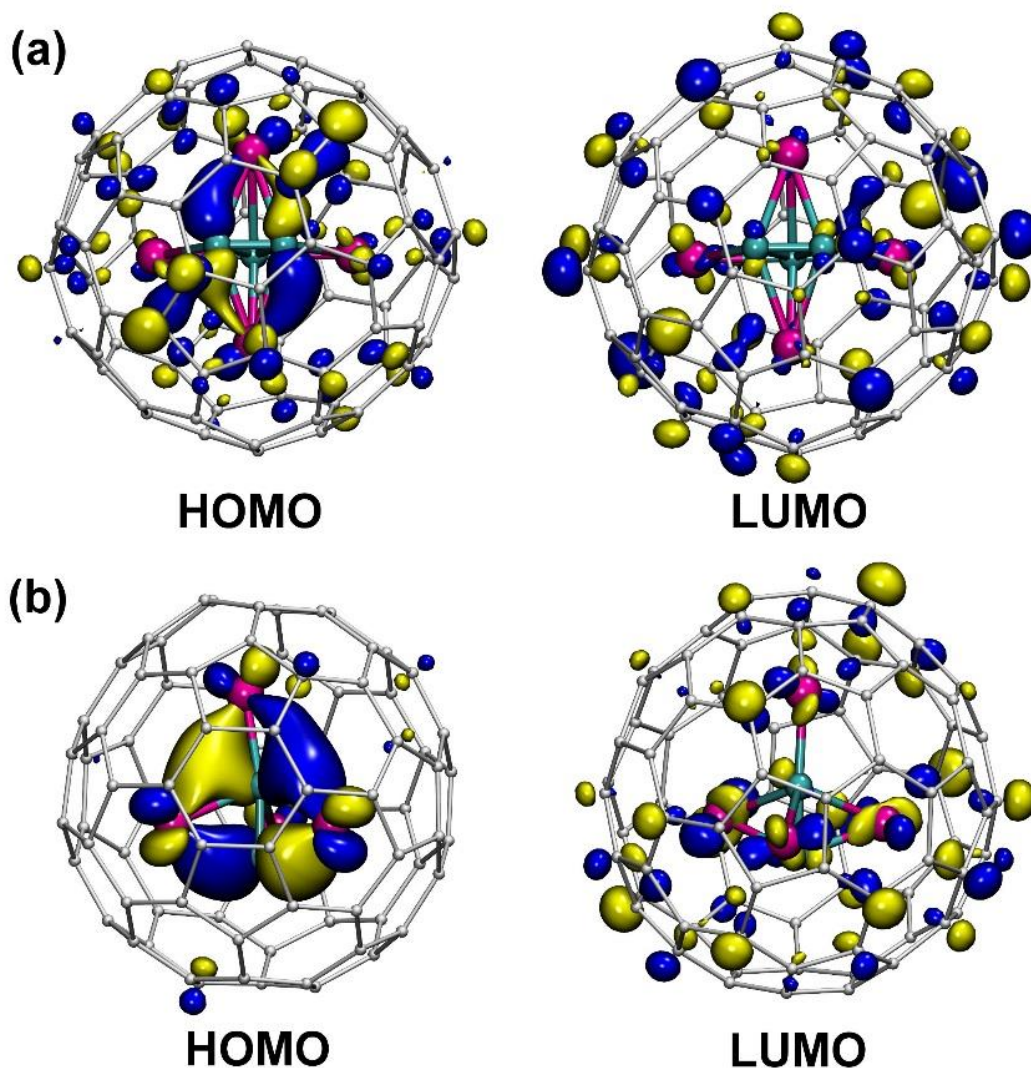


Figure 4.5 Frontier molecular orbitals in the $\text{Sc}_4\text{C}_3@C_{80}$ (a) and $\text{Sc}_4\text{C}_2@C_{80}$ (b).

The HOMO-LUMO gap of $\text{Sc}_4\text{C}_3@C_{80}$, 1.69 eV, is considerably larger than that of $\text{Sc}_4\text{C}@C_{80}$ and exceeds the $\text{Sc}_4\text{C}_2@C_{80}$ value of 0.94 eV predicted at the same level of theory. The high gap shows that the reasonable kinetic stability can be expected for $\text{Sc}_4\text{C}_3@C_{80}$.

Comparison of the HOMO and LUMO values along the $\text{Sc}_4\text{C}_x@C_{80}$ series we can see that increase of the number of carbon atoms in the cluster stabilizes HOMO and increase LUMO energies (and, accordingly, the gap is increasing). In all EMFs the HOMO is

localized on the cluster, but the intracluster Sc–C bonding interactions in Sc₄C₂@C₈₀ and Sc₄C₃@C₈₀ result in more stable structures than Sc₄C@C₈₀ with Sc-based HOMO. The trend found for HOMO energies is reproduced also in DFT-predicted ionization potentials (IPs). The lowest energy isomer of Sc₄C@C₈₀ with tetrahedral cluster has very small value of 5.47 eV, whereas IP value for the planar cluster is 5.92 eV. The latter value is close to that Sc₄C₂@C₈₀, IP = 6.04 eV. Sc₄C₃@C₈₀ has the largest IP of 6.69 eV. We can tentatively conclude that the high intensity of the Sc₄C@C₈₀⁺ peak is likely due to the low IP rather than due to the significant content of this compound in the fullerene extract. Similar situation was found for Y₃@C₈₀, whose yield is vanishingly small, but the EMF exhibit one of the most intense peaks in the positive ion LDI-TOF mass spectrum of the raw Y-EMF extract¹⁹⁰. On the contrary, Sc₄C₃@C₈₀ is considerably more difficult to ionize than Sc₄C₂@C₈₀ and Sc₄C@C₈₀, and the fact that it is still detectable in the mass spectrum shows that its content in the extract can be considerable or that the signal in the mass spectrum corresponds to a different type of endohedral cluster. Thus, due to its reasonable kinetic stability, Sc₄C₃@C₈₀ might be a plausible target for the isolation.

Table 4-1 Frontier MO energies, IP, and EA values (eV) of Sc₄C_x@C₈₀ (x = 1–3)

	HOMO	LUMO	gap _{H-L}	IP	EA
Sc ₄ C@C ₈₀ -tetrahedral	-4.107	-3.633	0.474	5.922	2.274
Sc ₄ C@C ₈₀ -planar	-4.541	-3.496	1.045	5.466	2.321
Sc ₄ C ₂ @C ₈₀	-4.784	-3.814	0.935	6.040	2.509
Sc ₄ C ₃ @C ₈₀	-5.299	-3.233	1.684	6.692	2.316

4.2.4 QTAIM analysis of the intracluster bonding in Sc₄C_x@C₈₀ species

Analysis of the valence states of Sc atoms described in the previous sections gives formal description of the clusters in Sc₄C@C₈₀ and Sc₄C₃@C₈₀ as [(Sc^{2.5+})₄C⁴⁻]⁶⁺ and [(Sc³⁺)₄(C₃)⁶⁻]⁶⁺. But diversity of Sc/C endohedral clusters requires more detailed analysis of the intracluster bonding interactions. For this goal, Bader's Quantum Theory of Atoms in Molecules (QTAIM) has been employed. In particular, two parameters are important: (i) QTAIM atomic charges obtained by integration of the electron density over atomic basins and (ii) delocalization indices δ(A, B), which is defined as a number of electron pairs shared by atoms A and B. By this definition, δ(A, B) is similar to the bond order understood in Lewis terms, however for polar bond the index is usually smaller than expected bond order because of the shift of the electron density towards more electronegative atoms. Table 4.2 lists formal charge distribution, actual QTAIM charges,

and intracuster delocalization indices in Sc₄C_x@C₈₀ (x = 1–3) and some other relevant EMFs. Extended discussion of QTAIM description of the bonding in EMFs was given before in refs. ^{148,188}

Table 4-2 QTAIM atomic charges, *q*, in Sc₄C_{1–3}@C₈₀ and selected other EMFs

EMF	Formal charges	<i>q</i> (cluster)	<i>q</i> (Sc) ^{ab}	Σ _{Sc}	<i>q</i> (C/O) ^b	Σ _C
Sc ₄ C@C ₈₀	[(Sc ^{2.5+}) ₄ C ⁴⁻] ⁶⁺	4.46	1.63×2 1.65×2	6.58	-2.12	
Sc ₄ C ₂ @C ₈₀	[(Sc ^{2.5+}) ₄ C ⁴⁻] ⁶⁺	4.21	1.56×4	6.24	-2.03	
	[(Sc ³⁺) ₄ (C ₂) ⁶⁻] ⁶⁺	3.91	Sc1: 1.65 Sc2: 1.63×3	6.52	C1: -1.54 C2: -1.08	-2.61
Sc ₄ C ₃ @C ₈₀	[(Sc ³⁺) ₄ (C ₃) ⁶⁻] ⁶⁺	3.73	Sc1: 1.61×2 Sc2: 1.64×2	6.49	C1: -0.79×2 C2: -1.18	-2.76
	[(Sc ³⁺) ₂ (C ₂) ²⁻] ⁴⁺	2.13	1.73×2	3.46	-0.66×2	-1.33
Sc ₂ @C ₈₂	[(Sc ²⁺) ₂] ⁴⁺	2.47	1.25, 1.22	2.47		
Sc ₄ O ₂ @C ₈₀	[(Sc ³⁺) ₂ (Sc ²⁺) ₂ (O ²⁻) ₂] ⁶⁺	3.87	Sc ^{II} : 1.46×2 Sc ^{III} : 1.76×2	6.43	-1.28×2	-2.56

^a “×*n*” denotes the presence of *n* equivalent atoms in the molecule

^b for numbering of atoms, see Fig. 4.4

Table 4-3 Intracuster delocalization indices in Sc₄C_{1–3}@C₈₀ and selected other EMFs

	δ(Sc, C) ^a	δ(C, C) ^a	δ(Sc, Sc)
Sc ₄ C@C ₈₀ - <i>I_h</i> (7) tetrahedral	0.71×4		0.06×6
Sc ₄ C@C ₈₀ - <i>I_h</i> (7) planar	0.74×4		0.11×4 0.04×2
Sc ₄ C ₂ @C ₈₀ - <i>I_h</i> (7)	Sc1–C1: 0.81	1.30	Sc1–Sc2: 0.08×3
	Sc1–C2: 0.09		Sc2–Sc2': 0.07×3
	Sc2–C1: 0.46×3		
	Sc2–C2: 0.59×3		
Sc ₄ C ₃ @C ₈₀ - <i>I_h</i> (7)	Sc1–C1: 0.36×4	C1–C1': 1.27	Sc1–Sc1': 0.10
	Sc1–C2: 0.38×2	C1–C2:	Sc1–Sc2: 0.07×3
	Sc2–C1: 0.47×2	2×0.89	Sc2–Sc2': 0.03
	Sc2–C2: 0.50×2		
Sc ₂ C ₂ @C ₈₂	0.32×4	2.43	0.02
Sc ₂ @C ₈₂			0.59
Sc ₄ O ₂ @C ₈₀	Sc ^{II} –O: 0.60×2	0.13	Sc ^{II} –Sc ^{II} : 0.24
	Sc ^{III} –O: 0.51×4		Sc ^{II} –Sc ^{III} : 0.08×3 Sc ^{III} –Sc ^{III} : 0.05

^a “×*n*” denotes the presence of *n* equivalent bond in the molecule, prime denotes symmetry equivalent atom of the same type (e.g. Sc1 and Sc1' are symmetry equivalent atoms)

It should be emphasized that QTAIM atomic charge should not be mixed with formal charge or oxidation state etc. The latter are integer value and are useful for simple description but do not represent the real distribution of electron density. QTAIM charges are more realistic and are always lower than formal charges because bonding distribution is never fully ionic. Therefore, we do not expect an exact match between oxidation states and QTAIM charges.

The bonding in Sc₄C cluster is rather simple. All Sc atoms form a single bond to the central carbon. The $\delta(\text{Sc}, \text{C})$ values of 0.7 are similar to those in nitride clusterfullerenes, the values are smaller than one because of the bond polarity, since the central carbon atoms acquires rather large negative charge exceeding -2 . This is almost twice smaller than the formal charge, but is still the largest negative charge for a single central atom in all known clusterfullerenes. The charges of Sc atoms depend on the cluster geometry, being +1.63 to 1.65 in the tetrahedral cluster and +1.56 in the square one. These values are slightly smaller than in EMFs with typical +3 state (e.g., $q(\text{Sc})$ in Sc₂C₂@C₈₂ and Sc₃N@C₈₀ is +1.7). At the same time, the QTAIM Sc charges in EMFs with formal +2 state of Sc are much smaller, 1.22-1.25 in Sc₂@C₈₂, or +1.46 for Sc^{II} atoms in Sc₄O₂@C₈₀. In the square cluster geometry, the intracuster interaction are more covalent than in the tetrahedral cluster which can be deduced from smaller atomic charges of Sc atoms and slightly larger $\delta(\text{Sc}, \text{C})$ and $\delta(\text{Sc}, \text{Sc})$ indices. As discussed above, although the HOMO of Sc₄C@C₈₀ has noticeable Sc–Sc bonding component, individual Sc–Sc indices are rather small. However, summing up all $\delta(\text{Sc}, \text{Sc})$ indices gives the net values of 0.36 and 0.52 electron pairs participating in delocalized Sc–Sc bonding in tetrahedral and quadratic Sc₄C clusters, respectively. For comparison, the Sc–Sc bond order in Sc₂@C₈₂ is 0.59, whereas in Sc₄O₂@C₈₀ the $\delta(\text{Sc}^{\text{II}}, \text{Sc}^{\text{II}})$ index is 0.24 and the sum of all $\delta(\text{Sc}, \text{Sc})$ values is 0.61.

Increasing the number of carbon atoms in the cluster obviously leads to a more complex bonding situation. As mentioned above, C₂ unit can adopt different formal charges, which also affects the QTAIM parameters. For instance, the formal charge of the acetylide unit in Sc₂C₂@C₈₂ is -2 and a triple C–C bond might be expected. QTAIM gives the $\delta(\text{C}, \text{C})$ value of 2.43 and the total charge of -1.33 . In Sc₄C₂@C₈₀, the formal charge of the C₂ unit is -6 , whereas the QTAIM charge is -2.61 (-1.54 for $\mu_4\text{-C}_1$ and -1.08 for $\mu_3\text{-C}_2$, see Fig. 4.4 for atom labeling) and the $\delta(\text{C}, \text{C})$ value is 1.30. Analysis of the delocalization indices shows that the Sc–C bonding in Sc₄C₂@C₈₀ is more covalent than in Sc₂C₂@C₈₂: the $\delta(\text{Sc}, \text{C})$ values in the latter are all equal 0.32, whereas in the

former the values for bonded Sc and C atoms span the range of 0.46–0.81. The total number of electron pairs shared between Sc atoms and C₂ unit is 1.30 in Sc₂C₂@C₈₂ and 4.06 in Sc₄C₂@C₈₀ (which translates to the average Sc–C₂ bond orders of 0.65 and 0.86, respectively).

In Sc₄C₃@C₈₀, the charges of Sc atoms are virtually identical to those of Sc₄C₂@C₈₀, and the charge of the C₃ unit is only slightly more negative the charge of acetylide group in Sc₄C₂@C₈₀. In the C₃ cluster, the bond order of the shorter C1–C1' bond is 1.27, which is similar to the $\delta(\text{C}, \text{C})$ value in Sc₄C₂@C₈₀, however the C1/C1' charges in Sc₄C₃@C₈₀ are only –0.79 (compare to –1.54 and –1.08 in Sc₄C₂@C₈₀). The C2 carbon in Sc₄C₃ has more negative charge, –1.18. Besides, a much smaller delocalization index of 0.89 is found for the C1–C2 bonds, which is reasonable taking into account the length of the C1–C2 bond, 1.627 Å. The $\delta(\eta^3\text{-Sc1}, \text{C})$ delocalization indices are all 0.36–0.38, i.e. close to the $\delta(\text{Sc}, \text{C})$ values in Sc₂C₂@C₈₂, and thus the $\eta^3\text{-Sc1-C}_3$ bond order is roughly 1.10. The $\eta^2\text{-Sc2-C}$ bond orders, 0.47–0.50, are noticeably higher than in the $\eta^3\text{-Sc1-C}$ bonds. Thus, Sc atoms share with the C₃ cluster 2.20 electron pairs via $\eta^3\text{-Sc-C}_3$ interactions and 1.94 electron pairs via $\eta^2\text{-Sc-C}_2$ interactions, and in total the Sc–C bonding in Sc₄C₃@C₈₀ involves 4.38 electron pairs. The intracluster bonding in Sc₄C₃@C₈₀ is thus more covalent than in Sc₄C₂@C₈₀, and hence the total cluster-to-cage electron transfer in the former (3.73 *e*), is smaller than in the latter (3.91 *e*). Interestingly, based on the magnetic criterion of aromaticity, the C₃ cluster in Sc₄C₃@C₈₀ is highly aromatic: the nuclear independent chemical shift (NICS¹⁹¹) computed in the center of the cluster is as large as –65.7 ppm.

To summarize the results of QTAIM analysis, we can conclude that the formal charge distribution should not be taken literally. In fact, the atomic charges of Sc atoms in Sc₄C@C₈₀ and Sc₄C₃@C₈₀ are not dramatically different, although their formal charges are +2.5 and +3, respectively. With the increase of the number of carbon atoms in the endohedral cluster, the covalency of the intracluster interactions is increasing, whereas the number of electrons donated by the cluster to the cage is decreasing.

4.2.5 Vibrational spectra of Sc₄C_{*x*}@C₈₀

Vibrational spectroscopy was proved to be useful for the analysis of the intracluster interactions⁷⁴. Besides, vibrational pattern of the given carbon cage is rather characteristic and hence can be used for the structure elucidation (although cluster can induce noticeable variations of the cage modes, see ref.¹⁹² for the comparison of the IR

spectra of $\text{La}_2@C_{80}$, $\text{Sc}_3\text{N}@C_{80}$, and $\text{Sc}_4\text{O}_2@C_{80}$). Therefore, we decided to analyze vibrational spectra of $\text{Sc}_4\text{C}_{1-3}@C_{80}$ species to aid in the structure elucidation. Figure 4.6 compares the IR spectra of four EMFs, two isomers of $\text{Sc}_4\text{C}@C_{80}$ with tetrahedral and square clusters, $\text{Sc}_4\text{C}_2@C_{80}$, and $\text{Sc}_4\text{C}_3@C_{80}$. We focus here predominantly on the analysis of the IR spectra since prediction of the resonance Raman intensities is less straightforward and depends on the excitation wavelength.

The number of cluster modes depends on the number of atoms in the cluster and varies from 15 in $\text{Sc}_4\text{C}@C_{80}$ to 21 in $\text{Sc}_4\text{C}_3@C_{80}$. From these numbers, six are always frustrated translations and rotations of the cluster with low vibrational frequencies. Large mass of Sc also leads to low frequency of vibrations with predominant contribution of Sc atoms. Thus, in addition to 6 “external” modes, several other cluster modes are found in the low-frequency range (below 400 cm^{-1}) either as pure cluster vibrations or mixed with the cage vibrations. As a result, for the conventional mid-IR spectra (where the range of $>400\text{ cm}^{-1}$ is accessible) only few cluster-based modes can be found, and all these vibrations are predominantly motions of the cluster carbon atoms.

In the $\text{Sc}_4\text{C}@C_{80}$ with tetrahedral cluster, translations of the central carbon atom is 3-fold degenerate and IR active. The computations shows that in the real $\text{Sc}_4\text{C}@C_{80}$ molecule the modes with predominant $\mu_4\text{-C}$ contributions are found at 555, 566, 597, and 600 cm^{-1} with modest IR intensity (see Fig. 4.6 where cluster-based modes are marked with arrows). All other vibrations in the $400\text{--}1600\text{ cm}^{-1}$ range are pure cage modes. In the square Sc_4C cluster, displacements of the central carbon atoms are split into an out-of-plane mode (computed frequency 265 cm^{-1}) and 2-fold degenerate in-plane motions ($620/639\text{ cm}^{-1}$). For the former, relatively high intensity is predicted, but low frequency makes its detection in the spectra difficult. Note that analogous out-of-plane motion of the nitrogen atom in $\text{Sc}_3\text{N}@C_{80}$ is found at 236 cm^{-1} ¹⁹³. For the in-plane motions of the carbon atom, very low intensity is predicted. This is different from $\text{Sc}_3\text{N}@C_{80}$, in which in-plane motion of the nitrogen atoms at 599 cm^{-1} has medium-strong intensity¹⁹³.

With the increase of the number of carbon atoms in the cluster more complex cluster modes may be expected, but only few of the modes result in considerable IR intensity. In the Sc_4C_2 cluster, significant absorption intensity in the mid-IR range is predicted only for the displacements of the $\mu_3\text{-C}$ atom in the plane parallel to the Sc_3 face of the Sc_4 tetrahedron. The frequency of this mode is 658 cm^{-1} . Stretching C–C mode of the acetylide unit is predicted at 1114 cm^{-1} , but absorption intensity of this vibration is very low.

In Sc₄C₃@C₈₀ we found three reasonably intense bands of the cluster marked with arrows in Figure 4.6. The medium intensity band at 607 cm⁻¹ corresponds to the motion of the C1–C1' fragment as a whole parallel to the Sc2–Sc2' bond. The weak absorption at 747 cm⁻¹ is due to a deformation of the C₃ triangle with C1–C2 bond stretching contribution, whereas the medium intensity band at 832 cm⁻¹ is an antisymmetric Sc2–C2 stretching vibration, in which the C2 atom is moving along the line connecting Sc2 and Sc2' atoms.

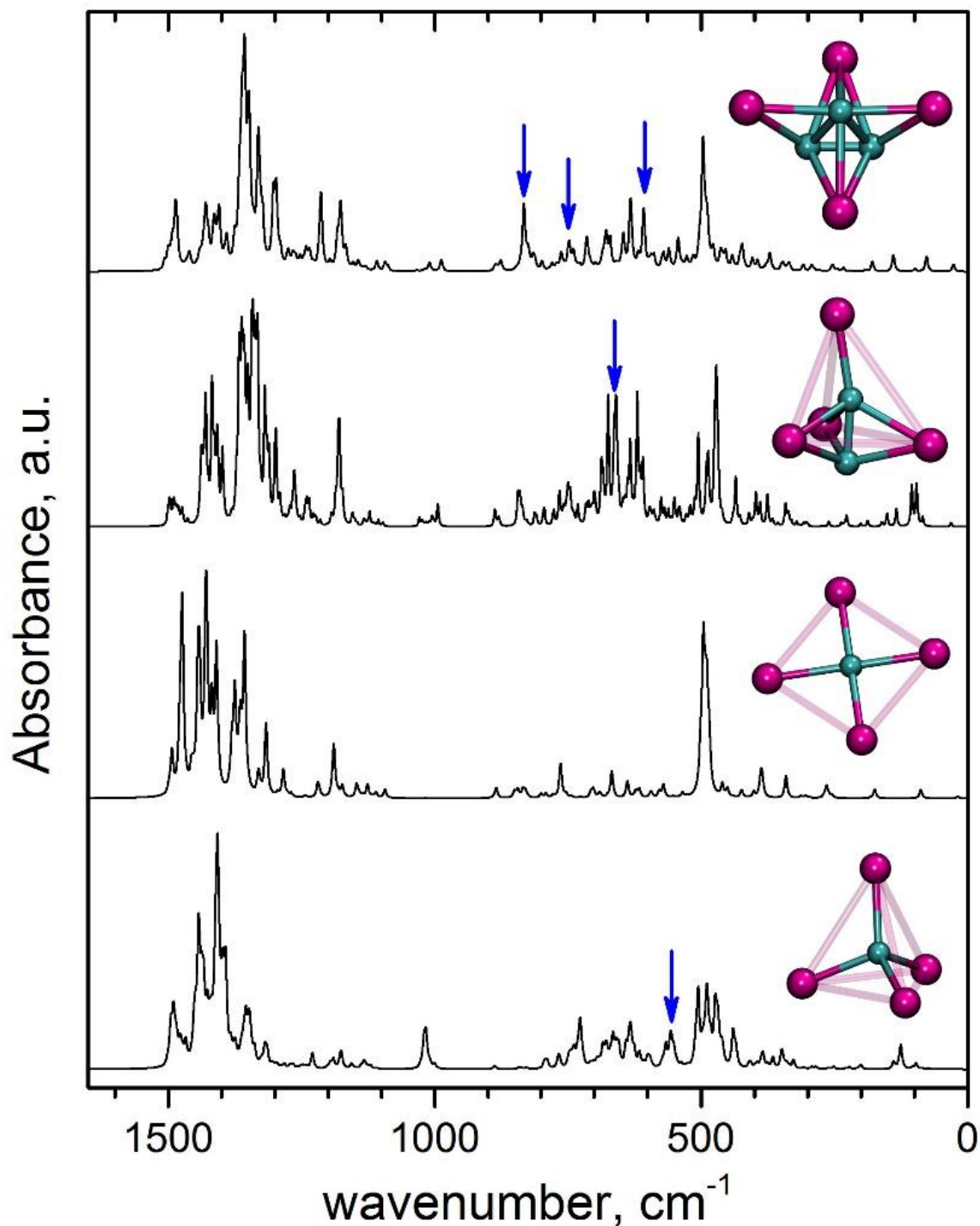


Figure 4.6 DFT-computed IR spectra of $\text{Sc}_4\text{C}_x@C_{80}$ ($x = 1-3$). Blue arrows mark cluster modes with considerable IR intensity in the $400-1600\text{ cm}^{-1}$.

Thus, analysis of the vibrational modes of $\text{Sc}_4\text{C}_x@C_{80}$ shows that only few cluster-based vibrations of these EMFs are available in the mid-IR spectra. All other vibrations seen in the spectra in the $400-1600\text{ cm}^{-1}$ range (Fig. 4.6) are due to the carbon cage. It is therefore remarkable that the vibrational patterns of the same $C_{80}-I_h(7)$ carbon cage are

very different showing that endohedral clusters impose substantial perturbation to the cage vibrations.

4.2.6 Sc₄C₃@C₇₈ and Sc₄C@C₈₂

Mass-spectrometry cannot distinguish between endohedral carbon atoms and carbon atoms of the fullerene cage, and hence assignment of the structure remains ambiguous. Therefore, we performed additional calculations to reveal the relative stability of Sc₄C₃@C₇₈ versus Sc₄C@C₈₀ and Sc₄C@C₈₂ versus Sc₄C₃@C₈₀.

For Sc₄C₃@C₇₈ we have chosen two cage isomers, the IPR $D_{3h}(5)$ and non-IPR C₂(22010). The former is typical for dimetallofullerenes and Sc₃N@C₇₈¹⁹⁴⁻¹⁹⁶, whereas the latter is found in nitride clusterfullerenes with large metal ions (Dy, Tm, Y, Gd¹⁹⁷⁻²⁰⁰). Optimization of molecular structures of Sc₄C₃@C₇₈ with different cluster positions inside the carbon cages showed that $D_{3h}(5)$ isomer is more preferable than C₂(22010) by 34 kJ/mol, but the most stable Sc₄C₃@C₇₈ structure is still 304 kJ/mol less stable than Sc₄C@C₈₀.

Three cage isomers were considered for Sc₄C@C₈₂ based on the results of the previous studies of nitride clusterfullerenes^{81,201}, namely C_{2v}(9), C_{2v}(39705), and C_s(39663). The C_{2v}(9) cage was found to be the most thermodynamically preferable followed by the C_{2v}(39705) (45 kJ/mol less stable for the lowest energy cluster configuration) and C_s(39663) (90 kJ/mol less stable). Sc₄C@C₈₂-C_{2v}(9) has small HOMO-LUMO gap, 0.54 eV, which is close to the value in Sc₄C@C₈₀. Importantly, Sc₄C@C₈₂-C_{2v}(9) is 101 kJ/mol more stable than Sc₄C₃@C₈₀.

Although relative stability arguments seemed to work reasonably well for the cage isomerism of EMFs, complete thermodynamic control of the EMF formation has not been proved. Thus, it is not clear if relative energies can be reliably used to sort out unstable EMFs with small or large cage size in XC₂@C_{2n}-versus-X@C_{2n+2} systems. On the one hand, enhanced stability of Ti₂C₂@C₇₈ over Ti₂@C₈₀ (ca. 100 kJ/mol) along with the more appropriate electronic structure and carbon cage symmetry was used as one of the arguments to deny a Ti₂@C₈₀ conjecture^{78,202}. Experimental evidences are also in favor of the carbide clusterfullerene structure of Ti₂C₈₀^{203,204}. On the other hand, our calculations show that Sc₂@C₈₂-C_{3v}(8) is 93 kJ/mol more stable than Sc₂C₂@C₈₀-C_{2v}(5), however both structures are characterized experimentally^{186,205}. Therefore, the energy difference of 100 kJ/mol cannot be considered as a sufficient argument to push aside the less stable structure. Thus, it is not possible to decide at this moment if Sc₄C₈₃ species in

the mass spectra of the EMF extract are due to Sc₄C₃@C₈₀ or Sc₄C@C₈₂ or a mixture of both. With much higher HOMO-LUMO gap, Sc₄C₃@C₈₀ is more kinetically stable, whereas Sc₄C@C₈₂ has higher thermodynamic stability. For Sc₄C₈₁ species, we believe that Sc₄C@C₈₀ is a more appropriate candidate than Sc₄C₃@C₇₈ due to the high strain in the latter induced by encapsulation of the large cluster within relatively small cage.

4.3. Conclusions

Two new species with composition Sc₄C₈₁ and Sc₄C₈₃ are detected in mass spectra of the Sc-EMF extract synthesized using CH₄ as a reactive gas. We theoretically performed thorough analysis of the possible molecular and electronic structure of such species, focusing at first on the Sc₄C@C₈₀-I_h(7) and Sc₄C₃@C₈₀-I_h(7) conjectures. The former is found to have Sc in a “+2.5” valence state. The cluster is fluxional and can exist in two almost isoenergetic forms with tetrahedral and planar geometries. Two cluster geometries give noticeable difference in electronic properties, in particular HOMO-LUMO gaps and orbital energies. Sc₄C@C₈₀ has low ionization potential and is probably not kinetically stable, which makes its isolation hardly possible. The most plausible structure of Sc₄C₃@C₈₀ has triangular aromatic C₃ cluster with two pairs of Sc atoms coordinating to the C₃ moiety with η^3 and η^2 hapticities. All Sc atoms are in the trivalent state, whereas the C₃ cluster has the formal charge -6 and is highly aromatic. Large HOMO-LUMO gap of Sc₄C₃@C₈₀ points to its reasonable kinetic stability, however thermodynamically Sc₄C₃@C₈₀ is 101 kJ/mol less stable than Sc₄C@C₈₂-C_{2v}(9) counterpart.

Chapter 5. Structures of heptagon- containing LaSc₂N@C_s(hept)-C₈₀ and its Prato and Bingel-Hirsch cycloaddition

5.1 Introduction

Recently, endohedral metallofullerene with heptagonal rings was successfully produced by the arc-discharge synthesis and characterized as LaSc₂N@C_s(hept)-C₈₀ by single-crystal X-ray diffraction.⁴⁵ Computational study reveals that an EMF with heptagonal rings can be as stable as conventional EMFs, and the fact that they have not been discovered before is due to their low yields, not their thermodynamic stability. Thermodynamically and kinetically preferred reaction sites in the heptagon-containing fullerene LaSc₂N@C_s(hept)-C₈₀ are also studied computationally for Prato and Bingel-Hirsch cycloaddition reactions. In both types of reactions the heptagon is not affected, and chemical reactivity is determined by the adjacent pentalene units. Thermodynamically controlled Prato addition is predicted to proceed regioselectively across the pentagon/pentagon edges, whereas the most reactive sites in kinetically-controlled Bingel-Hirsch reaction are the carbon atoms next to the pentagon/pentagon edge.

5.2. Computational Methods

All structures were first optimized at the PBE/TZ2P level with core-effective potentials for Sc, La, and Br using Priroda code.^{181,182} Then, single point energy calculations at the PBE-D3 level with Grimme's dispersion correction with Becke-

Johnson damping,^{206,207} DKH2 scalar relativistic correction and SARC-modification of def2-TZVP basis set^{208,209} were performed using Orca suite.²¹⁰

5.3 Results and Discussion

Figure 5.1 shows the molecular structure of $\text{LaSc}_2\text{N}@C_s(\text{hept})\text{-C}_{80}$ from a cocrystal grown with $\text{Ni}(\text{OEP})$ (OEP is the dianion of octaethylporphyrin). In agreement with Euler's theorem, C_{80} with one heptagonal face has 13 pentagons and 28 hexagons. The heptagon and the two flanking pentalene units are highlighted in red. As usually observed, metal ions, in this case the Sc ions, are located near the pentalene units. The LaSc_2N unit inside the cage is flat, but the heptagon is not. As seen at the bottom of the figure, the heptagon is folded along the line between C5A and C2A. The dihedral angle between the relatively planar C5A, C6A, C7A, C1A, and C2A portion and the planar C5A, C4A, C3A, and C2A portion is $158.05(7)^\circ$. In contrast, hexagons and pentagons in fullerenes are usually planar as they are in $\text{LaSc}_2\text{N}@C_s(\text{hept})\text{-C}_{80}$. In other aspects, the structure of $\text{LaSc}_2\text{N}@C_s(\text{hept})\text{-C}_{80}$ resembles that of its isomer, $\text{LaSc}_2\text{N}@I_h\text{-C}_{80}$, which was described earlier.²¹¹

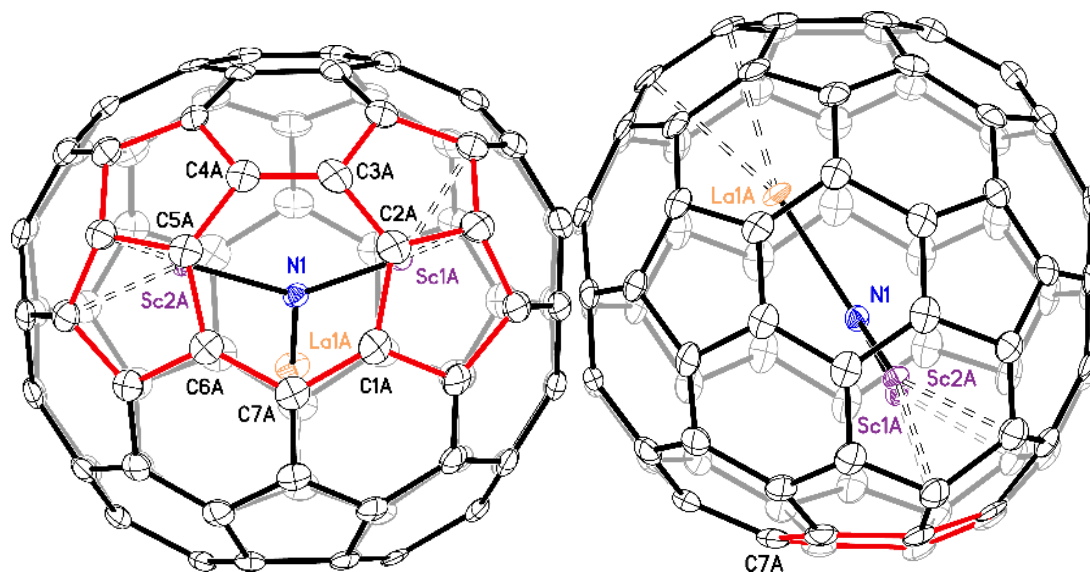


Figure 5.1 Two views of the structure of $\text{LaSc}_2\text{N}@C_s(\text{hept})\text{-C}_{80}$ as determined by a single crystal X-ray diffraction study of the cocrystal, $\text{LaSc}_2\text{N}@C_s(\text{hept})\text{-C}_{80}\cdot 2\text{Ni}(\text{OEP})\cdot 2\text{toluene}$, drawn with 30% thermal contours. The position of the heptagon and the two adjacent pentalene units are highlighted in red in the left figure while only the heptagon, which is non-planar, is coloured red in the right drawing. The dashed lines show the contacts between the metal ion and the nearest cage carbon atoms. The second orientation of the cage, the toluene molecules, and the hydrogen atoms were omitted for clarity. Reproduced from Ref.

To reveal the influence of the heptagonal face and non-uniform distribution of pentagons in LaSc₂N@C_s(hept)-C₈₀ on its stability, a series of DFT computations have been performed. The synthesis of nitride clusterfullerenes usually yields two isomers with the C₈₀ cage that dominate in the M₃N@C_{2n} fullerene mixture.²¹²⁻²¹⁴ The most abundant isomer has *I_h* cage symmetry, whereas the second most abundant structure is the isomer with the *D_{5h}* cage. Both isomers have enhanced stability due to the uniform distribution of pentagons minimizing the on-site Coulomb repulsion of six electrons transferred to the fullerene from the endohedral cluster.^{81,179} Table 5-1 lists relative energies of C₈₀⁶⁻ and nitride clusterfullerenes with different clusters encapsulated within three isomers of C₈₀. For all studied compounds, the isomers with *I_h*-C₈₀ cage have the lowest energies, which are therefore used as a reference. In the empty, hexaanionic state, the C_s(hept)-C₈₀ is 171 kJ/mol less stable than the *I_h* isomer. The *D_{5h}* isomer is the second most stable with the relative energy of 88 kJ/mol. Note that with such a high relative energy, C_s(hept)-C₈₀ is still the third most stable isomer of C₈₀⁶⁻. Encapsulation of nitride clusters only slightly affects relative stability of the *D_{5h}* isomers (it varies in the 60–70 kJ/mol range depending on the cluster), but stability of the C_s(hept)-C₈₀ isomer is dramatically enhanced. LaSc₂N@C_s(hept)-C₈₀ is only 27 kJ/mol less stable than the *I_h* isomer and is therefore substantially more stable than the *D_{5h}* isomer (note that the configuration of the LaSc₂N cluster with La atom coordinating one of the pentalene unit is 49 kJ/mol less stable than the experimentally observed structure). A similarly high stability is predicted for the Y₃N@C_s(hept)-C₈₀ (31 kJ/mol). Only for the smaller Sc₃N cluster is the relative energy of Sc₃N@C_s(hept)-C₈₀ higher than that of the Sc₃N@*D_{5h}*-C₈₀ isomer.

Table 5-1 Relative energies (kJ/mol) of three C₈₀⁶⁻ and M₃N@C₈₀ cage isomers.

	<i>I_h</i>	<i>D_{5h}</i>	C _s (hept)
C ₈₀ ⁶⁻	0	88	171
LaSc ₂ N@C ₈₀	0	61	27
Y ₃ N@C ₈₀	0	70	31
Sc ₃ N@C ₈₀	0	67	92

Thus, the DFT study revealed an unexpected high stability of the M₃N@C_s(hept)-C₈₀ isomer. For nitride cluster with large metals (Y and presumably lanthanides, which have similar ionic radii) the heptagon-containing isomer is considerably more stable than the

*D*_{5h} cage. If the isomeric distribution would be governed by the thermodynamic stability, a much higher yield of the heptagon-containing isomer might be expected (at least, exceeding that of the *D*_{5h} isomer). However, all experimental studies in the last decade contradict this expectation. Before the synthesis of LaSc₂N@C_s(hept)-C₈₀, there was only one report on the presence of the third isomer in the M₃N@C_{2n} mixture. In 2006, Yang and Dunsch reported the isolation of the third isomer of Dy₃N@C₈₀, but its structural characterization was not possible at that time.²¹⁵ The relative yield of Dy₃N@C₈₀ (III) was very low, similar to the low yield of the LaSc₂N@C_s(hept)-C₈₀ (about five times lower than that of the *D*_{5h} isomer).

The reasons for the low yield of C_s(hept)-C₈₀ structures might be in the kinetic factors, i.e. the ease of the structural rearrangement to other EMFs. Molecular dynamics simulations of the fullerene formation show that heptagonal rings are not uncommon for the intermediate structures, which are then annealed into the more stable fullerenes.¹⁰⁴ Comparison of the C_s(hept)-C₈₀ and *I*_h-C₈₀ isomers reveals their close similarity. These two structures are related by a Stone-Wales-like, heptagon/pentagon to hexagon/hexagon (7/5-6/6) realignment of the C₂ fragment highlighted in light green in Fig. 5.2a,b. The computations showed that the barrier to the concerted 7/5-6/6 realignment for C₈₀⁶⁻ is 680 kJ/mol (7.05 eV) (The barrier energy is defined as the energy of the transition state). Encapsulation of the LaSc₂N cluster reduces the barrier to 634 kJ/mol (6.57 eV). Other cases are also considered if coordination of metal atoms can catalyze the 7/5-6/6 realignment. If the LaSc₂N cluster is rotated so that the Sc atom is directed towards the rearranging fragment, the barrier remains virtually the same (630 kJ/mol), whereas coordination of the La ion increases the barrier to 655 kJ/mol (6.79 eV). These values are comparable to Stone-Wales barrier of *ca.* 7 eV predicted at the DFT level for empty fullerenes.^{216,217} Encapsulation of metal atoms was also predicted to reduce the barrier. For instance, in La@C₆₀ the barrier is reduced to 6.26 eV (versus 7.16 in C₆₀).²¹⁷

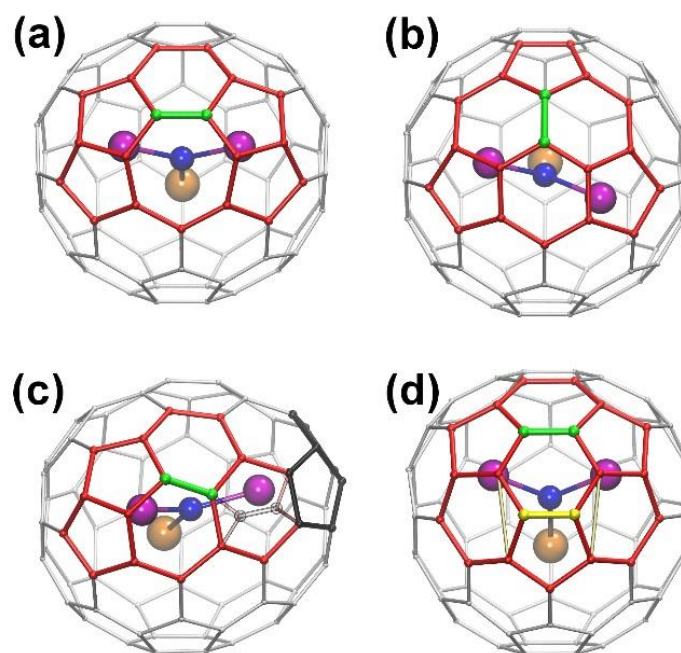


Figure 5.2 Molecular structures of LaSc₂N@C₈₀ isomers and related structures: (a) LaSc₂N@C_s(hept)-C₈₀; (b) LaSc₂N@I_h-C₈₀. The cage fragment near the heptagon is highlighted in red, the C-C bond which is “rotated” in the 7/5-6/6 realignment is highlighted in light green; (c) LaSc₂N@C₂(22010)-C₇₈ with the C₂(22010) cage which can be obtained from the LaSc₂N@C_s(hept)-C₈₀ via removal of one C₂ fragment; position of the removed fragment is shown as “ghost” atoms; the second pentagon pair in C₂(22010)-C₇₈ formed after removal of the C₂ fragment is highlighted in black; (d) LaSc₂N@C_{3_v}(8)-C₈₂; removal of the yellow-highlighted C₂ fragment from this structure and formation of missing C-C bonds (thin yellow lines) yields the LaSc₂N@C_s(hept)-C₈₀. In all structures, Sc atoms are magenta, La is orange, and N is blue.

Another mechanism possibly leading to LaSc₂N@C_s(hept)-C₈₀ and responsible for its consumption is addition/removal of C₂ fragment.²¹⁸ This mechanism is responsible for the formation of heptagonal rings in halogenated fullerenes.³⁴⁻³⁷ Removal of the C₂ fragment from the pentagon/pentagon edge in LaSc₂N@C_s(hept)-C₈₀ leads to LaSc₂N@C₇₈ with the non-IPR C₂(22010) cage isomer (Fig. 5.2c). This M₃N@C₇₈ isomer is usually formed in the synthesis of nitride clusterfullerenes with large cluster size,^{197-199,219} including the LaSc₂N@C_{2_n} system studied in this work. On the other hand, if a C₂ unit is added to the heptagonal ring of LaSc₂N@C_s(hept)-C₈₀, the isomer of LaSc₂N@C₈₂ with the C_{3_v}(8) cage symmetry can be formed (Fig. 5.2d). However, the C_{3_v}(8) cage isomer is usually the most abundant for clusterfullerenes with the formal four-fold electron transfer (e.g. carbides²²⁰ or sulfides¹¹), but is not common for nitride clusterfullerenes. Thus, the formation of the LaSc₂N@C_s(hept)-C₈₀ cage might be a result

of a top-down mechanism with the transient, unstable $\text{LaSc}_2\text{N}@C_{3v}(8)\text{-C}_{82}$ as the cage precursor.²⁰

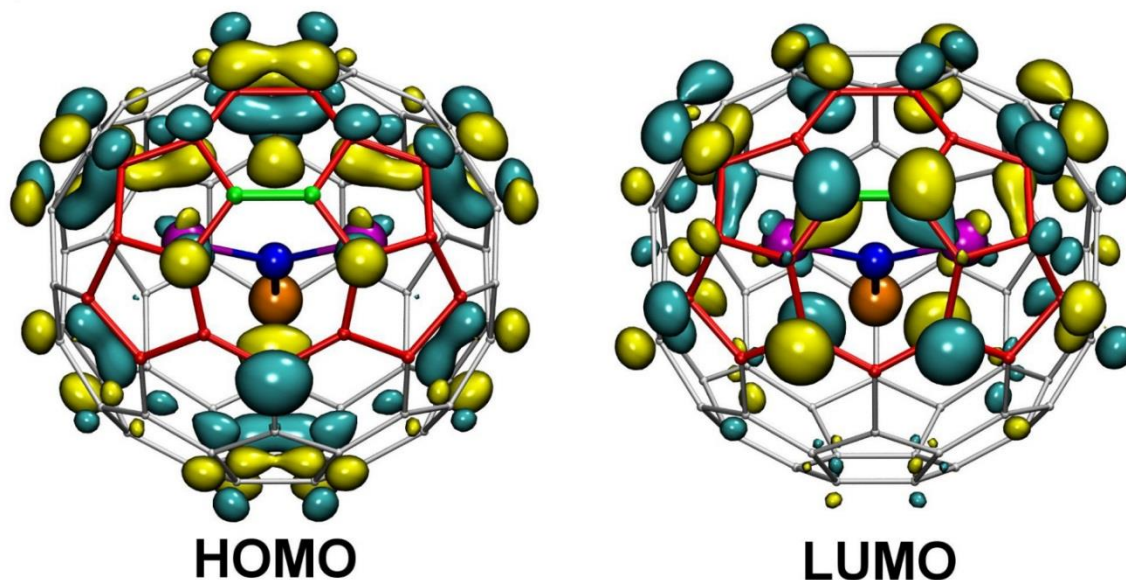


Figure 5.3 HOMO and LUMO of $\text{LaSc}_2\text{N}@C_s(\text{hept})\text{-C}_{80}$ (isovalue 0.035 a.u.) computed at the PBE/TZVP level.

The spatial distribution of the HOMO and LUMO in $\text{LaSc}_2\text{N}@C_s(\text{hept})\text{-C}_{80}$ is visualized in the Fig. 5.3. Both MOs are delocalized over the carbon cage, have noticeable but not prevailing contributions from the heptagonal ring and adjacent pentalene fragments, and have negligible contributions from the metal atoms. The LUMO has also enhanced contributions from the carbon atoms at the hexagon/heptagon edge that are highlighted in green in Figs. 5.2 and 5.3. Note that this bond is the shortest C-C bond in the molecule (DFT bond length 1.403 Å, the next shortest value is 1.411 Å). The crystallographic values for this C-C bond length are 1.374(15) Å and 1.362(18) Å for the two different cage orientations.

For prospective application of such new type of endohedral metallofullerenes, next we analyse how the presence of the heptagon affects the chemical properties of unconventional EMFs. In particular, we perform a systematic computational study of the preferable reaction pathways of Prato and Bingel-Hirsch cycloadditions reactions to heptagon-containing $\text{LaSc}_2\text{N}@C_{80}$ molecule.

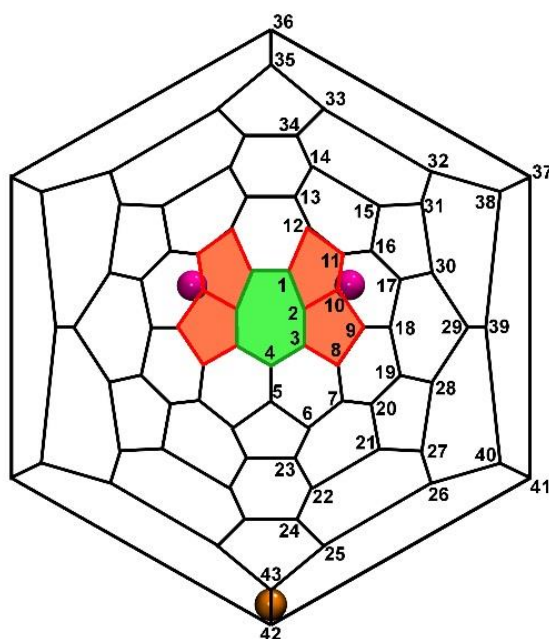
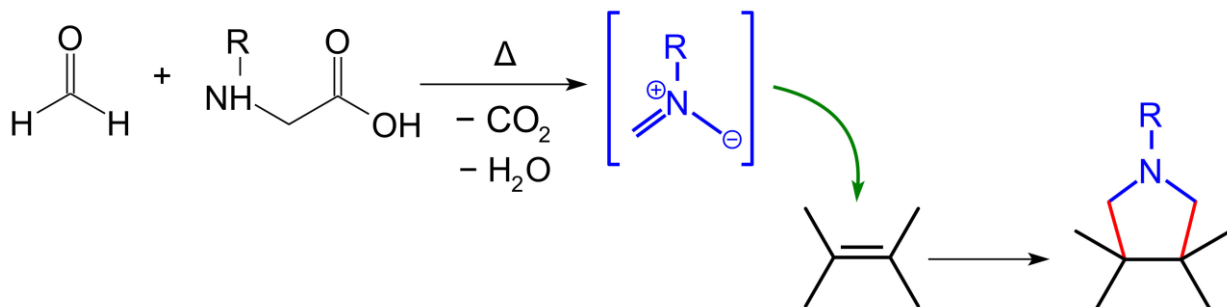


Figure 5.4 Schlegel diagram of LaSc₂N@C_s(hept)-C₈₀ with quasi-spiral numbering system of carbon atoms used in this work. Heptagon and pairs of adjacent pentagons are highlighted in green and red, respectively, whereas position of Sc and La atoms are marked with magenta and orange circles.

In Prato reaction,²²¹ amino acid (e.g. sarcosine) reacts with aldehyde to form an ylide, which then reacts with a fullerene CC bond via 1,3-dipolar cycloaddition to form a pyrrolidine ring:



Prato reaction of M₃N@I_h-C₈₀ is studied very well both experimentally and computationally.²²²⁻²²⁹ This highly symmetric cage with rotating M₃N cluster has only two addition sites located on pentagon/hexagon and hexagon/hexagon edges (denoted as [5,6] and [6,6], respectively). [5,6] adduct is more preferable for clusters of smaller size (such as Sc₃N), whereas increase of the cluster size stabilizes the [6,6] isomer, which becomes predominant product for the Gd₃N@C₈₀.^{223,225,226} Reaction is known to proceed under thermodynamic control (although kinetic products may be formed first²²⁶⁻²²⁹), and

hence addition sites can be predicted based on the relative stability of the isomeric adducts.

The C_s-symmetric cage of LaSc₂N@C_s(hept)-C₈₀ has 64 inequivalent CC bonds, and all of them can be considered as potential addition sites. Table 5.2 lists several most stable isomers and all four heptagon-based adducts. Note that inversion of the pyrrolidine ring and NH fragment yield four conformers for each addition site. For a given addition site the energies of the conformers can vary within 10 kJ/mol. The values discussed hereafter correspond to the lowest energy conformers.

Table 5-2 Selected LaSc₂N@C₈₀(CH₂)₂NH isomers, their relative energies and HOMO-LUMO gaps, and corresponding geometry parameters in pristine LaSc₂N@C₈₀.

CC ^a	Type ^b	ΔE ^c	gap _{H-L} ^d	d(CC) ^e	θ _p ^f
2-10	6-[5,5]-7	0.0	1.21	1.445	13.50/15.96
15-31	6-[5,6]-6	31.7	1.11	1.436	10.09/9.97
11-12	6-[5,6]-6	32.4	1.19	1.465	14.27/9.74
20-21	6-[5,6]-6	35.3	1.06	1.436	11.37/10.61
9-10	5-[5,6]-6	36.0	1.16	1.450	13.06/15.96
17-30	5-[5,6]-6	37.0	0.73	1.445	11.21/10.36
13-13'	6-[6,6]-6	38.5	1.33	1.442	7.52/7.52
...					
1-2	5-[5,7]-6	70.9	0.85	1.455	7.33/13.5
2-3	5-[5,7]-6	74.0	0.75	1.465	13.5/7.03
1-1'	5-[6,7]-5	84.8	0.86	1.403	7.33/7.33
3-4	5-[6,7]-6	106.1	0.80	1.461	7.03/7.10

^a addition site, see Fig. 5.4 for numbering of carbon atoms; ^b numbers in the square brackets denote polygons, whose junction forms addition site, whereas the number before and after square brackets denote the rings at the vertices of the addition site (e.g. 6-[5,6]-7 means pentagon/hexagon edge located between hexagon and heptagon), ^c relative energy, in kJ/mol, ^d HOMO-LUMO gap, in eV; ^e CC bond lengths in pristine LaSc₂N@C₈₀, in Å; ^f POAV pyramidalization angles, θ_p, of carbon atoms in pristine LaSc₂N@C₈₀.

Inspection of all optimized LaSc₂N@C₈₀(CH₂)₂NH isomers showed that one addition site, the **2-10** bond at the pentagon/pentagon junction, is particular preferable for cycloaddition (Figure 5.5). Corresponding cycloadduct is separated from all other isomeric adducts by the energy gap of 30 kJ/mol and can be expected to be obtained regioselectively. The HOMO-LUMO gap of the cycloadduct is 1.21 eV, which is slightly higher than the gap in the pristine LaSc₂N@C₈₀, 1.15 eV. At the same time, both HOMO and LUMO of the adduct (-5.03/-3.81 eV) are destabilized by ca 0.2 eV with respect to the LaSc₂N@C₈₀ values (-5.23/-4.08 eV).

Among the six addition sites with relative energies between 30 and 40 kJ/mol, five are [5,6] edges, including two [5,6] adducts at the perimeter of the pentalene unit (**11-12**, **9-10**). Remarkably stable is the [6,6] adduct at the **13-13'** bond in the pyrene fragment (carbon atoms at the triple hexagon junctions are usually less reactive).

The lowest energy heptagon-based cycloadduct is the [5,7] adduct across the 1–2 bond (70.9 kJ/mol) followed by another [5,7] adduct to the 2–3 bond (74.0 kJ/mol). [6,7] adducts are even less stable (84.8 kJ/mol for 1–1' and 106.1 kJ/mol for 3–4). In fact, [6,7]-adduct to the 3–4 bond is one of the least thermodynamically stable structures among the whole set of LaSc₂N@C₈₀(CH₂)₂NH adducts. The highest energy, 128.7 kJ/mol, is found for the adduct across the 7–8 bond.

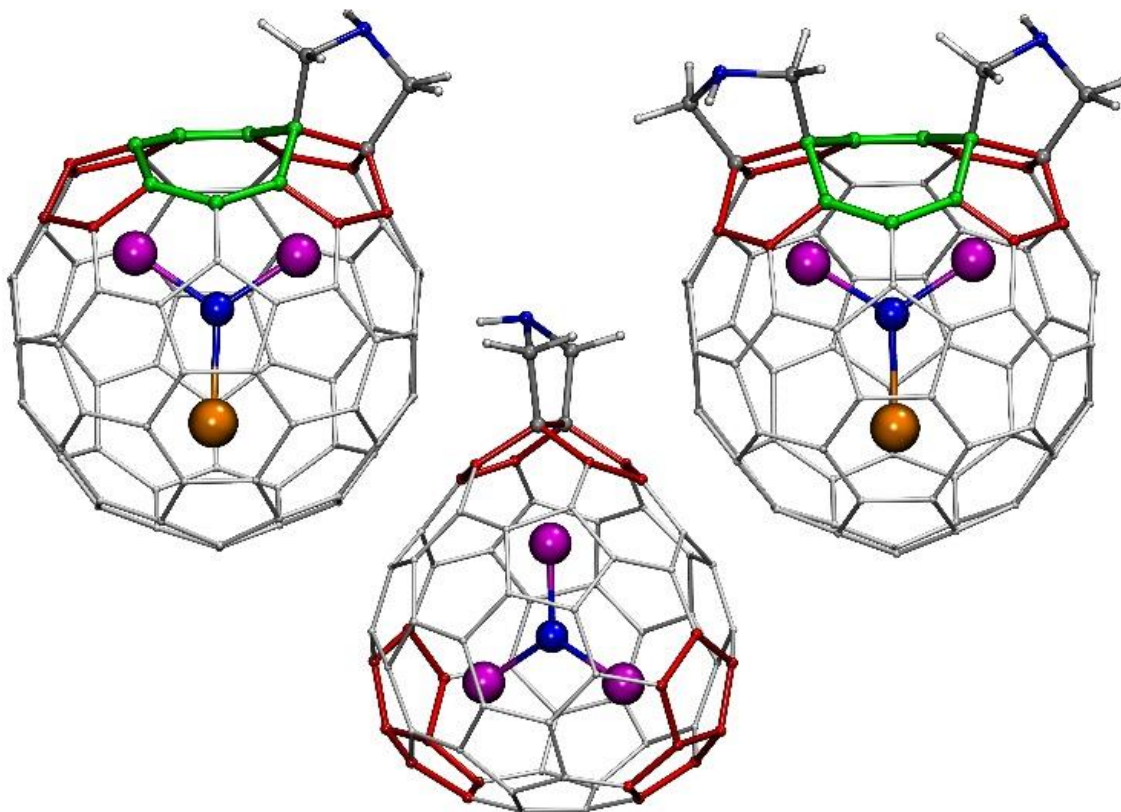
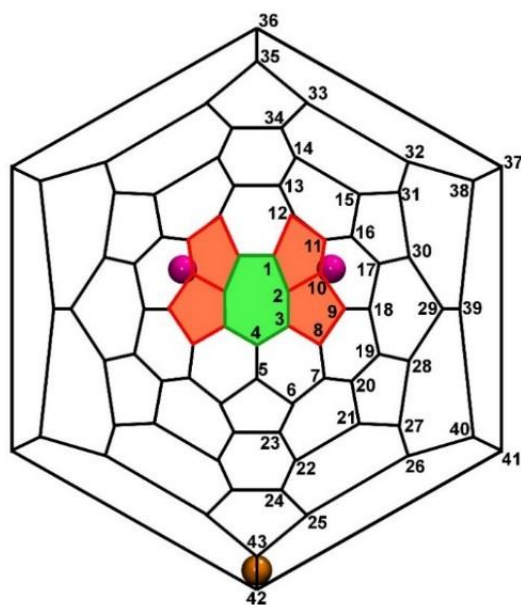


Figure 5.5 The most stable LaSc₂N@C₈₀(CH₂)₂NH, bis LaSc₂N@C₈₀[(CH₂)₂NH]₂, and Sc₃N@C₆₈(CH₂)₂NH cycloadducts. Heptagon ring is highlighted in green, pentalene units are highlighted in red. N, Sc and La atoms are blue, magenta and orange, respectively.

Table 5-3. POAV pyramidalization angles in DFT-optimized LaSc₂N@C_s(hept)-C₈₀

atom	θ_p	atom	θ_p
1	7.328	23	10.548
2	13.498	24	9.297
3	7.03	25	10.855
4	7.103	26	8.864
5	9.464	27	10.114
6	10.129	28	10.366
7	8.593	29	8.887
8	8.34	30	10.355
9	13.059	31	9.967
10	15.961	32	8.693
11	14.267	33	10.326
12	9.735	34	9.942
13	7.523	35	10.934
14	8.249	36	8.952
15	10.09	37	10.126
16	10.573	38	10.332
17	11.207	39	10.109
18	9.345	40	10.306
19	9.539	41	9.993
20	11.367	42	11.619
21	10.606	43	12.762
22	8.911		

**Table 5-4** CC bond lengths ($d(\text{CC})$, in Å) in DFT-optimized LaSc₂N@C_s(hept)-C₈₀

bond	$d(\text{CC})$	bond	$d(\text{CC})$	bond	$d(\text{CC})$	bond	$d(\text{CC})$
1-1'	1.403	10-11	1.466	20-21	1.436	30-31	1.442
1-2	1.455	11-12	1.465	21-22	1.424	31-32	1.427
1-12	1.453	11-16	1.421	21-27	1.445	32-33	1.417
2-3	1.465	12-13	1.465	22-23	1.425	33-34	1.449
2-10	1.445	13-13'	1.442	22-24	1.444	33-34	1.449
3-4	1.461	13-14	1.467	23-23'	1.434	33-35	1.436
3-8	1.452	14-15	1.440	24-24'	1.431	34-34'	1.430
4-5	1.427	14-34	1.418	24-25	1.450	35-36	1.434
5-6	1.446	15-16	1.447	25-26	1.445	36-37	1.430
6-7	1.411	15-31	1.436	25-43	1.468	37-38	1.435
6-23	1.442	16-17	1.455	26-27	1.435	37-41	1.460
7-8	1.441	17-18	1.449	26-40	1.434	38-39	1.436
7-20	1.428	17-30	1.445	27-28	1.440	39-40	1.442
8-9	1.460	18-19	1.432	28-29	1.429	40-41	1.457
9-10	1.450	19-20	1.444	29-30	1.428	41-42	1.449
9-18	1.450	19-28	1.440	29-39	1.433	42-43	1.469

We tried to rationalize relative stability of fulleropyrrolidine cycloadducts based on the CC bond length in the pristine molecule or pyramidalization of carbon atoms (quantified in terms of POAV²³⁰ angles θ_p), but this analysis did not reveal any clear correlation between geometry parameters and preferable reaction (see Tables 5-2, 5-3 and 5-4). The atoms C2 and C10 at the [5,5] edge are among the most pyramidal ones in the LaSc₂N@C₈₀ molecule, so pyramidalization may play a role here. But there is no correlation between pyramidalization angles and relative stabilities for higher energy isomers. For instance, **9–10** adduct in the most pyramidal region of the pristine fullerene (θ_p angles are 13.06/15.96°) has similar stability to the **13–13'** isomer with quite flat carbon atoms ($\theta_p = 7.52^\circ$). Likewise, the bond length also does not correlate with the stability of the adducts. **1–1'** is the shortest CC bond in the pristine fullerene (1.403 Å), but corresponding adducts is rather unstable (84.8 kJ/mol). The **2–10** bond length of the [5,5] edge, 1.445 Å, is in the middle of the CC bond lengths range in the LaSc₂N@C₈₀, 1.403–1.469 Å. Analysis of the HOMO and LUMO distributions²³¹ also does not give a reasonable suggestion of the most stable adducts. Thus, it is not possible to rationalize reactivity using simple structural and electronic arguments based on the pristine LaSc₂N@C₈₀ molecule.

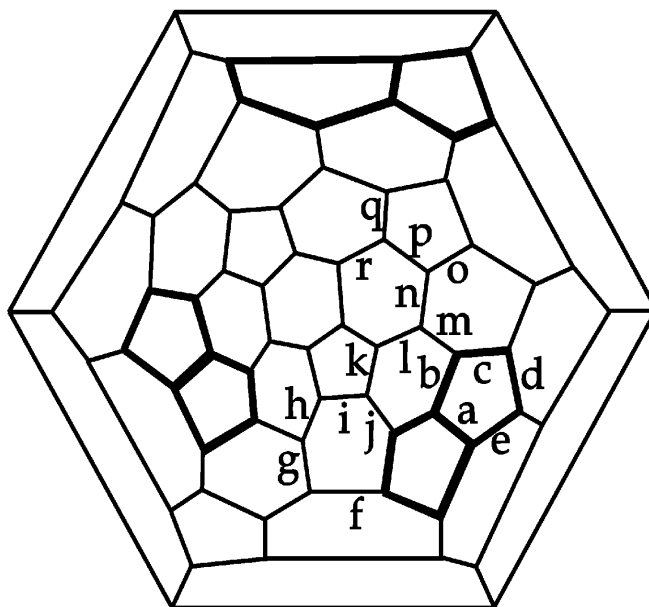


Figure 5.6 Schlegel diagram of Sc₃N@C₆₈

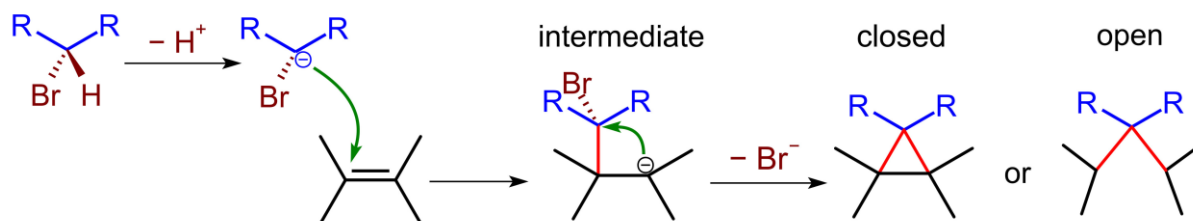
Table 5-5 Relative energies of $\text{Sc}_3\text{N}@C_{68}(\text{CH}_2)_2\text{NH}$ adducts (kJ/mol)

CC bond	$\Delta E(\text{PBE})$	$\text{gap}_{\text{H-L}}$	$\Delta E(\text{PBE-D3})$
a	0.0	1.29	0.0
b	20.3	1.11	19.7
g	33.2	1.35	40.9
i	39.1	0.88	43.4
e	40.1	0.82	
h	40.5	1.12	
d	41.4	1.35	
q	46.5	1.02	
o	46.7	1.12	
k	49.6	1.01	
c	49.7	1.02	
p	51.2	1.02	
j	62.0	1.18	
m	70.5	1.04	
l	71.6	1.05	
n	77.9	0.94	
r	88.5	1.09	
f	95.6	0.55	

The preference of the cycloaddition across the pentagon/pentagon edge in the pentalene is quite remarkable. To our knowledge, Prato reaction for non-IPR EMFs has not been considered before. Thus, we also computed fulleropyrrolidine adducts of $\text{Sc}_3\text{N}@C_{68}$, whose carbon cage also violates the isolated pentagon rule and has three pentalene units.²³² Computations of the cycloadducts across all 18 non-equivalent CC bonds of the $\text{Sc}_3\text{N}@C_{68}$ molecule showed that the most thermodynamically preferable is addition to the [5,5] edge (Figure 5.5). Other adducts are higher in energy by at least 20 kJ/mol (see Figure 5.6 and Table 5-5). Thus, enhanced reactivity of the pentagon/pentagon edges in the Prato cycloaddition may be a general rule for non-IPR EMFs.

The preference for the addition to the [5,5] bond is also preserved at the second step of the cycloaddition. Computations of all 118 bis-adducts obtained by $(\text{CH}_2)_2\text{NH}$ addition to the **2'-10'** monoadduct of $\text{LaSc}_2\text{N}@C_{80}$ showed that the second pentalene unit will be functionalized with equally high with formation of the C_5 -symmetric (**2'-10',2-10**) bis-adduct (Figure 5.5).

In Bingel-Hirsch reaction,^{233,234} a carbanion formed via proton abstraction from the bromomalonate attacks the fullerene double bond with formation of the intermediate, which then converts to the cycloadduct via removal of the Br⁻ anion:



The product can be either "closed" methanofullerene (typical for empty fullerenes²³⁵ and Sc₃N@C₇₈²³⁶) or "open" methanofulleroid (typical for nitride clusterfullerenes²³⁷⁻²⁴¹). Bingel-Hirsch addition to nitride clusterfullerenes is found to be kinetically driven.^{239,241} Alegret *et al.* showed that addition sites can be predicted based on (i) the lowest energy intermediate carbanion, then followed by (ii) the lowest-energy transition state for the Br⁻ abstraction.²³⁹

To find the most kinetically-favourable addition sites in LaSc₂N@C₈₀, first we computed all 129 intermediates obtained by addition of CH₂Br anion to symmetry inequivalent cage carbon atoms (for each cage carbon atom, there are three conformers of the [LaSc₂N@C₈₀CH₂Br]⁻ intermediate with different directions of the C-Br bond). The most stable intermediates are obtained by CH₂Br⁻ addition to four carbon atoms around the pentagon/pentagon edge (C1, C3, C9, and C11), and two carbon atoms next to them (C16 and C18) (Table 5-7). For these intermediates we further computed transition states (TS) for the Br⁻ removal. Reaction barriers were found to be in the range of 90–120 kJ/mol (with respect to corresponding intermediates).

Based on the low energy intermediate and reaction barrier, the most kinetically favoured Bingel cycloadduct is **11–16** (Fig. 5.7). Although the corresponding intermediate is somewhat less stable than the intermediates based on the C1 atom, the barrier to the Br⁻ removal in **11–16** is much lower, and hence this cycloadduct is expected to be formed much faster. The HOMO-LUMO gap of **11–16** is 1.15 eV; the energies of the frontier MOs (-5.01/-3.87 eV) are 0.2 eV higher than in the pristine LaSc₂N@C₈₀.

Table 5-6 Relative energies of intermediates [LaSc₂N@C₈₀CH₂Br]⁻

C-C	ΔE(PBE)	ΔE(PBE-D3)	C-C	ΔE(PBE)	C-C	ΔE(PBE)	C-C	ΔE(PBE)
1-12	0.0	0.0	33-35	40.9	23-22	60.1	5-4	82.4
1-2	1.8	1.6	7-20	42.2	23-6	60.3	39-38	83.0
1-1'	5.1	5.2	7-6	42.3	25-43	60.5	39-40	83.9
11-16	5.5	7.7	12-13	42.7	43-25	60.5	5-6'	85.2
11-12	6.8	9.3	12-1	43.5	43-25'	60.5	5-6	85.3
11-10	9.4	11.9	29-28	43.6	43-42	60.9	39-29	85.7
3-8	11.0	12.2	29-30	44.0	23-23'	61.8	27-26	90.1
16-17	13.3	13.4	29-39	44.9	22-23	62.2	27-28	90.1
16-15	15.6	15.4	19-28	45.9	4-5	62.3	27-21	90.7
3-4	14.6	16.2	36-35	46.4	8-7	62.8	34-14	92.7
16-11	17.9	17.7	12-11	47.0	22-21	63.7	34-33	93.9
9-18	15.7	18.1	36-37	47.0	8-9	64.5	34-34'	95.1
9-8	17.1	19.6	36-37'	47.1	41-40	65.4	35-33	98.6
3-2	17.7	19.1	7-8	47.6	22-24	65.5	35-33'	98.7
18-17	19.1	21.9	19-20	48.5	41-37	65.9	35-36	98.9
18-19	19.7	22.1	30-29	50.8	24-24'	66.2		
42-41	20.4	29.3	19-18	51.4	41-42	66.5		
42-43	20.9	29.9	17-18	53.2	24-22	67.1		
18-9	21.8	24.4	30-31	53.8	37-38	67.2		
9-10	22.2	24.4	17-30	54.1	37-36	68.3		
15-14	25.9		17-16	55.8	24-25	68.4		
15-31	26.2		20-7	55.9	4-3	69.1		
13-13'	28.8		28-27	56.1	4-3'	69.1		
13-14	28.8		28-19	56.2	38-32	69.3		
10-2	32.1		20-21	56.4	38-39	69.4		
10-9	32.1		8-3	56.7	37-41	70.3		
2-3	33.0		30-17	56.8	38-37	71.2		
13-12	34.5		32-33	57.1	31-15	72.2		
10-11	35.3		28-29	57.4	31-32	73.4		
26-27	35.4		40-39	58.0	31-30	74.6		
26-40	35.5		20-19	58.3	21-30	76.4		
14-34	35.8		32-38	58.6	6-7	76.6		
15-16	35.9		32-31	59.0	21-20	76.8		
14-15	36.4		25-26	59.1	6-5	77.4		
26-25	36.6		40-26	59.4	21-27	77.4		
14-13	37.5		40-41	59.5	6-23	77.7		
2-1	37.6		25-24	59.7				
2-10	37.9							
33-34	38.7							
33-32	39.0							

Table 5-7 The lowest energy [LaSc₂N@C₈₀CH₂Br]⁻ intermediates (ΔE_I), transition states of Br⁻ removal (ΔE_{TS}), and relative energies of corresponding LaSc₂N@C₈₀CH₂ cycloadducts (ΔE_{CA})^a

CC ^b	ΔE_I	ΔE_{TS}^c	ΔE_{CA}	CC ^b	ΔE_I	ΔE_{TS}^c	ΔE_{CA}
1-12	0.0	115.9	46.8	16-17	13.4	101.1	16.7
1-2	1.6	124.2	34.9	16-15	15.4	117.7	82.3
1-1'	5.2	120.0	102.7	16-11	17.7	97.1	51.8
11-16	7.7	95.1	51.8	9-18	18.1	90.7	7.7
11-12	9.3	100.0	34.0	9-8	19.6	109.7	31.5
11-10	11.9	107.0	8.2	9-10	24.4	93.9	28.9
3-8	12.2	95.7	17.1	18-17	21.9	98.3	7.4
3-4	16.2	109.5	38.0	18-19	22.1	102.3	74.3
3-2	19.1	107.4	5.3	18-9	24.4	96.9	7.7
42-41	29.3	89.3	16.1	42-43	29.9	92.0	0.0

^a all values in kJ/mol; ^b the first number is the carbon atom to which the carbanion is bonded in the intermediate, the second one – the atom which forms new C–C bond in the process of Br⁻ abstraction; ^c TS energies are referred to corresponding intermediates.

Taking into account possible uncertainties of few kJ/mol in DFT calculations, the adducts **1-12**, **3-8**, and **9-18** cannot be not be fully excluded (Figure 5.7). All kinetically favoured structures have rather high relative energies and thus are not favoured thermodynamically (e.g., relative energy of **11-16** is 51.8 kJ/mol). The most thermodynamically stable LaSc₂N@C₈₀CH₂ isomer is obtained by addition across the **42-43** bond, which is coordinated by the La ion. Because of the relatively unstable intermediate (29.9 kJ/mol), this adduct is not favoured kinetically.

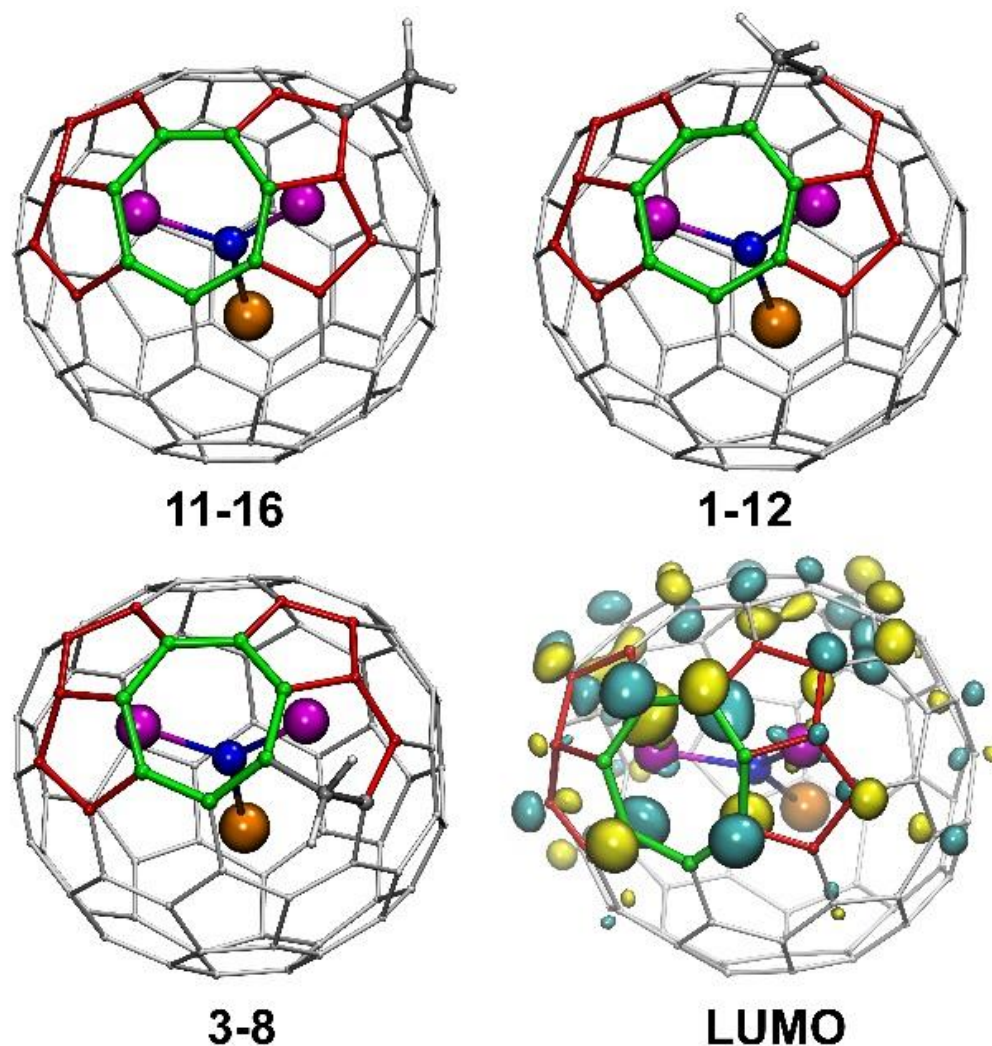


Figure 5.7 The most kinetically favoured $\text{LaSc}_2\text{N}@C_{80}\text{CH}_2$ adducts: **11–16**, **1–12**, **3–8**. Also shown is the LUMO of $\text{LaSc}_2\text{N}@C_5(\text{hept})\text{-C}_{80}$.

Interestingly, the **11–16** site of $\text{LaSc}_2\text{N}@C_{80}$ is similar to the most favourable addition site in Bingel-Hirsch cycloaddition to $\text{Sc}_3\text{N}@C_{68}$. Thus, similar to Prato reaction, reactivity of non-IPR nitride clusterfullerenes in Bingel-Hirsch reaction is dictated by the pentalene units, whereas the heptagon edges remain non-functionalized. We could not find unequivocal correlation between the structural parameters of the pristine $\text{LaSc}_2\text{N}@C_{80}$ and the reactivity. At the same time, analysis of the frontier MOs shows that the most stable $[\text{LaSc}_2\text{N}@C_{80}\text{CH}_2\text{Br}]^-$ intermediates are formed with the cage atoms having the highest LUMO coefficients in the pristine $\text{LaSc}_2\text{N}@C_{80}$ molecule (Figure 5.7). Likewise, Bingel-Hirsch addition to $\text{Sc}_3\text{N}@C_{68}$ proceeds via the carbon atoms with the highest LUMO contribution.

5.4 Conclusions

More than 25 years of the fullerene research resulted in formulation of the number of rules that govern the fullerene stability and molecular structures. One of the first rules to be established for empty cage fullerenes was the IPR, which stated that adjacent pentagons are destabilizing and should be avoided.²⁴² The avoidance of the rings other than pentagons and hexagons is another such rule that even found its way into the commonly accepted definition of fullerenes. While the IPR is a useful guide to predicting cage structures for endohedral fullerenes it was not designed for that purpose. The discovery of Sc₃N@C₆₈⁴⁰ and Sc₂@C₆₆^{41,42} in 2000 demonstrated that non-IPR cages could be stabilized when there were metals inside the cage. In this chapter, we showed that avoidance of heptagonal rings is also not necessary to obtain stable fullerene structures without externally attached groups. The first endohedral metallofullerene with one heptagonal ring has been synthesized and proposed that its low yield has to be ascribed to the kinetic factors rather than to thermodynamic stability. Hence, EMF synthesis may not be always operating under thermodynamic control. Besides, detailed computational study of the nitride clusterfullerene LaSc₂N@C_s(hept)-C₈₀ showed that the heptagonal ring is not reactive either in thermodynamically or kinetically controlled cycloaddition reactions. However it would not be correct to claim that the presence of the heptagon has no effect on the chemical reactivity of the molecule. The heptagon induces formation of two pentalene units, and the analysis shows that the most chemically reactive sites in the LaSc₂N@C_s(hept)-C₈₀ molecule are related to these structural elements. It is found that thermodynamically controlled Prato reaction should proceed with high regioselectivity across the pentagon/pentagon edges (**2–10**). In kinetically controlled Bingel-Hirsch cycloaddition, the most reactive site is the CC bond next to the pentalene (**11–16**). Very similar behaviour is found for another non-IPR nitride clusterfullerene, Sc₃N@C₆₈. Thus, we can conclude that the reactivity pattern described for LaSc₂N@C_s(hept)-C₈₀ is common for non-IPR clusterfullerenes.

Chapter 6. QM/MD simulations of dynamic metallofullerene self-Assembly with cooling gas and reactive gas

6.1 Introduction

Since the discovery of fullerenes in 1985,¹¹¹ scientists have been intrigued by the efficiency with which C₆₀ and other fullerenes form during carbon vapor condensation, and have sought to explain this process. Until now, many mechanisms have been proposed by both experiments and theoretical predictions (see details in chapter 1.3). He gas experimentally considered as cooling gas plays a role of importance which can greatly influence yield of fullerenes during formation process. The presence of helium or argon was theoretically considered in fullerene growth and shrinking simulations by Saha *et al.*¹⁰⁷. In those studies it was shown that, depending on the carbon concentration in simulation boxes with periodic boundary conditions, the fullerene cages can either grow (high external carbon concentration) or shrink (low external carbon concentration). Explicit use of He in tight binding MD simulations of fullerene formation has been made by Laszlo.²⁴³ The temperature of the He gas was controlled by Nose-Hoover thermostat, whereas the carbon gas was equilibrated via interactions with He atoms. In this such process, reasonable cage structures were obtained from 60 carbon atoms at 2000 K. However it remains unclear how the system would evolve if more or less carbon atoms were used in the simulations. Therefore, in this chapter we firstly demonstrate the effect of the cooling gas (He atoms) using QM/MD simulations based on DFTB potentials. Then we systemically investigate the Sc, Ti, Fe based metallofullerenes formation mechanism at atomic level.

First NCFs synthesis is unexpected with N₂ leak into fullerene generator chamber which should be avoid at that time⁷. A small portion of nitrogen gas as reactive gas was introduced into the Krätschmer-Huffman generator² with graphite rods containing metal oxides producing a

yield 3–5% of NCFs. Generally yield of EMFs reached only 2% or less in the fullerene soot and was exceeded 10-fold higher amounts of empty fullerenes. While by substitution from nitrogen gas to NH_3 as the reactive gas^{14,15}, relative yield of the NCFs has been dramatically enhanced, and for the first time NCFs are the main fullerene products in the soot with less than 5% empty cages^{16,17}. The improvement of the NH_3 method is that the empty fullerenes are significantly depressed, so the task of separating the NCFs from the empty fullerenes (EF) simplified when compared to introduction of N_2 gas approach. Although successful application of NH_3 method has been a breakthrough for NCFs synthesis, the role of NH_3 gas still remains mysterious. For instance, why the NH_3 can eliminate the empty cages but NCFs survive. CH_4 owing the same character but no nitride clusterfullerenes produced as NH_3 is applied to synthesis M-Ti-carbide clusterfullerenes (M=Y, Nd, Gd, Dy, Er, Lu)²⁴⁴. Therefore, in this chapter another aim is to understand NH_3/CH_4 effect as reactive gas during fullerene formation by extensive QM/MD simulations.

6.2 Models and Computational Methods

The MD simulations are performed using the DFTB+ program.²⁴⁵ Energies and nuclear gradients for carbon species were evaluated using both non-charge-consistent^{134,246} (NCC) and self-charge-consistent¹⁰⁹ (SCC) approximation of DFTB potentials in combination with a finite electronic temperature approach ($T_e = 5000$ K). SCC-DFTB method was found to be less reliable as will be discussed below, and so majority of reported results are obtained with NCC-DFTB using mio-0-1 DFTB parameter for C-C, C-N, C-H, N-H, N-N, H-H interaction, trans 3d-0-1 parameters for Ti, Fe,²⁴⁷ and modified parameters for Sc–Sc and Sc–C.²⁴⁸ Interaction of He atoms with He, H, C, N, Sc, Ti, Fe are described by the classical UFF force field.²⁴⁹

In each simulation, carbon (in the form of C_2 units), scandium and helium atoms were randomly placed into a periodically bound cubic box, whose size was chosen to keep the carbon density in the range of the experimental scale (10^{20} – 10^{21} cm^{-3}). Initial velocities were assigned randomly in accordance with Maxwell-Boltzmann distribution for $T = 2000$ K, and the temperature of the system was then kept at 2000 K using Nosé–Hoover thermostat with a coupling constant of 500 cm^{-1} . In the first series of simulations aimed at the understanding of the role of the cooling gas, 200 carbon atoms were placed inside the $80 \times 80 \times 80$ \AA^3 box, the number of He atoms was 0, 100, 200, 300, or 500, and the number of Sc atoms was either 0 or 6. For each combination of C/Sc/He atoms, 10 independent simulations were performed

propagating the system for at least 200 ps (i.e., totally 100 trajectories were studied). In the second series aimed at the detailed study of the Sc encapsulation mechanism, the number of C and He atoms was reduced to 100 and 50, respectively, the size of the box was $50 \times 50 \times 50 \text{ \AA}^3$, whereas the number of Sc atoms was kept 6 to increase the probability of encapsulation., 10 trajectories were studied with these initial conditions. The third series aimed at the detailed study of effects of reactive gas, the number of 100C/40He/6-15Sc with NH_3 and CH_4 respectively in the size of the box $50 \times 50 \times 50 \text{ \AA}^3$, whereas the number of 10 atomic N atoms was also added to increase the probability of N containing fullerenes (aza-,cyano-, nitride-clusterfullerenes).

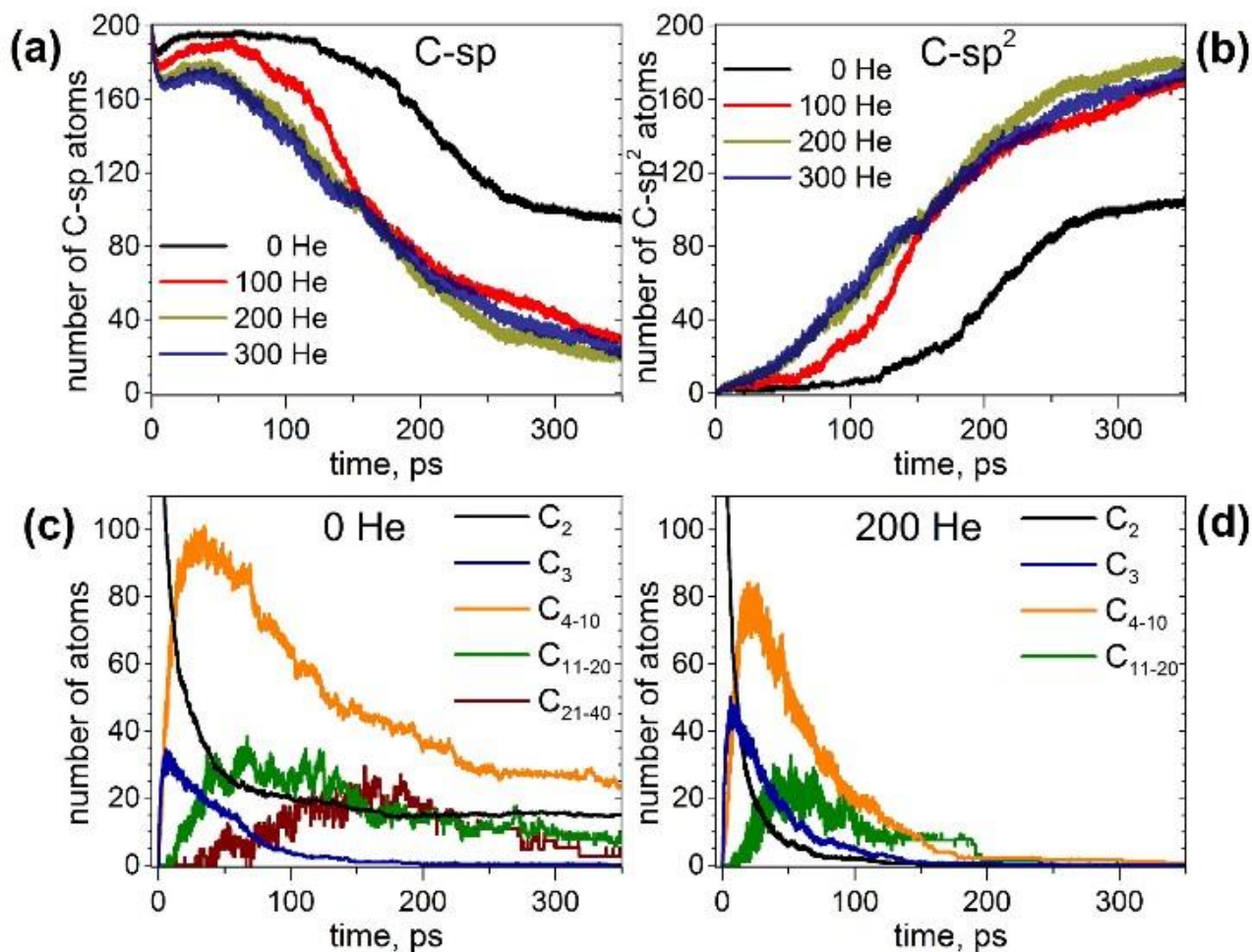


Figure 6.1 (a,b) Evolution of the number of (a) C-sp and (b) C-sp² atoms during MD simulations of the fullerene formation with different number of He atoms. (c,d) Evolution of the number of carbon atoms in C₂ and C₃ fragments and chains of different length (C₄–C₁₀, C₁₁–C₂₀, and C₂₁–C₄₀) in MD simulations without He (c) and in the presence of 200 He atoms (d). Each curve is averaged over 10 independent trajectories.

For *ab initio* MD simulations, we use the projector augmented-wave (PAW) pseudopotential plane-wave method with an energy cutoff of 280 eV as implemented in the VASP.²⁵⁰ Perdew-Burke-Ernzerhof (PBE) function was used for the exchange correlation term.¹²¹ A Nosé-Hoover NVT thermostat set at 2000 K similar to DFTB calculation, and velocity Verlet algorithm with the step of 1 fs was used to propagate the system. Molecular structures were visualized using VMD package.¹⁵²

6.3 Results and Discussion

6.3.1 Influence of He on the empty fullerene formation

From 100 trajectories studied with and without He atoms, many resulted in formation of fullerene cages. In general, the mechanism of their formation is the same with and without He, and includes (1) formation and growth of polyynes chains from C₂ units; (2) formation of large ring structures when chains become too long; (3) aggregation and self-cycloaddition with formation of carbon network system with more and more pentagon, hexagon, and heptagons forming at this stage; (4) formation of closed-cage structures (fullerenes) as the process evolves further. However, the presence of He in the system dramatically affects the rate of the process, the length of the polyynes chains and their lifetime, and eventually the yield and the size of the produced fullerene cages. To describe the effect of the cooling gas in the fullerene formation process, first we analyze how the presence of He affects elementary steps of the formation mechanism. Figure 6.1 compares the evolution of the number of C-sp and C-sp² atoms in the MD simulations (C-sp is defined as carbon atom bonded with one or two other carbon, whereas C-sp² is defined as carbon atom bonded to three other carbons). Obviously, consumption of C-sp atoms in the presence of He is much faster. Whereas in He-free simulations roughly a half of all carbons are still in the C-sp state after 300 ps, the number is reduced to ca 20% when He is introduced into the system. Likewise, increase of the number of C-sp² atoms is much faster in the presence of He. Variation of the number of He atoms from 100 to 300 does not lead to a significant difference over the longer time scale (300 ps), although a noticeable deviation for a system with 100 He atoms is seen on a shorter time scale (< 150 ps).

For an analysis of the carbon distribution between different chain structures, we chosen simulations without He and in the presence of 200 He atoms. Figure 6.1c,d shows evolution of individual C₂ and C₃ fragments as well as net values for free short chains (C₄–C₁₀), medium-size chains (C₁₁–C₂₀) and longer chains (C₂₁–C₄₀). In the absence of He, the number of C₂ units

decrease steeply during the first 70 ps, but then their concentration shows the tendency of leveling off and remains near 10% all the way through 200–350 ps. Consumption of C_2 units in the presence of He is much faster and is not levelling off, so that all C_2 units are consumed already before 100 ps.

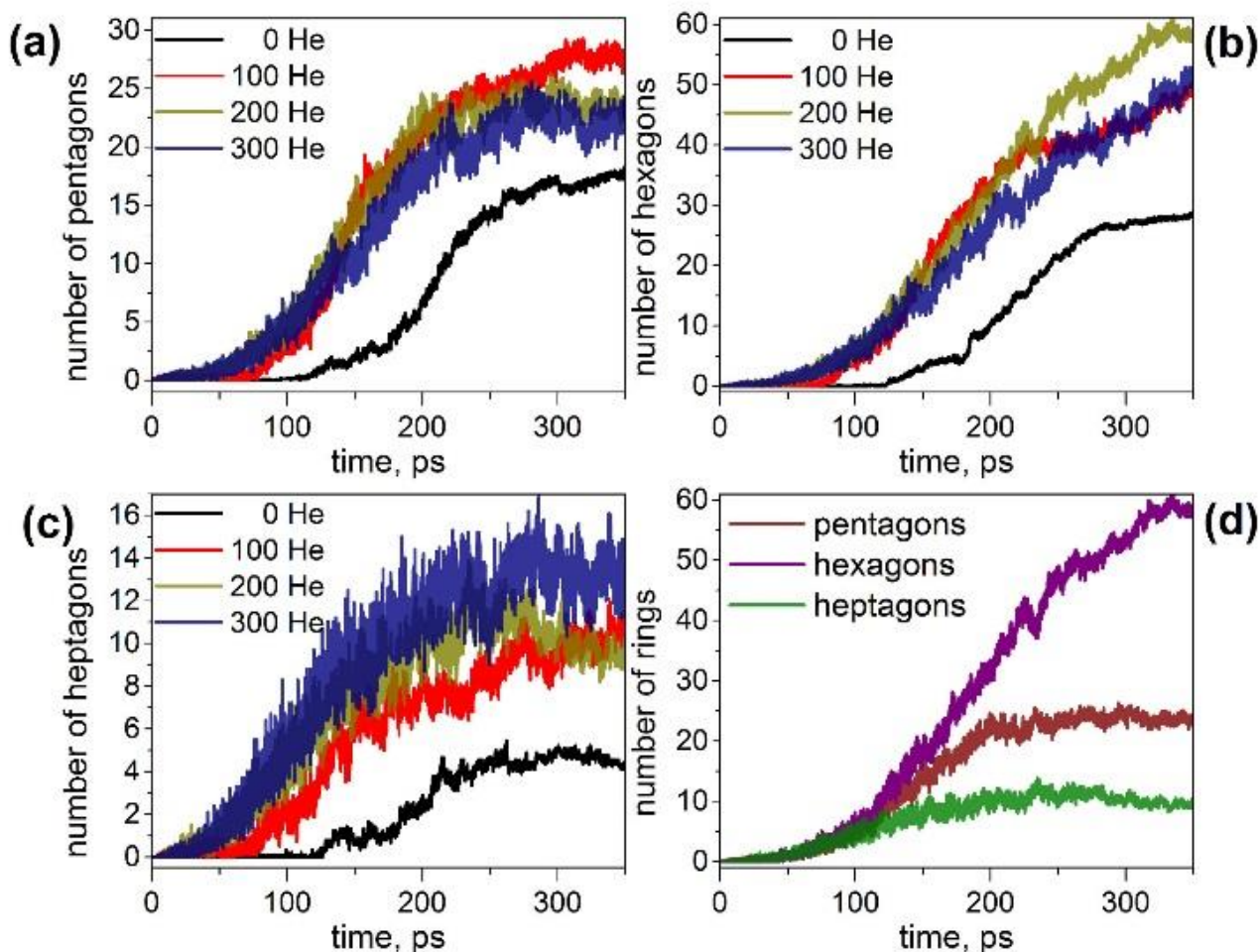


Figure 6.2 (a-c) Evolution of the number of (a) pentagons, (b) hexagons, and (c) heptagons formed during MD simulations of the fullerene formation with different number of He atoms; (d) number of pentagons, hexagons, and heptagons formed in simulation with 200 He atoms. Each curve is averaged over 10 independent trajectories.

A bimolecular reaction between two C_2 units' results in the C_4 chain, but such a reaction is exothermic and often leads to a dissociation of the product giving C_3 fragment and a single carbon atom. As a result, C_3 units are the most abundant species after C_2 at the short time scale, which agrees with their high concentration in hot carbon vapors.²⁵¹ Reaching the maximum at ca 6–8 ps (18% and 25% of all carbon in the absence and presence of He, respectively), the

concentration of C_3 fragments starts to decrease in favor of longer chains and reduces to negligible values at 150 ps in both types of simulations. Thus, the presence of He increases the number of C_3 fragments at the maximum, but the overall time profiles are similar.

Starting from C_4 and beyond, the presence of He leads to a faster formation of chains and their shorter lifetimes. The number of carbon atoms in C_4 – C_{10} chains reaches maximum (ca 40% of all carbons) at 15–25 ps, and then decreases exponentially till 180 ps. The fraction of carbons in longer chains increases to ca 40 ps (the value at maximum is ca 15%), remains in this range for next 30 ps, and then starts to decrease but not as steep as the fraction of shorter chains. After 100 ps the average number of carbons in such chains is below 10 which means that in some of the simulations such chains already disappear, whereas in other 1 or 2 chains still remain. After 200 ps, all chains are consumed in the presence of 200 He atoms. In He-free simulations, the concentrations of shorter and longer chains reach maximum at similar time as with He, but their decay is then dramatically slower. Note also that the highest fraction of carbon in C_4 – C_{10} chains over the trajectories is ca 50% (versus 40% in simulation with He). After 350 ps the fraction carbons in C_4 – C_{10} chains is ca 15%, and that of C_{11} – C_{20} chains is ca 4% (again, 1–2 chains in roughly half of trajectories). Beyond 250 ps, the systems seems to be stationary (i.e. no significant development). In the presence of He, we did not observe formation of long chains (>20 atoms) in statistically meaningful amounts, but in He-free conditions such long chains were observed in several trajectories. The number of carbon atoms in such chains increase to ca 150–200 ps, but then decays to negligible values after 350 ps.

This analysis shows that the presence of He results in faster evolution of carbon chains into carbon networks. In conditions of the simulations, all free chains were formed and consumed during the first 200 ps. On the contrary, many carbon chains, including the long ones, survived after 350 ps in the absence of He. It should be noted that the statistics discussed above concerns only free linear chains. We did not analyzed branched chains or chains terminated on one side by bonding to carbon clusters because determination of their lengths is rather ambiguous. However, the principal effect of the cooling gas on chain length distribution is similar for these chains as well. A faster formation of carbon networks in the presence of He can be exemplified by plotting the number of small carbon rings. The majority of the rings formed are pentagons, hexagons, and heptagons, and their number versus time is shown in Fig. 6.2. In He-free conditions, the first C_5 – C_7 rings appear after ca 120 ps, whereas in the presence of He, 5–8 pentagons, 7–12 hexagons, and 3–7 heptagons are already formed at this moment. All curves

show roughly a sigmoidal shape, and the curves obtained in He-free conditions are shifted to a later time and have smaller number of rings in the end of trajectories. In particular, the sigmoidal growth of the number of pentagons levels off after ca 220–250 ps with formation of 23–27 pentagons in the presence of He and 18 rings in He-free conditions (the values are for 350 ps). The number of hexagons grows continuously in the presence of He up to ca 50–60 rings at 350 ps, whereas in He-free conditions the number levels off after 300 ps near 28 rings. Finally, the number of heptagons reaches maximum at ca 250 ps, and then shows a sign of slow decrease. The number of heptagons formed in He-free conditions is roughly 3 times smaller than in the presence of He.

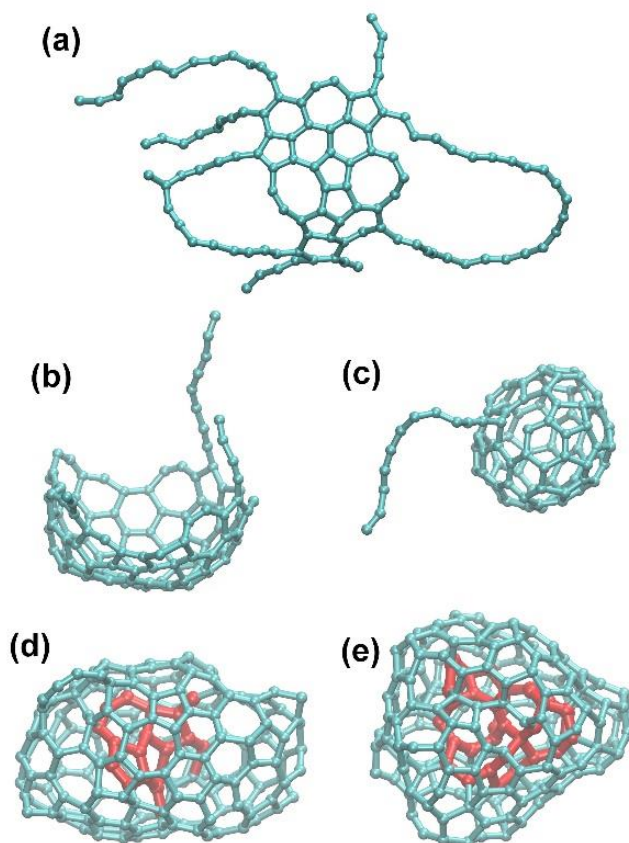


Figure 6.3 (a-c) Examples of the carbon clusters obtained in He-free conditions: (a) “flake”, (b) half-cage; (c) fullerene cage with carbon chain “antenna”. (d-e) Typical structures with endohedral carbons obtained at high He pressure: 300 He (d) and 500 He (e). Endohedral carbon atoms are colored in red. Note that the structure obtained with 500 He is more compact (has less empty space) than the structure obtained with 300 He atoms.

The chain and ring statistics discussed above show that the presence of He improves conditions for fullerene formation. Indeed, from 10 He-free trajectories, only 5 resulted in

fullerene cages after 350 ps. In three others the process stopped at the nucleation stage, and two simulations produces half-cages with large diameter (Fig. 6.3). The fullerenes cages formed in successful trajectories often have carbon chain “antennas” (Fig. 6.3). At 0 He pressure, in most cases we observed only one nucleation center, which slowly grows by absorbing long chains (which can also live long time).

The situation changes dramatically when He is introduced into the system. With 100 and 200 He atoms, each trajectory resulted in fullerenes cages (thus, the fullerene yield is increased dramatically as can be seen in Fig. 6.4). Most of the cages formed were free of carbon chain “antennas”. Moreover, in more than half of simulations two cages were formed in one trajectory (and some of them merged afterwards to produce a larger cage). Thus, in the presence of He gas fullerenes are formed faster, and they are smaller at the initial stages. A plausible explanation of this influence is that the carbon diffusion is slowed down by He atoms. The carbon vapor has more relaxation time to form reasonable size of condensation nuclei which finally form fullerenes of regular sizes. The proceeding of the nucleation stage is also considerably altered in the presence of He. In He-free trajectories, a typical scenario is formation of one large and relatively flat carbon flake, which is rather stable kinetically and often does not transform into the cage structures (hence high degree of trajectories not leading to fullerenes). In the presence of He, faster nucleation results in concurrent formation of two-three nucleation centers. Large flat flakes are thus not formed as they curl up into the more compact structures at earlier stages hence leading to a faster growth of smaller cages (C_{40} – C_{80}). Such cages have many defects and tend to grow further via absorption of carbon chains and fusion of two small cages into larger ones. The latter process is probably less feasible in real arc-discharge synthesis, when the carbon vapor is expanding adiabatically and the density of carbon vapor becomes lower over time reducing the probability of such fusion.

When 300 He atoms were used in the MD simulation, similar high yield of fullerene formation was observed. However, in several trajectories we found the structures comprising endohedral carbon clusters with enhanced number of four-coordinated carbon atoms (Fig. 6.3d). To clarify if this can be an effect of the high He pressure, an additional series of simulations was performed with the number of He atoms in the box increased to 500. With such a large number of He atoms, all 10 trajectories produced “droplets” of amorphous carbon (see Fig. 6.3e for an example) proving that the high pressure of cooling gas has a deteriorating effect on the fullerene formation. I.e., under high He pressure the carbon clusters tend to be as compact as possible, and such

amorphous agglomerates have smaller volume than the hollow-caged fullerenes. It is likely that the particles formed in such extreme conditions may be further annealed to nanodiamond or carbon onions as they are normally produced with higher gas pressure than fullerenes or even in liquids,²⁵²⁻²⁵⁵ however further exploration of such structures is beyond the goals of this work. Thus, in harmony with experimental studies, the results show that fullerenes are efficiently formed in a certain interval of He pressures. Too low or too high pressure reduce the yield, albeit with different mechanisms. Interestingly, none of the simulations produced He inside the cages.

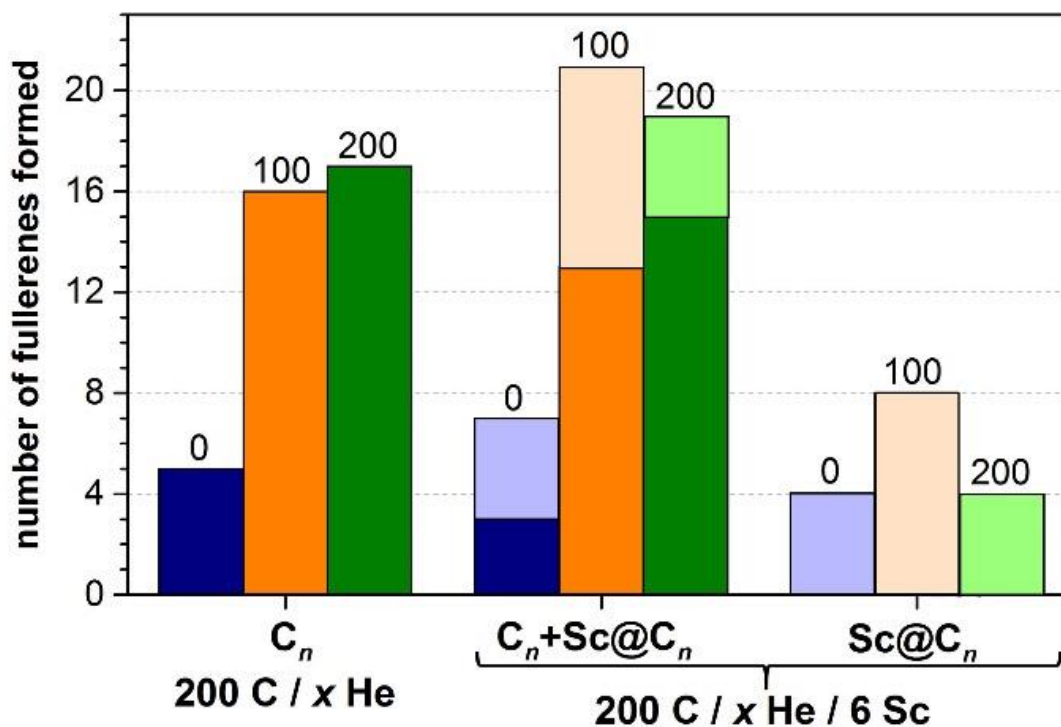


Figure 6.4 Comparison of the number of produced fullerenes in 10 trajectories with different number of He atoms (0, 100, and 200) and with/without 6 Sc atoms. For trajectories with Sc atoms, the yield of Sc-EMF is shown separately (rightmost columns) as well as together with empty cages (columns in the middle).

6.3.2 Sc endohedral fullerene formation

Sc-EMFs in He-free conditions. MD simulations performed in the presence of 6 Sc atoms showed that the metal imposes a considerable influence on the process efficiency in He-free conditions. From ten trajectories, only one failed to produce a fullerene (versus 5 “failed” trajectories without Sc). Five trajectories resulted in Sc-encapsulated monometallo-fullerenes

and four gave empty fullerenes. In two cases we observed formation of “networked” Sc fullerenes (i.e. with Sc taking the place of a carbon atom in the cage wall). Thus, in He-free conditions, the presence of Sc atoms significantly increases the yield of fullerene structures.

Analysis of the trajectories shows that Sc atoms form multiple Sc–C bonds at all stages of the fullerene formation. At the beginning, Sc coordinates to C₂ units and longer carbon chains. When carbon chains start to nucleate and develop into polyaromatic flakes, Sc atoms bond to the free valencies at their perimeters as illustrated in Figure 6.5. This bonding is strong enough to prevent dissociation even at 2000 K, but is still rather labile so that Sc atoms typically move along the perimeter from one bonding site to another as well as along the surface of the flake. Such Sc atoms also easily bond to free carbon chains and hence can also serve for a faster transfer of additional carbon to the growing cages. Presumably, coordination of Sc induces faster curling of such flat flakes into cages (Fig. 6.5), which may be a reason of the catalytic activity of Sc in the fullerene formation. Namely, bonding of a carbon atom to Sc weakens its bonding to neighboring carbons, thus facilitating the local transformations in the carbon network. When cage-like structures with large holes and numerous dangling bonds are formed at first, Sc atoms are bonded to such edges and remain there all the way through the cage formation. Whether Sc atoms are trapped inside or left outside the cage after its closure, seems to be more or less random. In rare cases, the structures can be stabilized also in a “networked” cage as shown in Fig. 6.5i.

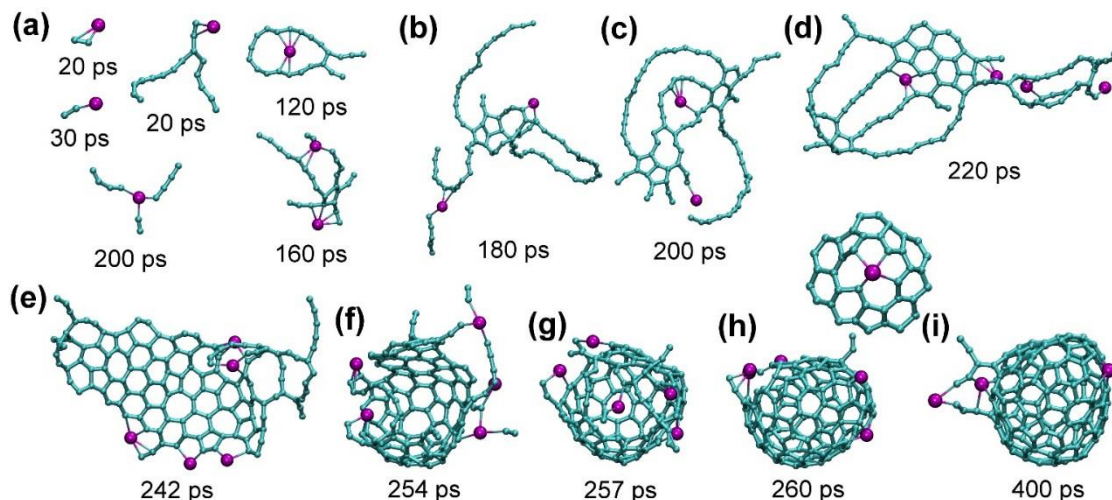


Figure 6.5 (a) Bonding of Sc to small carbon clusters at different moments of the trajectory in He-free conditions: two Sc–C₂ fragments, bonding to carbon chain, carbon ring, simultaneous bonding to C₂ and two C₄ fragments, and bonding to an early nucleation center. (b-e) development of the flake from nucleation center, (e-h) curling of the flake up into the fullerene cage. (i) the “final” cage after additional 140 ps annealing. Note that Sc atom in (f) is bonded to the forming cage and simultaneously to C₂ and longer chains. Also shown above (h) and (i) is the “networked” Sc atom on a place of a carbon atom in the fullerene cage: this fragment was formed near 260 ps and survived till the end of simulation at 400 ps.

Sc-EMFs formation in the presence of He. The presence of He has ambivalent effect on the Sc-EMF formation. Addition of 100 He atoms doubles the yield of EMFs in comparison to He-free conditions (Fig. 6.4), but in the presence of 200 He atoms the yield is dropped back (although the yield of empty fullerenes remains high). The main reason for the negative influence of higher He pressure is breaking of Sc–C bonds by collisions with He atoms. This can be illustrated by studying the time when a metal atom has at least one carbon at the distance closer than 3 Å. The histogram in Fig. 6.6 shows that in He-free condition, majority of Sc atoms are bonded to carbon atoms most of the time (the distribution has maximum at 80-90%). Completely different pattern is observed in the presence of 100 He atoms. The distribution becomes rather diffuse with almost equal values all over the 0-90% range. Note that the longer times are dominated by endohedral Sc atoms since they always have carbon atoms at short distances. Increase of the number of He atoms in the system increases the frequency of Sc-He collision and dramatically decreases the Sc–C bond lifetime: the maxima of distributions are found at 20% and 10% for 200 and 300 He atoms, respectively.

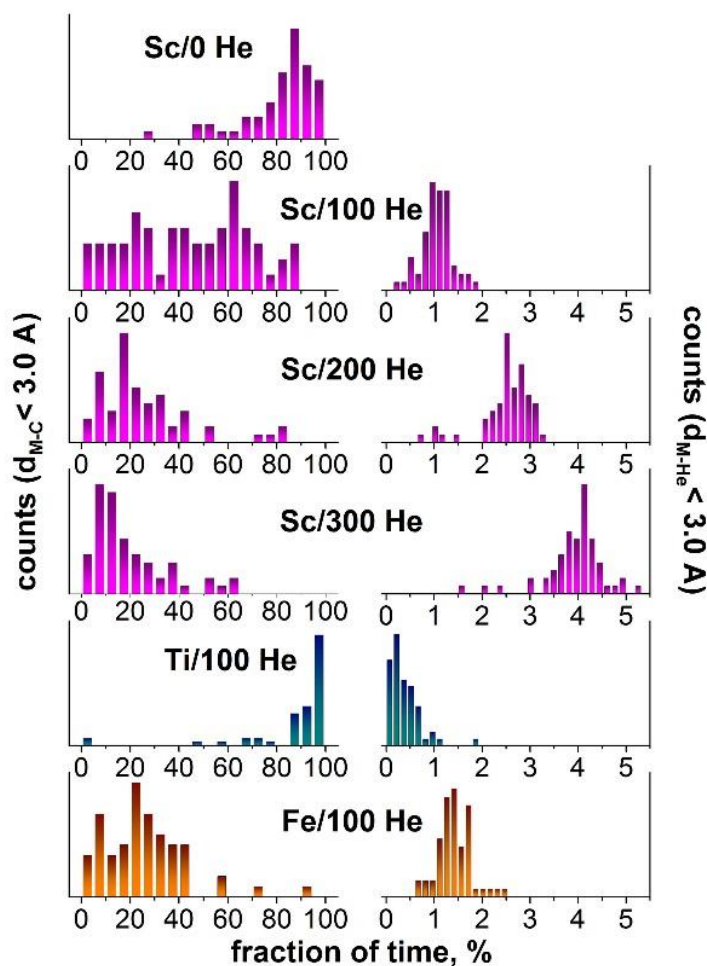


Figure 6.6 Left: the fraction of time when metal atom has at least one carbon atom at the distance shorter than 3 Å. Each histogram is based on 60 values obtained after analysis of 10 trajectories in $80 \times 80 \times 80 \text{ \AA}^3$ box with 200 C atoms, 6 metal atoms (Sc, Ti, or Fe), and indicated number of He atoms (0, 100, 200, or 300). Right: the same for metal-He distance shorter than 3 Å. In effect, the left column describes the net lifetime of metal-carbon bonds, whereas the right column visualizes the frequency of metal-He collisions. Note that when metal atom is encapsulated in the fullerene, it always has carbon atoms at short distances and at the same time it is shielded from He atoms. Hence, fast formation of Ti-EMFs results in the sharp Ti-C distribution at 85–100% and the short time of exposure to He, which can be compared to that of Fe not forming EMFs.

Another reason for a lower yield of Sc-EMFs with the increase of He pressure is faster formation of fullerenes. Relatively slow nucleation and formation of large kinetically stable flakes in He free conditions gives the system sufficient time to gather several Sc atoms at the growing cage. And although not all He-free trajectories with Sc ended up with endohedral fullerenes, Sc atoms were bonded to *all* growing fullerenes. With He atoms in the system,

nucleation and fullerene growth are faster and often avoid formation of large flakes such as shown in Fig. 6.5e. In the conditions of the concurrent formation of 2–3 cages, some of the fullerenes were formed before they had a chance to “meet” any Sc atom. Whereas with 100 He atoms we still could observe formation of flattened and rather long-living flakes in several trajectories (which were then coordinated by Sc atoms and sometimes resulted in the EMF formation), with 200 He atoms in the system such intermediates were not observed at all.

We conclude that in the presence of He, Sc has no dramatic effect on the fullerene formation mechanism. But propensity of Sc to form metal-carbon bonds leads to a coordination of Sc to free valences of the forming carbon cage, which may eventually result in the encapsulation. Collisions with He decrease the Sc–C bond lifetime, and therefore the *relative* yield of Sc-EMFs to the empty cages decreases with the increase of the He pressure from 5:4 for He-free conditions to 10:13 for 100 He atoms and further to 4:20 for 200 He atoms (Fig. 6.4). Nonetheless, the highest *absolute* yield of Sc-EMFs is achieved with 100 He atoms, because dramatic increase of the fullerene formation yield is able to compensate the shortening of the Sc–C bond lifetime. Further increase of the He pressure, while preserving the high yield of empty fullerenes, reduces the probability of EMF formation. This result shows that the optimum He pressure can be different for the synthesis of empty and endohedral fullerenes.

The influence of metal/carbon ratio and carbon density. Having clarified the influence of He, we also studied how EMF formation is affected by the metal/carbon ratio and carbon density. First, we performed two series of MD simulations with the same size of the box ($80 \times 80 \times 80 \text{ \AA}^3$), which contained 100 He atoms, 6 Sc atoms, and either 100 or 60 carbons (versus 200 carbon atoms discussed above). With 100 C atoms in the box, all trajectories resulted in the fullerene formation, however only two of them gave Sc-EMFs ($\text{Sc}@C_{45}$ and $\text{Sc}@C_{63}$, Fig. 7c). Whereas simulation with 200 C atoms usually resulted in 2–3 cages per trajectory, a two-fold decrease of the carbon density reduced the number of cages to one per trajectory (only once two small cages were formed). Further decrease of the carbon density to 60 atoms in the $80 \times 80 \times 80 \text{ \AA}^3$ box had devastating impact on the fullerene formation: from ten trajectories, eight failed and two gave empty fullerenes.

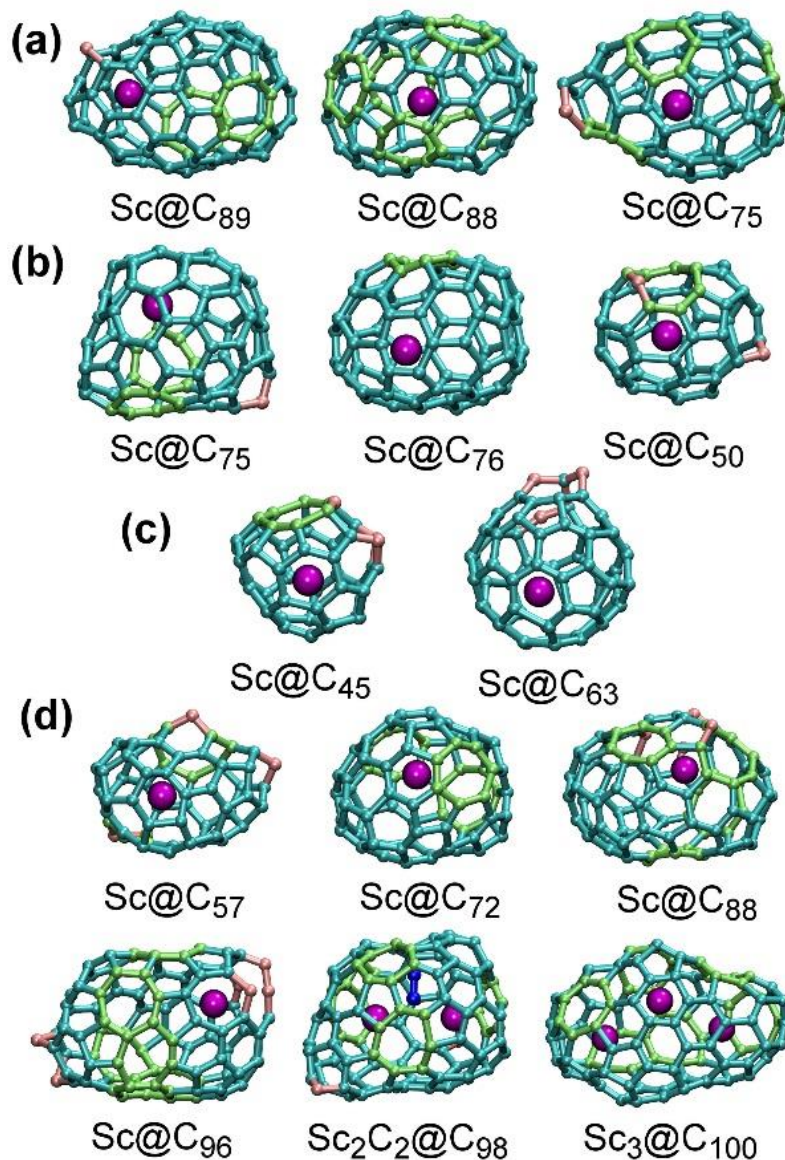


Figure 6.7 Examples of Sc-EMFs formed in MD simulation: (a) in the He-free 200 C/6 Sc system inside the $80 \times 80 \times 80 \text{ \AA}^3$ box; (b) in the 200 C/6 Sc/100 He system inside the $80 \times 80 \times 80 \text{ \AA}^3$ box; (c) in the 100 C/6 Sc/100 He system inside the $80 \times 80 \times 80 \text{ \AA}^3$ box; (d) in the 100 C/6 Sc/50 He system in the $50 \times 50 \times 50 \text{ \AA}^3$ box. Carbon atom and CC bonds are shown as cyan (pentagons and hexagon), light green (heptagon and other non-classical rings), or pink (carbene atoms). Endohedral carbons in Sc₂C₂@C₉₈ are shown in blue.

A much higher EMF yield in the 100 C/6 Sc system was achieved when the system was placed in the box of the smaller size ($50 \times 50 \times 50 \text{ \AA}^3$) and the number of He atoms in the smaller size box was reduced to 50. These conditions were found to be the most favorable for the EMF formation: eight trajectories ended up in the Sc monometallofullerenes, one resulted in trimetallofullerene Sc₃@C₁₀₀, and one resulted in formation of the carbide clusterfullerene

$\text{Sc}_2\text{C}_2@\text{C}_{98}$ (Fig. 6.7). Importantly, in the smaller box each trajectory produced only one fullerene cage (instead of two-three cages for 200 C atoms in the larger box). Thus, high Sc/C ratio and rather high density favor EMF formation. Increase of the probability of the Sc encapsulation via increase of its density and effective increase of the probability of the Sc–C bonding.

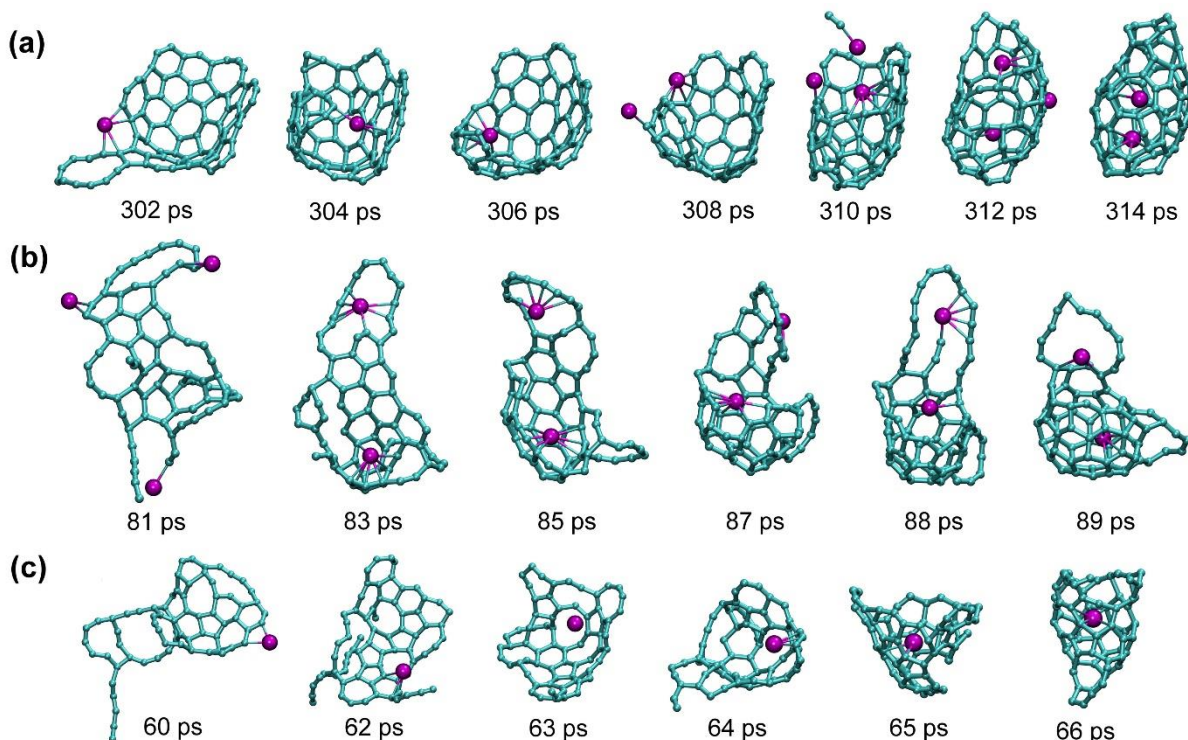


Figure 6.8 Representative examples of the Sc encapsulation during the Sc-EMF formation: (a) 200 C/6 Sc/100 He system, the procedure resulted in dimetallofullerenes $\text{Sc}_2@\text{C}_{82}$ (an empty fullerene was also formed in this trajectory); three Sc atoms are coordinated to the growing cage just before its closure (310 ps), but only two of them are eventually encapsulated within the fullerene; (b) 100 C/6 Sc/50 He system; two Sc atoms were coordinated to the carbon cluster, but only of them is eventually encapsulated; note that the cage after its closure is rather small and is fused to two large carbon rings, which are absorbed by the cage in the course of further annealing to make $\text{Sc}@\text{C}_{72}$ (see also Fig. 6.7d and Fig. 6.9); (c) another trajectory from the 100 C/6 Sc/50 He system; the structure formed at 66 ps is highly defected $\text{Sc}@\text{C}_{66}$, which then grew to $\text{Sc}@\text{C}_{96}$ (see Fig. 6.7d) by capture of other carbon fragments.

Mechanism of Sc encapsulation. Successful formation of a series of Sc-EMFs in MD simulations allows us to analyze the mechanism of the Sc encapsulation during the Sc-EMF formation. Typical examples of the encapsulation process are shown in Figure 6.8, and Figure

6.9 sketches the whole mechanism of the fullerene formation for Sc@C₇₂ (the structure of this EMF is shown in Fig. 6.7d and the mechanism of Sc encapsulation is shown in Fig. 6.8b).

As in the empty fullerene formation, the carbon cluster goes through the stages of polyynes chains, formation of rings and their further condensation with formation of extended “flakes” (Fig. 6.9). The flake formation and its further dwelling in this kinetically stable state can be quite long (tens and even hundreds of picoseconds), but once the flake starts to curl up into the fullerene cage, the process then proceeds very fast and is usually fulfilled within few picoseconds (Fig. 6.8).

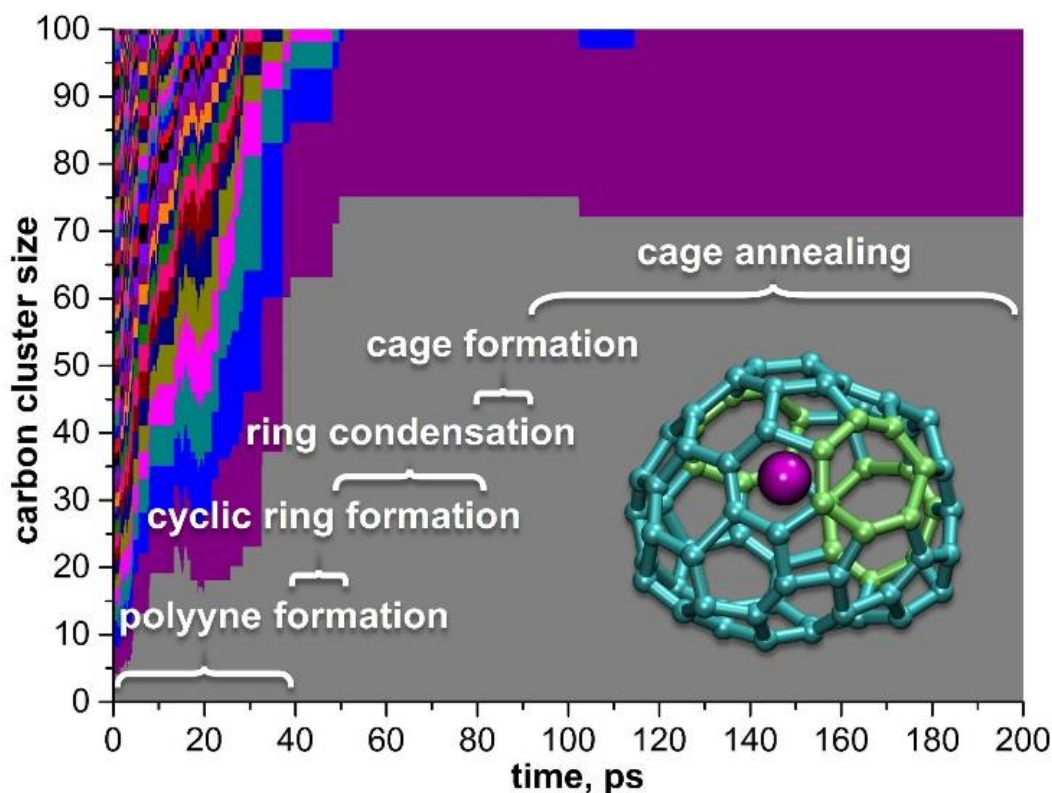


Figure 6.9 An overview of the Sc-EMF formation mechanism based on the trajectory, which resulted in Sc@C₇₂. Detailed mechanism of the cage formation in this trajectory is shown in Fig. 6.8b. Each color filled correspond to the carbon cluster, its height scales as the number of carbon atoms: after 100 ps, only two clusters are left, Sc@C₇₂ and C₂₈.

A starting point in all three examples in Fig. 6.8 is an extended carbon flake coordinated by one-two Sc atoms. Sc atoms are stronger bonded to the periphery via Sc–C σ -bonds, but can also migrate along the whole surface of the flake, where they form coordination bonds between Sc atoms and the π -system of the carbon network. When the flake starts to form a fullerene cage, Sc atoms continue their motions along the flake’s surface and can be trapped directly by the

rapidly forming cage (Fig. 6.8c, 63–66 ps). In other cases, Sc atom(s) is pushed towards the edge of the forming cage, but does not leave the carbon cluster because of the sufficiently strong Sc–C σ -bonding. Continued oscillation between the edges of the orifice and the middle of the forming cage eventually lead to encapsulation (Fig. 6.9a,b).

Networked Sc-fullerenes. In two He-free trajectories we also observed another mechanism of Sc integration into the carbon cage. Bonding of Sc to the edge of the flake during its closure to the cage resulted in the formation of the networked fullerenes with metal atoms replacing the carbon atom in the fullerene cage. In one trajectory such state survived several picoseconds and then the Sc atom was encapsulated within the cage, but in the second trajectory (Fig. 6.5) such a state survived for longer than 140 ps.

Since networked Sc was not found in simulation with He, we proposed that such state can be stable only in He free conditions. To verify it, we took used coordinates and velocities of carbon and Sc atoms from Fig. 6.5g and added 100 He atoms to the system (He temperature was also set to 2000 K) and followed 10 independent trajectories. After addition of He, the networked Sc survived for only few picoseconds: in 7 trajectories it was pushed out of the cage, and in three trajectories formed endohedral fullerenes. Thus, we conclude that stabilization of “networked” Sc fullerenes can take place only without He, and hence can hardly take place in real experimental conditions.

Importantly, all MD simulation discussed above were performed in the original DFTB formalism¹³⁴ (also known as NCC-DFTB). The second generation of the DFTB method included self-consistent charge correction¹⁰⁹ (SCC-DFTB) and was expected to be more applicable for the problems with inhomogeneous charge distribution such as EMF formation. However, attempts to apply SCC-DFTB for the Sc-EMF formation always resulted in networked Sc-fullerenes which were then stable infinitely long (> 2 ns). Formation of endohedral fullerene with SCC-DFTB approach was not observed at all; instead, He atoms were often encapsulated with the fullerene cages. To clarify if NCC- or SCC-DFTB are more reliable for this system, we performed *ab initio* (DFT) MD simulation. In agreement with NCC-DFTB results, DFT-based MD simulations showed that networked Sc-fullerene are not very stable and encapsulation proceeded within one picosecond. Thus, we propose that available SCC-DFTB potentials for Sc-C interactions overestimate stability of multiply Sc-C bonded Sc atoms and hence are not applicable for MD simulations of the EMF formation (at least, without re-parameterization).

Defects in formed cages. The fullerene cages formed in our MD studies within 200-400 ps had a number of defects, as can be seen in Fig. 6.7. The most common defects are heptagons (so far, only one EMF structure is known to have heptagon,²³¹ whereas all other structurally characterized EMFs consist of pentagons and hexagons) and carbene-type carbon atoms (i.e. carbon bonded to two other carbon atoms instead of three). The presence of carbene carbons results in the odd number of carbon atoms in some EMF cages. Finally, the number of pentagon adjacencies is also rather large. Thus, the procedure developed in this work does not produce defect-free fullerene cages. Annealing at 2000 K is not also efficient for rearrangement, at least for heptagons. We conclude that the use of nose-Hoover thermostat during annealing is not efficient since rearrangement in the carbon framework (such as Stone-Wales transformation) requires local increase of kinetic energy, which is prevented by the thermostat. Since this work has no aim at the obtaining of defect-free carbon cages but is rather focused on the overall mechanism of the EMF formation and metal encapsulation, we did pursue the question of the cage annealing further and leave it for future works.

6.3.3 Effect of reactive gas during Sc based EMFs formation

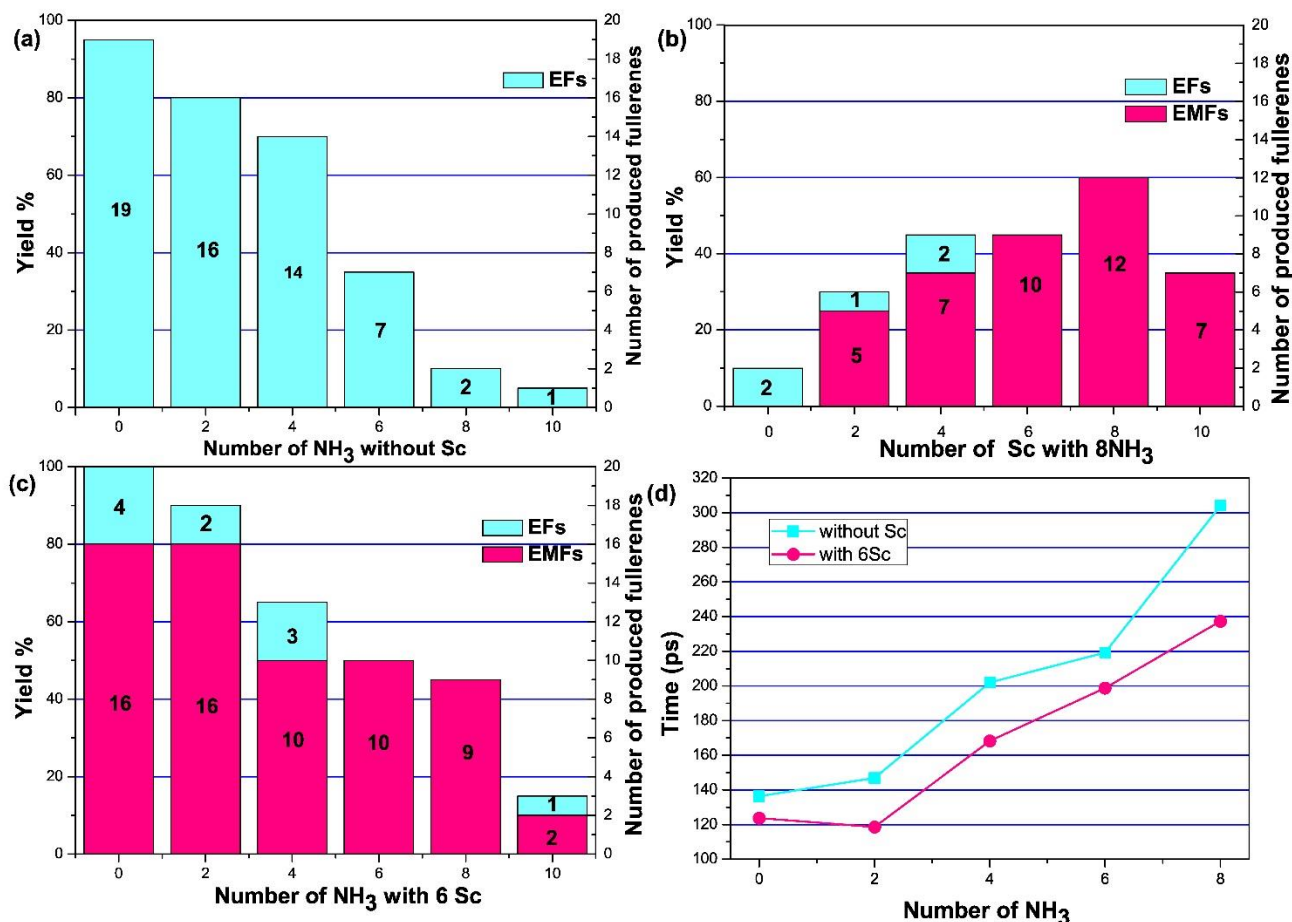


Figure 6.10 (a) Yields of empty fullerenes (EFs) as function of different number of NH_3 in absence of Sc atoms. (b) Yields of EFs and Sc based EMFs as function of different number of Sc with 8NH_3 . (c) Yields of EFs and Sc based EMFs as function of different number of NH_3 with 6Sc. (d) Average time of successful fullerene formation based on the systems of (a) and (c). EFs and EMFs are colored in light cyan and pink respectively.

Different ratio of NH_3 (0, 2, 4, 6, 8, 10) with 50 C_2 units and 40 He atoms are applied into $50 \times 50 \times 50 \text{ nm}^3$ PBC cubic box to understand the correlation between yield of empty fullerenes (EFs) and NH_3 gas. Yield of EFs without presence of NH_3 can reach 95% in 20 independent MD simulations as shown in figure 6.10 (a). 19 EFs are produced, and one typical example is as shown in figure 11 (a). We notice that there are few heptagons usually coordinating with pentagon pairs on the carbon wall which has been observed experimentally.²⁵⁶ Formation mechanism of EFs are already studied broadly and well established,^{90,122,257-262} so we skip the

details here. By increasing concentration of NH_3 , the yield of EFs decreased roughly as linear function with slope of -9.93. Only 2 successful EFs are found with more than 6 NH_3 , the other trajectories yield PAHs such as graphene flakes, half fullerene cages with H passivation on edges as main products shown in figure 6.11 (b) and (c). In the absence of NH_3 , only one such flake structure has been found in 20 trajectories. For graphene flake, we can see the edge constituted with zigzag and 5/7 type of edge which is well consistent with TEM studies.²⁶³⁻²⁶⁵ The average formation time by counting the time of cage closure is very sensitive to the reactive gas pressure. When number of NH_3 molecules reached 6, it takes roughly 2 times longer to close the cage than without the reactive gas. Since only few EFs were produced with 8 and 10 NH_3 molecules after 20 attempts within 400 ps (the main products are half cages and open cage structures as show as in figure 6.11 (e)), we can't obtain precise formation time, but with no doubt the time should be much longer than that with low gas pressure. Clearly, H atoms can greatly hinder the formation of EFs, the question is why formation of EMFs is not hindered simultaneously? For the pursuit of the answer, we keep constant pressure by introducing 8 NH_3 and vary the number of Sc atoms. From figure 6.10 (b), we can clearly see that introduction of Sc atoms significantly enhances the yields of EMFs while keeping the yield of EFs low, which agrees with experimental results perfectly. We notice that even with only 2 Sc adding to the system, the yield is increased 6-fold in comparison to the metal-free condition. The maximal number of EMFs can reach more than 10 with 6-8 Sc atoms (molar ratio Sc:C=1:16.7-1:12.5) which is quite close to the molar ratio 1:15 used in experiments, but further increase of the number of Sc atoms to 10 noticeably decreased the yield because Sc is crowding on the carbon cup or form large Sc clusters and makes cage difficult to be closed. From 6.10 (c), the yields of EMFs decrease step by step along with more and more NH_3 introduced with constant 6 Sc. Comparing figure 6.10 (b) and (c), we can find that the amount of H and metal atoms have competition in yields of EFs and EMFs. From the analysis of fullerene formation, we can conclude that it is getting difficult to form nucleation center with the presence of H, but when Sc is introduced, Sc-C nucleation is more easier. Strong Sc-C network are formed with several dangling bonds around Sc at the early stage (less than ca. 50-100ps) which is quite similar with Sc-EMFs formation with He gas (see details in the section of Networked Sc-fullerenes). In contrast to the condition without Sc atoms, some small carbon nucleus terminated by H atoms have been formed first and then self-assemble dependably due to low chemical activity. The relative low ratio of pentagon results in planar PAHs as main production such as graphene flakes.

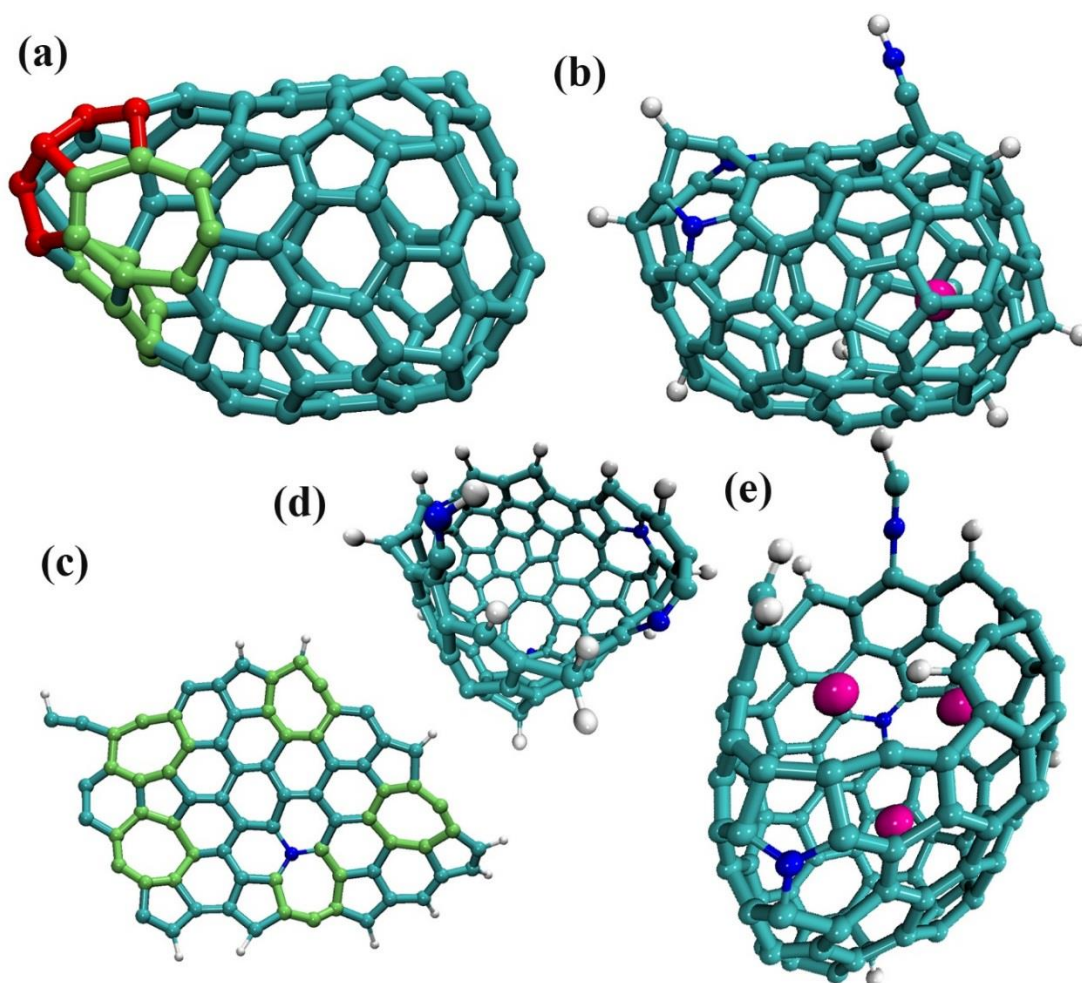


Figure 6.11 (a) and (b) are a typical empty fullerene and a Sc based EMFs. (c) and (d) are graphene flake and half cage as PAHs productions respectively. (e) An open Sc based EMFs after 400 ps. Carbon, nitrogen, hydrogen, scandium atoms are coloured in cyan, blue, white and pink, respectively. Heptagon and pentagon pairs are highlighted in light green and red.

All the sp^2 carbon and rings start to form at nearly the same timing (50 ps), and three lines have very similar behavior as shown as in figure 6.12. Note that by presence of NH_3 and Sc or not both sp^1 and sp^2 carbons exhibit nearly the same time evolution with synchronous behavior, which is different from He-free condition. The majority of the rings formed are pentagons, hexagons, and heptagons, and their number versus time is shown in figure 6.13. We can clearly see that few more pentagons and heptagons have been produced with the same number of hexagons with pure carbon vapor due to high yield of empty cages.

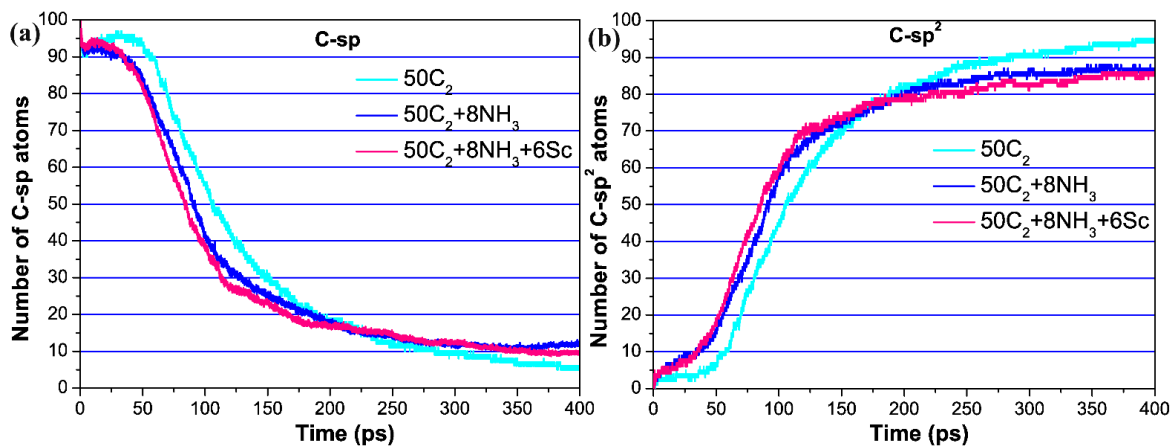


Figure 6.12 Evolution of the average number of (a) C-sp and (b) C-sp² atoms during 20 times MD simulations of the fullerene formation with 50 C₂ (light cyan), 50 C₂/8 NH₃ (blue) and 50 C₂/8 NH₃/6 Sc atoms (pink).

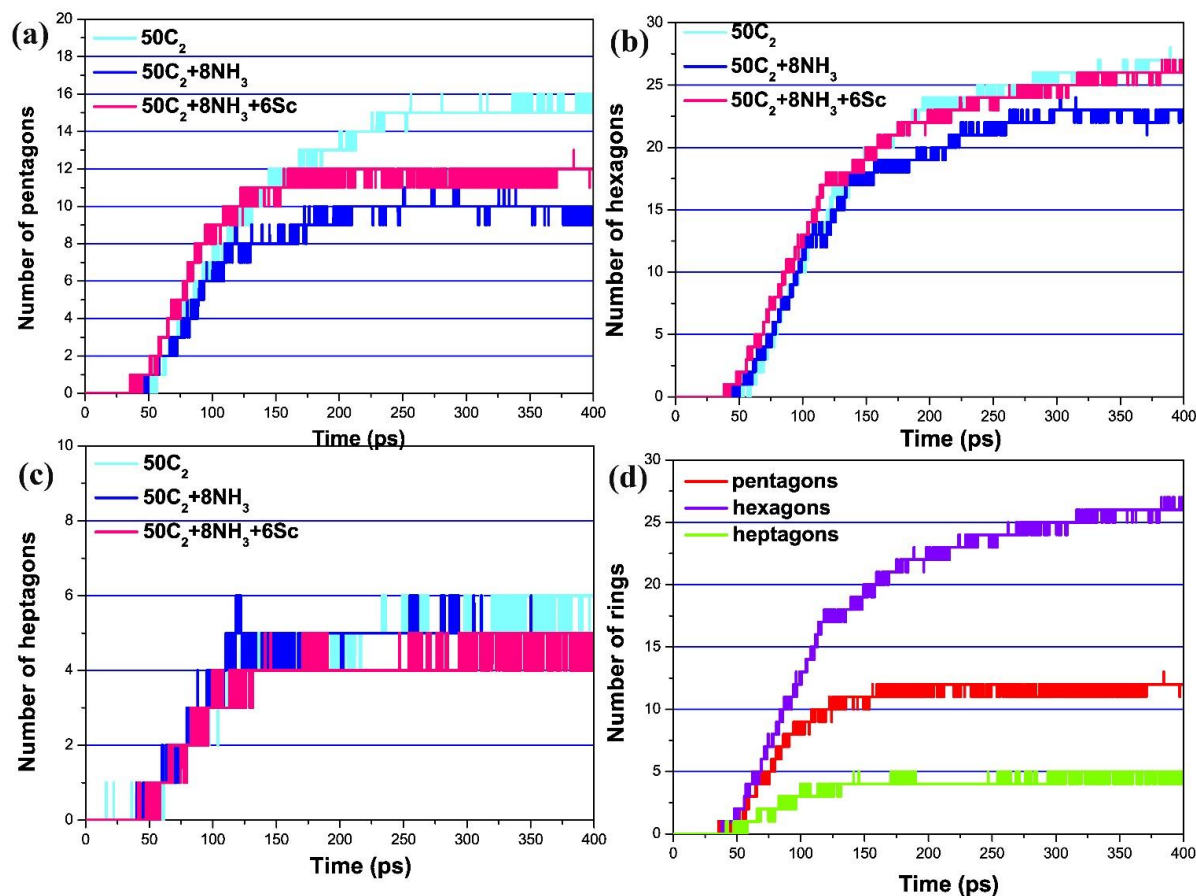


Figure 6.13 Evolution of the average number of (a) pentagons (b) hexagons and (c) heptagons during 20 times MD simulations of the fullerene formation with 50 C₂ (light cyan), 50 C₂/8 NH₃ (blue) and 50 C₂/8 NH₃/6 Sc atoms (pink). (d) Average number of pentagons (red), hexagons (purple), and heptagons (light green) formed in simulation with 50 C₂/8 NH₃/6 Sc atoms.

The cage closure process usually happens at around 100 ps during carbon cage formation stage without reactive gas. Therefore, Sc atoms have been encapsulated during this period leading mainly to mono- and dimetallofullerenes. Although many successful trajectories have been obtained after relatively short propagation time, only once formation of tri-metallofullerene was observed, whereas tetra-metallofullerenes (such as experimentally observed $\text{Sc}_4\text{C}_n@C_{80}$ ($n=1,2,3$)²⁶⁶) have not been detected at all because the cage closed too fast to enable multiple encapsulation. Figure 6.10 (d) clearly shows that the average time of cage formation, 120-140 ps without reactive gas, is prolonged to more than 240 ps in reactive gas atmosphere. Note that the average time is only counting successful trajectories ending in formation of fullerenes, whereas “open” cages are neglected (although they may also form fullerenes on a longer time scale). Therefore, the time is underestimated. To summarize, the key role of NH_3 gas in the EMF formation is that it can prolong the cage closure process which endows more than two metal and non-metal atoms encapsulated inside the fullerene.

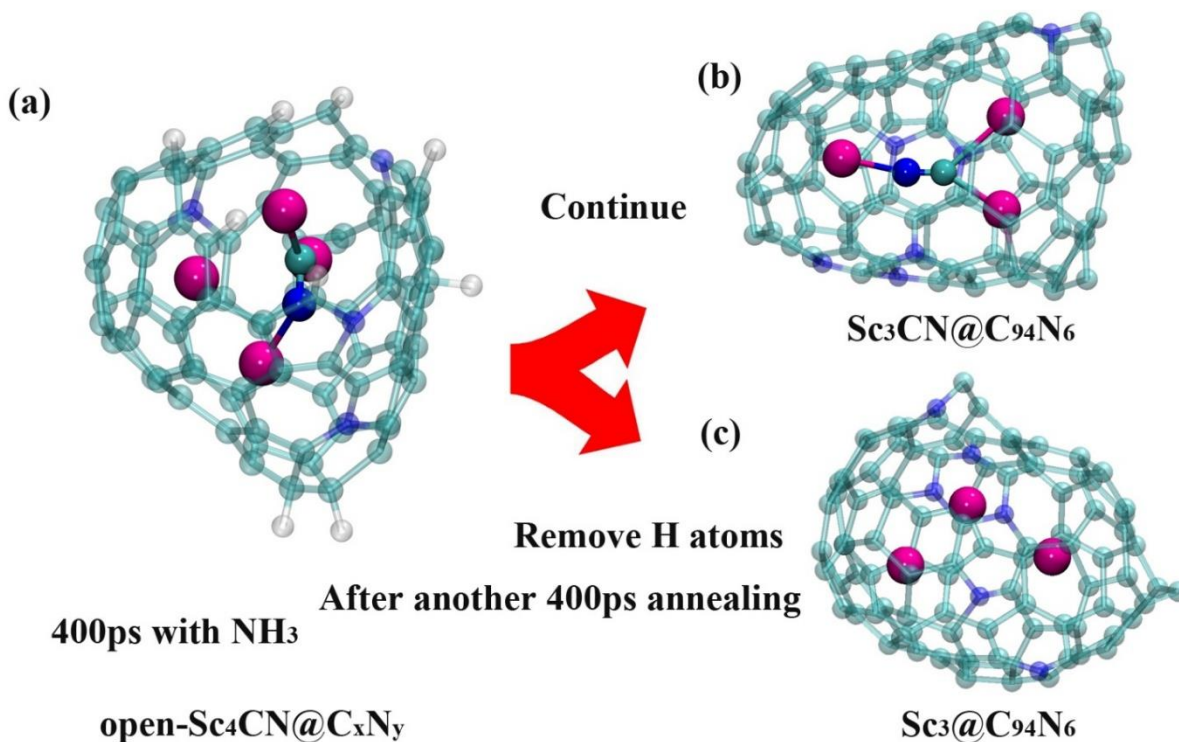


Figure 6.14 (a) is an open cage fullerene coordinating with 4 Sc atoms and CN unit inside. (b) is cyano-clusterfullerene after annealing another 400 ps from (a). (c) is tri-metallofullerene clusterfullerene after annealing another 400 ps from (a) without H. Carbon, nitrogen, hydrogen, scandium atoms are coloured in cyan, blue, white and pink, respectively.

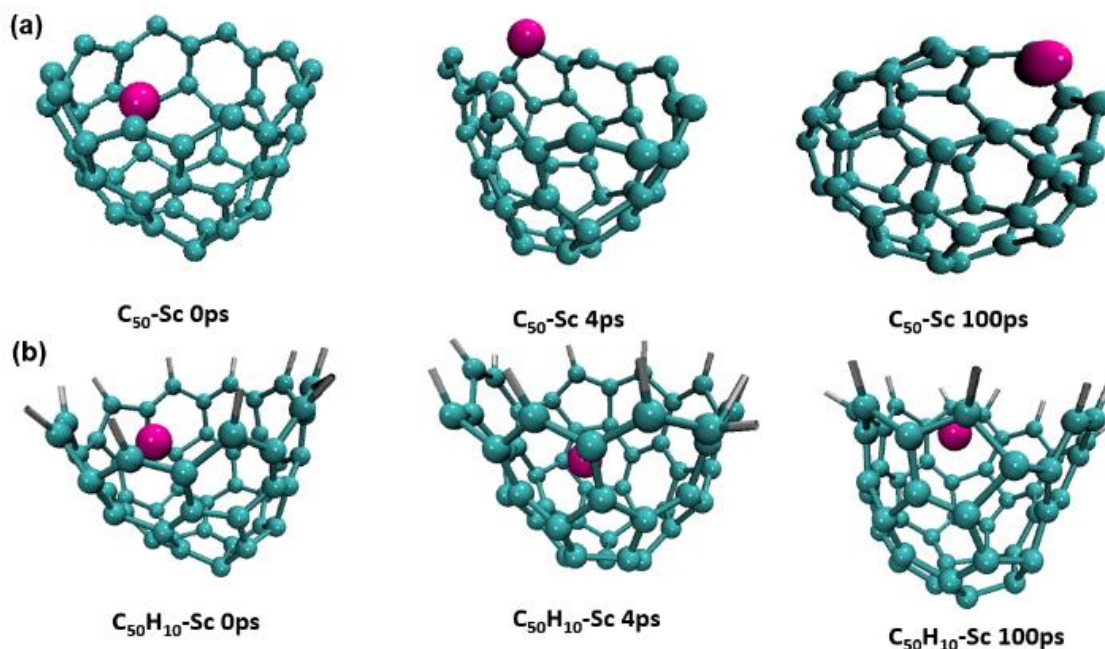


Figure 6.15. Key snapshots of half empty carbon cage (a) and the cage saturated with H atoms (b) coordinating with single Sc atom.

Hydrogen atoms also play another vital role during the fullerene formation, in particular for intracluster encapsulation. From QM/MD simulations, we observe that a half carbon cage saturated by H atoms has been produced along with Sc_3CN as intracluster after 400ps as shown as in figure 6.14 (a). Four Sc atoms coordinating with CN unit have been encaged into the carbon cup (half-closed cage) with H atoms terminating the free valencies at the edge. After another 400ps of annealing process, one Sc atom left the cage resulting in three Sc atoms surrounding the CN unit in the endohedral cluster (see Fig. 6.14 (b)). In the separate model trajectory, we removed all hydrogen atoms from the structure shown in Fig. 6.14(a) and proceeded further with simulations. In these conditions, the CN unit left the cage immediately yielding the trimetallofullerene shown in Figure 6.14 (c). In order to address the role more clearly and exclude other factors, we employed a simple model as shown as in Fig. 6.15: a carbon “cup” was either left with free valencies at the edge (Fig. 6.15(a)) or the edge was saturated with H atoms. Then Sc atom was introduced into the system and MD simulations were followed. In H-free system, Sc tends to stay at the edge with 96% fraction of time due to the strong Sc-C σ bonding. Without additional carbon source, the “cup” appeared to be too small to form a closed cage leaving Sc at the edge all the time. On the contrast, when those dangling bonds were terminated by H, Sc

prefers to stay in the middle of carbon cup most of the time (99% of time), which endows the possibility for a further cluster formation via encapsulation of other Sc atoms.

For another reactive gas CH_4 , we found a very similar behavior during the fullerenes formation as for NH_3 if same ratio of hydrogen-to-carbon is applied. Therefore, here we skip the details and directly go to the results. We can avoid aza-fullerenes with N atoms embedded into the carbon cage by using CH_4 . Hundred independent trajectories yielded about 20% carbide metallofullerenes, 10% methano-clusterfullerenes and 70% metallofullerenes.

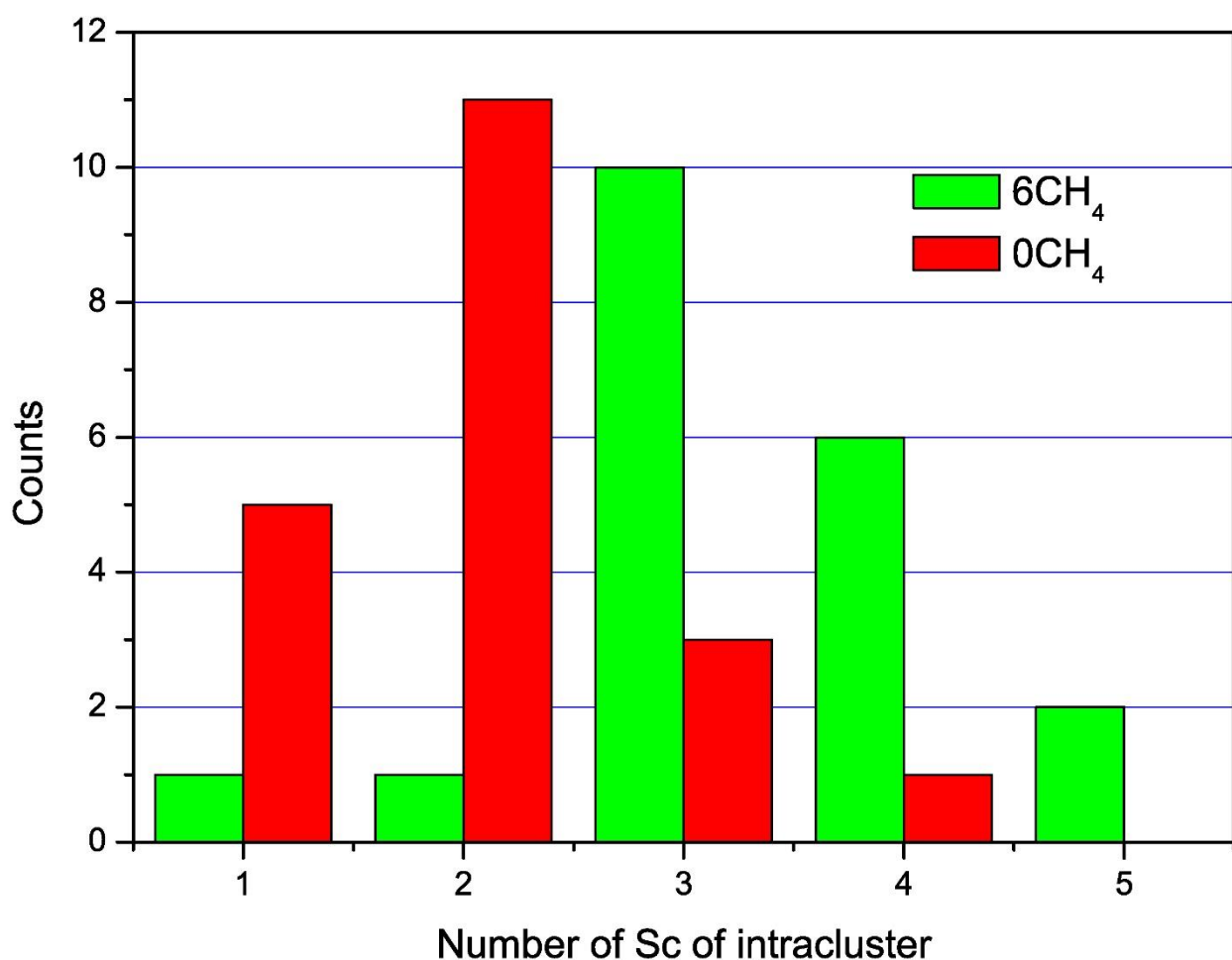


Figure 6.16 The number of intracluster Sc atoms in the endohedral fullerenes formed after 400 ps in the system containing 100 C, 15 Sc/40 He/6 CH₄ (green bars) or without CH₄ (red bars). 20 trajectories were studied for each system. Due to very long formation time with CH₄ gas, Sc atoms encapsulated by half-cages were also counted.

According to the discussion *vide supra*, we can conclude that hydrogen-containing reactive gas is important for complex clusterfullerene formation based on three reasons. Firstly, H atom suppress empty cages production, while metal atoms catalyze EMF formation resulting in high yield of EMF. Secondly, H atoms lag the cage closure and then endow the possibility of larger cluster encaged. Thirdly, H atoms saturate the dangling bonds at the edge and benefit to the generated complex cluster locating inside the cage cup rather than on the edge. In order to further illustrate these factors, we performed another 20 QM/MD simulations with 100 C, 40 He, and 15 Sc atoms with or without the presence of 4 molecules of CH₄. The aim was to reveal whether more complex endohedral clusters can be formed with reactive gas when a lot of Sc atoms are available. Figure 6.16 clearly shows that in the presence of CH₄, the main products are tri- (10/20) and tetra-metallofullerenes (6/20). In the absence of methane, mono- (5/20) and dimetallo-Sc-fullerenes (11/20) are formed preferentially in spite of rather large amount of Sc atoms in the system. These simulations clearly show that the presence of hydrogen-containing reactive gas dramatically influences the process of EMF formation by facilitating encapsulation of a larger number of metal atoms and hence affording higher yields of EMF with complex multiatomic endohedral clusters.

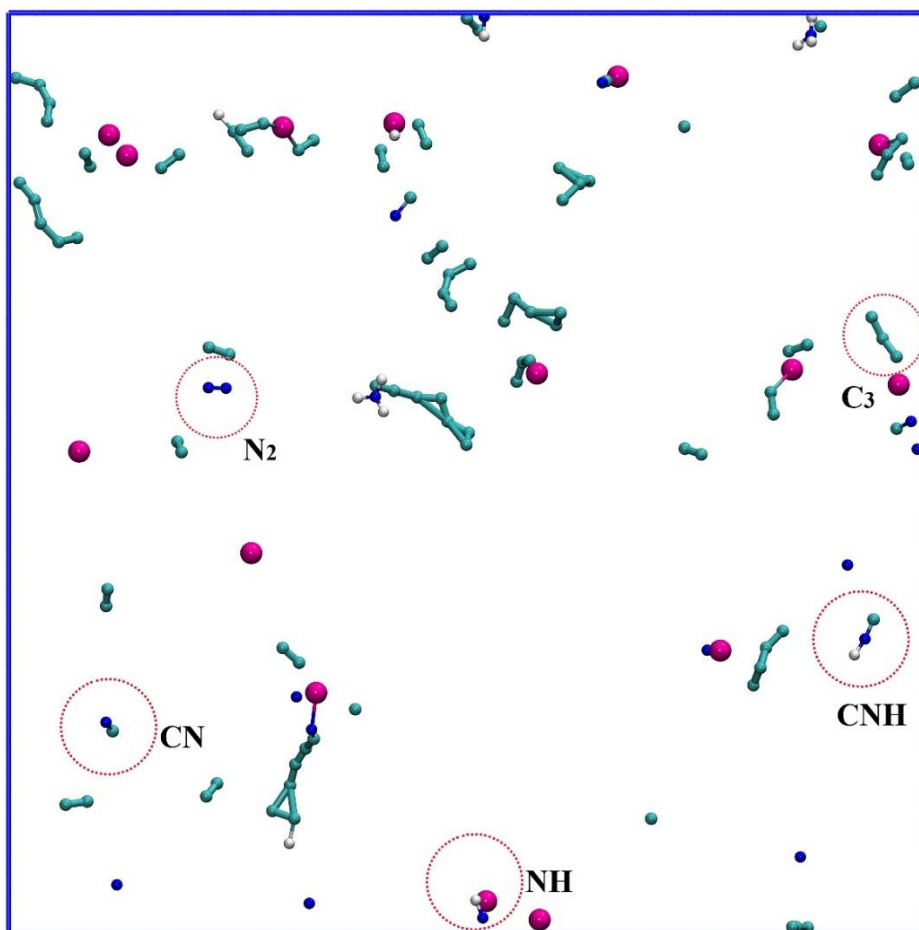


Figure 6.17 Key typical snapshot of EMF formation at early stage (5ps) with 50 C_2 (cyan), 40 He (not shown), 4 NH_3 gas and 10 N (blue for N and white for H) and 10 Sc (pink).

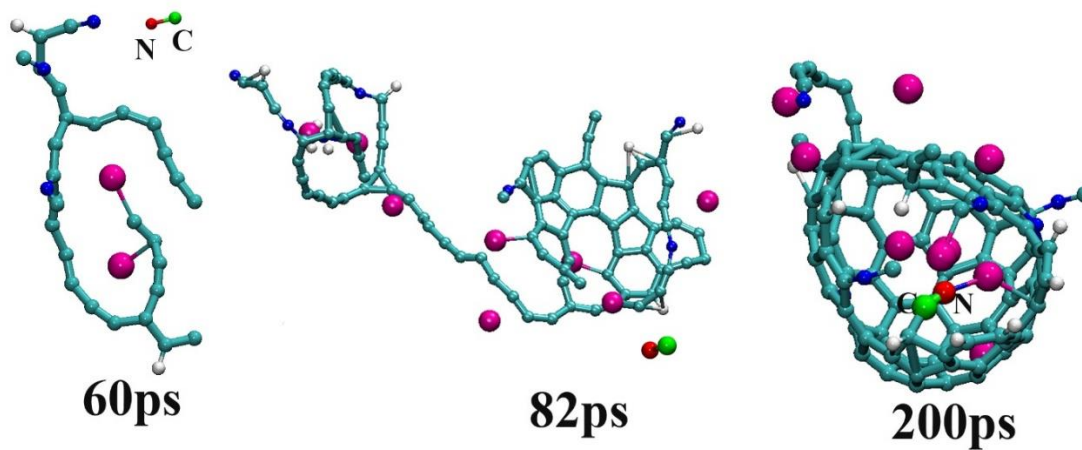


Figure 6.18 Key snapshots of cyano-clusterfullerene formation. CN at 200 ps unit is highlighted in red-green ball-stick.

Sc-EMF formation with complex intracluster

Our simulations showed successful formation of EMFs with complex intraclusters such as carbide-clusterfullerenes $\text{Sc}_4\text{C}_2@C_n$, $\text{Sc}_3\text{C}_2@C_n$, $\text{Sc}_2\text{C}_2@C_n$, cyano-clusterfullerenes $\text{Sc}_3\text{CN}@C_n\text{N}_m$, methano-clusterfullerene $\text{Sc}_3\text{C}_3\text{H}_6@C_n$ and so forth. One intriguing question is where the intracluster comes from and how it is trapped inside the cage. As shown as in figure 6.17, at the beginning, C_2 and NH_3 units decompose and recombine with atomic N source into different types of small units such as C_3 , CN , N_2 , C_2H . Note that we can find several CN units in the trajectories when 10 additional N atoms were introduced to enhance the yield of cyano clusterfullerene, but without those 10 N, we still found such CN units formed during “decomposition” of NH_3 , albeit with low yield. Experiments also suggest CN units can be detected in plasma with carbon vapor and nitrogen source²⁶⁷ which is consistent with our results. The early stage of such EMF formation is almost the same as we discuss above, some polyene chains are firstly self-assembly coordinating Sc atoms as central points, and then they combined to a carbon network with few H atoms saturating the dangling bonds at the edge. Some N atoms merge into the carbon wall or form CN “antenna” highlighted in red-green rod following the merge of two small carbon network as shown as in figure 6.18. CN units have very strong carbon-nitrogen bond, which preserves its entity when internal Sc atoms with CN unit at the edge being encapsulated along with C-C bond breaking. We notice that the Sc_4CN cluster can remain in the carbon cup for sufficient time until the cage closure is accomplished as shown in figure 6.14 (a) and (b). Another possible mechanism of such internal cluster formation is that Sc atoms inside the cage can capture free CN unit because of strong binding strength. Then such fullerene undergoes the same ways as we mentioned above. For carbide clusterfullerenes, carbide unit (C_2) coordinates with Sc atoms in the same ways as cyano unit does.

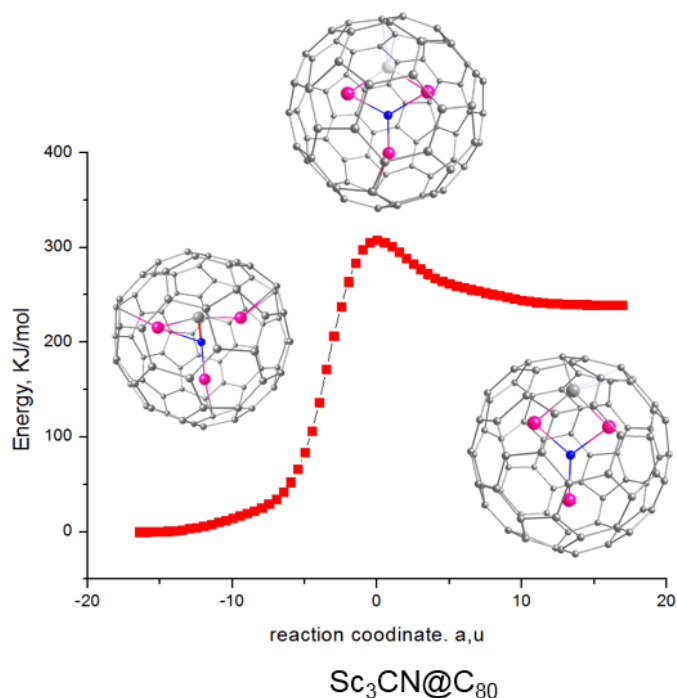


Figure 6.19 Reaction path from $\text{Sc}_3\text{CN}@C_{80}$ to $\text{Sc}_3\text{N}@C_{80}+\text{C}$ by GGA/DFT. Carbon, Sc and N are coloured in grey, pink and blue, respectively.

The possible mechanisms of nitride metallofullerenes formation

Over 200 successful trajectories of EMF formation, including mono-, di-, tri-metallofullerenes, carbide-, cyano-, methano-clusterfullerenes, aza-fullerenes have been obtained, but we did not observe any nitride clusterfullerenes during the whole formation processes. Atomic nitrogen is very active leading to fast formation of chemical bonds with carbon atoms instead of binding to Sc present in the system in relatively low abundance. Therefore, formation of the isolated Sc_3N cluster followed by its encapsulation within the cage is nearly impossible. At the same time, we observed formation of CN units by abstraction of hydrogen from NH_3 , and the resulting CN units readily coordinate to 3 Sc atoms producing cyano-clusterfullerenes. The difference between this kind of fullerenes and trimetallic nitride fullerene is the superfluous carbon atom. We hypothesized that nitride clusterfullerenes can be formed via detachment of the carbon atom from the CN unit in the Sc_3NC cluster. To verify the possibility of such process, we calculate the reactive path of the carbon detachment in conventional $\text{Sc}_3\text{CN}@C_{80}-I_h$ (Fig. 6.19). For the reaction leading from the Sc_3NC cluster to the Sc_3N cluster and one C-atom attaching the cage, the barrier height is ca. 330 kJ/mol, and the reaction energy is 250 kJ/mol. High reaction energy in this case may be caused by a formation

of defected “C₈₁” cage from the highly stable C₈₀-I_h cage, and hence the process can be more energetically favored when CN unit is broken inside the defected cage. However, the high reaction barrier is presumably caused by the strong C-N bonding and hence can be hardly reduced by variation of the carbon cage. Therefore, it is nearly impossible to directly observe CN bond breaking at 2000 K during QM/MD simulations due to the high bond-breaking barrier. However, directly increasing thermal fluctuation by setting higher temperature leads to a carbon cage breaking. Previous studies also suggest that temperatures higher than 3000 K result in C-C bond breaking. However, it should be noted that at least two processes with much higher barrier energies, the helium atom insertion into C₆₀ (ca. 940 kJ/mol) and Stone-Wales transformation in fullerenes (ca. 600-680 kJ/mol), take place in experimental conditions. Therefore, the CN bond breaking is also possible to occur following nitride fullerene formation. Further studies may require longer propagation times and application of the different type(s) of thermostats, which however goes beyond the scope of this work.

6.3.4 Iron and Titanium metallofullerenes

Iron/carbon system. To verify the validity of our computational approach for the EMF formation, we have performed MD simulations for two other metals, Ti and Fe, using an 80×80×80 Å³ box, 200 carbons, 100 He atoms, and 6 metal atoms analogously to Sc runs. Under these conditions we did not observe formation of Fe-encapsulated fullerenes. All ten trajectories resulted in formation of empty cages. Behavior of Fe atoms during the fullerene formation was similar to that of Sc, i.e. Fe atoms also tended to form Fe-C bonds. However, these bonds are considerably weaker than the Sc-C bonds, which leads to a shorter Fe-C bond lifetime. This effect can be clearly seen in Figure 6.6: the lifetime distribution for metal-carbon bonds in the Fe/100 He system is shifted to shorter lifetimes when compared to the Sc/100 He system and is similar to the Sc-C distribution in the system with 200 He atoms. This result points to an important role played by the metal-carbon bonding in the endohedral fullerene formation. Perfect agreement with experimental data which did not show Fe-EMFs either in arc-discharge or in laser-ablation experiments.

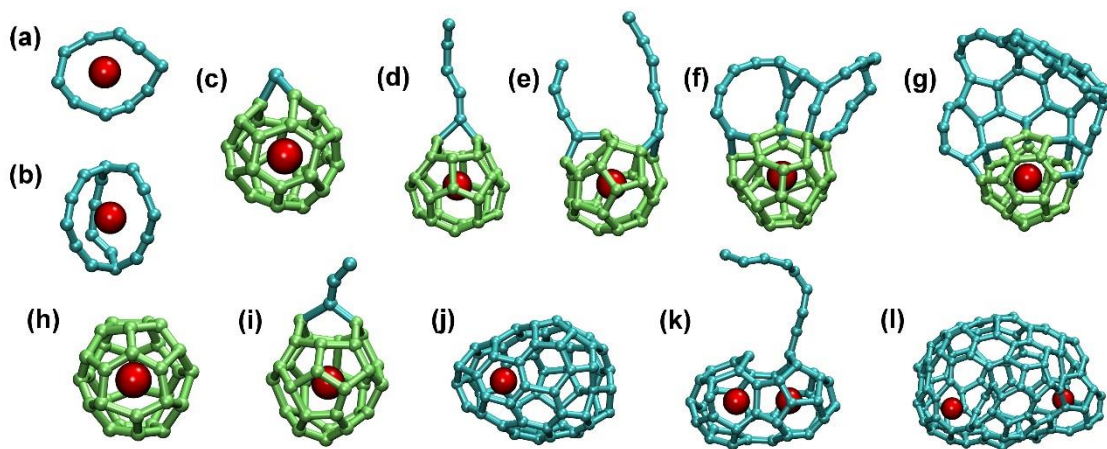


Figure 6.20 Stable Ti-C_n clusters and EMFs formed in MD simulations: (a) Ti-C_{10} ring; (b) Ti@C_{16} proto-cage; (c-g) structures with common Ti@C_{28-T_d} motif with additional (c) carbon atom, (d) carbon chain, (e) two chains, (f) fused rings, and (g) fused “flake”; (h) defect-free $\text{Ti@C}_{30-C_{2v}(3)}$; (i) $\text{Ti@C}_{30-C_{2v}(3)}$ with an additional C_3 chain; (j) Ti@C_{66} ; (k) small-cage di-Ti EMF with an additional carbon chain C_9 ; (l) large-cage di-Ti EMF. In (c-i) fragments of regular Ti@C_{28} or Ti@C_{30} cages are shown in light green, all other carbon are shown in cyan color, Ti atoms are dark red.

Formation of Ti-EMFs. The importance of the strength of the metal-carbon bonding is further corroborated in the study of the Ti-C system. At the level of our DFTB simulations the Ti-C bonds appear to be much stronger than the Sc-C bonds, as can be clearly seen in the lifetime distribution histogram (Fig. 6.6). Ti atoms were coordinated to the carbon clusters at the early stages of their growth and, due to the strong Ti-C bonds, such agglomerates could not be broken by collision with He atoms. Furthermore, unlike almost innocent Sc atoms, Ti atoms played a role of “assembly points” for the fullerene cages, thus dramatically affecting the fullerene growth. Figure 6.20 shows some intermediate Ti-carbon cluster detected at different stages of the trajectories. For instance, quite stable were carbon rings with Ti atoms in the middle (for Sc, such rings were also observed, but they did not survive for a long time). Thus, Ti atoms templated formation of small carbon cages round them. Quite a typical motif is Ti@C_{28-T_d} , the endohedral fullerene which efficiently formed in laser-ablation experiments.^{268,269} We observed formation Ti@C_{28} in several trajectories, but usually this cage had some defect, such as single carbene-type atom inserted into the C-C bond, or a longer chain bonded to the cage, or a larger carbon flake fused to Ti@C_{28} (Fig. 6.20c-g). The small cages could then grow via absorption of carbon fragments or fuse together forming di- and even tri-metallofullerenes. At the end, almost all Ti atoms formed EMFs, either small-to-medium size monometallofullerenes, or di- to tri-

metallofullerenes with larger cage sizes (each trajectory produced 3–4 Ti-EMFs, whereas empty cages were not formed). Typical examples of larger cages and agglomerates are shown in Fig. 6.20j-1.

To analyze how the system may develop under smaller T/C ratio, the simulations were performed with only one Ti atom per 200 C atoms in the same box size. Ti-EMFs were not obtained only in two trajectories from ten: both afforded only empty fullerenes and Ti atom coordinated to a small carbon cluster (a ring or a chain). Among eight Ti-EMFs formed in successful trajectories, two had $\text{Ti}@C_{28}\text{-}T_d$ structure with attached chains, and one was $\text{Ti}@C_{30}\text{-}C_{2v}(3)$, also with an additional chain fragment. Medium to large size $\text{Ti}@C_{2n}$ EMFs were obtained in other runs; importantly, these EMFs also had smaller Ti-EMFs as their precursors. Thus, even in the presence of a large excess of carbon, Ti is still prone to form small fullerenes, whose kinetic stability then depends on the regularity of the cage structure. $\text{Ti}@C_{28}$ and $\text{Ti}@C_{30}$ EMFs are rather stable, whereas intermediate structures with large number of defects are more eager to capture additional carbon fragments and grow further.

Formation mechanism of $\text{Ti}@C_{30}\text{-}C_{2v}(3)$. Due to the smaller cage size, Ti-EMF cages produced in MD simulations have smaller number of defects than Sc-EMFs. For instance, heptagons are rare for Ti-EMFs in our simulations, whereas they are quite common for Sc-EMF and empty fullerenes obtained in this work (Fig. 6.7). As already mentioned, $\text{Ti}@C_{28}\text{-}T_d$ motif is quite persistent and was formed in at least 5 from 20 trajectories. In one trajectory we also observed the formation of the defect-free $\text{Ti}@C_{30}$ EMF with $C_{2v}(3)$ cage isomer (Fig. 6.20h), which is also believed to be formed in the laser-ablation studies of Ti/graphite system.²⁶⁸⁻²⁷⁰

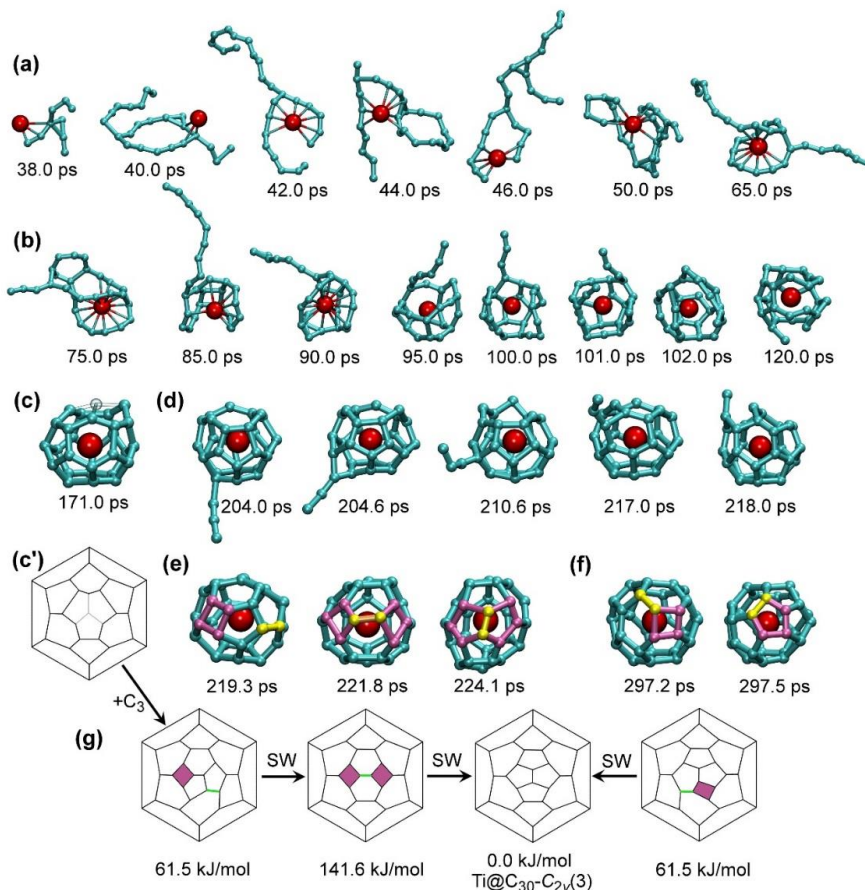


Figure 6.21 Mechanism of the $\text{Ti@C}_{30}\text{-C}_{2v}(3)$ formation in MD simulations. (a) formation of the Ti-C_9 cluster and its growth to Ti-C_{27} ; (b) condensation of long chains into the fullerene cage surrounding Ti atom; (c, c') molecular structure and Schlegel diagram of Ti@C_{27} resembling $\text{Ti@C}_{28}\text{-}T_d(1)$ with one atom missing (position of the missing atom is shown as a “ghost” atom in (c) and is indicated with pale lines in (c')); (d) attachment of the C_3 chain to Ti@C_{27} and its migration along the fullerene surface to the orifice with subsequent ingestion; (e) Ti@C_{30} isomer with four-membered ring, its SW transformation into the structure with two four-membered ring, and formation of $\text{Ti@C}_{30}\text{-C}_{2v}(3)$ after the next SW transformation; (f) formation of $\text{Ti@C}_{30}\text{-C}_{2v}(3)$ from the isomer with one four-membered ring in a direct SW transformation; (g) Schlegel diagrams describing stages (e) and (f), relative energies are for PBE/TZ2P-optimized structures. The Ti–C distances shorter than 2.8 \AA are denoted as bonds for the structures formed before 90 ps; at later stages these bonds are omitted for the sake of clarity. In (e) and (f), square rings are highlighted in purple, and the bonds to undergo a SW transformation are highlighted in yellow (or green in Schlegel diagrams); in (e) and (f) this coloring is preserved in $\text{Ti@C}_{30}\text{-C}_{2v}(3)$ to highlight its genetic relationships to the structures with square rings.

The growth of $\text{Ti@C}_{30}\text{-C}_{2v}(3)$ from the carbon vapor in MD simulations is depicted in figure 6.21. The process started with coordination of Ti atom to a branched C_9 fragment at 38 ps (Fig. 6.21a). Over the next few picoseconds, the cluster grew further by absorbing addition carbon chains from the vapor. The cluster composition at this stage is rather labile, and carbon atoms can be equally likely absorbed and ejected. Thus, the number of carbon atoms in the cluster was 9 at 38 ps, 23 at 40 ps, 25 at 42 ps, then two carbon were lost at 46 ps, the cluster grew again to C_{25} at 48 ps, lost 4 carbons at 55 ps, then gained C_2 at 65 ps, and finally stabilized its size at C_{27} after 75 ps. All the way from 38 to 75 ps the cluster can be described as a very labile conglomerate of branched medium-size chains, sporadically closing into carbon rings around Ti. After 75 ps, the chains started to condense into smaller rings ($\text{C}_4\text{--C}_6$) forming a proto-cage with Ti atom in the center. Figure 6.21b depicts how the C_9 chain attached to the growing carbon cage is gradually “eaten” by the growing cage over the period of ca 30 ps, till it is completely transformed to the cage-like structure after 100 ps. At this moment, although the small fullerene cage is already distinguishable, carbons still move with large amplitudes, which often results in breaking of CC bonds. E.g., a small fullerene structure is first observed at 120 ps, but complete stabilization is achieved tens picoseconds later. Fig. 6.21c shows the Ti@C_{27} cage formed as a result of this process (see also its Schlegel diagram at Fig. 6.21c’). The structure is closely resembling the $\text{Ti@C}_{28}\text{-}T_d$ EMF missing one carbon at the triple-pentagon junction, so that the cage has a large orifice. Due to its high kinetic stability, the Ti@C_{27} remained almost intact over the next 30 ps, till it absorbed a C_3 fragment at 204 ps (Fig. 6.21d; note that at this moment only few free carbon fragments are left, and hence such collisions are much rarer than during the first 70 picoseconds). Although initially attached to the site opposite to the “missing” carbon atom, the C_3 chain then quickly (within few ps) migrated closer to the orifice, where it was ingested into the fullerene cage producing the Ti@C_{30} fullerene (Fig. 6.21e). Note that the mechanism of C_3 capture shown in Fig. 6.21d is similar to the results of DFT and MD simulations for C_2 addition to small Ti@C_{2n} cages reported recently by Poblet et al.²⁶⁸ The cage isomer formed at 219.3 ps had a defect, a four-membered ring. Quite rapidly, within next 2.5 ps, this isomer underwent a Stone-Wales (SW) transformation (pseudo-rotation of one C–C bond by ca 90°) to form the second four-membered ring at 221.8 ps. Finally, within the next 2.3 ps, another Stone-Wales transformation took place producing the defect-free $\text{Ti@C}_{30}\text{-C}_{2v}(3)$ a 224.1 ps (Fig. 6.21e). Although the $\text{C}_{2v}(3)$ isomer is the most thermodynamically stable form of Ti@C_{30} , the newly-formed cage was still rather labile and transformed into the structure with defects from

time to time. At 297.2 ps we again observed formation of the Ti@C_{30} isomer with a four-membered ring. This isomer again produced $\text{Ti@C}_{30}\text{-C}_{2v}(3)$, but this time in a single SW step as depicted in Fig. 6.21f. For the sake of clarity, Figure 6.21g also shows Schlegel diagrams of Ti@C_{30} isomers and their transformations observed in MD simulations.

Interestingly, the isomer of Ti@C_{30} with four-membered ring is similar to the $\text{Ti@C}_{28}\text{-}T_d$ cage with an added C_2 unit. When optimized at the PBE/TZ2P level, this isomer is 61.5 kJ/mol less stable than $\text{C}_{2v}(3)$, whereas the isomer with two four-membered rings is 141.6 kJ/mol less stable. Importantly, Ti@C_{30} has two other “classical” isomers (built from pentagons and hexagons), with the relative energies of 80.3 kJ/mol for $\text{C}_{2v}(2)$ and 259.3 kJ/mol for $D_{5h}(1)$ cages. Thus, the structure with one four-membered ring is more stable than the classical isomer $\text{C}_{2v}(2)$. Even more importantly, four-membered rings are less destabilizing defects for small cages, whereas for large cages we observed heptagons as typical defects in MD simulations (Fig. 6.7) and also in experiment.²³¹

6.4 Conclusions

In this work we performed extended molecular dynamics simulations to reveal the mechanism of the endohedral fullerene formation. We found that the presence of the proper amount of He gas has a crucial effect on the empty fullerene formation. Collisions with He reduce the lifetime of the Sc–C bonds and hence decrease the Sc-EMF formation yield. However, moderate He pressure are still preferable for Sc-EMF because of the large increase of the fullerene formation. Moderate amount of reactive gas such as NH_3 and CH_4 can also boost Sc-EMF formation with three or four Sc atoms, which is rarely the case with the absence of reactive gas. The special role of hydrogen in the clusterfullerene formation is revealed in our simulations.

In the Sc-EMF formation mechanism, the special step is encapsulation of Sc atoms. We showed that Sc is bonded to the edges as well as the middle part of the carbon flakes, which eventually curl up to form fullerene cages. As Sc-C bond are rather strong, they do not dissociate during the cage closure, which often leads to the metal encapsulation. In few cases, carbene or cyano also strongly coordinates with internal Sc which directly leads to carbide and cyano-clusterfullerenes

In general, we can conclude that the propensity of a given metal to form EMFs strongly depends on the strength of the metal-carbon bonding. For Ti with strong Ti–C bonds, the stronger bonding resulted in formation of small cages repeating the experimental data on the

dominance of Ti@C₂₈ in laser ablation studies. On the contrary, Fe with weak Fe–C bonding does not form Fe-EMFs at all. Reactive gas has less impact than Sc system due to strong Ti-C bonds, so we can still observe Ti@C₂₈ for many times.

Chapter 7. Free-standing single-atom thick iron membranes suspended in graphene pores

7.1 Introduction

The success and promise of atomically thin carbon, namely, graphene²⁷¹ has triggered enormous enthusiasm for the study of other two-dimensional (2D) materials such as hBN, MoS₂ and MoSe₂^{272,273}. These 2D films are able to be reduced to atomically thin layers while still maintaining mechanical integrity because they are layered structures where the bonding within a layer is covalent while the inter-layer bonding occurs through weak van der Waals interactions thus allowing individual layers to be easily separated. With bulk metals, at first glance, the nature of metallic bonding and their three dimensional structure prohibit them from existing as a mono-atomic layer. The only reports for atomically thin metallic layers, thus far, are hetero-epitaxial structures in which the metal atoms bond with the underlying substrates^{274,275}. On the other hand, because of non-directional metallic bonding and the excellent plasticity of metals, at the nanoscale, one can build few-atom or even single-atom bridges^{276,277}. Many single atomic metallic layers (e.g. Fe, Co, Mn) are attractive due to their inherent magnetic properties. For the case of two-dimensional (2D) Fe monolayers the magnetic moment is expected to be 3.1 μ_B which is markedly higher than its bulk counterpart (2.2 μ_B), and in addition 2D Fe should have a large perpendicular magnetic anisotropy²⁷⁸. Hence, 2D magnets could be promising for magnetic recording media. Most of what is known on 2D magnets is based on theoretical investigations. These studies point to their magnetic properties being highly sensitive to their structure²⁷⁹. Face centered cubic (FCC) Fe and body centered cubic (BCC) Fe ultrathin films have been grown on Cu, W, SiC, MgO and other surfaces²⁷⁹⁻²⁸³. However, these structures interact with the underlying substrate. Free-standing 2D metal films do not suffer from substrate based influences thus preserving coordination and electron

confinement. Experimental and theoretical works have focused on the interactions between graphene and single metal atoms (including Fe atoms)²⁸⁴⁻²⁸⁶ or clusters²⁸⁷. Zhao and *et al.* show that porous graphene under electron beam irradiation can be extended to enable Fe atoms and clusters to entirely seal small perforations in graphene and form a single atomic crystalline Fe layer.

In this chapter, free-standing mono-atomic suspended Fe membranes is firstly demonstrated theoretically. By investigating the energy difference, ΔE , between a suspended Fe monolayer and a nanoparticle using the equivalent number of Fe atoms, one can estimate that the largest stable membrane should be ca. 12 atoms wide or $3 \times 3 \text{ nm}^2$ which is in excellent agreement with the experimental observation. Besides, from DFTB and DFT simulation, the possibility of C embedded into the Fe membrane can be fully excluded which agrees well with electron energy loss spectroscopy (EELS) measurement. First principles calculations confirm greatly enhanced magnetic properties for single atom thick 2D Fe membranes.

7.2 Computational Methods

Spin-unrestricted density functional theory (DFT) computations were carried out through an all-electron method within the generalized gradient approximation with the Perdew-Burke-Ernzerhof (PBE) function as implemented in the DMol³ program package in Materials Studio of Accelrys Inc. The double numerical-polarized basis set that includes all occupied atomic orbitals with a second set of valence atomic orbitals plus polarized d-valence orbitals was used. The real-space global orbital cut-off radius was set as 4.8 Å. The interlayer distance was set to 20 Å, which is large enough to minimize artificial interlayer interactions. Fully relaxed geometries were obtained by optimizing all atomic positions until the energy, maximum force, maximum displacement were less than $2 \times 10^{-5} \text{ Ha}$, 0.005 Ha/Å and 0.005 Å, respectively. The k-points samplings were $3 \times 3 \times 1$ in the Brillouin zone. The same method was used to determine the lattice constants of BCC Fe. After optimization the calculated lattice value was 2.87 Å which is in excellent agreement with the experimental value of 2.87 Å.

7.3 Results and Discussion

Under close inspection pure Fe can be found as small nano-crystals forming on the surface of the graphene, as single atoms or small clusters at the edge of pores in clean graphene or as 2D crystalline membranes suspended across perforations in the graphene.

Typical examples are provided in Figure 7.1. In the case of nano-crystalline structures forming on the surface of the graphene (Fig. 7.1B, C), the measured lattice constants obtained from the Fourier domain from numerous micrographs indicates that they are either body centered cubic (BCC) or hexagonal close packed (HCP) Fe structures. These structures match image simulations of BCC and HCP Fe nano-crystals as for example shown in the insets of Fig. 7.1 B,C in which both the stick and ball models and image simulations are provided. In general, the Fe nano-crystals contain 200 to 1,000 Fe atoms. It is important to note that the EELS studies on Fe membranes show no carbon signal. However, if only a few carbon atoms form in the lattice they might not be within the EELS detection limits. To better explore this possibility we employ DFT calculations to determine the feasibility of C incorporation within a Fe 2D square lattice as illustrated in figure 7.2. In our DFT simulations the following relaxations are allowed; the C atoms can reside either in-plane or out-of-plane, and in addition the Fe atoms are not forced to sit in-plane. The DFT calculations confirm that including a C atom within the square lattice configuration is unstable indicating that carbide phases are unlikely. This is in full agreement of experimental studies, in which despite elongated irradiation periods no carbide phases were ever observed.

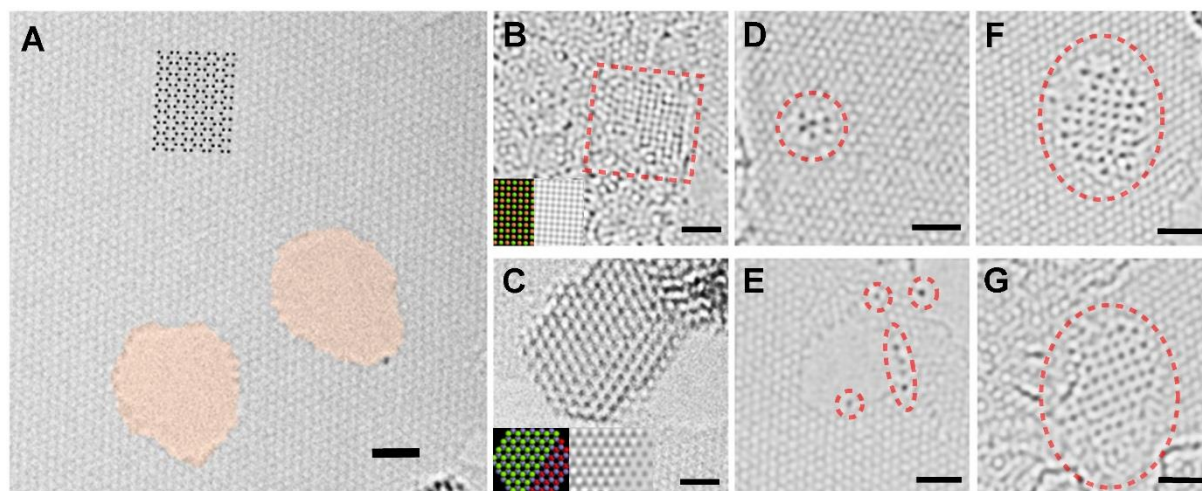


Figure 7.1 Graphene perforations and different Fe clusters. (A) graphene perforations (highlighted). (B) BCC Fe nanocrystal with atomic structure and image simulation as inset. (C) Hexagonal close packed Fe nanocrystal which has a step on it. The atomic structure and an image simulation is provided in the inset. (D) A several atom cluster embedded in graphene. (E) Many individual Fe atoms residing on the edges of graphene. (F, G) Two typical mono-atomic Fe layers suspended in a perforation in graphene. The scale bars is 1 nm. Reproduced from Ref. 127

To investigate the likelihood of carbon absorption on the surface of the 2D Fe membranes, we conducted additional dynamics simulations (DFTB method) using a well-established approach²⁸⁸⁻²⁹⁰. Firstly, we assume that a single carbon atom could be embedded in the 2D Fe monolayer as shown in figure 7.2, and then we assign the C atom (target atom) a kinetic energy T in the structure with a velocity perpendicular to the sheet, which allows its presence in the lattice without immediate reconstruction. We increased T (displacement threshold T_d) until ejection of the atom occurred. The simulation results showed the embedded carbon atom easily breaks away with only 5.9 eV (n.b. the energy transfer by the 80kV electron beam to a carbon atom can reach up to 16 eV). This indicates that C attachment in this form is not stable since irradiating electrons will eject it. Moreover, T_d for carbon attachment in other possible configurations (e.g. single or dimer carbon absorption on the surface) is lower, and hence they are removed with even lower energies.

In the case of individual Fe atoms or few-atom clusters, they tend to get trapped in small vacancies and pores in the graphene and are easily visible due to their high contrast relative to the graphene lattice. Typical examples are provided in Fig. 7.1D (Fe cluster in a pore) and Fig. 7.1E (individual atoms trapped at pore edges). Typically these atoms are mobile around the edges when irradiated with electrons. These observations have been reported by others.²⁸⁴ What is more interesting here is that the ability of larger numbers of Fe atoms to get trapped within a pore and form an ordered 2D crystalline lattice. Examples of such 2D Fe crystalline structures can easily be seen in Fig. 7.1F,G where the high contrast Fe atoms fill a pore with the atoms arranging themselves, for the most part, in an ordered manner. The lattice constant for the observed nano-crystals is $2.65 \pm 0.05 \text{ \AA}$ which is significantly larger than that for the (200) Miller-index plane distance for face centered cubic (FCC) phase or the (110) plane distance for BCC Fe.

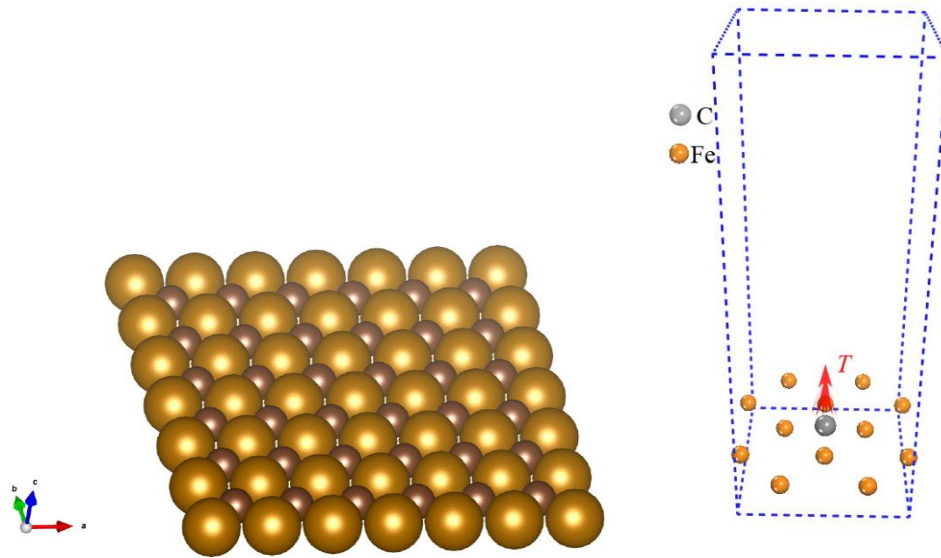


Figure 7.2 Left figure represents a virtual Fe carbide configuration. DFT calculations indicate such a configuration is unstable. Gold atoms (Fe), Brown atoms (C). Right figure is dynamical calculation of a C atom in a 2D Fe membrane under electron beam irradiation. The C atom cannot stay in the lattice as it is easily ejected by the electron beam.

Table 7-1 The calculated energy for different lattice distance 2D Fe membrane

Lattice constant (Å)	Energy difference (eV/Fe atom)
1.87	1.86
1.91	1.42
2.05	0.46
2.12	0.24
2.2	0.07
2.23	0.03
2.28	0
2.3	0
2.33	0
2.4	0.03
2.55	0.18
2.62	0.26
2.69	0.35
2.76	0.45
2.8	0.51
2.83	0.56
2.9	0.67
3.04	0.89
3.11	0.99
3.18	1.10
3.25	1.21

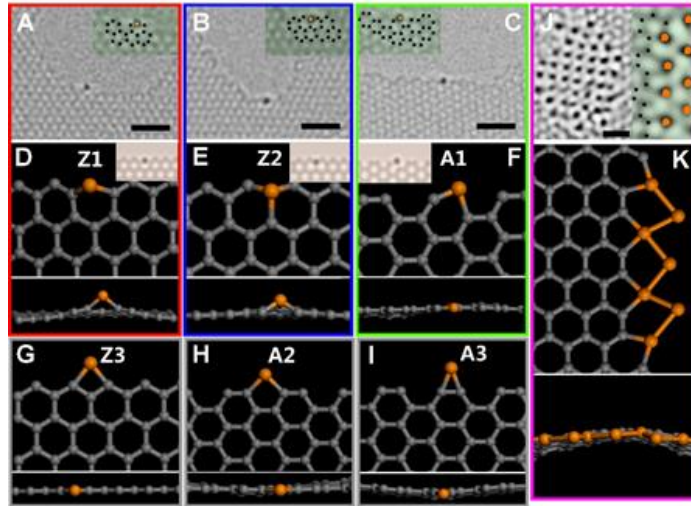


Figure 7.3 The interface between a mono-atomic Fe layer and graphene and local strain mapping (A) LVACTEM image of the Z1 configuration as illustrated in (D). The insets shows the highlighted edge structure with carbon (black) atoms and Fe (orange) atoms highlighted. (B,C) LVACTEM images of the Z2 and A1 configurations (E and F respectively). The insets shows the highlighted edge structure with carbon (black) atoms and Fe (orange) atoms highlighted. The scale bars in (A-C) are 1 nm. (D-I) first principle calculation results showing top and cross-section views of different single Fe atoms binding to different graphene edge configurations. The insets for (D-F) show the corresponding image simulations from the stick and ball structure provided in the main panel. (J, K) The (110) Fe with armchair edge visible in a LVACTEM image and first principle calculated configuration, respectively. The scale bar in (J) is 0.5 nm.

To better comprehend these monolayer Fe structures, density functional calculations based on the generalized gradient approximation (GGA) with the Perdew-Burke-Ernzerhof (PBE) function¹²¹ is conducted. The calculations show the in-plane square lattice of monolayer Fe is energetically favored over the other possible 2D configurations, including tetragonal, hexagonal, etc. The calculations suggest the most stable lattice constant for monolayer Fe is around 2.35 Å, which is smaller than the experimental value of 2.65 ± 0.05 Å, however the calculated energy difference between 2.35 Å and 2.65 Å is not large (0.2 eV/atom) as shown as in Table 7-1. In addition, some physical aspects not considered in the calculations could lead to a larger lattice constant. For example, the effect of spin-orbit coupling and perpendicular magnetic anisotropy in atomically thin films will lead to energy variations. More importantly, strain due to lattice alignment and mismatch between graphene and 2D monolayer Fe cannot be ignored, particularly since the calculations show the in-plane Young's modulus of monolayer iron is ca. 160 GPa, which is an order of magnitude smaller than that of graphene (1TPa). Moreover, the

phonons in monolayer Fe will differ from bulk 3D Fe²⁹¹ since the fraction of anharmonic vibrations increases with the reduction of thin film thickness which leads to a larger thermal expansion. To investigate this, an additional self-consistent lattice dynamics calculation or ab-initio molecular dynamics calculation would be required²⁹².

One can get a sense of local strain effects by first looking at the interface between iron atoms attached to different graphene edges. Two possible binding configurations are possible between Fe atoms and graphene, namely, binding to the basal plane or at an open end or edge. In practice binding at the basal plane is relatively common whilst metallic atom binding at the open edges is rare even though such binding has been theoretically proposed²⁹³. The Fe atoms always bind at open graphene edges, for example at the edges of a pore as shown in Fig. 7.3A-C. Such Fe atom attachments is also studied by using first principle DFT calculations (see binding energy in Table 7-2). Since the most stable edge terminations for graphene are the armchair and zigzag configurations²⁹⁴ six possible configurations for single Fe atoms are considered at armchair or zigzag edges including an arrangement in which Fe atoms replace the first two rows of carbon atoms at an open edge (Fig. 7.3D-I). Despite the bonding energies not being at a minimum in the substitution configuration in which an Fe atom replaces a single carbon atom in a hexagonal ring (configurations Z1, Z2 and A1 in Fig. 7.3D-F, respectively), as compared to configurations Z3, A2 and A3 (Fig. 7.3G-I, respectively), they are favored since upon removal of an Fe atom an incomplete hexagon structure is left which is energetically unfavorable (as compared to zigzag or armchair terminations). Thus, the reaction barrier for the removal of substitution Fe atoms is high. Indeed, this is what experiments present, where for the most part, Fe atoms are imaged as substituting a C atom in a benzene ring at the edge of graphene, as shown in Fig. 7.3A-C. For comparison, image simulations based on the structures used for the first principles calculations are provided as insets in Fig. 7.3D-F.

Although substitution configurations are more stable, the formation of a Fe mono-atomic layer occurs with a continuous placement of Fe atoms along the edges that are not always set in a substitution configuration. For example, linking configurations such as Z3 (Fig. 7.3G) and A2 (Fig. 7.3H) are also found as can be seen in Fig. 7.3J. The linking formation shown in Fig. 7.3I is rarely observed and this is due to its reduced bonding energy. Linking formations are observed in monolayer Fe-graphene junctions as illustrated in Fig. 7.3J and the corresponding calculated structure is also given (Fig. 7.3K).

Another aspect to consider at the Fe membrane-graphene interface is the preferential alignment of Fe atoms. For example, considering the graphene zigzag and armchair edges and the lattice constant for monolayer Fe, the best lattice match is twice the Fe (110) plane distance (1.9 Å) with an armchair edge (2.1 Å). This configuration provides the lowest mismatch strain and interfacial energy and is an alignment configuration in the experiments as can be seen in the diffraction information.

Table 7-2 The calculated binding energy for different configurations of Fe atom and graphene edges

	Free energy/Hartree	Corresponding Pure Graphene structure	Free energy/Hartree	Binding energy/eV
zigzag defect (Z2)	-3973.798838	Pure Carbon corresponding to Z2	-2710.231398	-3.19
armchair edge_Fe1 (A2)	-4013.6411	Carbon(A2)	-2749.990833	-5.45
armchair edge_Fe3 (A1)	-3975.508553	Carbon(A1)	-2711.936265	-3.33
zigzag edge_Fe2 (Z1)	-3973.087813	Carbon(Z1)	-2709.545344	-2.52
zigzag edge_Fe1 (Z3)	-4011.291721	Carbon(Z3)	-2747.629722	-5.77
armchair edge_Fe2 (A3)	-4013.598932	Carbon(A3)	-2750.047052	-2.77
iron atom	-1263.449813			

Now turn to the formation and stability of single-atom thick Fe membranes whilst under electron irradiation. Typically Fe atoms on the surface of the graphene are mobile whilst exposed to electron irradiation. If they encounter a small hole (a few nm wide) the atoms collect and rearrange themselves within it to form a monolayer crystalline Fe membrane. The formation process usually occurs in a matter of seconds. Fig. 7.4A shows a hole in the graphene with a number of Fe atoms perched by an edge. After 3 seconds electron irradiation (1 pA/nm²) the Fe atoms have moved into the hole and arranged themselves neatly in to a crystalline 2D Fe membrane (Fig. 7.4B). Once a suspended Fe membrane has formed in a graphene pore it is relatively stable in that it can sustain

electron irradiation for several minutes after which it starts collapse (Fig. 7.4C-J). Closer examination shows the Fe monolayer edge disconnects firstly from a zigzag edge while Fe (110) membrane-armchair interfaces tend to remain stable for far longer before forming an amorphous particle (see circled regions in Fig. 7.4E and 7.4F). This is in agreement with analysis above in which armchair interfaces are shown to be the most stable configurations.

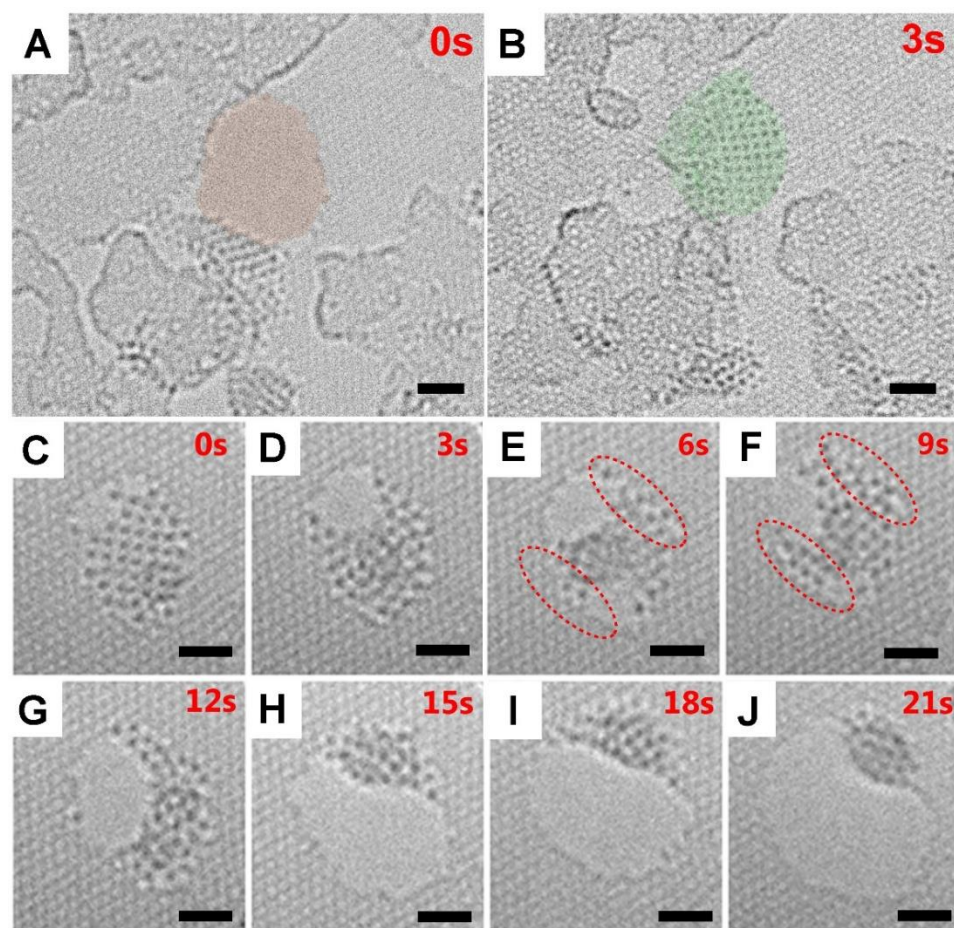


Figure 7.4 Formation and collapse of a suspended single-atom Fe layer under electron irradiation **(A)** A Fe cluster at the edge of a graphene pore (highlighted). **(B)** After three seconds, the Fe atoms move in to the perforation and form a single atom Fe membrane sealing the entire graphene pore. **(C-J)** Continued electron irradiation leads to the collapse of the 2D Fe membrane. The Fe (110) - armchair graphene interfaces are the most stable and are highlighted in (E,F). All scale bars denote 1nm. Reproduced from Ref. 127

The diameter-stability dependence is also studied. By investigating the energy difference, ΔE , between a suspended Fe monolayer and a nanoparticle using the equivalent number of Fe atoms one can estimate the largest stable Fe membrane that can form. The energy difference, ΔE , is given by:

$$\Delta E = E_{\text{Fe-C}} + E_{\text{MLFe}} - E_{\text{Fe}}$$

Where $E_{\text{Fe-C}}$ is the binding energy between the Fe membrane and graphene interface, E_{MLF} is the total energy of the Fe monolayer, and E_{Fe} is the total energy of the Fe nanoparticle including the surface energy. If we consider a $N \times N$ Fe membrane, viz., the width has N atoms. The total amount of N^2 Fe atoms will correspond to one cubic structure (with all facets as BCC (100) surfaces). Therefore we rewrite above equation as

$$\Delta E = N^2 E_{\text{MLFe}} + 4N E_{\text{Fe-C}} - N^2 E_{\text{Fe}} - 6N^{4/3} \Omega^{2/3} E_s$$

Note, here E_{Fe} is the bulk BCC Fe energy excluding surface energy, while the last term includes the six surfaces for a cubic nanoparticle. Substituting in all the calculated energies, and assuming the interface energy $E_{\text{Fe-C}}$ is the average energy of the different configurations we have;

$$\Delta E = (-2.7\text{eV})N^2 + (-3\text{eV})4N - (-4.8\text{eV})N^2 - (1\text{eV})6N^{4/3}$$

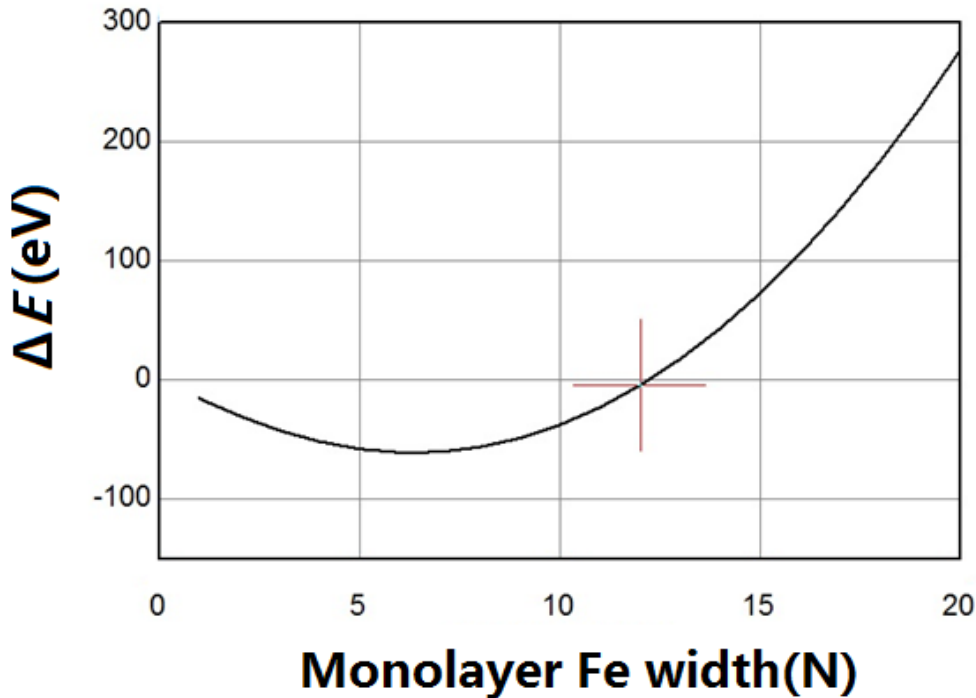


Figure 7.5 The energy difference between a 2D Fe membrane and a 3D Fe nanoparticle. The crossover where a nanoparticle becomes more favorable than a 2D membrane occurs around a membrane width comprised 12 atoms.

We can plot the above ΔE as a function of N (Fig. 7.5), and find where the curve crosses the x axis. This yields equilibrium state around $N=12$. This means that for $N < 12$, a mono-atomic Fe layer is more stable while for $N > 12$ a 3D nanoparticle is favored. This is in excellent agreement with the experimental observation in which the largest observed diameters are around 10 atoms.

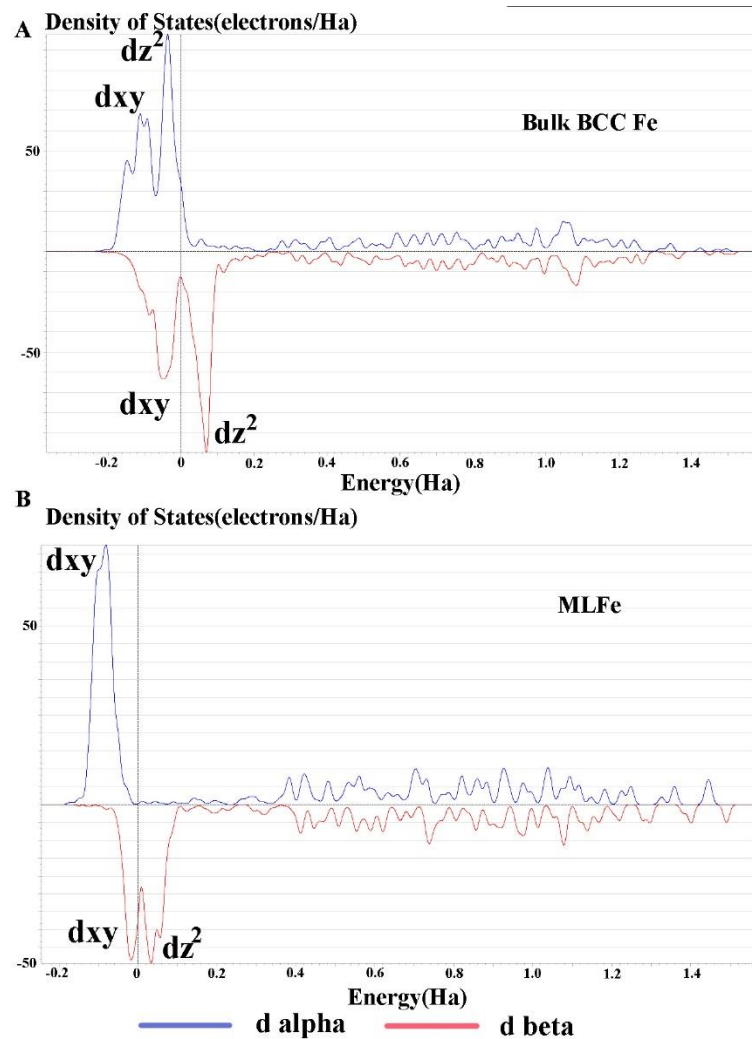


Figure 7.6 (A) Partial density of states (pDOS) for bulk BCC Fe and (B) pDOS for a monoatomic layer of Fe with a square lattice having a lattice spacing 2.65 Å. The colors of the lines are illustrated below each figure, i.e. d alpha stands for the spin up orbital for d electrons while d beta stands for the spin down orbital for d electrons.

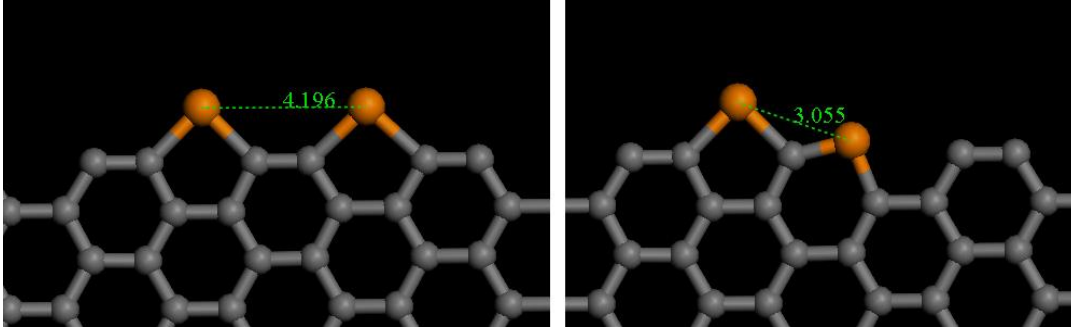


Figure 7.7 The two most probable configurations for Fe atom placement at the interface of a membrane based on DFT calculations

The band structure of a freestanding monolayer Fe membrane is examined through spin polarized DFT calculations using the experimentally derived lattice constant (2.65 Å) and compare it to the (calculated) band structure of bulk BCC Fe. By comparing the partial density of states one can see for the spin up (majority) orbitals, the d_{z^2} orbital for 2D Fe is significantly smaller than for bulk BCC Fe in figure 7.6. This is primarily due to the 2D nature of the Fe membrane since the d_{z^2} orbital is out-of-plane while the d_{xy} orbital is in-plane. The first principles calculations show a significantly enhanced magnetic moment for single atom thick Fe membranes (3.08 μ_B) as compared to bulk BCC Fe (2.1 μ_B) in good agreement with previously calculated values²⁷⁸. The total magnetic moment is slightly decreased by the Fe-C boundary effect but still much larger than the bulk value. For a typical five member ring containing an Fe atom, the magnetic moments are 2.36 and 3.03 μ_B , respectively (see Fig. 7.7). Therefore, it is reasonable to assume that when the Fe membrane is embedded in graphene, its magnetic property will be affected by the boundary Fe atoms, none the less, the total magnetic moment is still much larger than for its bulk counterpart.

7.4 Conclusions

In summary, the free-standing mono-atomic suspended Fe membranes is studied theoretically. These 2D Fe nano-membranes are shown to have a square lattice with a 2.65 Å lattice constant at room temperature. We also estimate that the largest stable membrane should be ca. 12 atoms wide or $3 \times 3 \text{ nm}^2$ which is in excellent agreement with the experimental observation. Besides, from DFTB and DFT simulations, the possibility of C embedded into the Fe membrane can be fully excluded which agrees with electron energy loss spectroscopy (EELS) measurement. A significantly enhanced magnetic moment for single atom thick Fe membranes (3.08 μ_B) is found by DFT as compared to bulk BCC Fe (2.1 μ_B), because of the 2D nature of the Fe membrane since the d_{z^2} orbital

is out-of-plane while the d_{xy} orbital is in-plane. These studies provide valuable data for further more accurate and in-depth theoretical investigations. The potential of perforated graphene as a support for 2D membranes is shown and one can anticipate new 2D structures from a variety of elements to emerge.

Reference

- (1) Heath, J. R.; O'Brien, S. C.; Zhang, Q.; Liu, Y.; Curl, R. F.; Tittel, F. K.; Smalley, R. E. *J Am Chem Soc* **1985**, *107*, 7779.
- (2) Kratschmer, W.; Lamb, L. D.; Fostiropoulos, K.; Huffman, D. R. *Nature* **1990**, *347*, 354.
- (3) Klingeler, R.; Kann, G.; Wirth, I.; Eisebitt, S.; Bechthold, P. S.; Neeb, M.; Eberhardt, W. *The Journal of Chemical Physics* **2001**, *115*, 7215.
- (4) Chai, Y.; Guo, T.; Jin, C.; Haufler, R. E.; Chibante, L. P. F.; Fure, J.; Wang, L.; Alford, J. M.; Smalley, R. E. *The Journal of Physical Chemistry* **1991**, *95*, 7564.
- (5) Akasaka, T.; Nagase, S.; Kobayashi, K.; Wälchli, M.; Yamamoto, K.; Funasaka, H.; Kako, M.; Hoshino, T.; Erata, T. *Angewandte Chemie International Edition in English* **1997**, *36*, 1643.
- (6) Popov, A. A.; Zhang, L.; Dunsch, L. *Acs Nano* **2010**, *4*, 795.
- (7) Stevenson, S.; Rice, G.; Glass, T.; Harich, K.; Cromer, F.; Jordan, M. R.; Craft, J.; Hadju, E.; Bible, R.; Olmstead, M. M.; Maitra, K.; Fisher, A. J.; Balch, A. L.; Dorn, H. C. *Nature* **1999**, *401*, 55.
- (8) Iiduka, Y.; Wakahara, T.; Nakajima, K.; Tsuchiya, T.; Nakahodo, T.; Maeda, Y.; Akasaka, T.; Mizorogi, N.; Nagase, S. *Chem Commun* **2006**, *0*, 2057.
- (9) Wang, T.-S.; Feng, L.; Wu, J.-Y.; Xu, W.; Xiang, J.-F.; Tan, K.; Ma, Y.-H.; Zheng, J.-P.; Jiang, L.; Lu, X.; Shu, C.-Y.; Wang, C.-R. *Journal of the American Chemical Society* **2010**, *132*, 16362.

- (10) Stevenson, S.; Mackey, M. A.; Stuart, M. A.; Phillips, J. P.; Easterling, M. L.; Chancellor, C. J.; Olmstead, M. M.; Balch, A. L. *J Am Chem Soc* **2008**, *130*, 11844.
- (11) Dunsch, L.; Yang, S.; Zhang, L.; Svitova, A.; Oswald, S.; Popov, A. A. *J Am Chem Soc* **2010**, *132*, 5413.
- (12) Komatsu, K.; Murata, M.; Murata, Y. *Science* **2005**, *307*, 238.
- (13) Yamamoto, K.; Saunders, M.; Khong, A.; Cross, R. J.; Grayson, M.; Gross, M. L.; Benedetto, A. F.; Weisman, R. B. *Journal of the American Chemical Society* **1999**, *121*, 1591.
- (14) Dunsch, L.; Krause, M.; Noack, J.; Georgi, P. *Journal of Physics and Chemistry of Solids* **2004**, *65*, 309.
- (15) Dunsch, L.; Georgi, P.; Krause, M.; Wang, C. R. *Synthetic Metals* **2003**, *135*, 761.
- (16) Yang, S.; Kalbac, M.; Popov, A.; Dunsch, L. *Chemistry-a European Journal* **2006**, *12*, 7856.
- (17) Yang, S. F.; Dunsch, L. *Journal of Physical Chemistry B* **2005**, *109*, 12320.
- (18) Dunsch, L.; Krause, M.; Noack, J.; Georgi, P. *Journal of Physics and Chemistry of Solids* **2004**, *65*, 309.
- (19) Jin, P.; Tang, C. C.; Chen, Z. F. *Coordination Chemistry Reviews* **2014**, *270*, 89.
- (20) Zhang, J.; Bowles, F. L.; Bearden, D. W.; Ray, W. K.; Fuhrer, T.; Ye, Y.; Dixon, C.; Harich, K.; Helm, R. F.; Olmstead, M. M.; Balch, A. L.; Dorn, H. C. *Nature Chemistry* **2013**, *5*, 880.
- (21) Wang, T.; Wu, J.; Feng, Y. *Dalton Transactions* **2014**, *43*, 16270.

- (22) Wu, J.; Wang, T.; Ma, Y.; Jiang, L.; Shu, C.; Wang, C. *Journal of Physical Chemistry C* **2011**, *115*, 23755.
- (23) Stevenson, S.; Mackey, M. A.; Stuart, M. A.; Phillips, J. P.; Easterling, M. L.; Chancellor, C. J.; Olmstead, M. M.; Balch, A. L. *Journal of the American Chemical Society* **2008**, *130*, 11844.
- (24) Mercado, B. Q.; Olmstead, M. M.; Beavers, C. M.; Easterling, M. L.; Stevenson, S.; Mackey, M. A.; Coumbe, C. E.; Phillips, J. D.; Phillips, J. P.; Poblet, J. M.; Balch, A. L. *Chemical Communications* **2010**, *46*, 279.
- (25) Mercado, B. Q.; Chen, N.; Rodriguez-Forteza, A.; Mackey, M. A.; Stevenson, S.; Echegoyen, L.; Poblet, J. M.; Olmstead, M. M.; Balch, A. L. *Journal of the American Chemical Society* **2011**, *133*, 6752.
- (26) Dunsch, L.; Yang, S.; Zhang, L.; Svitova, A.; Oswald, S.; Popov, A. A. *Journal of the American Chemical Society* **2010**, *132*, 5413.
- (27) Chen, N.; Chaur, M. N.; Moore, C.; Pinzon, J. R.; Valencia, R.; Rodriguez-Forteza, A.; Poblet, J. M.; Echegoyen, L. *Chemical Communications* **2010**, *46*, 4818.
- (28) Hernandez, E.; Ordejon, P.; Terrones, H. *Phys. Rev. B* **2001**, *63*19, 193403.
- (29) Nagase, S.; Kobayashi, K.; Akasaka, T. *Theochem-J. Mol. Struct.* **1999**, *462*, 97.
- (30) Fowler, P. W.; Heine, T.; Mitchell, D.; Orlandi, G.; Schmidt, R.; Seifert, G.; Zerbetto, F. *Journal of the Chemical Society-Faraday Transactions* **1996**, *92*, 2203.
- (31) Ayuela, A.; Fowler, P. W.; Mitchell, D.; Schmidt, R.; Seifert, G.; Zerbetto, F. *J. Phys. Chem.* **1996**, *100*, 15634.

- (32) Wang, W.-W.; Dang, J.-S.; Zheng, J.-J.; Zhao, X. *J. Phys. Chem. C* **2012**, *116*, 17288.
- (33) Tan, Y.-Z.; Xie, S.-Y.; Huanh, R.-B.; Zheng, I.-S. *Nat. Chem.* **2009**, *1*, 450.
- (34) Troshin, P. A.; Avent, A. G.; Darwish, A. D.; Martsinovich, N.; Abdul-Sada, A. K.; Street, J. M.; Taylor, R. *Science* **2005**, *309*, 278.
- (35) Ioffe, I. N.; Mazaleva, O. N.; Sidorov, L. N.; Yang, S.; Wei, T.; Kemnitz, E.; Troyanov, S. I. *Inorg. Chem.* **2013**, *52*, 13821.
- (36) Ioffe, I. N.; Chen, C.; Yang, S.; Sidorov, L. N.; Kemnitz, E.; Troyanov, S. I. *Angew. Chem.-Int. Edit. Engl.* **2010**, *49*, 4784.
- (37) Yang, S.; Wang, S.; Kemnitz, E.; Troyanov, S. I. *Angew. Chem.-Int. Edit. Engl.* **2014**, *53*, 2460.
- (38) Yang, S.; Wei, T.; Wang, S.; Ioffe, I. N.; Kemnitz, E.; Troyanov, S. I. *Chem.-Asian J.* **2014**, DOI: 10.1002/asia.201402859.
- (39) Tan, Y.-Z.; Chen, R.-T.; Liao, Z.-J.; Li, J.; Zhu, F.; Lu, X.; Xie, S.-Y.; Li, J.; Huang, R.-B.; Zheng, L.-S. *Nat Commun* **2011**, *2*, 420.
- (40) Stevenson, S.; Fowler, P. W.; Heine, T.; Duchamp, J. C.; Rice, G.; Glass, T.; Harich, K.; Hajdu, E.; Bible, R.; Dorn, H. C. *Nature* **2000**, *408*, 427.
- (41) Wang, C. R.; Kai, T.; Tomiyama, T.; Yoshida, T.; Kobayashi, Y.; Nishibori, E.; Takata, M.; Sakata, M.; Shinohara, H. *Nature* **2000**, *408*, 426.
- (42) Yamada, M.; Kurihara, H.; Suzuki, M.; Guo, J. D.; Waelchli, M.; Olmstead, M. M.; Balch, A. L.; Nagase, S.; Maeda, Y.; Hasegawa, T.; Lu, X.; Akasaka, T. *J. Am. Chem. Soc.* **2014**, *136*, 7611.
- (43) Popov, A. A.; Yang, S.; Dunsch, L. *Chem. Rev.* **2013**, *113*, 5989.

- (44) Mercado, B. Q.; Beavers, C. M.; Olmstead, M. M.; Chaur, M. N.; Walker, K.; Holloway, B. C.; Echegoyen, L.; Balch, A. L. *J. Am. Chem. Soc.* **2008**, *130*, 7854.
- (45) Zhang, Y.; Ghiassi, K. B.; Deng, Q.; Samoylova, N. A.; Olmstead, M. M.; Balch, A. L.; Popov, A. A. *Angewandte Chemie-International Edition* **2015**, *54*, 495.
- (46) Fowler, P. W.; Manolopoulos, D. E. *Nature* **1992**, *355*, 428.
- (47) Fowler, P. W.; Zerbetto, F. *Chemical Physics Letters* **1995**, *243*, 36.
- (48) Nakao, K.; Kurita, N.; Fujita, M. *Phys. Rev. B* **1994**, *49*, 11415.
- (49) Kobayashi, K.; Nagase, S.; Akasaka, T. *Chemical Physics Letters* **1995**, *245*, 230.
- (50) Kobayashi, K.; Nagase, S. *Chemical Physics Letters* **1998**, *282*, 325.
- (51) Kobayashi, K.; Nagase, S. *Chemical physics letters* **1997**, *274*, 226.
- (52) Kroto, H. *Nature* **1987**, *329*, 529.
- (53) Zywietz, T. K.; Jiao, H. J.; Schleyer, P. V.; de Meijere, A. *Journal of Organic Chemistry* **1998**, *63*, 3417.
- (54) Kobayashi, K.; Nagase, S.; Yoshida, M.; Osawa, E. *Journal of the American Chemical Society* **1997**, *119*, 12693.
- (55) Yang, S.; Popov, A. A.; Dunsch, L. *Angewandte Chemie-International Edition* **2007**, *46*, 1256.
- (56) Chen, N.; Mulet-Gas, M.; Li, Y.-Y.; Stene, R. E.; Atherton, C. W.; Rodriguez-Fortea, A.; Poblet, J. M.; Echegoyen, L. *Chemical Science* **2013**, *4*, 180.
- (57) Wakahara, T.; Nikawa, H.; Kikuchi, T.; Nakahodo, T.; Rahman, G. M. A.; Tsuchiya, T.; Maeda, Y.; Akasaka, T.; Yoza, K.; Horn, E.; Yamamoto, K.;

Mizorogi, N.; Slanina, Z.; Nagase, S. *Journal of the American Chemical Society* **2006**, *128*, 14228.

(58) Kato, H.; Taninaka, A.; Sugai, T.; Shinohara, H. *Journal of the American Chemical Society* **2003**, *125*, 7782.

(59) Lu, X.; Nikawa, H.; Tsuchiya, T.; Maeda, Y.; Ishitsuka, M. O.; Akasaka, T.; Toki, M.; Sawa, H.; Slanina, Z.; Mizorogi, N.; Nagase, S. *Angewandte Chemie-International Edition* **2008**, *47*, 8642.

(60) Yang, S.; Popov, A. A.; Dunsch, L. *Journal of Physical Chemistry B* **2007**, *111*, 13659.

(61) Beavers, C. M.; Chaur, M. N.; Olmstead, M. M.; Echegoyen, L.; Balch, A. L. *Journal of the American Chemical Society* **2009**, *131*, 11519.

(62) Ma, Y.; Wang, T.; Wu, J.; Feng, Y.; Xu, W.; Jiang, L.; Zheng, J.; Shu, C.; Wang, C. *Nanoscale* **2011**, *3*, 4955.

(63) Mercado, B. Q.; Beavers, C. M.; Olmstead, M. M.; Chaur, M. N.; Walker, K.; Holloway, B. C.; Echegoyen, L.; Balch, A. L. *Journal of the American Chemical Society* **2008**, *130*, 7854.

(64) Beavers, C. M.; Zuo, T.; Duchamp, J. C.; Harich, K.; Dorn, H. C.; Olmstead, M. M.; Balch, A. L. *Journal of the American Chemical Society* **2006**, *128*, 11352.

(65) Zuo, T.; Walker, K.; Olmstead, M. M.; Melin, F.; Holloway, B. C.; Echegoyen, L.; Dorn, H. C.; Chaur, M. N.; Chancellor, C. J.; Beavers, C. M.; Balch, A. L.; Athans, A. J. *Chemical Communications* **2008**, 1067.

(66) Zheng, H.; Zhao, X.; Ren, T.; Wang, W.-W. *Nanoscale* **2012**, *4*, 4530.

(67) Nagase, S.; Kobayashi, K.; Akasaka, T. *Journal of Molecular Structure-Theochem* **1999**, *461*, 97.

- (68) Slanina, Z.; Uhlik, F.; Nagase, S. *Journal of Physical Chemistry A* **2006**, *110*, 12860.
- (69) Zheng, H.; Zhao, X.; Wang, W.-W.; Yang, T.; Nagase, S. *Journal of Chemical Physics* **2012**, *137*.
- (70) Yang, T.; Zhao, X.; Xu, Q.; Zhou, C.; He, L.; Nagase, S. *Journal of Materials Chemistry* **2011**, *21*, 12206.
- (71) Yang, T.; Zhao, X.; Xu, Q.; Zheng, H.; Wang, W.-W.; Li, S.-T. *Dalton Transactions* **2012**, *41*, 5294.
- (72) Zhao, X.; Gao, W.-Y.; Yang, T.; Zheng, J.-J.; Li, L.-S.; He, L.; Cao, R.-J.; Nagase, S. *Inorganic Chemistry* **2012**, *51*, 2039.
- (73) Popov, A. A.; Dunsch, L. *Journal of the American Chemical Society* **2007**, *129*, 11835.
- (74) Popov, A. A. *Journal of Computational and Theoretical Nanoscience* **2009**, *6*, 292.
- (75) Rodriguez-Forteza, A.; Alegret, N.; Balch, A. L.; Poblet, J. M. *Nature Chemistry* **2010**, *2*, 955.
- (76) Popov, A. A.; Krause, M.; Yang, S.; Wong, J.; Dunsch, L. *Journal of Physical Chemistry B* **2007**, *111*, 3363.
- (77) Cao, B. P.; Wakahara, T.; Tsuchiya, T.; Kondo, M.; Maeda, Y.; Rahman, G. M. A.; Akasaka, T.; Kobayashi, K.; Nagase, S.; Yamamoto, K. *Journal of the American Chemical Society* **2004**, *126*, 9164.
- (78) Tan, K.; Lu, X. *Chem. Commun.* **2005**, 4444.
- (79) Li, F.-F.; Chen, N.; Mulet-Gas, M.; Triana, V.; Murillo, J.; Rodriguez-Forteza, A.; Poblet, J. M.; Echegoyen, L. *Chemical Science* **2013**, *4*, 3404.

- (80) Olmstead, M. M.; de Bettencourt-Dias, A.; Duchamp, J. C.; Stevenson, S.; Marciu, D.; Dorn, H. C.; Balch, A. L. *Angewandte Chemie-International Edition* **2001**, *40*, 1223.
- (81) Popov, A. A.; Dunsch, L. *Journal of the American Chemical Society* **2007**, *129*, 11835.
- (82) Zhang, J.; Fuhrer, T.; Fu, W.; Ge, J.; Bearden, D. W.; Dallas, J.; Duchamp, J.; Walker, K.; Champion, H.; Azurmendi, H.; Harich, K.; Dorn, H. C. *Journal of the American Chemical Society* **2012**, *134*, 8487.
- (83) Yang, H.; Jin, H.; Zhen, H.; Wang, Z.; Liu, Z.; Beavers, C. M.; Mercado, B. Q.; Olmstead, M. M.; Balch, A. L. *Journal of the American Chemical Society* **2011**, *133*, 6299.
- (84) Yang, H.; Jin, H.; Hong, B.; Liu, Z.; Beavers, C. M.; Zhen, H.; Wang, Z.; Mercado, B. Q.; Olmstead, M. M.; Balch, A. L. *Journal of the American Chemical Society* **2011**, *133*, 16911.
- (85) Mercado, B. Q.; Jiang, A.; Yang, H.; Wang, Z.; Jin, H.; Liu, Z.; Olmstead, M. M.; Balch, A. L. *Angewandte Chemie-International Edition* **2009**, *48*, 9114.
- (86) Yang, H.; Lu, C.; Liu, Z.; Jin, H.; Che, Y.; Olmstead, M. M.; Balch, A. L. *Journal of the American Chemical Society* **2008**, *130*, 17296.
- (87) Che, Y.; Yang, H.; Wang, Z.; Jin, H.; Liu, Z.; Lu, C.; Zuo, T.; Dorn, H. C.; Beavers, C. M.; Olmstead, M. M.; Balch, A. L. *Inorganic Chemistry* **2009**, *48*, 6004.
- (88) Popov, A. A.; Dunsch, L. *Chemistry-a European Journal* **2009**, *15*, 9707.

- (89) Meijer, G.; Bethune, D. S. *The Journal of chemical physics* **1990**, *93*, 7800.
- (90) Goroff, N. S. *Accounts of chemical research* **1996**, *29*, 77.
- (91) Zhang, Q.-L.; O'Brien, S.; Heath, J.; Liu, Y.; Curl, R.; Kroto, H.; Smalley, R. *The Journal of Physical Chemistry* **1986**, *90*, 525.
- (92) Curl, R. F.; Smalley, R. E. *Scientific American* **1991**, *265*, 54.
- (93) Smalley, R. *Accounts of chemical research* **1992**, *25*, 98.
- (94) Heath, J. In *ACS symposium series* 1991; Vol. 481, p 1.
- (95) Stone, A.; Wales, D. *Chemical Physics Letters* **1986**, *128*, 501.
- (96) Taylor, P. R.; Bylaska, E.; Weare, J. H.; Kawai, R. *Chemical physics letters* **1995**, *235*, 558.
- (97) Von Helden, G.; Hsu, M. T.; Kemper, P. R.; Bowers, M. T. *The journal of chemical physics* **1991**, *95*, 3835.
- (98) Von Helden, G.; Gotts, N. G.; Bowers, M. T. *Nature* **1993**, *363*, 60.
- (99) Shelimov, K. B.; Hunter, J. M.; Jarrold, M. F. *International Journal of Mass Spectrometry and Ion Processes* **1994**, *138*, 17.
- (100) Page, A. J.; Ding, F.; Irle, S.; Morokuma, K. *Rep. Prog. Phys.* **2015**, *78*, 036501.
- (101) Zheng, G. S.; Wang, Z.; Irle, S.; Morokuma, K. *J. Nanosci. Nanotechnol.* **2007**, *7*, 1662.
- (102) Irle, S.; Zheng, G. S.; Wang, Z.; Morokuma, K. *J. Phys. Chem. B* **2006**, *110*, 14531.
- (103) Irle, S.; Zheng, G. S.; Witek, H. A.; Morokuma, K.; Elstner, M. *Abstr. Pap. Am. Chem. Soc.* **2005**, *229*, U855.

- (104) Irle, S.; Zheng, G. S.; Elstner, M.; Morokuma, K. *Nano Lett.* **2003**, *3*, 1657.
- (105) Irle, S.; Zheng, G. S.; Elstner, M.; Morokuma, K. *Nano Letters* **2003**, *3*, 465.
- (106) Zheng, G. S.; Irle, S.; Morokuma, K. *J. Chem. Phys.* **2005**, *122*, 7.
- (107) Saha, B.; Irle, S.; Morokuma, K. *J. Phys. Chem. C* **2011**, *115*, 22707.
- (108) Seifert, G.; Joswig, J.-O. *WIREs Comput. Mol. Sci.* **2012**, *2*, 456.
- (109) Elstner, M.; Porezag, D.; Jungnickel, G.; Elsner, J.; Haugk, M.; Frauenheim, T.; Suhai, S.; Seifert, G. *Phys. Rev. B* **1998**, *58*, 7260.
- (110) Frauenheim, T.; Seifert, G.; Elstner, M.; Hajnal, Z.; Jungnickel, G.; Porezag, D.; Suhai, S.; Scholz, R. *Phys. Status Solidi B* **2000**, *217*, 41.
- (111) Kroto, H. W.; Heath, J. R.; O'Brien, S. C.; Curl, R. F.; Smalley, R. E. *Nature* **1985**, *318*, 162.
- (112) Goeres, A.; Sedlmayr, E. *Chemical physics letters* **1991**, *184*, 310.
- (113) Wakabayashi, T.; Achiba, Y. *Chemical physics letters* **1992**, *190*, 465.
- (114) Lu, X.; Feng, L.; Akasaka, T.; Nagase, S. *Chemical Society Reviews* **2012**, *41*, 7723.
- (115) Rodriguez-Forteza, A.; Balch, A. L.; Poblet, J. M. *Chem. Soc. Rev.* **2011**, *40*, 3551.
- (116) Yamaguchi, Y.; Maruyama, S. *Eur. Phys. J. D* **1999**, *9*, 385.
- (117) Maruyama, S.; Yamaguchi, Y.; Kohno, M.; Yoshida, T. *Fullerene Sci. Technol.* **1999**, *7*, 621.
- (118) Hohenberg, P.; Kohn, W. *Physical review* **1964**, *136*, B864.
- (119) Kohn, W.; Sham, L. J. *Physical Review* **1965**, *140*, A1133.
- (120) Perdew, J. P.; Zunger, A. *Physical Review B* **1981**, *23*, 5048.

- (121) Perdew, J. P.; Burke, K.; Ernzerhof, M. *Physical Review Letters* **1996**, *77*, 3865.
- (122) Irle, S.; Zheng, G. S.; Wang, Z.; Morokuma, K. *Journal of Physical Chemistry B* **2006**, *110*, 14531.
- (123) Zhao, J.; Deng, Q.; Avdoshenko, S. M.; Fu, L.; Eckert, J.; Rümmeli, M. H. *Proceedings of the National Academy of Sciences* **2014**, *111*, 15641.
- (124) Heine, T.; Seifert, G.; Fowler, P. W.; Zerbetto, F. *Journal of Physical Chemistry A* **1999**, *103*, 8738.
- (125) Enyashin, A.; Ivanovskii, A. *Chemical Physics Letters* **2011**, *509*, 143.
- (126) Zhao, J.; Deng, Q.; Bachmatiuk, A.; Sandeep, G.; Popov, A.; Eckert, J.; Rümmeli, M. H. *Science* **2014**, *343*, 1228.
- (127) Addicoat, M. A.; Stefanovic, R.; Webber, G. B.; Atkin, R.; Page, A. J. *Journal of chemical theory and computation* **2014**, *10*, 4633.
- (128) Elstner, M. *Theoretical Chemistry Accounts* **2006**, *116*, 316.
- (129) Nosé, S. *Molecular physics* **1984**, *52*, 255.
- (130) Nosé, S. *The Journal of chemical physics* **1984**, *81*, 511.
- (131) Hoover, W. G. *Physical Review A* **1985**, *31*, 1695.
- (132) Martyna, G. J.; Klein, M. L.; Tuckerman, M. *The Journal of chemical physics* **1992**, *97*, 2635.
- (133) Foulkes, W. M. C.; Haydock, R. *Physical review B* **1989**, *39*, 12520.
- (134) Porezag, D.; Frauenheim, T.; Kohler, T.; Seifert, G.; Kaschner, R. *Physical review. B, Condensed matter* **1995**, *51*, 12947.
- (135) Eschrig, H. *Optimized LCAO Method and the Electronic Structure of Extended Systems. Series: Research Reports in Physics, ISBN: 978-3-662-02564-2. Springer Berlin Heidelberg (Berlin, Heidelberg), Edited by Helmut Eschrig* **1989**, *1*.

- (136) Frauenheim, T.; Weich, F.; Köhler, T.; Uhlmann, S.; Porezag, D.; Seifert, G. *Physical Review B* **1995**, *52*, 11492.
- (137) Sitch, P.; Frauenheim, T.; Jones, R. *Journal of Physics: Condensed Matter* **1996**, *8*, 6873.
- (138) Widany, J.; Weich, F.; Köhler, T.; Porezag, D.; Frauenheim, T. *diamond and Related Materials* **1996**, *5*, 1031.
- (139) Weich, F.; Widany, J.; Frauenheim, T. *Physical review letters* **1997**, *78*, 3326.
- (140) Gutierrez, R.; Frauenheim, T.; Köhler, T.; Seifert, G. *Journal of Materials Chemistry* **1996**, *6*, 1657.
- (141) Haugk, M.; Elsner, J.; Frauenheim, T. *Journal of Physics: Condensed Matter* **1997**, *9*, 7305.
- (142) Pariser, R. *The Journal of Chemical Physics* **1956**, *24*, 250.
- (143) Ohno, K. *Theoretica chimica acta* **1964**, *2*, 219.
- (144) Klopman, G. *Journal of the American Chemical Society* **1964**, *86*, 4550.
- (145) Mataga, N.; Nishimoto, K. *Z. phys. Chem* **1957**, *13*, 140.
- (146) Popov, A. A.; Yang, S.; Dunsch, L. *Chemical Reviews* **2013**, *113*, 5989.
- (147) Zhang, J.; Fuhrer, T.; Fu, W.; Ge, J.; Bearden, D. W.; Dallas, J. L.; Duchamp, J. C.; Walker, K. L.; Champion, H.; Azurmendi, H. F.; Harich, K.; Dorn, H. C. *Journal of the American Chemical Society* **2012**, *134*, 8487.
- (148) Popov, A. A.; Dunsch, L. *Chem.-Eur. J.* **2009**, *15*, 9707.
- (149) Laikov, D. N. *Chemical Physics Letters* **2005**, *416*, 116.
- (150) Laikov, D. N.; Ustynyuk, Y. A. *Russian Chemical Bulletin* **2005**, *54*, 820.
- (151) Laikov, D. N. *Chemical Physics Letters* **1997**, *281*, 151.

- (152) Humphrey, W.; Dalke, A.; Schulten, K. *J. Molec. Graphics* **1996**, *14*, 33.
- (153) Yang, S.; Liu, F.; Chen, C.; Jiao, M.; Wei, T. *Chemical Communications* **2011**, *47*, 11822.
- (154) Chen, N.; Beavers, C. M.; Mulet-Gas, M.; Rodriguez-Forteza, A.; Munoz, E. J.; Li, Y.-Y.; Olmstead, M. M.; Balch, A. L.; Poblet, J. M.; Echegoyen, L. *Journal of the American Chemical Society* **2012**, *134*, 7851.
- (155) Beavers, C. M.; Jin, H.; Yang, H.; Wang, Z.; Wang, X.; Ge, H.; Liu, Z.; Mercado, B. Q.; Olmstead, M. M.; Balch, A. L. *Journal of the American Chemical Society* **2011**, *133*, 15338.
- (156) Kurihara, H.; Lu, X.; Iiduka, Y.; Nikawa, H.; Hachiya, M.; Mizorogi, N.; Slanina, Z.; Tsuchiya, T.; Nagase, S.; Akasaka, T. *Inorganic Chemistry* **2012**, *51*, 746.
- (157) Krause, M.; Hulman, M.; Kuzmany, H.; Dubay, O.; Kresse, G.; Vietze, K.; Seifert, G.; Wang, C.; Shinohara, H. *Physical Review Letters* **2004**, *93*.
- (158) Feng, Y.; Wang, T.; Wu, J.; Feng, L.; Xiang, J.; Ma, Y.; Zhang, Z.; Jiang, L.; Shu, C.; Wang, C. *Nanoscale* **2013**, *5*, 6704.
- (159) Kurihara, H.; Lu, X.; Iiduka, Y.; Mizorogi, N.; Slanina, Z.; Tsuchiya, T.; Akasaka, T.; Nagase, S. *Journal of the American Chemical Society* **2011**, *133*, 2382.
- (160) Iiduka, Y.; Wakahara, T.; Nakajima, K.; Tsuchiya, T.; Nakahodo, T.; Maeda, Y.; Akasaka, T.; Mizorogi, N.; Nagase, S. *Chemical Communications* **2006**, 2057.
- (161) Wang, C. R.; Kai, T.; Tomiyama, T.; Yoshida, T.; Kobayashi, Y.; Nishibori, E.; Takata, M.; Sakata, M.; Shinohara, H. *Angewandte Chemie-International Edition* **2001**, *40*, 397.
- (162) Nishimoto, Y.; Wang, Z.; Morokuma, K.; Irle, S. *Physica Status Solidi B-Basic Solid State Physics* **2012**, *249*, 324.

- (163) Inoue, T.; Tomiyama, T.; Sugai, T.; Shinohara, H. *Chemical Physics Letters* **2003**, *382*, 226.
- (164) Yang, T.; Zhao, X.; Li, S.-T.; Nagase, S. *Inorganic Chemistry* **2012**, *51*, 11223.
- (165) Burke, B. G.; Chan, J.; Williams, K. A.; Fuhrer, T.; Fu, W.; Dorn, H. C.; Puretzky, A. A.; Geohegan, D. B. *Physical Review B* **2011**, *83*.
- (166) Cao, B. P.; Hasegawa, M.; Okada, K.; Tomiyama, T.; Okazaki, T.; Suenaga, K.; Shinohara, H. *Journal of the American Chemical Society* **2001**, *123*, 9679.
- (167) Yumura, T.; Sato, Y.; Suenaga, K.; Iijima, S. *Journal of Physical Chemistry B* **2005**, *109*, 20251.
- (168) Tan, K.; Lu, X. *Chemical Communications* **2005**, 4444.
- (169) Li, F.-F.; Chen, N.; Mulet-Gas, M.; Triana, V.; Murillo, J.; Rodriguez-Fortea, A.; Poblet, J. M.; Echegoyen, L. *Chemical Science* **2013**, *4*, 3404.
- (170) Yang, S.; Chen, C.; Popov, A.; Zhang, W.; Liu, F.; Dunsch, L. *Chemical Communications* **2009**, 6391.
- (171) Chen, C.; Liu, F.; Li, S.; Wang, N.; Popov, A. A.; Jiao, M.; Wei, T.; Li, Q.; Dunsch, L.; Yang, S. *Inorganic Chemistry* **2012**, *51*, 3039.
- (172) Deng, Q.; Junghans, K.; Popov, A. A. *Theoretical Chemistry Accounts* **2015**, *134*, 1.
- (173) Krause, M.; Ziegls, F.; Popov, A. A.; Dunsch, L. *ChemPhysChem* **2007**, *8*, 537.
- (174) Wang, T.-S.; Chen, N.; Xiang, J.-F.; Li, B.; Wu, J.-Y.; Xu, W.; Jiang, L.; Tan, K.; Shu, C.-Y.; Lu, X.; Wang, C.-R. *J. Am. Chem. Soc.* **2009**, *131*, 16646.
- (175) Tan, K.; Lu, X.; Wang, C. R. *J. Phys. Chem. B* **2006**, *110*, 11098.

- (176) Feng, Y.; Wang, T.; Wu, J.; Zhang, Z.; Jiang, L.; Han, H.; Wang, C. *Chem. Commun.* **2014**, *50*, 12166.
- (177) Mercado, B. Q.; Olmstead, M. M.; Beavers, C. M.; Easterling, M. L.; Stevenson, S.; Mackey, M. A.; Coumbe, C. E.; Phillips, J. D.; Phillips, J. P.; Poblet, J. M.; Balch, A. L. *Chem. Commun.* **2010**, *46*, 279.
- (178) Suzuki, T.; Maruyama, Y.; Kato, T.; Kikuchi, K.; Nakao, Y.; Achiba, Y.; Kobayashi, K.; Nagase, S. *Angew. Chem.-Int. Edit. Engl.* **1995**, *34*, 1094.
- (179) Rodriguez-Forteza, A.; Alegret, N.; Balch, A. L.; Poblet, J. M. *Nat Chem* **2010**, *2*, 955.
- (180) Wang, T.; Wang, C. *Acc. Chem. Res.* **2014**, *47*, 450.
- (181) Laikov, D. N.; Ustynuk, Y. A. *Russ. Chem. Bull.* **2005**, *54*, 820.
- (182) Laikov, D. N. *Chem. Phys. Lett.* **1997**, *281*, 151.
- (183) Neese, F. *University of Bonn* **2008**.
- (184) Keith, T. A. In *AIMAll (Version 14.04.17)*, <http://aim.tkgristmill.com> 2014.
- (185) Lu, Q.; Song, W.; Meng, J.; Wan, J. *J. Mol. Model.* **2013**, *19*, 1205.
- (186) Kurihara, H.; Lu, X.; Iiduka, Y.; Mizorogi, N.; Slanina, Z.; Tsuchiya, T.; Nagase, S.; Akasaka, T. *Chem. Commun.* **2012**, *48*, 1290.
- (187) Valencia, R.; Rodriguez-Forteza, A.; Stevenson, S.; Balch, A. L.; Poblet, J. M. *Inorg. Chem.* **2009**, *48*, 5957.
- (188) Popov, A. A.; Avdoshenko, S. M.; Pendás, A. M.; Dunsch, L. *Chem. Commun.* **2012**, *48*, 8031.
- (189) Popov, A. A.; Chen, N.; Pinzón, J. R.; Stevenson, S.; Echegoyen, L. A.; Dunsch, L. *J. Am. Chem. Soc.* **2012**, *134*, 19607.
- (190) Popov, A. A.; Zhang, L.; Dunsch, L. *ACS Nano* **2010**, *4*, 795.

- (191) Schleyer, P. v. R.; Maerker, C.; Dransfeld, A.; Jiao, H.; Hommes, N. J. R. v. E. *J. Am. Chem. Soc.* **1996**, *118*, 6317.
- (192) Popov, A. A.; Kästner, C.; Krause, M.; Dunsch, L. *Fullerenes, Nanotubes and Carbon Nanostructures* **2014**, *22*, 202.
- (193) Krause, M.; Kuzmany, H.; Georgi, P.; Dunsch, L.; Vietze, K.; Seifert, G. *J. Chem. Phys.* **2001**, *115*, 6596.
- (194) Cao, B. P.; Wakahara, T.; Tsuchiya, T.; Kondo, M.; Maeda, Y.; Rahman, G. M. A.; Akasaka, T.; Kobayashi, K.; Nagase, S.; Yamamoto, K. *J. Am. Chem. Soc.* **2004**, *126*, 9164.
- (195) Yamada, M.; Wakahara, T.; Tsuchiya, T.; Maeda, Y.; Kako, M.; Akasaka, T.; Yoza, K.; Horn, E.; Mizorogi, N.; Nagase, S. *Chem. Commun.* **2008**, 558.
- (196) Olmstead, M. M.; de Bettencourt-Dias, A.; Duchamp, J. C.; Stevenson, S.; Marciu, D.; Dorn, H. C.; Balch, A. L. *Angew. Chem.-Int. Edit.* **2001**, *40*, 1223.
- (197) Popov, A. A.; Krause, M.; Yang, S. F.; Wong, J.; Dunsch, L. *J. Phys. Chem. B* **2007**, *111*, 3363.
- (198) Beavers, C. M.; Chaur, M. N.; Olmstead, M. M.; Echegoyen, L.; Balch, A. L. *J. Am. Chem. Soc.* **2009**, *131*, 11519.
- (199) Zhang, J.; Bearden, D. W.; Fuhrer, T.; Xu, L.; Fu, W.; Zuo, T.; Dorn, H. C. *J. Am. Chem. Soc.* **2013**, *135*, 3351.
- (200) Ma, Y.; Wang, T.; Wu, J.; Feng, Y.; Xu, W.; Jiang, L.; Zheng, J.; Shu, C.; Wang, C. *Nanoscale* **2011**, *3*, 4955.
- (201) Mulet-Gas, M.; Rodríguez-Fortea, A.; Echegoyen, L.; Poblet, J. M. *Inorg. Chem.* **2013**, *52*, 1954.
- (202) Yumura, T.; Sato, Y.; Suenaga, K.; Iijima, S. *J. Phys. Chem. B* **2005**, *109*, 20251.

- (203) Hino, S.; Kato, M.; Yoshimura, D.; Moribe, H.; Umemoto, H.; Ito, Y.; Sugai, T.; Shinohara, H.; Otani, M.; Yoshimoto, Y.; Okada, S. *Phys. Rev. B* **2007**, *75*, 125418.
- (204) Sato, Y.; Yumura, T.; Suenaga, K.; Moribe, H.; Nishide, D.; Ishida, M.; Shinohara, H.; Iijima, S. *Phys. Rev. B* **2006**, *73*, 193401.
- (205) Kurihara, H.; Lu, X.; Iiduka, Y.; Mizorogi, N.; Slanina, Z.; Tsuchiya, T.; Akasaka, T.; Nagase, S. *J. Am. Chem. Soc.* **2011**, *133*, 2382.
- (206) Grimme, S.; Antony, J.; Ehrlich, S.; Krieg, H. *J. Chem. Phys.* **2010**, *132*, 154104.
- (207) Grimme, S.; Ehrlich, S.; Goerigk, L. *J. Comput. Chem.* **2011**, *32*, 1456.
- (208) Pantazis, D. A.; Neese, F. *J. Chem. Theory Comput.* **2009**, *5*, 2229.
- (209) Pantazis, D. A.; Chen, X.-Y.; Landis, C. R.; Neese, F. *J. Chem. Theory Comput.* **2008**, *4*, 908.
- (210) Neese, F. *WIREs Comput. Mol. Sci.* **2012**, *2*, 73.
- (211) Stevenson, S.; Rose, C. B.; Maslenikova, J. S.; Villarreal, J. R.; Mackey, M. A.; Mercado, B. Q.; Chen, K.; Olmstead, M. M.; Balch, A. L. *Inorg. Chem.* **2012**, *51*, 13096.
- (212) Dunsch, L.; Yang, S. *Small* **2007**, *3*, 1298.
- (213) Yang, S. F.; Dunsch, L. *J. Phys. Chem. B* **2005**, *109*, 12320.
- (214) Zhang, J.; Stevenson, S.; Dorn, H. C. *Acc. Chem. Res.* **2013**, *46*, 1548.
- (215) Yang, S. F.; Dunsch, L. *Chem.-Eur. J.* **2006**, *12*, 413.
- (216) Bettinger, H. F.; Yakobson, B. I.; Scuseria, G. E. *J. Am. Chem. Soc.* **2003**, *125*, 5572.
- (217) Choi, W. I.; Kim, G.; Han, S.; Ihm, J. *Phys. Rev. B* **2006**, *73*, 4.

- (218) Dunk, P. W.; Kaiser, N. K.; Hendrickson, C. L.; Quinn, J. P.; Ewels, C. P.; Nakanishi, Y.; Sasaki, Y.; Shinohara, H.; Marshall, A. G.; Kroto, H. W. *Nat Commun* **2012**, *3*, 855.
- (219) Svitova, A. L.; Popov, A. A.; Dunsch, L. *Inorg. Chem.* **2013**, *52*, 3368.
- (220) Iiduka, Y.; Wakahara, T.; Nakajima, K.; Tsuchiya, T.; Nakahodo, T.; Maeda, Y.; Akasaka, T.; Mizorogi, N.; Nagase, S. *Chem. Commun.* **2006**, 2057.
- (221) Maggini, M.; Scorrano, G.; Prato, M. *Journal of the American Chemical Society* **1993**, *115*, 9798.
- (222) Osuna, S.; Swart, M.; Solà, M. *Phys. Chem. Chem. Phys.* **2011**, *13*, 3585.
- (223) Cardona, C. M.; Kitaygorodskiy, A.; Echegoyen, L. *Journal of the American Chemical Society* **2005**, *127*, 10448.
- (224) Aroua, S.; Yamakoshi, Y. *J. Am. Chem. Soc.* **2012**, *134*, 20242.
- (225) Chen, N.; Zhang, E. Y.; Tan, K.; Wang, C. R.; Lu, X. *Org. Lett.* **2007**, *9*, 2011.
- (226) Aroua, S.; Garcia-Borràs, M.; Osuna, S.; Yamakoshi, Y. *Chem.-Eur. J.* **2014**, *20*, 14032.
- (227) Cai, T.; Slobodnick, C.; Xu, L.; Harich, K.; Glass, T. E.; Chancellor, C.; Fettinger, J. C.; Olmstead, M. M.; Balch, A. L.; Gibson, H. W.; Dorn, H. C. *J. Am. Chem. Soc.* **2006**, *128*, 6486.
- (228) Rodriguez-Fortea, A.; Campanera, J. M.; Cardona, C. M.; Echegoyen, L.; Poblet, J. M. *Angew. Chem.-Int. Edit.* **2006**, *45*, 8176.
- (229) Aroua, S.; Garcia-Borràs, M.; Bölter, M. F.; Osuna, S.; Yamakoshi, Y. *J. Am. Chem. Soc.* **2014**, DOI: 10.1021/ja511008z.
- (230) Haddon, R. C.; Scott, L. T. *Pure Appl. Chem.* **1986**, *58*, 137.

- (231) Zhang, Y.; Ghiassi, K. B.; Deng, Q.; Samoylova, N. A.; Olmstead, M. M.; Balch, A. L.; Popov, A. A. *Angew. Chem.-Int. Edit. Engl.* **2015**, *52*, 495.
- (232) Olmstead, M. M.; Lee, H. M.; Duchamp, J. C.; Stevenson, S.; Marciu, D.; Dorn, H. C.; Balch, A. L. *Angew. Chem.-Int. Edit.* **2003**, *42*, 900.
- (233) Bingel, C. *Chem. Ber.-Recl.* **1993**, *126*, 1957.
- (234) Hirsch, A.; Lamparth, I.; Karfunkel, H. R. *Angew. Chem.-Int. Edit. Engl.* **1994**, *33*, 437.
- (235) Hirsch, A.; Brettreich, M. *Fullerenes. Chemistry and Reactions.*; Wiley-VCH Verlag GmbH & Co. KGaA: Weinheim, 2005.
- (236) Cai, T.; Xu, L.; Shu, C.; Champion, H. A.; Reid, J. E.; Anklin, C.; Anderson, M. R.; Gibson, H. W.; Dorn, H. C. *J. Am. Chem. Soc.* **2008**, *130*, 2136.
- (237) Lukoyanova, O.; Cardona, C. M.; Rivera, J.; Lugo-Morales, L. Z.; Chancellor, C. J.; Olmstead, M. M.; Rodriguez-Forteza, A.; Poblet, J. M.; Balch, A. L.; Echegoyen, L. *J. Am. Chem. Soc.* **2007**, *129*, 10423.
- (238) Pinzon, J. R.; Zuo, T. M.; Echegoyen, L. *Chem.-Eur. J.* **2010**, *16*, 4864.
- (239) Alegret, N.; Rodríguez-Forteza, A.; Poblet, J. M. *Chem.-Eur. J.* **2013**, *19*, 5061.
- (240) Alegret, N.; Chaur, M. N.; Santos, E.; Rodríguez-Forteza, A.; Echegoyen, L.; Poblet, J. M. *J. Org. Chem.* **2010**, *75*, 8299.
- (241) Cai, T.; Xu, L.; Shu, C.; Reid, J. E.; Gibson, H. W.; Dorn, H. C. *J. Phys. Chem. C* **2008**, *112*, 19203.
- (242) Kroto, H. W. *Nature* **1987**, *329*, 529.
- (243) Laszlo, I. *Europhys. Lett.* **1998**, *44*, 741.

- (244) Junghans, K.; Schlesier, C.; Kostanyan, A.; Samoylova, N. A.; Deng, Q.; Rosenkranz, M.; Schiemenz, S.; Westerström, R.; Greber, T.; Büchner, B. *Angewandte Chemie International Edition* **2015**.
- (245) Aradi, B.; Hourahine, B.; Frauenheim, T. *J. Phys. Chem. A* **2007**, *111*, 5678.
- (246) Seifert, G.; Porezag, D.; Frauenheim, T. *International Journal of Quantum Chemistry* **1996**, *58*, 185.
- (247) Zheng, G.; Witek, H. A.; Bobadova-Parvanova, P.; Irle, S.; Musaev, D. G.; Prabhakar, R.; Morokuma, K.; Lundberg, M.; Elstner, M.; Köhler, C.; Frauenheim, T. *J. Chem. Theory Comput.* **2007**, *3*, 1349.
- (248) Nishimoto, Y.; Wang, Z.; Morokuma, K.; Irle, S. *Phys. Status Solidi B* **2011**, *249*, 324.
- (249) Rappe, A. K.; Casewit, C. J.; Colwell, K. S.; Goddard, W. A.; Skiff, W. *M. J. Am. Chem. Soc.* **1992**, *114*, 10024.
- (250) Hafner, J. *J. Comput. Chem.* **2008**, *29*, 2044.
- (251) Van Orden, A.; Saykally, R. *J. Chem. Rev.* **1998**, *98*, 2313.
- (252) Bartelmess, J.; Giordani, S. *Beilstein Journal of Nanotechnology* **2014**, *5*, 1980.
- (253) Bogana, M. P.; Colombo, L. *Appl. Phys. A-Mater. Sci. Process.* **2007**, *86*, 275.
- (254) Lange, H.; Sioda, M.; Huczko, A.; Zhu, Y.; Kroto, H. W.; Walton, D. R. *M. Carbon* **2003**, *41*, 1617.
- (255) Marks, N. A.; Lattemann, M.; McKenzie, D. R. *Phys. Rev. Lett.* **2012**, *108*, 075503.

- (256) Zhang, Y.; Ghiassi, K. B.; Deng, Q.; Samoylova, N. A.; Olmstead, M. M.; Balch, A. L.; Popov, A. A. *Angewandte Chemie International Edition* **2015**, *54*, 495.
- (257) Yamaguchi, Y.; Maruyama, S. *Chemical Physics Letters* **1998**, *286*, 336.
- (258) Dunk, P. W.; Kaiser, N. K.; Hendrickson, C. L.; Quinn, J. P.; Ewels, C. P.; Nakanishi, Y.; Sasaki, Y.; Shinohara, H.; Marshall, A. G.; Kroto, H. W. *Nature Communications* **2012**, *3*.
- (259) Irle, S.; Zheng, G.; Wang, Z.; Morokuma, K. *Nano* **2007**, *2*, 21.
- (260) Rodriguez-Fortea, A.; Irle, S.; Poblet, J. M. *Wiley Interdisciplinary Reviews-Computational Molecular Science* **2011**, *1*, 350.
- (261) Saha, B.; Shindo, S.; Irle, S.; Morokuma, K. *Acs Nano* **2009**, *3*, 2241.
- (262) Zheng, G. S.; Irle, S.; Elstner, M.; Morokuma, K. *Journal of Physical Chemistry A* **2004**, *108*, 3182.
- (263) Girit, Ç. Ö.; Meyer, J. C.; Erni, R.; Rossell, M. D.; Kisielowski, C.; Yang, L.; Park, C.-H.; Crommie, M.; Cohen, M. L.; Louie, S. G. *science* **2009**, *323*, 1705.
- (264) Koskinen, P.; Malola, S.; Häkkinen, H. *Physical Review B* **2009**, *80*, 073401.
- (265) He, K.; Robertson, A. W.; Fan, Y.; Allen, C. S.; Lin, Y.-C.; Suenaga, K.; Kirkland, A. I.; Warner, J. H. *ACS nano* **2015**.
- (266) Deng, Q.; Junghans, K.; Popov, A. *Theoretical Chemistry Accounts* **2015**, *134*, 1.
- (267) Churilov, G. N.; Osipova, I. V.; Novikov, P. V.; Lopatin, V. A.; Krylov, A. S.; Tomashevich, Y. V.; Petrakovskaya, E. A. *Fullerenes Nanotubes and Carbon Nanostructures* **2010**, *18*, 584.

- (268) Marc, M.-G.; Abella, L.; Dunk, P. W.; Rodriguez-Forteza, A.; Kroto, H. W.; Poblet, J. M. *Chem. Sci.* **2015**, *6*, 675.
- (269) Dunk, P. W.; Kaiser, N. K.; Mulet-Gas, M.; Rodríguez-Forteza, A.; Poblet, J. M.; Shinohara, H.; Hendrickson, C. L.; Marshall, A. G.; Kroto, H. W. *J. Am. Chem. Soc.* **2012**, *134*, 9380.
- (270) Guo, T.; Diener, M. D.; Chai, Y.; Alford, M. J.; Haufler, R. E.; McClure, S. M.; Ohno, T.; Weaver, J. H.; Scuseria, G. E.; Smalley, R. E. *Science* **1992**, *257*, 1661.
- (271) Novoselov, K. S.; Geim, A. K.; Morozov, S. V.; Jiang, D.; Zhang, Y.; Dubonos, S. V.; Grigorieva, I. V.; Firsov, A. A. *Science* **2004**, *306*, 666.
- (272) Jin, C.; Lin, F.; Suenaga, K.; Iijima, S. *Physical Review Letters* **2009**, *102*.
- (273) Komsa, H.-P.; Krasheninnikov, A. V. *Journal of Physical Chemistry Letters* **2012**, *3*, 3652.
- (274) Qian, D.; Jin, X. F.; Barthel, J.; Klaua, M.; Kirschner, J. *Physical Review Letters* **2001**, *87*, art. no.
- (275) Wedler, G.; Schneider, C. M.; Trampert, A.; Koch, R. *Physical Review Letters* **2004**, *93*.
- (276) Ohnishi, H.; Kondo, Y.; Takayanagi, K. *Nature* **1998**, *395*, 780.
- (277) Lagos, M. J.; Sato, F.; Galvao, D. S.; Ugarte, D. *Physical Review Letters* **2011**, *106*.
- (278) Izquierdo, J.; Vega, A.; Balbas, L. C.; Sanchez-Portal, D.; Junquera, J.; Artacho, E.; Soler, J. M.; Ordejon, P. *Physical Review B* **2000**, *61*, 13639.
- (279) Lorenz, R.; Hafner, J. *Physical Review B* **1996**, *54*, 15937.
- (280) Lu, W. C.; Zhang, K. M.; Xie, X. D. *Physical Review B* **1993**, *48*, 18159.

- (281) Gay, J. G.; Richter, R. *Physical Review Letters* **1986**, *56*, 2728.
- (282) Wuttig, M.; Thomassen, J. *Surface Science* **1993**, *282*, 237.
- (283) Lehnert, A.; Dennler, S.; Blonski, P.; Rusponi, S.; Etzkorn, M.; Moulas, G.; Bencok, P.; Gambardella, P.; Brune, H.; Hafner, J. *Physical Review B* **2010**, *82*.
- (284) Robertson, A. W.; Montanari, B.; He, K.; Kim, J.; Allen, C. S.; Wu, Y. A.; Olivier, J.; Neethling, J.; Harrison, N.; Kirkland, A. I.; Warner, J. H. *Nano Letters* **2013**, *13*, 1468.
- (285) Cretu, O.; Krasheninnikov, A. V.; Rodriguez-Manzo, J. A.; Sun, L.; Nieminen, R. M.; Banhart, F. *Physical Review Letters* **2010**, *105*.
- (286) Krasheninnikov, A. V.; Lehtinen, P. O.; Foster, A. S.; Pyykko, P.; Nieminen, R. M. *Physical Review Letters* **2009**, *102*.
- (287) Wang, H.; Li, K.; Yao, Y.; Wang, Q.; Cheng, Y.; Schwingenschloegl, U.; Zhang, X. X.; Yang, W. *Scientific Reports* **2012**, *2*.
- (288) Kotakoski, J.; Jin, C.; Lehtinen, O.; Suenaga, K.; Krasheninnikov, A. *Physical Review B* **2010**, *82*, 113404.
- (289) Kotakoski, J.; Meyer, J.; Kurasch, S.; Santos-Cottin, D.; Kaiser, U.; Krasheninnikov, A. *Physical Review B* **2011**, *83*, 245420.
- (290) Banhart, F.; Li, J.; Krasheninnikov, A. *Physical Review B* **2005**, *71*, 241408.
- (291) Stankov, S.; Roehlsberger, R.; Slezak, T.; Sladeczek, M.; Sepiol, B.; Vogl, G.; Chumakov, A. I.; Rueffer, R.; Spiridis, N.; Lazewski, J.; Parlinski, K.; Korecki, J. *Physical Review Letters* **2007**, *99*.
- (292) Grimvall, G.; Magyari-Koepe, B.; Ozolins, V.; Persson, K. A. *Reviews of Modern Physics* **2012**, *84*, 945.

(293) Matsuda, Y.; Deng, W.-Q.; Goddard, W. A., III *Journal of Physical Chemistry C* **2010**, *114*, 17845.

(294) Girit, C. O.; Meyer, J. C.; Erni, R.; Rossell, M. D.; Kisielowski, C.; Yang, L.; Park, C.-H.; Crommie, M. F.; Cohen, M. L.; Louie, S. G.; Zettl, A. *Science* **2009**, *323*, 1705.

Acknowledgement

First, my deepest gratitude is given to my supervisor, Dr. Alexey Popov, for his continuous support and encouragement during my Ph.D. study. His expertise and knowledge of fullerenes science, as well as many other academic disciplines, continues to amaze me. I would like to express my sincere gratitude to Prof. Dr. Gotthard Seifert for the insightful comments and discussions. I am thankful to Prof. Dr. Bernd Büchner for the help and support during my stay in IFW. I am also very grateful to Prof. Dr. Stephan Irlé and his group at Nagoya University. I also wish to thank Prof. Dr. Thomas Heine from Jacobs University for financial support to go to Japan. Meanwhile, I would like to thank the rest of my dissertation committee.

Many thanks go to my colleagues in our department including Frank Ziegs, Dr. Stanislav M Avdoshenko, Dr Fupin Liu, Dr. Jiaxiang Chen, Dr. Evgenia Dmitrieva, Katrin Junghans, Christin Schlesier, Natalia Samoylova, Denis Krylov, Ariane Brandenburg, Sandra Schiemenz, Marco Rosenkranz, Alexander Berger, Yang Zhang, Peter Machata. It has been a great pleasure for me to work in our department. I must thank my closest friend, Dr Jiong Zhao, for his excellent experimental work and the happy time we played together.

Additionally, I would like to thank Prof. Youhua Luo in East China University of Science and Technology University and Dr. Lina Zhao, Prof. Xingfa Gao, Prof. Yuliang Zhao in Institute of High Energy Physics for guiding me to the field.

Encouragement always comes from my parents and my fiancée, Chenglei Yan, and their high expectations and belief in me always gave me confidence and unlimited power for my research. Without you, none of these would have mattered. 我永远爱你们.

List of publications

1. **Deng Q**, Popov AA. Clusters encapsulated in endohedral metallofullerenes: how strained are they? *Journal of the American Chemical Society*. 2014;136(11):4257-4264. (Chapter 3)
2. Zhao J, **Deng Q**, Bachmatiuk A, et al. Free-standing single-atom-thick iron membranes suspended in graphene pores. *Science*. 2014;343(6176):1228-1232. (Chapter 7)
3. **Deng Q**, Junghans K, Popov A. Carbide clusterfullerenes with odd number of carbon atoms: molecular and electronic structures of Sc₄C@C₈₀, Sc₄C@C₈₂, and Sc₄C₃@C₈₀. *Theoretical Chemistry Accounts*. 2015;134(2):1-12. (Chapter 4)
4. **Deng Q**, Popov AA. Prato and Bingel–Hirsch cycloaddition to heptagon-containing LaSc₂N@C_s(hept)-C₈₀: importance of pentalene units. *Chemical Communications*. 2015;51(26):5637-5640. (Chapter 5)
5. Zhang Y, Ghiassi KB, **Deng Q**, et al. Synthesis and Structure of LaSc₂N@C_s(hept)-C₈₀ with One Heptagon and Thirteen Pentagons. *Angewandte Chemie International Edition*. 2015;54(2):495-499. (Chapter 5)
6. Zhao J, **Deng Q**, Avdoshenko SM, Fu L, Eckert J, Rümmele MH. Direct in situ observations of single Fe atom catalytic processes and anomalous diffusion at graphene edges. *Proceedings of the National Academy of Sciences*. 2014;111(44):15641-15646.
7. **Deng Q**, Zhao L, Gao X, Zhang M, Luo Y, Zhao Y. Single Layer of Polymeric Cobalt Phthalocyanine: Promising Low-Cost and High-Activity Nanocatalysts for CO Oxidation. *Small*. 2013;9(20):3506-3513.
8. **Deng Q**, Zhao L, Luo Y, Zhang M, Zhao L, Zhao Y. Carbon-tuned bonding method significantly enhanced the hydrogen storage of BN–Li complexes. *Nanoscale*. 2011;3(11):4824-4829.
9. **Deng Q**, Zhao L, Luo Y, Zhang M, Jing L, Zhao Y. Ferromagnetism/antiferromagnetism transition between semihydrogenated and fully-aminated single-wall carbon nanotubes. *Nanoscale*. 2011;3(9):3743-3746.
10. **Deng Q**, Zhao L-X, Feng X-J, et al. Exploring stability of 32-atom gold–silver mixed clusters. *Computational and Theoretical Chemistry*. 2011;976(1):183-187.
11. Zhang M, Chen S, **Deng Q**, He L, Zhao L, Luo Y. Structures and electronic properties of M@ Au₆ (M= Al, Si, P, S, Cl, Ar) clusters: a density functional theory investigation. *The European Physical Journal D-Atomic, Molecular, Optical and Plasma Physics*. 2010;58(1):117-123.
12. Lu J, Zhang B, **Deng Q**, Wang J, Lu Y, Zhu W. The nature and magnitude of specific halogen bonds between iodo-perfluorobenzene and heterocyclic systems. *International Journal of Quantum Chemistry*. 2011;111(10):2352-2358.
13. **Deng Q**, Heine, T, Irle, S, Popov, A. QM/MD Simulations of dynamic metallofullerenes self-assembly with cooling gas. Submitted (Chapter 6)
14. **Deng Q**, Popov, A. Quantum dynamics simulations reveal the effect of reactive gas and growth mechanisms of carbide and cyano-clusterfullerenes. In preparation (Chapter 6)

VERSICHERUNG GEMÄSS § 5A

**der Promotionsordnung der Fakultät Mathematik und Naturwissenschaften an
der
Technischen Universität Dresden**

Hiermit versichere ich, dass ich die vorliegende Arbeit ohne unzulässige Hilfe Dritter und ohne Benutzung anderer als der angegebenen Hilfsmittel angefertigt habe; die aus fremden Quellen direkt oder indirekt übernommenen Gedanken sind als solche kenntlich gemacht. Die Arbeit wurde bisher weder im Inland noch im Ausland in gleicher oder ähnlicher Form einer anderen Prüfungsbehörde vorgelegt.

ERKLÄRUNG GEMÄSS § 5B

Die vorliegende Arbeit wurde am Leibniz-Institut für Festkörper- und Werkstoffforschung Dresden unter Betreuung von Dr. Alexey Popov und unter Betreuung von Prof. Dr. Gotthard Seifert am Technischen Universität Dresden. Dresden angefertigt.